Technische Universität München

Ingenieurfakultät Bau Geo Umwelt

Lehrstuhl für Methodik der Fernerkundung

Inversion for Limb Infrared Atmospheric Sounding

Jian Xu

Vollständiger Abdruck der von der Ingenieurfakultät Bau Geo Umwelt
der Technische Universität München zur Erlangung des akademischen Grades eines
Doktor-Ingenieurs (Dr.-Ing.)
genehmigten Dissertation.

Vorsitzender: Univ.-Prof. Dr.-Ing. Uwe Stilla

Prüfer der Dissertation:

1. Priv.-Doz. Dr.-Ing. habil. Adrian Doicu
2. Univ.-Prof. Dr.-Ing. habil. Richard Bamler
3. Univ.-Prof. Dr. rer. nat. habil. Stefan Bühler, Universität Hamburg

Die Dissertation wurde am 27.11.2014 bei der Technische Universität München
eingereicht und durch die Ingenieurfakultät Bau Geo Umwelt
am 02.04.2015 angenommen.

Abstract

Recently, several new generation instruments for far infrared and microwave remote sensing of the Earth's atmosphere have been launched, and enables us to observe the atmospheric composition based upon the thermal emission technique. These new technologies and observational data pave the way for more dedicated atmospheric research missions in the future. The impetus for my thesis is the growing interest in robust inversion algorithms for solving nonlinear inverse problems arising in atmospheric remote sensing. A retrieval code PILS (Profile Inversion for Limb Sounding) which allows for high resolution radiative transfer computations and the reconstruction of atmospheric parameters from infrared and microwave limb sounding measurements is presented.

The employed forward model simulates physically realistic limb emission spectra in an efficient manner, by taking into account the instrument performance and the measurement characteristics. In particular, automatic differentiation (AD) techniques providing a rapid and reliable implementation of exact Jacobians, are a special optimization feature of the forward model.

The inversion methodology is essentially based on a nonlinear least squares framework with adaptive (direct and iterative) numerical regularization approaches. The performance of these regularization techniques relies on the design of the regularization parameter choice methods and the a posteriori stopping rules. The characterization of the retrieval error, including the smoothing error, the noise error, and the model parameters error, assesses the accuracy of the regularized solution.

An intercomparison between PILS and the retrieval code developed by the Netherlands Institute for Space Research (SRON), dealing with radiative transfer and inversion calculations with predefined input, aims to clarify the correctness and consistency of the implementations. Small differences in the forward model mainly result from continuum absorption and the integration of the radiative transfer equation. The possible causes of discrepancies in the retrieval results are the consequences of the different inversion methods employed (regularization, a priori information) and discretization.

Retrieval results pertaining to trace gas retrievals from balloon-borne measurements by TELIS (TErahertz and submillimeter LImb Sounder) are discussed by analyzing both synthetic and real radiance spectra. A sensitivity study of hydroxyl radical (OH) retrieval is used to evaluate the inversion performance of PILS and to reveal the initial expectation of TELIS's measurement capabilities (e.g. critical error sources, data quality).

Furthermore, retrieval results of ozone (O_3), hydrogen chloride (HCl), carbon mon-

oxide (CO), and OH from the winter flights during 2009–2011 are presented to assess the performance of the TELIS 1.8 THz channel and to judge the reliability of PILS by comparing with the data products obtained by the TELIS 480–650 GHz channel and other limb sounders. These observations offer opportunities for the scientific community to make an extensive investigation into the stratospheric chemistry and dynamics, and to study the atmospheric environment over the polar region of the Northern Hemisphere.

Keywords

- Ill-posed inverse problems
- Infrared (and microwave) radiative transfer
- Automatic differentiation
- Numerical regularization
- Trace gas retrievals
- PILS
- TELIS

Zusammenfassung

In letzter Zeit kamen zur Fernerkundung der Erdatmosphäre vermehrt Instrumente zum Einsatz, mit deren Hilfe die Bestimmung von Spurengaskonzentrationen aus Ferninfrarot- und Mikrowellen-Emissionsspektren möglich war. Derartige Sensoren können als Prototyp für zukünftige satellitengestützte Atmosphärenmissionen angesehen werden. Meine Arbeit hatte das Ziel, ein zuverlässiges, flexibles und effizientes Programm für die Lösung nichtlinearer inverser Probleme der atmosphärischen Fernerkundung zu entwickeln – gerade auch im Hinblick auf die genannten neuartigen Instrumente zur Messung von Ferninfrarot- und Mikrowellen-Emissionsspektren. Das hier vorgestellte Programme PILS – Profile Inversion for Limb Sounding – erfüllt diesen Zweck. Es ermöglicht Strahlungstransfer-Modellierung mit hoher spektraler Auflösung und die Ableitung atmosphärischer Zustandsgrössen aus Messungen, die in der Horizontal-Sondierung (Limbgeometrie) gewonnen wurden.

Das Vorwärtsmodell erlaubt eine effiziente und physikalisch realistische Simulation der Limb Emissionsspektren unter Berücksichtigung der Instrument- und Messcharakteristika. Automatische Differenzierungstechniken werden genutzt und ermöglichen eine schnelle und zuverlässige Implementierung von exakten Jacobi-Matrizen.

Die Inversion basiert im Wesentlichen auf einer nichtlinearer Ausgleichsrechnung (Least Squares Fit) mit adaptiver (direkter oder iterativer) numerischen Regularisierung. Diese Vorgehensweise garantiert, dass die gewonnene Lösung nicht durch Fehler in den Messdaten dominiert wird. Der Erfolg ("performance") der Regularisierung hängt wesentlich von der Wahl des Regularisierungs-Parameters und den a posteriori Abbruch-Kriterien ab. Die Charakterisierung des Retrieval-Fehlers erlaubt eine Bewertung der Genauigkeit der Lösung gemeinsam mit einer Abschätzung der möglichen Fehlerkomponenten, d.h. Messfehler, Glättefehler und Modellfehler (Strahlungstransfer- und Instrumenten-Parameter).

Zur Verifizierung von PILS wurden Vergleiche zwischen meinen Strahlungstransfer-Modellierungen und der Inversionen und einem von SRON (Netherlands Institute for Space Research) entwickelten Programmpaket durchgeführt. Der Vergleich zeigte eine weitgehende Übereinstimmung, wobei die festgestellten kleinen Abweichungen der modellierten Spektren aus unterschiedlichen Kontinuum-Absorptionsdaten und unterschiedlichen Lösungsverfahren für die Berechnung der Strahlungstransferintegrale resultieren. Unterschiede in den abgeleiteten Konzentrations-Profilen sind durch verschiedene Ansätze für die Lösung des inversen Problems bedingt, insbesondere Art der Regulari-

sierung, Wahl des a priori Profil(s) und Diskretisierung.

Ein anderer Hauptaspekt meiner Arbeit war die Ableitung von Spurengaskonzentrationen aus Intensitäts-Spektren des ballongetragenen Instruments TELIS (TErahertz and submillimeter LImb Sounder). Mit Hilfe synthetischer Spektren wurde eine Sensitivitätsstudie durchgeführt, in der die Möglichkeiten zur Fernerkundung des Hydroxyl-Radikals (OH) aus typischen Ferninfrarot Limb-Spektren von TELIS untersucht wurden. Die entscheidenen Fehlerquellen wurden identifiziert und die zu erwartenden Produktqualität wurde abgeschätzt.

Die Daten der drei in Nordschweden durchgeführten TELIS Mess-Kampagnen (Winter 2009, 2010 und 2011) wurden ausgewertet und die Verteilung von OH, Ozon (O_3), Wasserstoffchlorid (HCl) und Kohlenmonoxid (CO) bestimmt. Durch Vergleiche mit unabhängigen Fernerkundunsprodukten von verschiedenen satellitengestützten Limbsensoren im Mikrowellen und Infrarotbereich konnte gezeigt werden, dass die Auswertung der TELIS-Daten mit Hilfe des PILS-Programmpakets Resultate mit sehr hoher Qualität liefert. Die von TELIS gewonnenen Daten tragen daher wesentlich zu Untersuchungen der Stratosphärenchemie und -dynamik bei und ergänzen Studien zur polaren Atmosphäre.

Keywords

- Schlechtgestellte inverse Probleme
- Infrarot und Mikrowellen Strahlungstransfer
- Automatische Differenzierung
- Numerische Regularisierung
- Spurengas-Retrieval
- PILS
- TELIS

Selbstständigkeitserklärung

Hiermit erkläre ich, Jian Xu, die vorliegende Dissertation selbstständig und ohne unzulässige fremde Hilfe verfasst zu haben. Ich versichere, dass ich ausschlielich die angegebenen Quellen und Hilfen Anspruch genommen habe.

München, 26 November 2014
Jian Xu

Acknowledgements

This thesis has been kept on track and been seen through to completion with the support and encouragement of numerous people including my family, my supervisors, my friends, colleagues, and several institutions. At the end of my thesis I would like to thank all those people who made this thesis possible and an unforgettable experience for me. I wish all of them good health and happiness forever.

Foremost, I would like to express my warmest gratitude to my principle supervisor Adrian Doicu, who has supported me with his knowledge and enthusiasm whilst allowing me the room to work in my own way. His comments and corrections were always well founded and helpful. The good advice provided by Prof. Dr. Richard Bamler and Prof. Dr. Stefan Bühler, has been invaluable on an academic level, for which I am extremely grateful.

I take this opportunity to sincerely acknowledge Franz Schreier, who has supported me over the past five years (since my Master thesis) with his patience, flexibility and knowledge. Whenever I got stuck on any problem, he could be counted on to help me figure out a way from a new angle. This thesis would not have been completed without his supervision and constant encouragement.

Many thanks also go to Prof. Dr. Thomas Trautmann for offering me the opportunity to work on this thesis at DLR, as well as his encouraging and constructive feedback on my thesis.

The work was jointly sponsored by the German Academic Exchange Service (DAAD) and the Remote Sensing Technology Institute, DLR. It is an honour for me to work at the Remote Sensing Technology Institute of DLR. The knowledge and experience I gained during these years at DLR are beyond my imagination. The Department of Atmospheric Processors provided me with the facilities being required and conductive conditions for my work, which buttressed me to perform my work comfortably.

Most of the results described in this thesis would not have been obtained without a close collaboration with the TELIS instrument team at the Department of Experimental Methods. I greatly acknowledge the solid, up-to-date knowledge and precious experience from everyone of this team. Peter Vogt has spent much time and effort on preparing and delivering the TELIS Level-1 data products (and struggling with nonlinearities, sideband ratios, etc.). Manfred Birk, Georg Wagner, and Oleg Kiselev have offered much help and insight for a better understanding of the TELIS instrument and its measurement characteristics.

Furthermore, I wish to acknowledge the people from the TELIS/MIPAS-B/mini-DOAS consortium: Gerald Wetzel, Hermann Oelhaf, and Guido Maucher from KIT for sharing the MIPAS-B retrievals and geolocation data; Arno de Lange and Jochen Landgraf from SRON for many fruitful discussions during the previous meetings.

In addition, some names should not go unmentioned: Yasuko Kasai, Phillipe Baron, and Hideo Sagawa from the SMILES-NICT team, Kaley Walker from the ACE-FTS team. I am thankful for their aspiring guidance, invaluably constructive criticism, and friendly advice during the cooperative work and several conferences. Their visions during the inspirational discussions were always motivating to me.

Special thanks also go to my colleagues at DLR, Bernd, Mayte, Sebastian, Nan, Mrs. Brigitte Rüba, Sabine, and many more, who have provided selfless help and generous suggestions in my daily work.

I am deeply indebted to my friends, Peter, Xiaoxiang, Husi, Nuannuan for their continuous support and encouragement.

Last but not least, this thesis is dedicated to my parents and Min, who have been always there cheering me up and stood by me throughout all the good and bad times.

Contents

List of Figures

List of Tables

Chapter 1

Introduction

Changes in Earth's atmosphere such as ozone (O_3) depletion, acid rain, and global warming are becoming a crucial environmental issue. Human activities result in emissions of principal greenhouse gases such as carbon dioxide (CO_2), methane (CH_4), nitrous oxide (N_2O), and the halocarbon compounds containing fluorine (F), chlorine (Cl), and bromine (Br). These gases accumulate in the atmosphere, and their concentrations increase with time. Stratospheric ozone depletion which has produced "ozone holes" (annual thinning of the ozone layer) over Antarctica and Arctic, is produced by increased concentrations of reactive halogen-containing gases in the stratosphere. These ozone losses create a negative radiative forcing of climate and an indirect cooling effect on the lower stratosphere. In the absence of other related changes (climate, circulation, etc.), climate–chemistry model simulations (see, e.g. [Austin et al., 2010]) suggest an ozone recovery chiefly due to the anticipated decrease in halogen loading [Ko et al., 2008]. In addition, the changes in concentrations of trace gases and climate system play a key role in the future behaviour of ozone.

To serve increased interest in the atmospheric environment, simultaneous measurements of ozone, related trace gases and temperature in the upper troposphere and stratosphere are required. Further, the growing demand for a better understanding of diurnal cycles of chemical interactions in the atmosphere has stressed the importance of prompt and accurate observations with high temporal and spatial resolution. Thus, advanced techniques which are capable of interpreting these observations can help us to better figure out the chemical processes between trace gases and the coupling with dynamic processes in the atmosphere.

1.1 Atmospheric Remote Sensing

Remote sensing is the science and art of identifying and measuring an object of interest without coming into physical contact with it. It offers great tools to observe the constituents and properties of the object (e.g. the Earth's atmosphere), ensuring that it is not disturbed. Different sensors record the transmitted energy as electromagnetic or acoustic radiation, and constitute a spectrum within specific bands.

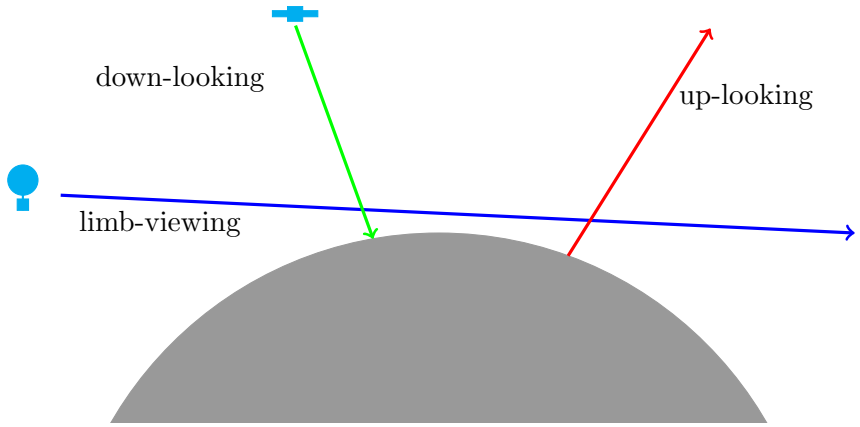

Figure 1.1: Observation geometries in atmospheric remote sensing. The primary observation geometries are up-looking, down-looking (nadir sounding), and limb-viewing.

Atmospheric remote sensing measurements can be characterized by different acquisition types and sensor positions. We distinguish

- ground-based measurements,
- aircraft (or airborne) measurements,
- balloon-borne measurements,
- satellite (or spaceborne) measurements.

In view of the type of the source of electromagnetic energy, there are two types of remote sensing techniques dedicated to atmospheric research: active remote sensing and passive remote sensing. Active remote sensors observe signals reflected or scattered from objects that are irradiated from artificially-generated energy sources, such as

- radar, e.g. POLDIRAD (**POL**arimetric **DI**versity Doppler **RAD**ar);
- laser, e.g. ALADIN (**A**tmospheric **LA**ser **D**oppler **IN**strument) on the ADM-Aeolus satellite.

In contrast, passive remote sensing utilizes sensors that detect either the solar radiation reflected from the Earth's surface or scattered in the atmosphere, or the thermal radiation emitted by the surface or the atmosphere.

In general, atmospheric sounders work in three observation geometries: up-looking, down-looking (nadir sounding), and limb-viewing mode (see Fig. 1.1). There are six major passive atmospheric sounding techniques based upon these viewing geometries:

- backscatter ultraviolet (BUV), e.g. GOME (**G**lobal **O**zone **M**onitoring **E**xperiment) [Burrows et al., 1999], GOME-2 [Callies et al., 2000], and SCIAMACHY (**SC**anning **I**maging **A**bsorption spectro**M**eter for **A**tmospheric **C**artograp**HY**) [Gottwald and Bovensmann, 2011];

- occultation, e.g. ACE-FTS (**A**tmospheric **C**hemistry **E**xperiment - **F**ourier **T**ransform **S**pectrometer) [Bernath et al., 2005] GOMOS (**G**lobal **O**zone **M**onitoring by **O**ccultation of **S**tars) [Kyrölä et al., 2004], HALOE (**HAL**ogen **O**ccultation **E**xperiment) [Russell et al., 1993], and SCIAMACHY;

- nadir near infrared, e.g. GOSAT (**G**reenhouse gases **O**bserving **SAT**ellite) [Kuze et al., 2009], and SCIAMACHY;

- nadir thermal emission, e.g. AIRS (**A**tmospheric **I**nfra**R**ed **S**ounder) [Aumann et al., 2003], GOSAT, IASI (**I**nfrared **A**tmospheric **S**ounding **I**nterferometer) [Cayla, 1993], and TES (**T**ropospheric **E**mission **S**pectrometer) [Beer, 2006];

- limb thermal emission, e.g. MIPAS (**M**ichelson **I**nterferometer for **P**assive **A**tmospheric **S**ounding) [Fischer et al., 2008], MLS (**M**icrowave **L**imb **S**ounder) [Barath et al., 1993; Waters et al., 2006], SMILES (**S**uperconducting sub**MI**llimeter-wave **L**imb-**E**mission **S**ounder) [Kikuchi et al., 2010], and SMR (**S**ub-**M**illimeter **R**adiometer) [Murtagh et al., 2002];

- limb scattering, e.g. OSIRIS (**O**ptical **S**pectrograph and **I**nfra**R**ed **I**mager **S**ystem) [Llewellyn et al., 2004], and SCIAMACHY.

Ground-based instruments, e.g. TCCON (**T**otal **C**arbon **C**olumn **O**bserving **N**etwork) [Wunch et al., 2011], operate in the up-looking mode.

In particular, instruments based on the limb emission technique detect the longwave radiation emitted in the atmosphere along the observer's line-of-sight and infer the concentration of chemical constituents. The spectral features of atmospheric constituents in the infrared and microwave are mostly due to vibrational–rotational transitions explained by the selection rule for infrared spectroscopy. Homonuclear diatomic molecules including hydrogen (H_2), oxygen (O_2), and nitrogen (N_2) do not possess a permanent dipole moment, and hence do not give a rise to a spectrum in the far infrared. This can be an advantage for remote sensing because the other gases in the atmosphere are primarily not transparent to this spectral range. However, heteronuclear diatomic molecules such as carbon monoxide (CO), hydrogen chloride (HCl), chlorine monoxide (ClO) and many polyatomic molecules (e.g. CO_2, H_2O, CH_4, etc.) have strong absorption and emission in the thermal infrared and microwave. From these emission features, trace gas concentration or temperature profiles can be derived. This work deals with the limb sounding measurements, with an emphasis on far infrared and microwave thermal emission.

1.2 Inverse Problems

In atmospheric remote sensing, the inverse problem is the process of deriving geophysical quantities from a given set of measurements. It is often referred to as a retrieval problem or simply *inversion*. The theoretical and computational aspects of the inverse theory can be found in a bunch of books, e.g. Twomey [1977]; Parker [1994]; Hansen [1998];

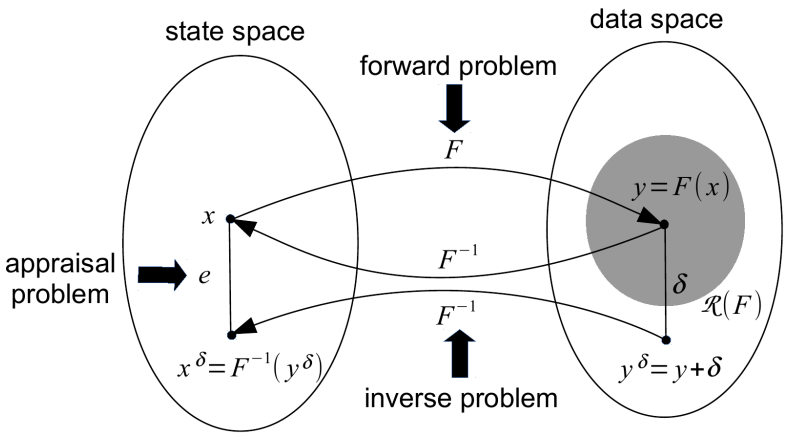

Figure 1.2: Forward model and inversion

Hofmann [1999]; Rodgers [2000]; Snieder and Trampert [2000]; Vogel [2002]; Doicu et al. [2010]; Hansen [2010], etc.

The fundamental functional relationship between the forward (or direct) problem and the inverse problem is illustrated in Fig. 1.2. The forward problem deals with the computation of the data y by applying the forward operator F on the state parameter function x (which incorporates the atmospheric parameters to be retrieved). Thus, we may write $y = F(x)$. The data belongs to the range of the forward operator F, i.e. $y \in \mathcal{R}(F)$ and consists of spectral radiances or transmissions. The inverse problem deals with the solution to the nonlinear equation $F(x) = y$. If $y \in \mathcal{R}(F)$, then the exact (true) solution x exists and is recovered by applying the inverse operator to y, i.e. $x = F^{-1}(y)$. In practice, the exact data y is unknown, and only its noisy version:

$$y^\delta \;=\; y + \delta \;, \tag{1.1}$$

where δ is the noise, is available. In this case, the solution to the nonlinear equation $F(x) = y^\delta$, given by $x^\delta = F^{-1}(y^\delta)$, is an estimate of the true solution x.

Unfortunately, most inverse problems arising in atmospheric remote sensing are ill-posed. According to Hadamard's definition, a problem is well-posed if

- a solution exists (existence);
- the solution is unique (uniqueness);
- the solution is stable with respect to perturbations in the data (stability).

If one of these conditions is violated, the problem is said to be ill-posed. When dealing with measurement data y^δ, the first Hadamard condition is not satisfied. Indeed, because δ is arbitrary, there is no guarantee that y^δ belongs to the range of the forward operator. In this case, we have $y^\delta \notin \mathcal{R}(F)$, and the nonlinear equation $F(x) = y^\delta$ is not solvable. The estimate x^δ, defined by $x^\delta = F^{-1}(y^\delta)$, represents the so-called least squares solution;

it is not a solution to the nonlinear equation $F(x) = y^\delta$ in the sense that $F(x^\delta) \neq y^\delta$. More precisely, we have $F(x^\delta) = \mathbb{P}_{\mathcal{R}(F)}(y^\delta)$, where $\mathbb{P}_{\mathcal{R}(F)}$ is the projection operator onto the range of the forward operator $\mathcal{R}(F)$. Violation of the stability condition, which is connected to the continuity of the inverse operator F^{-1}, is considered to be the most critical issue. In fact, the solution x^δ is said to be stable, if for $y^\delta \to y$ as $\delta \to 0$, we have $x^\delta = F^{-1}(y^\delta) \to x = F^{-1}(y)$. For ill-posed problems, the inverse operator F^{-1} is not continuous ($F^{-1}(y^\delta) \not\to F^{-1}(y)$ as $y^\delta \to y$), and small perturbations in the data may lead to large errors in the solution. Therefore, x^δ is not a reliable (or stable) approximation of x. To obtain a solution with physical meaning, some constraints should be imposed on x when solving the nonlinear equation $F(x) = y^\delta$. These constraints reflect our a priori knowledge on the solution, and the resulting solution method is known as *regularization*. An important aspect of the retrieval is the so-called appraisal problem, which consists in the estimation of the retrieval error $e = x - x^\delta$. As in practice, the exact solution x is unknown, several assumptions have to be considered for estimating e.

In a general framework, the data y can be a function of frequency/wavenumber or it may be a collection of discrete observations. In the first case, the problem is called a continuous problem, while in the second case it is called a semi-discrete problem. When both x and y are discrete, the corresponding problem is a discrete problem. In order to avoid possible confusions, vectors will be denoted by bold italic letters, e.g. $\boldsymbol{x}$ is a state vector, while x is a state parameter function. As any measurement system can deliver only a discrete, finite set of data, the problems arising in atmospheric remote sensing are semi-discrete. Moreover, due to the complexity of the radiative transfer, the forward model is a numerical model, which in turn, requires a discretization of the state parameter function. For these reasons, the atmospheric inverse problems that we are dealing with are discrete.

1.3 Software Development

Scientific research connected with the atmospheric environment requires plausible retrieval results. Currently, several new generation instruments pursuing remote sensing of the atmosphere in the infrared and microwave spectral range have been brought into action. These instruments trigger off an increased demand in high resolution radiative transfer model and robust inversion methods. A variety of relevant retrieval algorithms has been developed in the past decade, e.g. Qpack [Eriksson et al., 2005] based on the forward model ARTS (**A**tmospheric **R**adiative **T**ransfer **S**imulator) [Bühler et al., 2005; Eriksson et al., 2011], the retrieval tool KOPRAFIT [Höpfner et al., 2002] whose kernel is KOPRA (**K**arlsruhe **O**ptimized and **P**recise **R**adiative transfer **A**lgorithm) [Stiller et al., 2002], MOLIERE (**M**icrowave **O**bservation **LI**ne **E**stimation and **RE**trieval) [Urban et al., 2004], and MARC (**M**illimeter-wave **A**tmospheric-**R**etrieval **C**ode) [Carli et al., 2007]. All of these codes have been proved to tackle the computational challenges in the forward model and to solve ill-posed inverse problems occurring in atmospheric remote sensing, but only few of them (e.g. Qpack/ARTS) are open-source software. Aside from these retrieval codes for general purpose, a number of instrument-dedicated re-

trieval processors for infrared/microwave limb sounding have been developed by Ridolfi et al. [2000], Baron et al. [2002], Livesey et al. [2006], Takahashi et al. [2010], and Baron et al. [2011].

Recently at the Remote Sensing Technology Institute (IMF) of the German Aerospace Center (DLR), the retrieval code PILS (**P**rofile **I**nversion for **L**imb **S**ounding) [Xu et al., 2013] has been developed to derive geophysical parameters from limb measurements. The code is based on a forward model which is capable of performing radiative transfer calculations soundly and efficiently, and on a nonlinear least squares framework with direct and iterative numerical regularization schemes. Briefly, the main concepts underlying the software implementation can be summarized as follows:

- PILS is written in the Fortran programming language and built by `SCons` (a modern replacement for `make`) [Knight, 2005].
- Open source libraries including SLATEC [1993], LAPACK [Anderson et al., 1999], BLAS [Lawson et al., 1979], PORT [Fox et al., 1978] are used.
- Automatic differentiation [Griewank and Corliss, 1991; Griewank, 2000] for computing the Jacobian matrices is utilized.
- The program can be executed on different Linux distributions, and its execution is managed by two input files formatted by using Fortran `Namelist`.
- All data are read from external files or databases, except for a few physical and mathematical constants.

A detailed description of the physical and mathematical fundamentals will be provided in the next chapters.

1.4 Outline of Thesis

The task of these above-mentioned tools is to convert calibrated measurements of infrared/microwave radiances (known as Level-1b data) into estimates of atmospheric state parameters (known as Level-2 data, e.g. chemical composition, temperature). Such a procedure of producing these products is called Level-2 processing, and is the main subject of this thesis. In this work, we present the retrieval code PILS and discuss its applications to the analysis of limb emission sounding measurements (especially far infrared and microwave observations). First, a concise overview of atmospheric limb emission sounding techniques, focusing on a cryogenic balloon-borne instrument called TELIS (**TE**rahertz and submillimeter **LI**mb **S**ounder) [Birk et al., 2010] and its radiometric measurements, is given in Chap. 2. Chapter 3 briefly describes the physical and mathematical fundamentals of infrared and microwave radiative transfer, and presents numerical algorithms for high spectral resolution line-by-line calculations. In particular, the Jacobians (the partial derivatives of the forward model function with respect to the components of the state vector), are evaluated by means of automatic differentiation.

The inversion theory for nonlinear least squares problems, a variety of numerical regularization methods, and a theoretical error analysis are described in Chap. 4. In Chap. 5, the performance of PILS is evaluated by means of a sensitivity study of an OH retrieval in the TELIS 1.8 THz channel. A quantitative error analysis is performed by taking into account the most important error components: smoothing error, noise error, and model parameter errors. In Chap. 6, we present recent retrieval results of O_3, HCl, CO, and OH from real TELIS measurements observed during the past scientific balloon flights over the polar regions. Finally, Chap. 7 summarizes the work together with an outlook. Appendices A and B give supplementary details about far infrared measurements provided by TELIS, and the input configuration of PILS. A list of symbols and acronyms is given in Appendices C and D.

Chapter 2

Atmospheric Limb Emission Sounding

In this chapter, we briefly describe the principle of limb emission sounding techniques together with the state of the art in far infrared and microwave limb sounding. As the newly developed retrieval code PILS has been applied to the analysis of data observed by the balloon limb sounder TELIS, the related instrument and measurement concepts are particularly addressed.

2.1 Limb Emission

Limb observations are performed in the infrared and microwave region where the thermal radiation emitted by trace gases at various altitudes is detected, and in the ultraviolet, visible and near infrared spectral range where the instruments typically measure solar radiation backscattered from air masses in the limb. In contrast to nadir sounding techniques, the limb-viewing technique achieves a better vertical resolution, but this comes at the expense of a worse horizontal resolution because of a long horizontal path between the instrument and the tangent height. Compared to solar occultation instruments, infrared/microwave limb sounders acquire a better temporal coverage, because the thermal emission from the limb of the atmosphere is independent of any external source and can be observed continuously during day and night.

In limb-viewing geometry, the line of sight traverses the atmosphere tangentially without touching the surface, which is illustrated schematically in Fig. 2.1. The sensor is equipped with an antenna which makes it possible to adjust the viewing direction so that a sequence of spectra from different tangent altitudes can be recorded. Ideally, the vertical field-of-view is narrow and the recorded radiances are an accumulation of radiation emitted along the horizontal path with little vertical coverage. Because the air density decreases exponentially with height, the dominant contribution to the measured signal at a specific altitude originates predominantly from the tangent altitude. A limb scan through the atmosphere is characterized by its tangent height, and the height varies in an altitude range with a certain spacing. By taking a sequence of limb observations,

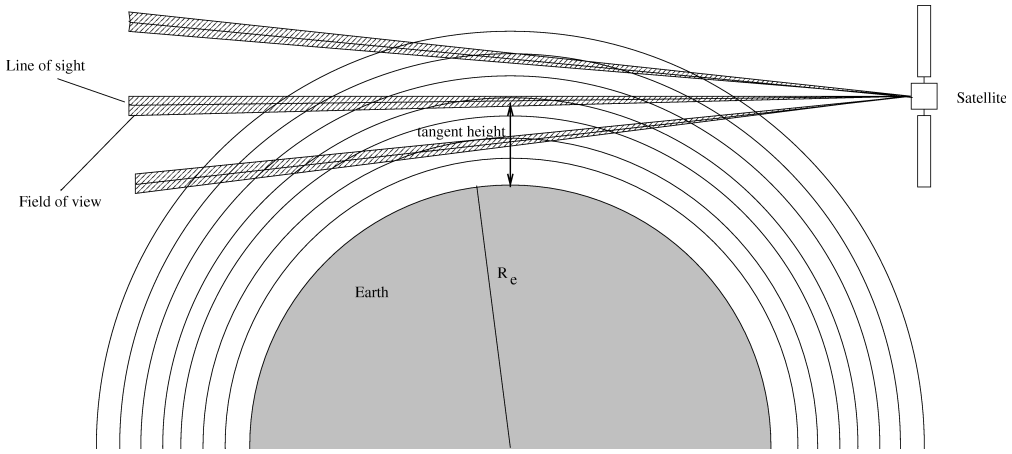

Figure 2.1: A schematic drawing of the observation geometry of limb emission sounding

the instrument is capable of recovering vertical profiles of temperature and atmospheric constituents.

2.2 History and State of the Art

Infrared limb sounding has been a widely used atmospheric remote sensing technique since the first instrument LRIR (**L**imb **R**adiance **I**nversion **R**adiometer) on Nimbus-6 launched in 1975, measuring CO_2 emission for temperature and pressure level determination. ATMOS (**A**tmospheric **T**race **MO**lecule **S**pectroscopy) [Abrams et al., 1996a,b] has obtained high resolution infrared spectra during several space missions (e.g. SPACELAB-3, ATLAS, etc.) since 1985. In 2002 the European Space Agency (ESA) launched the Earth-observing satellite Envisat, on which the Fourier transform spectrometer MIPAS was installed. Envisat/MIPAS observed the mid infrared radiation in the middle/upper atmosphere and spectrally resolved a large number of emission features of atmospheric minor constituents over a wide altitude region. Afterwards the ATMOS-based instrument ACE-FTS aboard the Canadian scientific satellite SCISAT-1 was launched in 2003. This instrument takes measurements of atmospheric absorption spectra during sunrise and sunset and studies the atmospheric chemistry and dynamics that affect stratospheric ozone depletion.

More and more space agencies and research institutes have tended to investigate the Earth's atmosphere by means of far infrared and microwave limb emission sounding because of its unique properties. A large number of trace gases have strong absorption features in the far infrared and microwave spectrum, and can therefore contribute to a deeper understanding of the global/regional atmospheric environment and/or chemical processes related to ozone destruction and climate change. Aerosols and ice clouds have limited effect on measurements, which also makes the observations in this spectral range preferable.

Application of this technique in atmospheric observations from space was pioneered

by the instrument MLS on UARS (**U**pper **A**tmosphere **R**esearch **S**atellite) in 1991. The major objective of UARS/MLS was to map the global distribution of chlorine monoxide (ClO) in the middle and upper stratosphere. The SMR radiometer aboard the Odin satellite was launched in 2001, and provides global information on ozone and species of importance for ozone chemistry by detecting the limb thermal emission in the spectral ranges of 486–504 and 541–581 GHz. In 2004, the National Aeronautics and Space Administration (NASA) launched an advanced successor to the first MLS, the Earth Observing System (EOS) MLS instrument on board of the Aura satellite, which measures several chemical species with better global and temporal coverage and resolution. Also, Aura/MLS delivered the first global measurements of hydroxyl (OH) and peroxyl (HO_2) that play an important role in regulating middle atmospheric ozone chemistry. The ability of monitoring OH is particularly fulfilled by an additional THz module [Pickett, 2006] in contrast to the UARS/MLS instrument. SMILES, a joint space-borne mission of the Japan Aerospace Exploration Agency (JAXA) and the National Institute of Information and Communications Technology (NICT), was attached to the Japanese Experiment Module (JEM) on the International Space Station (ISS) and delivered atmospheric observations from 12 October 2009 to 21 April 2010. As a trailblazer of a new generation of cryogenic limb sounders, SMILES used the 4 K superconductive heterodyne technology and obtained spectra with unprecedented low noise.

Spaceborne infrared/microwave limb emission spectroscopy has the superiority of continuous global-scale observations. However, to meet unique science requirements with highly reliable and stable technology, space based observational platforms are often expensive and have a long development period. Owing to lower costs and easier operations during the launch and operating phases as compared to satellites, limb sounders mounted on stratospheric balloon gondolas can presumably be a good alternative to map vertical profiles of trace gas concentrations and temperature in the middle atmosphere. Although the technique has some inherent drawbacks: a balloon can only be operated on a local scale within a short period (ideally up to 2–3 days), balloon-borne measurements with high sensitivity and flexible sampling density can attain scientific experience in the evaluation of infrared/microwave emission data dedicated to some interesting molecules observed by other limb sounders. Besides, a good understanding of balloon experiment performance has been proved to be valuable for the validation of spaceborne missions, e.g. the balloon version of MIPAS (MIPAS-B) [Friedl-Vallon et al., 2004]. Furthermore, they serve as precursors to future space instruments, e.g. BSMILES [Irimajiri et al., 2006], BMLS [Waters et al., 1984], etc. Last but not least, the balloon-borne instrument offers a prototype for new solutions to overcome the potential technical difficulties in the design of coming instruments.

For instance, OH possesses pairs of transition triplets in the far infrared spectral region, such as 61 cm^{-1} (1.8 THz), 83 cm^{-1} (2.5 THz), 101 cm^{-1} (3.0 THz), 118 cm^{-1} (3.5 THz). Carli et al. [1989] and Carlotti et al. [2001] observed the 3.5 THz feature with the balloon-borne far infrared Fourier transform spectrometer. Pickett and Peterson [1993] used a balloon-borne two-channel (101 and 118 cm^{-1}) Fabry-Perot instrument "FILOS" to measure OH and other chemical species in the upper atmosphere, and the

middle to upper stratospheric OH concentrations were estimated from thermal emission far infrared (83–230 cm^{-1}) observations with the balloon-borne "FIRS" Fourier transform spectrometer [Jucks et al., 1998].

2.3 Overview of the TELIS Instrument

TELIS is regarded as the follow-on to the heterodyne instrument THOMAS (**T**erahertz **OH** **M**easurement **A**irborne **S**ounder) [Englert et al., 2000] that has successfully been operated on DLR's FALCON research aircraft. The development of the instrument benefited from a close cooperation between several research institutes that provided considerable expertise. After a test flight in June 2008 which took place in Teresina, Brazil, TELIS participated in three successful scientific campaigns on 11 March 2009, 24 January 2010, and 31 March 2011. During all these flights, the balloon was launched from Esrange near Kiruna, Sweden. The latest joint flight took place on 7 September 2014 over Ontario, Canada.

2.3.1 Instrument concept

TELIS, developed by DLR-IMF in cooperation with the Netherlands Institute for Space Research (SRON) and the Rutherford Appleton Laboratory (RAL) in the United Kingdom, is a cryogenic three-channel heterodyne spectrometer designed to study atmospheric chemistry and dynamics with a focus on the stratosphere. Like SMILES, the instrument utilizes state-of-the-art superconducting heterodyne technology operated at 4 K, and was designed to be compact and lightweight, while providing high spectral resolution and extensive flight duration. The TELIS instrument was installed on a stratospheric balloon gondola together with the MIPAS-B instrument developed by the Karlsruhe Institute of Technology (KIT), and mini-DOAS (**D**ifferential **O**ptical **A**bsorption **S**pectrometer) operated by Heidelberg University. The gondola infrastructure was provided by the Karlsruhe team and has been used for the MIPAS balloon project since 1985. The primary scientific goal of the TELIS/MIPAS-B/mini-DOAS polar flights has been to measure the time-dependent chemistry of chlorine (Cl) and bromine (Br), and to achieve the closure of chemical families (NO_y, Cl_y, Br_y, HO_x) inside the polar vortex. A major benefit of the MIPAS-B concept is the achievement of complementary observations because it is a Fourier transform spectrometer covering a wide spectral interval throughout the mid infrared with high spectral resolution. However, the combination of mid infrared and far infrared/submillimeter technology is capable of observing even more molecules, e.g. OH, HO_2, HCl, and BrO. In the meanwhile, the combination of the two instruments is able to offer large synergies for cross-validation of measured parameters and chemical constituents. Moreover, these new technologies and observational data will pave the way for more dedicated atmospheric research missions in the future.

The ambitious spectral coverage of the TELIS instrument is accomplished by the use of three frequency channels: a tunable 1.8 THz channel [Suttiwong et al., 2009] with enhanced stability, a tunable 480–650 GHz channel [de Lange et al., 2010] based on

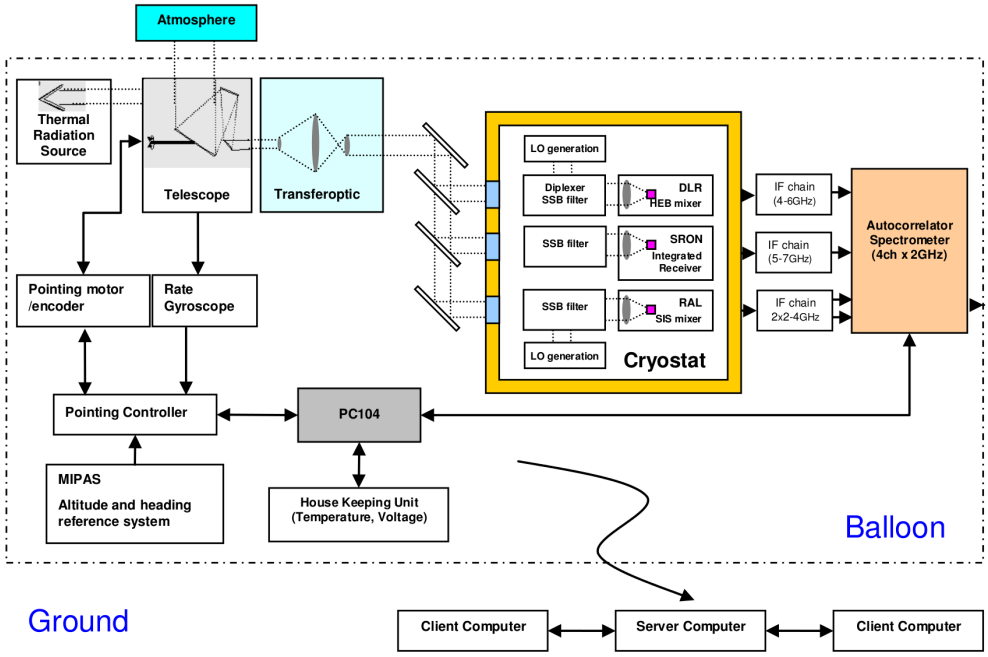

Figure 2.2: Block diagram representing the design of the TELIS instrument. Cryostat comprises three heterodyne receivers (the 1.8 THz, 480–650 GHz, and 500 GHz receivers operated by DLR, SRON, and RAL, respectively). Source: Birk et al. [2010].

the Superconducting Integrated Receiver (SIR) technology, and a miniaturized 500 GHz channel, designed by DLR, SRON, and RAL, respectively. TELIS measures the thermal emission of molecules against the cold cosmic background, thereby providing vertical concentration profiles by its three receivers. For each frequency channel, the detected molecules are summarized as follows:

1.8 THz**:** OH, HCl, O_3, CO, HO_2, HOCl, H_2O, HDO, $H_2^{17}O$, and $H_2^{18}O$;

480–650 GHz**:** ClO, BrO, HCl, O_3, HO_2, HOCl, HCN, H_2O, HDO, $H_2^{17}O$, and $H_2^{18}O$;

500 GHz**:** ClO, BrO, O_3, and N_2O.

Unfortunately, the 500 GHz channel did not deliver any useful measurements during the past balloon campaigns due to immensely high system noise temperatures (both on-ground and in-flight).

Figure 2.2 depicts the block diagram representing the design of the TELIS instrument. Simultaneous observations received by the three frequency channels is achieved by a quasi-optical beam splitting. The incoming atmospheric signals are transmitted from a dual offset Cassegrain telescope through the front-end transfer optics where the signals are separated and coupled into dedicated channels. At the polarizer, the reflected beam is coupled to the 500 GHz channel, and the transmitted beam having horizontal

polarization is further directed to a dichroic filter plate for separating the signals in the 1.8 THz channel and in the 480–650 GHz channel [Suttiwong, 2010]. At the TELIS back-end, a digital autocorrelator spectrometer with a spectral resolution of 2.16 MHz is used to yield the digitized autocorrelation of the measured signal as raw data. The signals of the THz/GHz channels are then split into four frequency segments with 500 MHz bandwidth and converted into the power spectra by the Fourier transform of the true autocorrelation function.

The TELIS 1.8 THz channel measures the signal at a local oscillator (LO) frequency f_{LO} between 1790 GHz and 1880 GHz. Because the instrument operates in a double sideband (DSB) mode, the recorded spectrum is then generated from the two sidebands with respect to f_{LO}, i.e. $f_{\mathrm{LO}} - f_{\mathrm{IF}}$ and $f_{\mathrm{LO}} + f_{\mathrm{IF}}$ with f_{IF} ranging from 4 to 6 GHz. In the case of the 480–650 GHz channel, f_{IF} ranges from 5 to 7 GHz.

In contrast to the balloon-borne Fourier transform spectrometer MIPAS-B, the different target molecules to be detected cannot be simultaneously covered by the TELIS instrument due to the requirement of different local oscillator configurations. A set of optimal LO frequencies f_{LO} has been determined by modelling the spectra in a double sideband mode using standard atmospheric constituent profiles and a common molecular spectroscopic database. The selection criteria of the TELIS instrument was to have isolated spectral lines of the target species with insignificant overlapping contributions from other interfering species. With the selected LO frequency, different spectral regions to be covered (so-called "microwindows") were checked in the same cryostat cooling cycle as the balloon flight itself was performed [Birk et al., 2010].

A real time processor manages the telescope by using a digital control loop to maintain an Earth-fixed pointing angle. The TELIS and MIPAS-B instruments are connected to the gondola frame by a number of springs, which may deteriorate the pointing stability. The pointing information for TELIS and MIPAS-B are received from the AHRS (**A**ttitude and **H**eading **R**eference **S**ystem) [Friedl-Vallon et al., 2004] which is a precise GPS-aided inertial navigation system delivering attitude and heading data of the gondola movements.

All devices of the instrument are controlled by a PC104 computer and operated in a Linux environment. The data received during the flight are directly sent to the ground server by using a MySQL database. The relevant housekeeping data comprising information about the instrument and its status (e.g. temperatures, voltages, etc.) are stored as well.

2.3.2 Measurement concept

The raw (Level-0) data received from the TELIS instrument is processed on ground in order to obtain the so-called Level-1b data product. It should be noted that Level-1a data are intermediate data resulting from the reconstruction and sorting operation of the raw data. The TELIS Level-1b data product contains radiometrically and spectrally calibrated radiance spectra along with the relevant geolocation information and tangent altitudes. Also included are related instrumental data, namely the sideband ratio, the antenna beam profile (field-of-view) measurements, and the parameters for radiometric

calibration (offset, gain, nonlinearity, hot/cold load temperatures).

During flight, a short term linear calibration scheme is employed. The radiometric calibration utilizes two blackbody signal references: an on-board blackbody unit is used as a hot signal reference, while the signal from pointing into deep space is used as a cold signal reference. The temperature of the cold blackbody is 2.725 K, whereas the temperature of the hot blackbody is subject to microwindow configuration and can be adjusted during the flight. The uncertainty in the temperature of the hot blackbody is estimated to be 1 K. To generate one calibrated output, three consecutive measurements of two reference blackbodies and the unknown radiance field (the radiation of the signal of the interest) are performed:

$$I_{\mathrm{atm}}(f) \;=\; \frac{I_{\mathrm{H}}(f) - I_{\mathrm{C}}(f)}{P_{\mathrm{H}}(f) - P_{\mathrm{C}}(f)} \left(P_{\mathrm{atm}}\,(f) - P_{\mathrm{C}}(f)\right) + I_{\mathrm{C}}(f)\ , \tag{2.1}$$

where the quantities I are given either in radiance or brightness temperature, and the quantities P refer to spectral power measured with the TELIS autocorrelator spectrometer. One up-looking spectrum at 65° (zenith angle of 25°) is used for the calibration measurement of the cold signal reference.

For TELIS, a radiometric examination of the entire system has been done via gas cell measurements in a laboratory by filling with methanol (CH_3OH) and carbonyl sulfide (OCS) for the 1.8 THz channel and the 480–650 GHz channel, respectively. Opaque lines of these two species with known intensity were recorded at different intermediate frequencies, which allows to investigate the dominant radiometric error sources caused by nonlinearities in the signal chain. Previous characterization campaigns showed radiometric errors of about 15 % for both frequency channels, which can further be propagated into the signal intensity and spectral shape. The radiometric error which can harm the retrieval performance is found to be mainly due to nonlinearities occurring in the calibration procedure. The minimization of these nonlinearities is a non-trivial task because some complex issues have to be resolved, such as the input-output relation, and the characteristics of electronic components embedded in the spectrometer. A detailed sensitivity study of the nonlinearity effect in the radiometric calibration chain is presented in Sect. 5.2.2.

To reduce the noise and drift effects, a polynomial fit of the measured hot and cold calibration spectra in time has been implemented in the latest version (3v02) of the Level-1b product. Further noise reduction by a method employing a sliding average in the frequency domain of the measured hot and cold spectra is currently under investigation.

In most cases, each radiance measurement as function of the intermediate frequency f_{IF} comprises both a series of individual limb sequences and the average of these subsequent sequences. For each measurement, the measured 951 frequency points are distributed over the 2 GHz IF-bandwidth (in four segments of 500 MHz). A single microwindow is normally measured for a time period of 10–20 minutes. In practice, however, a few microwindows were measured only for a single limb sequence because of a restricted measurement duration.

A single limb-scanning sequence comprises a series of radiance spectra with equidistant steps between two consecutive tangent points. Most of the limb sequences are

characterized by tangent heights range from 10 or 16 km up to 32.5 km discretized in 1.5 km steps. In the case of a few weak molecules (e.g. OH), the vertical spacing rises to 2 km, leading to a broader averaging kernel in the retrieval. In addition, TELIS measured two supplementary up-looking spectra at 6° and 12° respectively, and the impact of the atmosphere above the instrument may be assessed. Each spectrum was measured for 1.5 s and the calibrated spectra were measured approximately every 30 s. At the tangent point of the line-of-sight, the vertical resolution is estimated to be 1.5–3 km for observational frequencies around 1.8 THz. The horizontal (azimuth) resolution is roughly a factor of two worse due to the anamorphicity of the telescope [de Lange et al., 2010].

The tangent heights indicated in this work are the commanded tangent heights, but the actual ones are slightly deviated. This is because the error in the pointing of the telescope affect the actual pointing with respect to the received pointing data. The pointing uncertainty is determined by the stability of AHRS on the balloon gondola which is better than 1 arcmin. During previous flights, O_2 and O_3 measurements were also performed by TELIS to derive the pointing information. These measurements will be included in the future data processing.

To ensure the field-of-view (FoV) information and to measure the pointing offset angle, antenna beam profile measurements in the 1.8 THz and 480–650 GHz channels were carried out. The azimuthally collapsed antenna beam profile of the entire system was measured by using an approach developed by Pickett [2006] for the characterization of the 2.5 THz channel of Aura-MLS, and the effect of the telescope on the beam profile was measured by Fuerholz and Murk [2009]. For the THz-channel, one LO frequency 1800 GHz was measured; the two extreme LO frequencies 495.2 and 619.1 GHz were selected for the GHz-channel.

The antenna beam profiles of the 1.8 THz channel show no dependency on the LO frequency and are stable over time, whereas those of the 480–650 GHz channel are also stable over time, but depend on the LO frequency. Furthermore, the THz-channel profiles are much noisier as a result of the higher system noise temperature, and are narrower than the GHz-channel profiles.

According to the processed antenna beam profile measurements, the tangent offset with respect to the commanded tangent height (taken from AHRS pitch 0°) is 3.4 arcmin for the 1.8 GHz channel, which shows that the actual tangent height of a pencil beam is a bit higher than the commanded one. The antenna beam profile of the THz-channel is Gaussian shaped with a full width half maximum (FWHM) in the vertical direction of $0.1043 \pm 0.0008°$.

In the case of the 480–650 GHz channel, we have to consider the LO frequency dependent tangent offsets as well as antenna beam profile widths. The tangent offset ranges from −5.4 arcmin (at 619.1 GHz) to −6.6 arcmin (at 495.2 GHz), lowering the actual tangent height. The Gaussian curve has a FWHM of $0.1805 \pm 0.0004°$ for the highest frequency 619.1 GHz and $0.1987 \pm 0.0005°$ for the lowest frequency 495.2 GHz.

In a double sideband heterodyne receiver, the incoming signals are mixed with a pure LO signal, and the mixer output consists of two sideband responses separated from the LO. Thus, the recorded signal is essentially the contribution of the two sidebands

weighted by a gain ratio. The gain ratio between the two sidebands is represented by the sideband ratio, and ideally it would be 1.0, i.e. a perfect receiver would afford equal gain to signals observed in both sidebands. However, in practice the relative contribution of the upper sideband is likely to be different from that of the lower sideband. The instrument team has developed two independent methods to measure the sideband ratios. In the first method, the sideband ratio is initially measured by utilizing a high resolution Bruker Fourier transform spectrometer [Birk et al., 2010]. The second method relies on the gas cell measurements for fitting of the sideband ratio. According to the on-ground laboratory measurements, the sideband ratio is estimated to lie in the range of 0.95 to 1.05 for the 1.8 THz channel, and 0.6 to 1.4 for the 480–650 GHz channel.

For more information on the instrument design and measurement characteristics with respect to the 480–650 GHz channel we refer to de Lange et al. [2010, 2012].

Chapter 3

Radiative Transfer and Optimized Forward Model

In forward modelling, the requirements placed on the radiative transfer model are primarily determined by the observing conditions of the instrument, e.g. spectral range, observation geometry, and sensor type. This chapter presents an overview of the theoretical background of radiative transfer in the infrared and microwave spectral region by describing the principal equations and quantities. Furthermore, the implementation concepts of the radiative transfer and instrument modelling are introduced. In addition to the forward simulations, the implementation of automatic differentiation techniques is particularly labelled as a robust approach for evaluating Jacobians in PILS. For an assessment of the numerical performance, an intercomparison of the line-by-line calculations between the two radiative transfer modules used for the TELIS Level-2 data processing is presented.

3.1 Basics of Radiative Transfer Theory

The propagation of radiation through the Earth's atmosphere is affected by absorption, emission and scattering processes which are essentially dependent on pressure, temperature and chemical composition of the atmosphere. In the visible/ultraviolet and near infrared the atmospheric energy budget is essentially driven by solar radiation, while thermal emission by the atmosphere and surface dominates the energy budget in the infrared and microwave spectral range. Atmospheric scattering is important in the visible and near infrared (8–12.5 μm) and usually ignored in far infrared and microwave radiative transfer modelling. Another assumption of local thermodynamic equilibrium (LTE) is made, although the atmosphere is actually not in thermodynamic equilibrium as atmospheric parameters (temperature, pressure, and chemical potential) change in time and space. Nevertheless, this assumption is justified up to the top of the stratosphere and the source radiation given by the Planck function is valid. Exhaustive discussions of the radiative transfer theory can be found in several textbooks, e.g. Goody and Yung [1989]; Thomas and Stamnes [1999]; Liou [2002]; Bohren and Clothiaux [2006]; Petty

[2006]; Zdunkowski et al. [2007].

3.1.1 Equation of radiative transfer

Neglecting scattering and assuming the LTE state, the radiance (intensity) * at wavenumber ν (or frequency $f = c\nu$, with c being the speed of light in vacuum) received by an instrument at position s along the line-of-sight starting at s_0 ($s \geq s_0$) is given by the integral form of the Schwarzschild equation [Liou, 2002; Zdunkowski et al., 2007]

$$I(\nu, s) \;=\; I(\nu, s_0)\, \mathrm{e}^{-\tau(\nu; s_0, s)} \;+\; \int_{s_0}^{s} \mathrm{d}s'\; B(\nu, T(s'))\, \mathrm{e}^{-\tau(\nu; s', s)}\; \alpha(\nu, s')\;, \tag{3.1}$$

with $I(\nu, s_0)$ and $\alpha(\nu, s')$ representing the background contribution at position s_0 and the volume absorption coefficient, respectively. The source term $B(\nu, T)$ denotes the radiance emitted by a blackbody at temperature T and is described by the Planck function

$$B(\nu, T) \;=\; \frac{2hc^2\nu^3}{\mathrm{e}^{hc\nu/k_\mathrm{B}T} - 1}\;, \tag{3.2}$$

with h and k_B denoting the Planck constant and the Boltzmann constant, respectively. In the right side of Eq. (3.1), the first term is the attenuated radiation, whereas the second term describes the increase of radiance due to atmospheric thermal emission.

The atmospheric transmission is a dimensionless quantity ranging from zero to one. With the optical depth τ, the monochromatic transmission $\mathcal{T}(\nu)$ is given according to Beer's law by

$$\mathcal{T}(\nu; s_0, s) \;=\; \mathrm{e}^{-\tau(\nu; s_0, s)} \;=\; \exp\left[-\int_{s_0}^{s} \alpha(\nu, s')\; \mathrm{d}s'\right]\;. \tag{3.3}$$

Zero transmission $\mathcal{T} = 0$ means complete absorption, while complete transmission $\mathcal{T} = 1$ means zero absorption.

3.1.2 Molecular absorption coefficient

The volume absorption coefficient $\alpha(\nu, s)$ is characterized as the product of molecular cross section k_m and number density n_m summed over the molecules and an additional continuum term $\alpha^{(c)}$:

$$\alpha(\nu, s) \;=\; \sum_m k_m\left(\nu; p(s), T(s)\right)\; n_m(s) + \alpha^{(c)}(\nu, s)\;. \tag{3.4}$$

In principle, the volume absorption coefficient α depends on pressure p, temperature T, gas concentration profile and quantities associated with all contributing line transitions.

*The unit of the spectral radiance I defined as the power of radiation per unit time, per unit area, per unit solid angle, and unit wavenumber interval is $\left[\mathrm{erg/s}\ /\ (\mathrm{cm^2\,sr\,cm^{-1}})\right]$, while the unit is $\left[\mathrm{W}\ /\ (\mathrm{m^2\,sr\,Hz})\right]$ if the spectrum is a function of frequency.

For high resolution radiative transfer, a line-by-line calculation is the most straightforward approach. In general, the monochromatic absorption cross section at a wavenumber ν is computed by summing over the absorption contributions from many lines:

$$k_m(\nu; p, T) \;=\; \sum_l S_l(T)\; g\left(\nu; \hat{\nu}_l, \gamma_l(p, T)\right) \;, \tag{3.5}$$

with g and $\hat{\nu}_l$ being a normalized line shape function and the central wavenumber of transition l, respectively. The line strength at a certain temperature $S_l(T)$ is converted from the line strength at a reference temperature T_0 which is obtained from spectroscopic databases [Norton and Rinsland, 1991]:

$$S_l(T) \;=\; S_l(T_0)\; \frac{Q(T_0)}{Q(T)} \frac{\mathrm{e}^{(-E_\mathrm{i}/k_\mathrm{B}T)} \left(1 - \mathrm{e}^{-hc\hat{\nu}_l/k_\mathrm{B}T}\right)}{\mathrm{e}^{(-E_\mathrm{i}/k_\mathrm{B}T_0)} \left(1 - \mathrm{e}^{-hc\hat{\nu}_l/k_\mathrm{B}T_0}\right)} \;, \tag{3.6}$$

where E_i is the energy of the lower state where the transition occurs. The total partition sum $Q(T)$ is defined as the product of the vibrational function $Q_\mathrm{vib}(T)$ and the rotational function $Q_\mathrm{rot}(T)$, under the assumption that both partition functions are treated independently:

$$Q_\mathrm{vib}(T) \quad = \quad \prod_{n=1}^{N} \left[1 - \mathrm{e}^{-hc\nu_n/k_\mathrm{B}T}\right]^{-d_n} \;, \tag{3.7}$$

$$Q_\mathrm{rot}(T) \quad = \quad Q_\mathrm{rot}(T_0) \left(\frac{T}{T_0}\right)^{\beta} \;, \tag{3.8}$$

where N, d_n, and β represent the number of vibration modes with wavenumber ν_n, degeneracies, and the temperature coefficient of the rotational partition function, respectively.

Although the position of a spectral line is determined by the energy difference between the initial and final quantum state, emission and absorption due to a single state change of energy is practically never monochromatic. High resolution spectroscopy reveals that the individual spectral lines in the vibration–rotation absorption bands have a nonzero line width γ, i.e. each line is broadened out over a narrow wavenumber/frequency range. The broadening of spectral lines mainly results from

- the finite natural life time of an excited state (negligible for atmospheric spectroscopy);
- collisions between molecules;
- the Doppler effect due to the thermal motion of the molecules.

In the lower atmosphere, the governing process is pressure (collision) broadening of spectral lines that is represented by a Lorentzian line shape:

$$g_\mathrm{L}(\nu) \;=\; \frac{1}{\pi} \frac{\gamma_\mathrm{L}}{(\nu - \hat{\nu}_l)^2 + \gamma_\mathrm{L}^2} \;, \tag{3.9}$$

where γ_{L} is the Lorentz half width at half maximum (HWHM) of the line:

$$\gamma_{\mathrm{L}}(p,T) \;=\; \gamma_{\mathrm{L}}^{(\mathrm{air})}\;\frac{p}{p_0}\;\times\left(\frac{T_0}{T}\right)^{n}\;, \tag{3.10}$$

and $\gamma_{\mathrm{L}}^{(\mathrm{air})}$ is the air broadening coefficient. At high altitudes where the pressure is low, the shape of spectral lines is dominated by Doppler broadening and is defined by a Gaussian line shape:

$$g_{\mathrm{G}}(\nu) \;=\; \frac{1}{\gamma_{\mathrm{G}}}\sqrt{\frac{\ln 2}{\pi}}\;\exp\left[-\ln 2\left(\frac{\nu-\hat{\nu}_l}{\gamma_{\mathrm{G}}}\right)^2\right]\,, \tag{3.11}$$

where γ_{G} is the Doppler half width:

$$\gamma_{\mathrm{G}}(T) \;=\; \hat{\nu}_l\,\sqrt{\frac{2\ln 2\;k_{\mathrm{B}}T}{mc^2}}\;, \tag{3.12}$$

$\hat{\nu}_l$ is the line center position, T is the temperature, and m is the molecular mass. In the microwave regime, a correction to the Lorentz profile is given by the van Vleck-Weisskopf profile [Van Vleck and Weisskopf, 1945]:

$$g_{\mathrm{VVW}}(\nu) \;=\; \left(\frac{\nu}{\hat{\nu}_l}\right)^2\frac{\gamma_{\mathrm{L}}}{\pi}\left[\frac{1}{(\nu-\hat{\nu}_l)^2+\gamma_{\mathrm{L}}^2}+\frac{1}{(\nu+\hat{\nu}_l)^2+\gamma_{\mathrm{L}}^2}\right]\;. \tag{3.13}$$

The difference between the van Vleck-Weisskopf and the Lorentzian line shapes is most important in the far wings of the line and at low values of the line center position $\hat{\nu}_l$. The van Vleck-Huber profile [Van Vleck and Huber, 1977] is given by Eq. (3.13), except for the term $(\nu/\hat{\nu}_l)^2$ that is replaced with $(\nu\times\tanh(hc\nu/k_{\mathrm{B}}T))/(\hat{\nu}_l\times\tanh(hc\hat{\nu}_l/k_{\mathrm{B}}T))$.

Note that the height at which pressure broadening and Doppler broadening become comparable is weakly dependent on the mass of the radiating molecule and strongly related to the central wavenumber of the transition. For the reason that this height could be as low as the lower stratosphere and that an atmospheric radiance/transmission problem may extend from low to high altitude, it is important to take into account the combined effect of pressure broadening and Doppler broadening. On account of a spectral line being broadened by two types of mechanisms under different atmospheric conditions, the Voigt profile described by a convolution of the Lorentzian and Gaussian line shapes is appropriate to most practical cases in radiative transfer:

$$g_{\mathrm{V}}(\nu) \;=\; g_{\mathrm{L}}\otimes g_{\mathrm{G}} \;=\; \frac{1}{\gamma_{\mathrm{G}}}\sqrt{\frac{\ln 2}{\pi}}\;K(x,y) \tag{3.14}$$

with the Voigt function (normalized to $\sqrt{\pi}$)

$$K(x,y) \;=\; \frac{y}{\pi}\int_{-\infty}^{+\infty}\frac{\mathrm{e}^{-t^2}}{(x-t)^2+y^2}\;\mathrm{d}t\;. \tag{3.15}$$

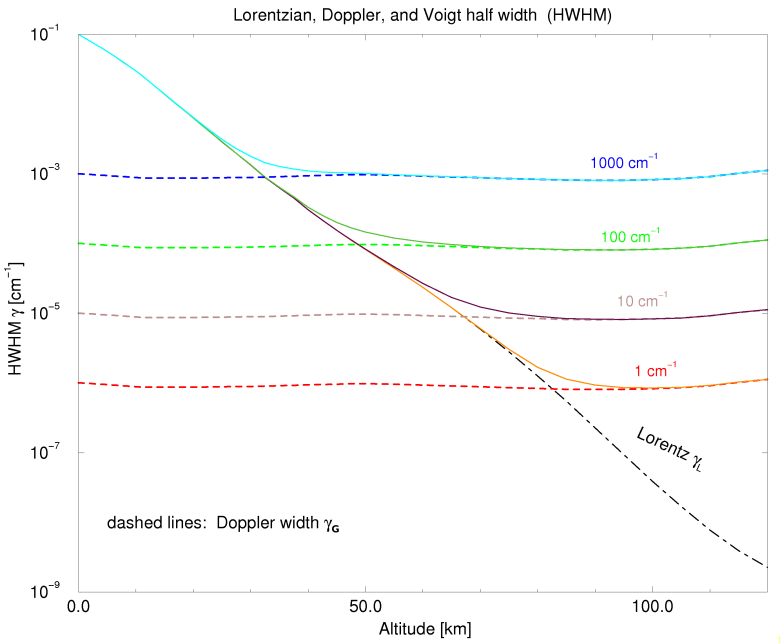

Figure 3.1: Half widths (HWHM) for Lorentz–, Gauss– (Doppler), and Voigt profiles as a function of altitude for a variety of line center position $\hat{\nu}_l$.

The dimensionless variables x and y are defined in terms of the distance from the line center $\nu - \hat{\nu}_l$, and the Lorentzian and Doppler half widths γ_L and γ_G:

$$x = \sqrt{\ln 2}\,\frac{\nu - \hat{\nu}_l}{\gamma_\mathrm{G}}\,, \tag{3.16}$$

$$y = \sqrt{\ln 2}\,\frac{\gamma_\mathrm{L}}{\gamma_\mathrm{G}}\,. \tag{3.17}$$

Several empirical approximations for the half width (HWHM) of a Voigt profile (defined by $g_\mathrm{V}(\nu_0 \pm \gamma_\mathrm{V}) = 1/2 g_\mathrm{V}(\nu_0)$) have been developed. For the approximation [Olivero and Longbothum, 1977]

$$\gamma_\mathrm{V} = \frac{1}{2}\left(c_1\gamma_\mathrm{L} + \sqrt{c_2\gamma_\mathrm{L}^2 + 4\gamma_\mathrm{G}^2}\right) \qquad \text{with} \quad c_1 = 1.0692,\ c_2 = 0.86639\,, \tag{3.18}$$

an accuracy of 0.02% has been determined, while for $c_1 = c_2 = 1$ the accuracy is in the order of one percent. Figure 3.1 shows a comparison of the Lorentzian, Gaussian (Doppler), and Voigt half widths. Since the Lorentz half width γ_L is proportional to pressure, it decreases roughly exponentially with altitude. On the contrary, the Doppler half width γ_G is not evidently dependent on altitude. The lines of the Voigt half width are in general pressure broadened in the lower atmosphere, while the transition to the Doppler broadening relies on the spectral range: near infrared and thermal infrared in the lower stratosphere, far infrared and microwave spectral region in the upper stratosphere or mesosphere.

However, the Voigt profile is an approximation of the line shape for the case that both pressure broadening and Doppler broadening are important, and is derived based on an assumption that the two broadening processes are independent of each other (which is not true in reality). The inadequacy of the Voigt profile has been experimentally proved for some molecules and a more accurate treatment is required. Some complications (e.g. Dicke narrowing, speed-dependences, line mixing) that could lead to deviations with respect to the measured absorption spectra, are beyond the scope of this work and will not be discussed here. For the refinements of the Voigt profile for modelling of these effects, we refer to [Varghese and Hanson, 1984; Ngo et al., 2013; Tran et al., 2013].

3.2 Implementation

At first glance, it could be argued that radiative transfer in the infrared and microwave spectral range is likely to be easier to model than that in the ultraviolet and visible range, since the source radiation is known and given by the Planck function in the LTE state.

Unfortunately, the line-by-line calculation of atmospheric radiance and transmission over a spectral range of interest is a challenging task as thousands or even tens of thousands of spectral lines must be taken into account in Eq. (3.5). Furthermore, approximating the Voigt function demands appropriate numerical algorithms to optimize the combination of efficiency and accuracy.

PILS's forward model is adapted from GARLIC (**G**eneric **A**tmospheric **R**adiation **L**ine-by-line **I**nfrared **C**ode) [Schreier et al., 2014] that is the modern Fortran (90/2008) re-implementation and extension of the Fortran 77 code MIRART (**M**odular **I**nfra**R**ed **A**tmospheric **R**adiative **T**ransfer) [Schreier and Schimpf, 2001; Schreier and Böttger, 2003]. GARLIC/MIRART is a versatile model designed for arbitrary observation geometry, sensor position, and instrumental characterizations. MIRART has been verified in the AMIL2DA (**A**dvanced **MI**PAS **L**evel **2** **D**ata **A**nalysis) project towards comprehensive comparison and characterization of different infrared radiative transfer models and retrieval processors used for MIPAS data processing, and participated in IRTMW01 (**I**nternational **R**adiative **T**ransfer **M**odelling **W**orkshop 20**01**) which was an intercomparison of microwave radiative transfer models developed by different research institutes. Presently, an extensive intercomparison of radiative transfer calculations between GARLIC, ARTS, and KOPRA is being conducted and preliminary results were presented by Schreier et al. [2013]. Furthermore, Mendrok et al. [2007] and Vasquez et al. [2013a] modelled multiple/single scattering to estimate cirrus cloud parameters from MIPAS data and to model SCIAMACHY's Venus observations, respectively. GARLIC is also used to assess the feasibility of detecting biosignatures in infrared spectra of Earth-like exoplanets [Vasquez et al., 2013b,c]. Likewise, BIRRA (**B**eer **I**nfra**R**ed **R**etrieval **A**lgorithm) [Gimeno García et al., 2011] developed for retrieval of vertical column densities from SCIAMACHY's near infrared nadir observations, is also built on GARLIC.

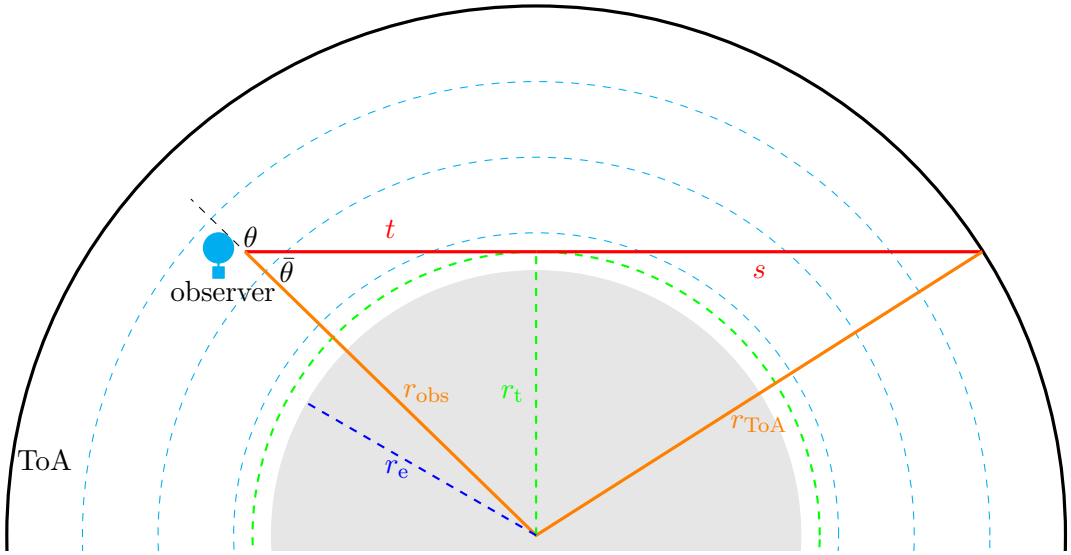

Figure 3.2: Observation geometry for the radiative transfer calculation in the limb-viewing case. Each point is characterized by the position on the line-of-sight and the altitude above the spherical surface with radius r_e.

3.2.1 Geometry of the line-of-sight

Currently, PILS considers only a one-dimensional (1-D) atmosphere, i.e. the atmosphere is assumed to be spherically symmetric. In a 1-D atmosphere, the whole shell has identical properties regardless of horizontal position, with all geophysical parameters (temperature, pressure, and gas concentration profiles) as a function of the altitude coordinate.

The limb-viewing geometry (see Fig. 3.2) is characterized by the tangent height of the line of sight ($z_t = r_t - r_e > 0$) or the zenith angle ($\theta > 90°$). When the zenith angle θ is known, the radius of the LoS tangent point r_t is computed as

$$r_t = r_{obs} \sin\theta \; ; \tag{3.19}$$

or once r_t is obtained, θ is calculated from

$$\theta = \pi - \arcsin \frac{r_t}{r_{obs}} \; . \tag{3.20}$$

The distance of the tangent point to the observer (obs) t and to the path end point (the top-of-atmosphere, abbreviated to ToA) s are given by

$$t = \sqrt{r_{obs}^2 - r_t^2} \; , \tag{3.21}$$

$$s = \sqrt{r_{ToA}^2 - r_t^2} \; , \tag{3.22}$$

and obviously, $t + s$ represents the distance from the observer to ToA.

Owing to atmospheric refraction, the line-of-sight is not a straight line but bends toward the center of the Earth. The bending of the optical path has to be taken into account as it brings about a curvilinear radiative transfer integral along the line-of-sight. Although the optical path in the case of limb sounding is still symmetric with respect to the tangent point by refraction, the tangent altitudes and the path lengths in each layer have to be recalculated. In the forward model we employ a modified version of the Edlén [1966] equation to determine the refractive index of air (adopted from Carlotti et al. [1998]):

$$\mu \;=\; 1 + 0.272632 \times 10^{-3} \;\left(\frac{n}{n_0}\right) \tag{3.23}$$

with the reference air density $n_0 = p_0/(k_\mathrm{B} T_0) = 2.54683 \times 10^{19}\,\mathrm{molec\ cm^{-3}}$ for $T_0 = 288.16\,\mathrm{K}$ and $p_0 = 1013.25\,\mathrm{hPa}$.

Considering refraction effects, the path are recalculated based on Snell's law in terms of spherical symmetry:

$$n_{i-1}\,(z_i + r_\mathrm{e})\sin(\theta_i) \;=\; n_i\,(z_{i+1} + r_\mathrm{e})\sin(\theta_{i+1})\;, \tag{3.24}$$

and note that the refraction effect lowers the actual tangent altitudes.

3.2.2 Path integration

Basically, the calculation of radiance and transmission according to Eqs. (3.1) and (3.3) respectively requires discretization (data are given only at a finite set of altitude levels). A standard scheme, the so-called "Curtis–Godson approach", subdivides the atmosphere in a series of homogeneous layers in which the gas conditions can be adequately approximated by mean values of atmospheric temperature, pressure, and concentration profiles. The radiance spectrum is obtained through recursive calculations, and the total transmission is given by the product of all layer transmissions [Clough et al., 1988; Edwards, 1988].

In contrast, GARLIC and PILS evaluate the integrals in Eqs. (3.1) and (3.3) by applying standard quadrature schemes [Kahaner et al., 1989]. The Beer integral for transmission is computed using the path distance s, while the calculation of radiance given by the integral form of the Schwarzschild equation can be performed using the optical depth τ:

$$I(\nu) \;=\; \int_0^s B\left(\nu, T(s')\right)\; \mathrm{e}^{-\int_0^{s'} \alpha(\nu,s'')\,\mathrm{d}s''} \alpha(\nu,s')\,\mathrm{d}s'\;, \tag{3.25}$$

$$\;=\; \int_0^\tau B\left(\nu, \tau(\nu,s')\right)\; \mathrm{e}^{-\tau(\nu,s')}\,\mathrm{d}\tau'\;, \tag{3.26}$$

where the integration variable in Eq. (3.1) is changed from the path distance s to optical depth τ. Note that the background term has been ignored here, and we set $s_0 = 0$ for simplicity.

The forward model of PILS computes the Schwarzschild integral in terms of optical depth τ. In view of the numerical scheme, the trapezoid–Laguerre quadrature [Schreier et al., 2014] which applies the trapezoidal rule to an integrand containing an exponential weight function (similar to the Gauss–Laguerre quadrature rule) has been implemented for the radiance and transmission calculations. Splitting the line-of-sight into n optical depth segments with subintervals $[\tau_{i-1}, \tau_i]$, Eq. (3.26) can be rewritten as

$$I(\nu) \;=\; \sum_{i=1}^{n} \int_{\tau_{i-1}}^{\tau_i} (a_i \tau(\nu, s') + b_i)\; \mathrm{e}^{-\tau(\nu,s')}\; \mathrm{d}\tau' \;, \tag{3.27}$$

by assuming linear interpolation of the terms B in each subinterval

$$B(\nu, \tau(\nu, s')) \approx a_i \tau(\nu, s') + b_i \;, \tag{3.28}$$

with $a_i = (B(\nu, \tau_i) - B(\nu, \tau_{i-1}))/(\tau_i - \tau_{i-1})$ and $b_i = B(\nu, \tau_{i-1}) - a_i \tau_{i-1}$. The contribution from the individual optical depth segments can be expressed in terms of B in each subinterval evaluated at discrete path grid points and the coefficients a_i depending on the optical depth segments (neglecting the ν dependence):

$$\begin{aligned} I \;&=\; (a_1 + B(\tau_0))\; \mathrm{e}^{-\tau_0} - (a_n + B(\tau_n))\; \mathrm{e}^{-\tau_n} + \sum_{i=1}^{n-1} (a_{i+1} - a_i)\; \mathrm{e}^{-\tau_i} \;, \\ &=\; B(0) - B(\tau)\; \mathrm{e}^{-\tau} + \sum_{i=1}^{n} a_i\; (\mathrm{e}^{-\tau_{i-1}} - \mathrm{e}^{-\tau_i}) \;, \\ &=\; B(0) - B(\tau)\; \mathrm{e}^{-\tau} + \sum_{i=1}^{n} (B(\tau_i) - B(\tau_{i-1}))\; \mathcal{E}\; (\tau_i - \tau_{i-1})\; \mathrm{e}^{-\tau_{i-1}} \;. \end{aligned} \tag{3.29}$$

Here, $\tau_0 = 0$ and $\tau_n = \tau$ according to Eq. (3.26), while $\mathbb{E}$ is the relative exponential function given by

$$\mathbb{E}(\Delta\tau_i) \equiv \frac{1 - \mathrm{e}^{-\Delta\tau_i}}{\Delta\tau_i} \;. \tag{3.30}$$

The relative error function can be robustly evaluated by using the Taylor expansion, since the quadrature nodes are monotone increasing.

In GARLIC, there are other available quadrature alternatives, e.g. an optimized overlapping parabola quadrature based on the `AVINT` routine from SLATEC [1993], and a quadrature using piecewise cubic Hermite interpolating polynomials (PCHIP) [Kahaner et al., 1989]. By default, for computational speed and numerical performance our forward model uses the trapezoid–Laguerre quadrature with optical depth as integration variable.

Concerning the limb-viewing geometry, the altitude-dependent atmospheric profiles are mapped to the path distance along the line-of-sight, e.g. $T(s) = T(z(s))$, $p(s) = p(z(s))$, etc. The distance from the observer to a path grid point $l^{\mathrm{J}}_{\mathrm{obs}}$ is given by

$$l^{\mathrm{J}}_{\mathrm{obs}} \;=\; t - l^{\mathrm{t}}_{\mathrm{J}} - \Delta d^{\mathrm{ToA}}_{\mathrm{obs}} \;, \tag{3.31}$$

$$l^{\mathrm{J}}_{\mathrm{obs}} \;=\; t + l^{\mathrm{t}}_{\mathrm{J}} - \Delta d^{\mathrm{ToA}}_{\mathrm{obs}} \;, \tag{3.32}$$

where $l_{\mathrm{J}}^{\mathrm{t}}$ and $\Delta d_{\mathrm{obs}}^{\mathrm{ToA}}$ are the distance from the path grid point to the tangent point and the difference between t and s, respectively. The calculation is implemented for two path segments, i.e. Eq. (3.31) for the segment from the observer to the tangent point and Eq. (3.32) for the segment from the tangent point to the path end point. It should be mentioned that $\Delta d_{\mathrm{obs}}^{\mathrm{ToA}}$ is only valid when the observer height z_{obs} is larger than the height of the top-of-atmosphere z_{ToA} (e.g. for a spaceborne instrument), otherwise (e.g. for a balloon and aircraft) it is zero:

$$\Delta d_{\mathrm{obs}}^{\mathrm{ToA}} = \begin{cases} t - s & \text{for } z_{\mathrm{obs}} > z_{\mathrm{ToA}} \ , \\ 0 & \text{otherwise} \ . \end{cases} \tag{3.33}$$

3.2.3 Molecular absorption computation

Because the integral in Eq. (3.15) cannot be calculated analytically, the Voigt function must be evaluated in a numerical manner, which turns out to be one of the main computational challenges in line-by-line modelling. The forward model employs an optimized combination of rational approximations of Humlíček [1982] and Weideman [1994] for the complex error function whose real part is the Voigt function. This approach achieves sufficient accuracy and efficiency [Schreier, 2011].

Still, a considerable number of function calculations require further optimizations. In the forward model the uniform wavenumber grid is chosen individually for each molecule, and for each altitude level with corresponding pressure and temperature. Schreier [2006] proposed a multigrid approach using a sequence of three wavenumber grids with increasing resolution, i.e. a coarser grid is used for contributions of lines that vary slowly in the wings, whereas a finer grid for contributions varying rapidly near the line center. Lagrange interpolation is used to merge the coarse and medium resolution superpositions together onto the ultimate fine grid. However, to overcome possible large errors introduced by Lagrange interpolation, cubic Hermite interpolation [e.g. Kahaner et al., 1989; Dahlquist and Björck, 2008] is presently implemented for the two-grid scheme in the forward model.

For the calculation of the molecular absorption cross sections, HITRAN (an acronym for **HI**gh-resolution **TRAN**smission, the latest version is 2012) [Rothman et al., 2013] or GEISA (**G**estion et **E**tude des **I**nformations **S**pectroscopiques **A**tmosphériques, the latest version is 2011) [Jacquinet-Husson et al., 2011], can be read by the forward model in order to obtain the required spectroscopic line parameters. MIRART can also read the spectroscopic data from the catalog compiled by the Jet Propulsion Laboratory (JPL) [Pickett et al., 1998] millimeter/submillimeter spectral region.

In addition to the line-by-line absorption, it has long been recognized that certain molecules possess continuum absorption which varies relatively slowly with wavenumber and pervades the entire infrared and microwave spectral region, i.e. the continuum term $\alpha^{(c)}$ in Eq. (3.4) must be taken into account. In order to account for the continuum absorption, the semi-empirical Clough–Kneizys–Davis (CKD) [Clough et al., 1989] model and the empirical Liebe et al. [1993] model have been implemented in the forward model. The Liebe model is the classical continuum model for the millimeter domain, while the

CKD model is popular due to its generality over a broader spectral range and was designed to work with the HITRAN line compilation.

3.2.4 Instrumental response and field-of-view functions

For any spectrometer, the limited spectral resolution results in a smearing effect on the incoming spectrum in the spectral domain. To model this effect, the monochromatic spectrum (in our case: radiance I) is convolved with an instrumental response function depending on the type of the instrument:

$$I^{(\mathrm{ILS})}(\nu) \;=\; I^{(\mathrm{mono})} \otimes R \;=\; \int_{-\infty}^{+\infty} R(\nu-\nu')\; I^{(\mathrm{mono})}(\nu')\; \mathrm{d}\nu' \;, \tag{3.34}$$

where R is the instrumental line shape (ILS) or the spectral response function (SRF). As for the 1.8 THz channel of the TELIS instrument, R is defined by the Fourier transform of a Hamming apodization function:

$$R(\nu-\nu') \;=\; \frac{L\;\left[1.08-0.64L^2(\nu-\nu')^2\right]\;\mathrm{sinc}\left[2\pi L(\nu-\nu')\right]}{1-4L^2(\nu-\nu')^2} \;, \tag{3.35}$$

where L is the maximum optical path difference (MOPD) in connection with the spectral resolution. A detailed explanation of the ILS function for the 480–650 GHz channel is given by de Lange et al. [2012].

Moreover, the final aperture of a spectrometer yields an additional widening of the ideal, infinitesimal narrow beam along the line of sight ("pencil beam", "infinitesimal field-of-view"), that can be modelled by convolving the pencil-beam spectrum with an angle-dependent field-of-view (FoV) function:

$$I^{(\mathrm{FoV})}(\nu,\bar{\alpha}) \;=\; I^{(\mathrm{pb})} \otimes \mathrm{FoV} \;=\; \int_{\mathrm{FoV}} I^{(\mathrm{pb})}(\nu,\alpha)\; \mathrm{FoV}(\alpha-\alpha')\; \mathrm{d}\alpha' \;, \tag{3.36}$$

where this FoV function can be approximated by a Box-, Gaussian-, or triangular shape function. For the TELIS instrument, the angle-dependent FoV functions in the 1.8 THz and the 480–650 GHz channels are defined as Gaussian curves with vertical FWHM of 0.1043° (6.3 arcmin) and 0.1805–0.1987° (10.8–11.9 arcmin), respectively.

It should be pointed out that the receiver of TELIS (and many other heterodyne instruments) operates in a double sideband mode. Therefore, the sideband ratio denoted by r is an important quantity which has to be considered. The recorded spectrum is basically the weighted superposition of the spectra of the two sidebands:

$$I \;=\; \frac{r}{r+1} I_{\mathrm{USB}} \;+\; \frac{1}{r+1} I_{\mathrm{LSB}} \;, \tag{3.37}$$

where I_{USB} and I_{LSB} denote the spectra of the upper and lower sidebands, respectively. For an ideal double sideband receiver r is equal to one, i.e. both sidebands offer equal gain response. But in practice, this is often not the case, and the effect of deviations in the sideband ratio from unity on retrieval results will be addressed in Sect. 5.2.3.

3.2.5 Miscellaneous

Interpolation of the atmospheric parameters onto a common grid is necessary if the profiles are read from a variety of datasets corresponding to different altitude grids. In GARLIC and PILS, the altitude grid of the first profile read from external files defines the final grid for the forward computation. Akima univariate interpolation, monotone piecewise cubic spline interpolation, monotone piecewise cubic Hermite interpolation, and Lagrange interpolation are implemented in the model.

The forward model calculates all quantities in the centimetre-gram-second (CGS) unit system internally, and yields the output data file depending on the request of the input file. In some cases, it is optional to express the spectra in a temperature scale, the so-called brightness temperature T_b. This may be obtained in a straightforward manner by "inverting" the Planck function to

$$T_\mathrm{b} \;=\; \frac{hc}{k_\mathrm{B}} \frac{\nu}{\ln \frac{2hc^2\nu^3}{I} + 1} \;. \tag{3.38}$$

Given the microwave region where $hc\nu/k_\mathrm{B}T \ll 1$, one can approximate T_b by the Rayleigh–Jeans law

$$T_\mathrm{b} \;=\; \frac{I}{2ck_\mathrm{B}\nu^2} \tag{3.39}$$

which indicates a linear scaling between I and T_b.

3.2.6 Job execution

Apart from some mathematical and physical constants specified in the code, most parameters (e.g. spectroscopic parameters, atmospheric profiles) are read from external data files, which has been designed to have a strict separation between code and data.

In analogy to GARLIC, PILS is managed by a user-defined input design for running the calculation (both forward and inverse aspects) request, But in contrast to GARLIC, PILS reads a main input file and a forward setup file. The main input file specifies the task (forward calculations or inversion) to be executed and its configurations (e.g. input data, numerical scheme, retrieval setup, etc.), while the forward setup file specifies the settings of the line-by-line calculation of absorption cross sections. A detailed description of the PILS input files is given in Appendix B.

3.3 Automatic Differentiation for Jacobian

The inversion of the integral equation of radiative transfer is accomplished by iterative methods based on a linearization of the forward model function $\boldsymbol{F}$ around the current iterate $\boldsymbol{x}$. The linearization process is based on a Taylor expansion and involves the Jacobians $\mathbf{K} = \partial\boldsymbol{F}/\partial\boldsymbol{x}$, or equivalently, the partial derivatives of the forward model function with respect to the components of the state vector. Consequently, efficient yet accurate computation of the Jacobian is of importance for the inversion, especially when

coping with the millions of spectra by spaceborne instruments. The differentiation is often performed by finite differencing, despite the tedious computational effort and the difficulties associated with the estimation of an appropriate amount of perturbation. Analytical derivatives are therefore preferable to finite differences, both for computational accuracy and speed. However, the implementation of analytical derivatives with hand-coding can be error-prone for a rather complex program as, for instance, the radiative transfer model.

Automatic or algorithmic differentiation tools has been a popular way of obtaining computer codes for derivatives evaluation. Given a code that evaluates an underlying function, automatic differentiation (AD) describes an approach to generate routines which compute the function's derivative(s) without having to derive the code by hand. The means of AD exploits the fact that any computer code that implements a function $y = f(x)$ can be decomposed into a sequence of elementary assignments, any one of which may be trivially differentiated by basic derivative "recipes". These "elemental" derivatives, evaluated at a particular argument, in accordance with the chain rule from derivative calculus are then used to generate the "entire" derivatives (e.g. the Jacobian matrices, gradients, and tangents). This process yields exact derivatives (compared to numerical differentiation), and more remarkably, it can be performed automatically by some kind of precompiler, which takes a computer source program as input and returns the differentiated source program with respect to the chosen variables.

For the simple function composition $y(x) = y\left(u\left(v\left(x\right)\right)\right)$, the chain rule gives

$$\frac{\mathrm{d}y}{\mathrm{d}x} \;=\; \frac{\mathrm{d}y}{\mathrm{d}u}\frac{\mathrm{d}u}{\mathrm{d}v}\frac{\mathrm{d}v}{\mathrm{d}x}\;. \tag{3.40}$$

Usually, there are two distinct differentiation modes, forward mode (tangent mode) and reverse mode. The forward mode specifies that one traverses the chain rule from right to left (i.e. first one computes $\mathrm{d}v/\mathrm{d}x$, then $\mathrm{d}u/\mathrm{d}v$, and last $\mathrm{d}y/\mathrm{d}u$), while the reverse mode traverses the chain rule from left to right. In other words, the forward mode builds a program that computes the variations of the dependent variables for given variations of the independent variables. The reverse mode generates a program to compute the gradient of the original program as given by a weighting of the dependent output variables.

Let us consider the function $y(x) = 2\sin\left(3x + 4\right)$; the derivative of y with respect to x is $\mathrm{d}y/\mathrm{d}x \;=\; 6\cos\left(3x + 4\right)$. The elementary operations for computing $y(x)$ are illustrated in Table 3.1, while the derivative code obtained by AD techniques is illustrated in Table 3.2. Here, one sweep of forward mode differentiation is performed with the seed $t_1' = 1$.

This concept can be extended to any arbitrary computer program. Using knowledge of only the basic rules of calculus, it is possible to compose a derivative code for even very complex algorithms. Currently, a number of AD tools are available for Fortran, C/C++, MATLAB, Python, etc. (for details, see `http://www.autodiff.org/`). The implementation of these AD tools can be classified into two categories: source code transformation and operator overloading. For a comprehensive study of the pros and cons of a variety of AD techniques see, e.g. Bischof and Bücker [2000].

Table 3.1: Code list for computing $y(x) = 2\sin(3x + 4)$.

Code event	Corresponding evaluation
$t_1 = x$	x
$t_2 = 3t_1$	$3x$
$t_3 = t_2 + 4$	$3x + 4$
$t_4 = \sin(t_3)$	$\sin(3x + 4)$
$t_5 = 2t_4$	$2\sin(3x + 4)$

Table 3.2: Derivative code list of forward mode for computing $y'(x) = 6\cos(3x + 4)$.

Derivative code	Corresponding derivative
$t_1' = 1$ (seed)	1
$t_2' = 3t_1'$	3
$t_3' = t_2'$	3
$t_4' = \cos(t_3)t_3'$	$3\cos(3x + 4)$
$t_5' = 2t_4'$	$6\cos(3x + 4)$

In spite of the great advantages compared to the numerical approaches, AD has not been widely used in the field of atmospheric remote sensing. Schreier and Schimpf [2001] and Schreier and Böttger [2003] used ADIFOR [Bischof et al., 1998] for computing the derivatives in the Fortran 77 MIRART code, and the computational speed has been greatly increased as compared to the finite difference approach. In this work, PILS utilizes TAPENADE [Hascoët and Pascual, 2013] which is a source-to-source AD tool for generating the desired derivatives in forward or reverse mode.

Technically, ADIFOR or TAPENADE first loads a source program comprising a top differentiation routine and all required subprograms as input, plus a request for differentiation indicating the dependent output variables, the independent input variables, and the mode of differentiation. It is not necessary to deliver the whole program of PILS, which may invoke some parts irrelevant for the generation of the Jacobian matrices. In the case of TAPENADE, the result of the differentiation is also displayed as a HTML output comprising the call graphs of the original and the differentiation routines.

The left panel (a) of Fig. 3.3 shows typical Jacobians for the data processing of spaceborne microwave limb sounders such as Aura/MLS. The finite difference approximations of the derivatives are calculated with 0.5 % and 50 % perturbations at the selected altitude level of 22 km. The run time using TAPENADE was 271.87 s, whereas the numerical approximations consumed 27 $\times$ 89.57 s. Here, the Jacobians with respect to the ozone volume mixing ratio (VMR) at 26 altitude levels are computed for a limb sequence corresponding to 11 tangent heights. The total computation time of the spectra and the Jacobians by using TAPENADE is only three times larger than the computational time

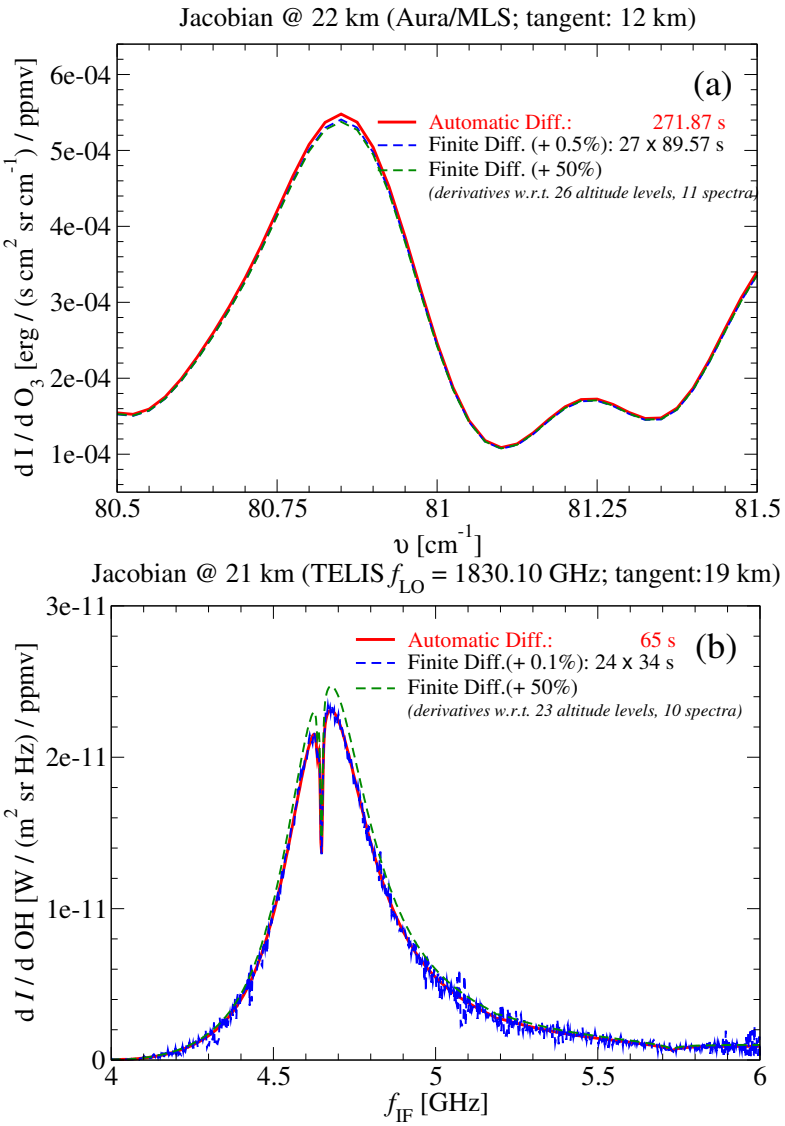

Figure 3.3: Results of automatic differentiation versus finite differences. Panel **(a)**: comparison of partial derivatives with respect to the O_3 volume mixing ratio in a typical wavenumber microwindow of Aura/MLS. The plotted derivatives are evaluated at an altitude level of 22 km and for a tangent altitude of 12 km. Panel **(b)**: comparison of partial derivatives with respect to the OH volume mixing ratio in a typical frequency microwindow of TELIS. The plotted derivatives are evaluated at an altitude level of 21 km and for a tangent altitude of 19 km.

of the spectra by forward simulation. In Fig. 3.3b, one column of the Jacobian matrix corresponding to the OH VMR at 21 km and in one typical frequency microwindow observed by TELIS is illustrated. The finite differences approximations of the derivatives are calculated with 0.1 % and 50 % perturbations. For TAPENADE the time required to

Table 3.3: Forward model parameters and input files for the intercomparison of the two Level-2 data processing codes PILS and AdL.

Forward model parameters and input files	Description
Sideband ratio	0.7–0.8
Pointing offset	−4.5 arcmin
Temperature profile	MIPAS-B retrievals
Pressure profile	ECMWF
Major gases (O_3, HCl, and ClO)	MIPAS-B and MLS profiles
Remaining interfering gases	AFGL subarctic winter model
Spectroscopic line parameters	HITRAN 2004

obtain the derivatives at 23 altitude levels for 10 tangent altitudes is just a factor of 2 as compared to that of the forward simulation. It should be noticed that an inappropriate choice of the perturbation amount is severe for the finite differences approach. Significant oscillations occur for the derivatives computed with 0.1 % perturbation, while the derivatives computed with 50 % perturbation shows an overestimate as compared to the exact derivative.

According to Fig. 3.3 the derivative code delivered by AD allows for significant computational speed-up and convincing accuracy, as compared with the finite difference method. Demonstrably, the AD techniques are superior to the finite difference method.

3.4 Verification

The purpose of model testing is to investigate the program performance. As an analytical solution to the radiative transfer equations does not exist under realistic conditions, a standard way of verifying the mathematical/numerical performance of radiative transfer models relies on a cross-checking against similar models. Several intercomparisons between GARLIC and other radiative transfer codes have been (or are currently being) performed, as mentioned in Sect. 3.2. In addition, an extensive intercomparison of forward calculations in conjunction with TELIS configurations has been carried out. The forward models are the two Level-2 data analysis programs developed by DLR (PILS) and SRON [de Lange et al., 2009, 2012] (hereafter referred to *AdL*), respectively. For model testing, a frequency microwindow ($f_{\mathrm{LO}} = 619.1$ GHz, $f_{\mathrm{IF}} = 5$–7 GHz) covering HCl lines of both isotopes is selected. The comparison procedure consists of line-by-line and radiative transfer calculations. To avoid any discrepancies stemming from instrumental, atmospheric, and spectroscopic parameters (from external sources), both forward models make use of the identical input parameters (see Table 3.3).

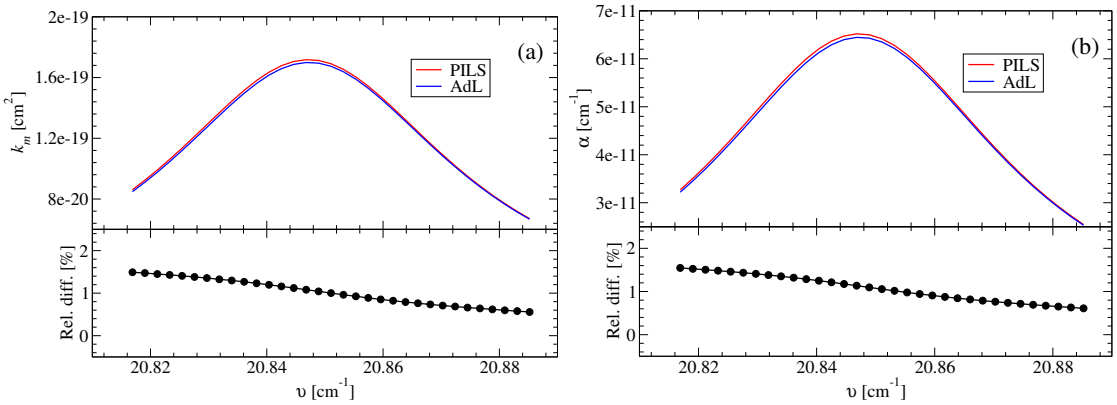

Figure 3.4: Comparison of **(a)** absorption cross sections and **(b)** absorption coefficient for one HCl line at the altitude level of 10 km. The results correspond to the two Level-2 data processing codes PILS and AdL, and both quantities are expressed as a function of wavenumber.

3.4.1 Monochromatic spectra: HCl only

It is essential to start with the simplest possible case, before moving on to more complex cases. The first exercise is to compare the following quantities by taking into account only one HCl transition line that is located at 20.8470 cm^{-1}:

- absorption cross sections,
- absorption coefficients,
- monochromatic pencil beam spectra with respect to single- and double sideband modes.

Figure 3.4 depicts the comparison of absorption cross sections and absorption coefficients as functions of wavenumber. Overall, the quantities computed by PILS are slightly larger than that by AdL, with a maximum 1.5 % relative difference. It has been identified that the differences between the two forward modules are mainly due to the different temperature conversion schemes of the line strength (values of total partition functions) and the values of the molecular mass of H^{37}Cl.

Figure 3.5 shows the monochromatic pencil beam spectra evaluated at a tangent height of 10 km computed by the two radiative transfer models. The upper panel (a) shows the spectra in brightness temperature units and for the upper sideband mode, while the lower panel (b) shows the radiance spectra in the double sideband mode. The absolute difference for the single sideband spectra ranges roughly from −0.2 to 0.2 K. For the double sideband spectra, the largest relative difference is about 5 % and corresponds to the peak value of the radiance around the intermediate frequency of approximately 5.9 GHz.

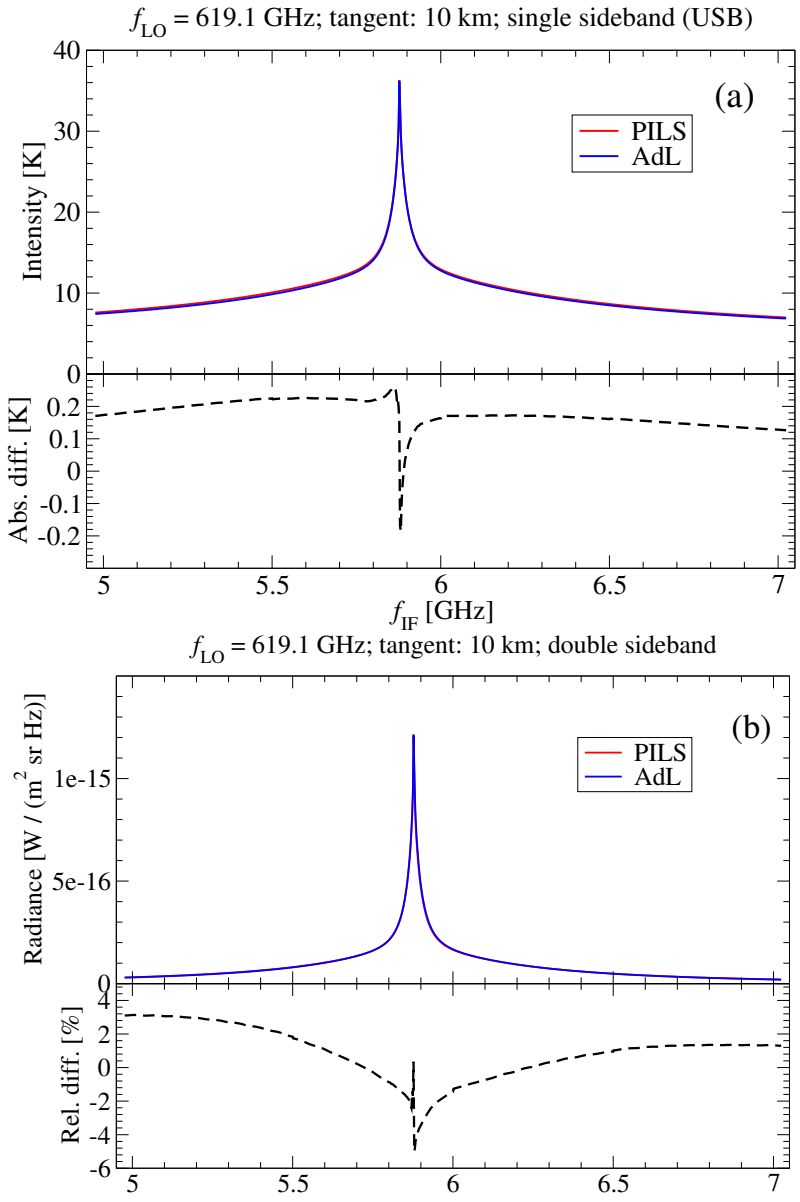

Figure 3.5: Comparison of monochromatic spectra for one HCl line at a tangent height of 10 km. Upper panel **(a)**: spectra in brightness temperature units and for the upper sideband. Lower panel **(b)**: radiance spectra in the double sideband mode.

3.4.2 TELIS-like spectra: all absorbers

A complete forward model comprises both atmospheric radiative transfer and sensor characteristics. The second exercise is to compare an entire TELIS-like limb sequence by convolving the monochromatic radiance spectra with the dedicated ILS function for the 480–650 GHz channel. The spectra covering the tangent heights between 10 and

32.5 km (equidistant spacing: 1.5 km) are plotted in Fig. 3.6. For this exercise, the real ILS function for the TELIS 480–650 GHz channel and all relevant molecules are considered so that the modelled spectra bear resemblance to the actual observations. Furthermore, a pencil beam is assumed (no FoV convolution), while the refraction effect and additional instrumental features (standing waves) are neglected.

At lower tangent heights (10 and 11.5 km), the discrepancies between the two forward models appear to be almost constant over the frequency range. When the tangent height increases, the differences between the two models mostly occur at the intermediate frequency points of approximately 5.9, 6.3, and 6.8 GHz where the emission line centers of HCl and O_3 are located. In the line wings where the absorption coefficient is very low, the different continuum models chosen by the two models result in differences. However, the differences in the continuum models may not be crucial for trace gas retrievals, because the continuum absorption can be included in the retrieval. Other factors for causing the differences in the spectra are the different interpolation approaches (atmospheric parameters as a function of altitude) and the integration of the radiative transfer equation.

In this section, we have presented a set of intercomparisons of radiative transfer results computed by the forward modules of two Level-2 retrieval codes (PILS and AdL). The model configurations with respect to the spectral range and the observing geometry are based on a submillimeter microwindow observed by TELIS's 480–650 GHz channel during the 2010 flight.

For one HCl line, discrepancies in the monochromatic spectra mostly stem from differences in the partition function and the value of the molecular mass. The TELIS-like spectra corresponding to an entire limb sequence show that PILS delivers accurate spectra by taking into account the instrument characteristics, which is fundamental to the inversion process.

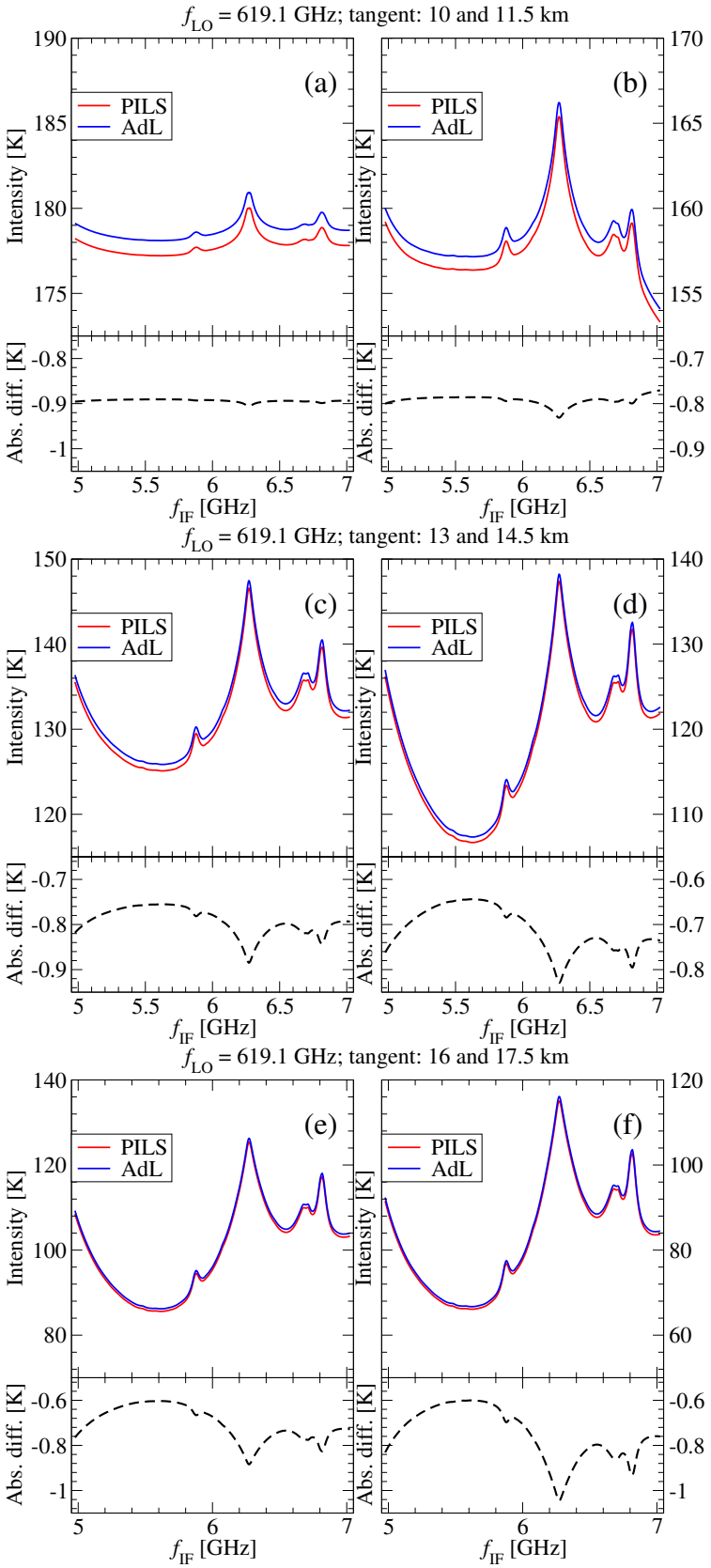

Figure 3.6: Comparison of modelled TELIS radiance spectra for a GHz-channel HCl microwindow. The results correspond to the two Level-2 processing codes PILS and AdL. The local oscillator frequency f_{LO} is set to 619.1 GHz and f_{IF} ranges from 5 to 7 GHz. For each pair of spectra, the corresponding residual in terms of absolute difference is shown in the lower panel. The plotted spectra are given in equivalent brightness temperature units. The comparisons are done for tangent heights of **(a)** 10, **(b)** 11.5, **(c)** 13, **(d)** 14.5, **(e)** 16, and **(f)** 17.5 km.

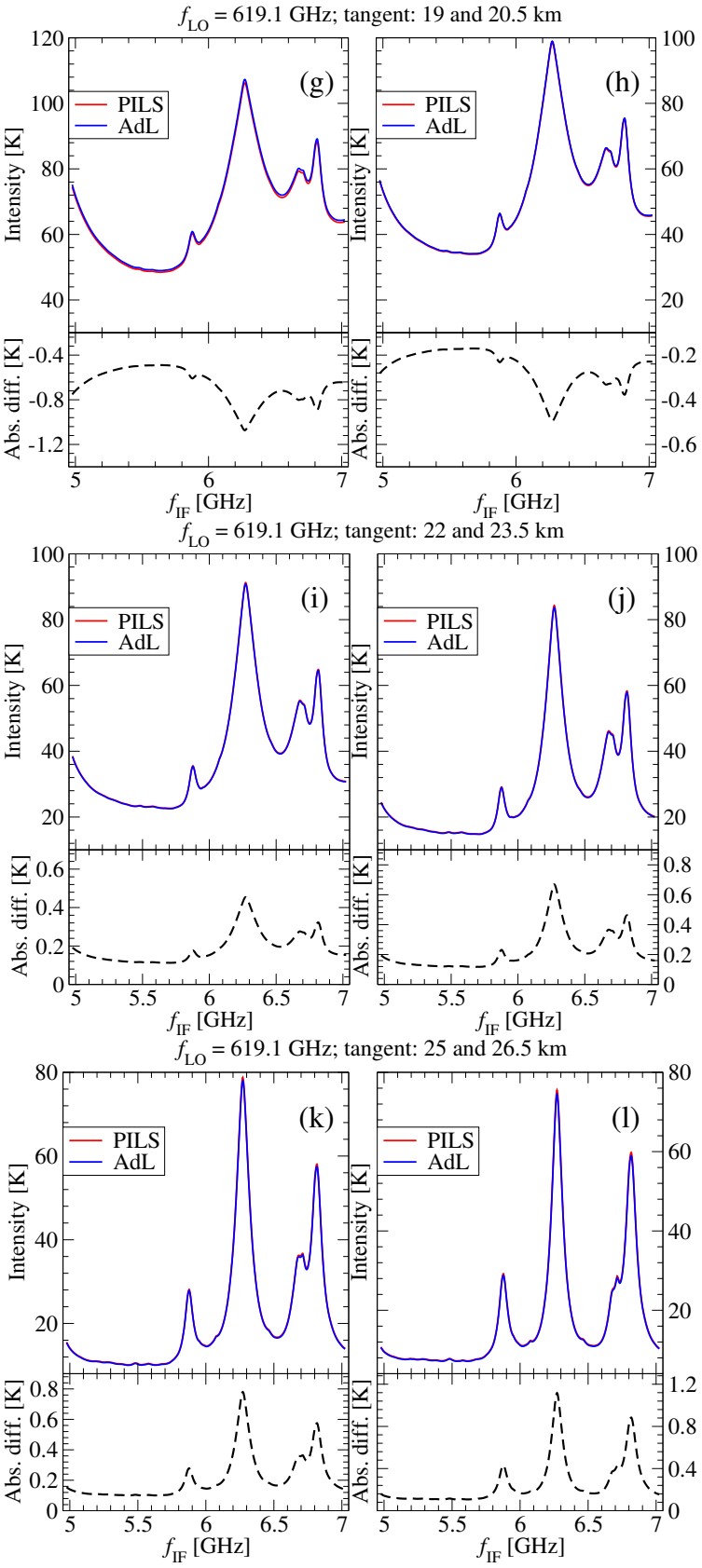

Figure 3.6: Continued from the previous page. The comparisons are done for tangent heights of **(g)** 19, **(h)** 20.5, **(i)** 22, **(j)** 23.5, **(k)** 25, and **(l)** 26.5 km.

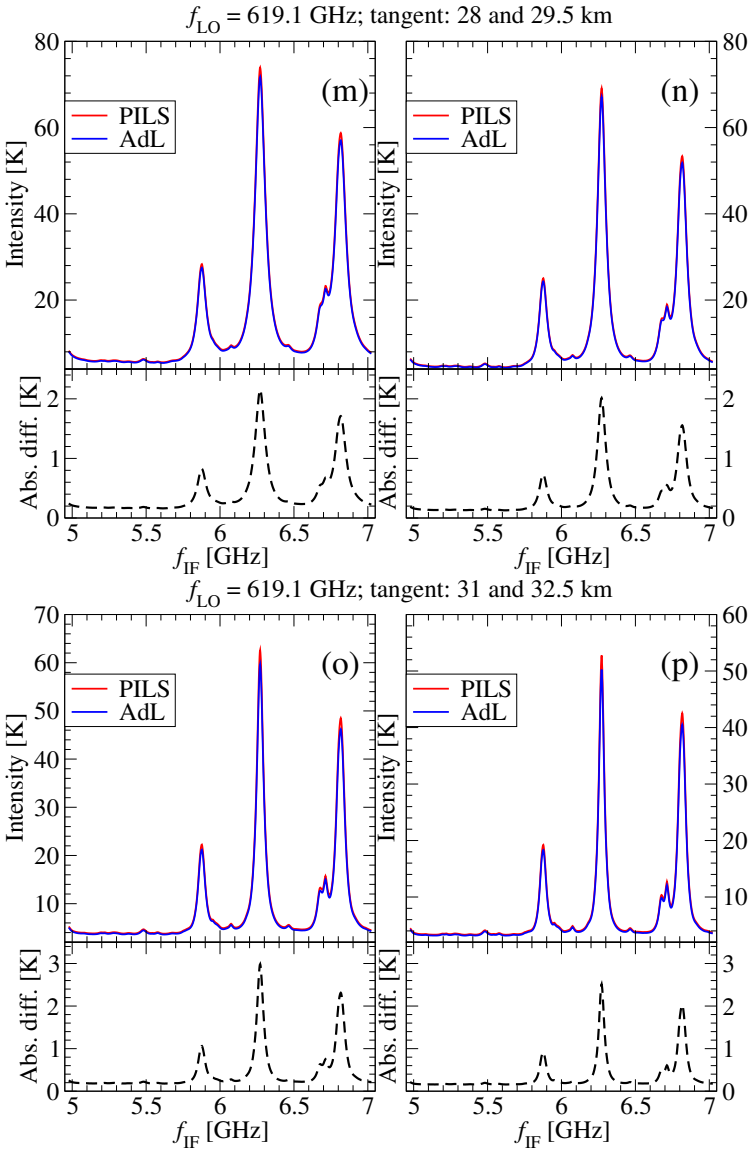

Figure 3.6: Continued from the previous page. The comparisons are done for tangent heights of **(m)** 28, **(n)** 29.5, **(o)** 31, and **(p)** 32.5 km.

Chapter 4

Inversion Methodology

Inverse problems arising in atmospheric remote sensing aim to estimate certain atmospheric state parameters based on indirect measurements (spectra) of these parameters. These problems are nonlinear, and mostly ill-posed in the sense that the noise in the data produces large errors in the state vector. The inversion frequently explores the simultaneous retrieval of several gas concentration profiles and optionally of some auxiliary (instrumental/geophysical) parameters, and works out the underlying multi-component problem by means of regularization.

In this chapter, the theoretical and practical aspects of the direct and iterative regularization methods for solving nonlinear inverse problems are presented. To assess the numerical performances of the methods, an example using TELIS submillimeter spectra is considered.

4.1 Retrieval Framework

The discretization of the radiative transfer equation (3.1) results in the nonlinear data model:

$$\boldsymbol{y} \;=\; \boldsymbol{F}(\boldsymbol{x}) \;. \tag{4.1}$$

Assuming that the exact data vector $\boldsymbol{y}$ is contaminated by measurement noise, we have the representation

$$\boldsymbol{y}^{\delta} \;=\; \boldsymbol{F}(\boldsymbol{x}) + \boldsymbol{\delta} \;, \tag{4.2}$$

where the mapping $\boldsymbol{F} : \mathbb{R}^n \to \mathbb{R}^m$ is the forward model, $\boldsymbol{x} \in \mathbb{R}^n$ is the state vector, $\boldsymbol{y}^{\delta} \in \mathbb{R}^m$ is the noisy data vector, and $\boldsymbol{\delta} \in \mathbb{R}^m$ is the noise vector. For inverse problems of limb sounding, the data vector is a concatenation of spectra corresponding to an entire limb-scanning sequence, in which case the reconstruction of the state vector from this data vector is known as the global–fit approach [Carlotti, 1988].

Essentially, the estimation of the state vector $\boldsymbol{x}$ from the measurement vector $\mathbf{y}^{\delta}$ can be formulated as a minimization problem involving the objective function

$$\mathcal{F}\,(\boldsymbol{x}) \;=\; \left\| \boldsymbol{F}(\boldsymbol{x}) - \boldsymbol{y}^{\delta} \right\|^2 \;. \tag{4.3}$$

The solution minimizing the residual $\mathcal{F}(\boldsymbol{x})$ in (4.3) is the least squares solution to the nonlinear equation $\boldsymbol{y}^\delta = \boldsymbol{F}(\boldsymbol{x})$. The minimization problem (4.3) can be solved by nonlinear optimization methods, e.g. the Gauss–Newton method. At the iteration step i, the objective function is approximated by its linearization around the current iterate $\boldsymbol{x}_i$,

$$\boldsymbol{F}(\boldsymbol{x}) \;\approx\; \boldsymbol{F}(\boldsymbol{x}_i) + \mathbf{K}_i\,(\boldsymbol{x} - \boldsymbol{x}_i) \;, \tag{4.4}$$

and the new iterate is computed as

$$\boldsymbol{x}_{i+1} \;=\; \boldsymbol{x}_i + \left(\mathbf{K}_i^T \mathbf{K}_i\right)^{-1} \mathbf{K}_i^T \left(\boldsymbol{y}^\delta - \boldsymbol{F}(\boldsymbol{x}_i)\right) \;. \tag{4.5}$$

Here,

$$\mathbf{K}_i \;=\; \mathbf{K}(\boldsymbol{x}_i) \;=\; \frac{\partial \boldsymbol{F}}{\partial \boldsymbol{x}}(\boldsymbol{x}_i) \in \mathbb{R}^{m \times n} \tag{4.6}$$

is the Jacobian matrix of $\boldsymbol{F}(\boldsymbol{x})$ evaluated at $\boldsymbol{x}_i$.

Unfortunately, inverse problems arising in atmospheric remote sensing are ill-posed, and the least squares solution is not a reliable estimate of the true solution. In order to obtain a solution with physical meaning, additional constraints have to be imposed on $\boldsymbol{x}$, a process which is referred to as *regularization*.

4.2 Numerical Regularization Methods

Figure 4.1 illustrates the least squares solution for an ozone retrieval problem. The O_3 profile is retrieved from a sequence of noise-free and noise-contaminated limb spectra recorded in the mid infrared spectral range (1000–1070 cm^{-1}). The altitude grid is discretized with steps of 1 and 2.5 km for 10–25 km and 25–50 km, respectively. The plots show that in the noise-free case, i.e. for the exact data vector $\boldsymbol{y}$, the least squares solution agrees well with the true solution; while in the noise-contaminated case, i.e. for the noisy data vector $\boldsymbol{y}^\delta$, the deviation between the least squares solution and the true solution increases with increasing signal-to-noise ratio. These behaviours are quantified in Table 4.1, which illustrates the relative solution errors in the solution. It should be pointed out that in the noise-free case, the solutions at different iteration steps oscillate around the true solution, and this fact indicates the instability of the inversion process.

An important tool for analyzing inverse problems is the singular value decomposition (SVD) of the Jacobian matrix, i.e.

$$\mathbf{K} \;=\; \mathbf{U}\mathbf{\Sigma}\mathbf{V}^T \;. \tag{4.7}$$

Here $\mathbf{U} = (\boldsymbol{u}_1, \boldsymbol{u}_2, \ldots, \boldsymbol{u}_m) \in \mathbb{R}^{m \times m}$ and $\mathbf{V} = (\boldsymbol{v}_1, \boldsymbol{v}_2, \ldots, \boldsymbol{v}_n) \in \mathbb{R}^{n \times n}$ are matrices with orthogonal (or orthonormal) columns, while $\mathbf{\Sigma}$ is an $m \times n$ rectangular diagonal matrix with the singular values arranged in a decreasing order on the diagonal

$$\mathbf{\Sigma} \;=\; \begin{bmatrix} \mathrm{diag}(\sigma_1, \sigma_2, \ldots, \sigma_n) & \mathbf{0} \\ \mathbf{0} & \mathbf{0} \end{bmatrix} \in \mathbb{R}^{m \times n} \;, \qquad \sigma_1 \geq \sigma_2 \geq \cdots \geq \sigma_n \geq 0 \;. \tag{4.8}$$

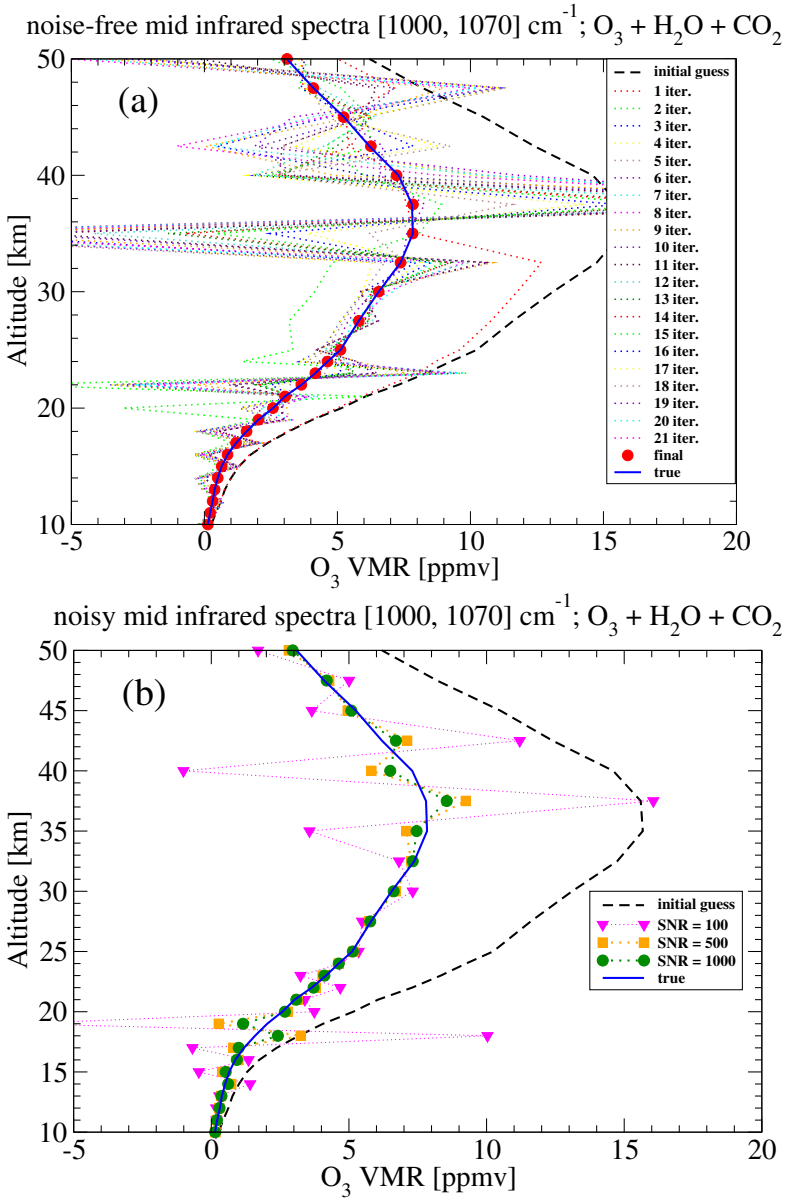

Figure 4.1: The least squares solution for an ozone test problem. The random noise is superimposed onto the noise-free spectra with the given signal-to-noise ratios. The least squares solution at different iteration steps **(a)** in the noise-free case and **(b)** in the noise-contaminated case. In these simulations H_2O and CO_2 are considered as interfering gases. The observation altitude is set to 800 km and the tangent height varies from 10 to 30 km in steps of 2 km. The dashed black line refers to the initial guess.

The condition number of the Jacobian matrix $\mathbf{K}$,

$$\text{cond}(\mathbf{K}) \;=\; \frac{\sigma_1}{\sigma_n} \tag{4.9}$$

Table 4.1: Absolute error in the least squares solution ($\|\boldsymbol{x} - \boldsymbol{x}_\mathrm{t}\|$, $\boldsymbol{x}_\mathrm{t}$ is the exact solution) and the number of iteration steps for the O_3 retrieval test problem and for four different noise settings. SNR denotes the signal-to-noise ratio of the simulated spectrum.

Noise	Absolute solution error	Number of iteration steps
noise-free	1.982×10^{-4}	22
SNR = 1000	1.794	19
SNR = 500	3.488	19
SNR = 100	18.651	19

is a quantifier of ill-posedness of an inverse problem. Basically, a large condition number reveals that the matrix is ill-conditioned, and that the inversion process is unstable under data perturbations (see also, e.g. Trefethen and Bau III [1997] for a thorough introduction to the SVD).

Fundamentally, a discrete ill-posed inverse problem is characterized by a Jacobian matrix with a large condition number. For the previous O_3 retrieval test problem, $\mathrm{cond}(\mathbf{K}_{O_3}) > 10^6$, and so, the least squares solution is very sensitive to any perturbation of the measurement and becomes physically meaningless as the signal-to-noise ratio decreases. This behaviour is apparent in Fig. 4.1 and Table 4.1, and to stabilize the solution, additional constraints have to be imposed.

From a general perspective, regularization methods can be essentially categorized into two classes according to the use of the regularization parameter:

- direct methods based on the minimization of certain objective functions and the estimation of the regularization parameter by some appropriate selection criteria;
- iterative methods, in which the number of iteration steps plays the role of a regularization parameter.

In the following, we introduce a classic direct regularization method (the method of Tikhonov regularization) and two iterative regularization methods (the iteratively regularized Gauss–Newton and regularizing Levenberg–Marquardt methods).

4.2.1 Tikhonov regularization

Tikhonov regularization [Tikhonov, 1963] is one of the most popular methods for regularizing ill-posed problem. By taking the so-called regularization matrix $\mathbf{L}$ into account, the objective function in Eq. (4.3) becomes

$$\mathcal{F}(\boldsymbol{x}) \;=\; \left\| \boldsymbol{F}(\boldsymbol{x}) - \boldsymbol{y}^\delta \right\|^2 + \lambda \left\| \mathbf{L}\,(\boldsymbol{x} - \boldsymbol{x}_\mathrm{a}) \right\|^2 \;, \tag{4.10}$$

where $\boldsymbol{x}_\mathrm{a}$ and λ denote the a priori state vector and the regularization parameter, respectively. Because the retrieval process is underdetermined, an a priori profile is often

needed and generally comprises a climatological estimate of the state vector. The residual term $\|\boldsymbol{f}(\boldsymbol{x})\|^2 = \|\boldsymbol{F}(\boldsymbol{x}) - \boldsymbol{y}^\delta\|^2$ quantifies the goodness of fit, namely how well the forward model at the solution approximates the given (noisy) data, whereas the penalty term $\|\mathbf{L}(\boldsymbol{x} - \boldsymbol{x}_\mathrm{a})\|^2$ measures the regularity of the solution. The goal of minimizing the Tikhonov function in Eq. (4.10) is to seek a solution providing an optimal compromise between the residual and the penalty term, and a global minimizer $\boldsymbol{x}_\lambda$ is termed a regularized solution. The regularization matrix $\mathbf{L}$ and the regularization parameter λ play important roles in whether this goal can be reasonably achieved.

The minimization problem (4.10) can be formulated as a least squares problem

$$\mathcal{F}(\boldsymbol{x}) \;=\; \|\boldsymbol{f}_\lambda(\boldsymbol{x})\|^2 \tag{4.11}$$

by introducing the augmented residual vector

$$\boldsymbol{f}_\lambda(\boldsymbol{x}) \;=\; \begin{bmatrix} \boldsymbol{F}(\boldsymbol{x}) - \boldsymbol{y}^\delta \\ \sqrt{\lambda}\mathbf{L}(\boldsymbol{x} - \boldsymbol{x}_\mathrm{a}) \end{bmatrix} \tag{4.12}$$

and the augmented Jacobian matrix

$$\mathbf{K}_\lambda(\boldsymbol{x}) \;=\; \begin{bmatrix} \mathbf{K}(\boldsymbol{x}) \\ \sqrt{\lambda}\mathbf{L} \end{bmatrix}. \tag{4.13}$$

By using the Gauss–Newton method for minimizing the Tikhonov function, the regularized solution can be found by the following iterative process:

$$\begin{aligned} \boldsymbol{x}_{\lambda,i+1} &= \boldsymbol{x}_\mathrm{a} + \left(\mathbf{K}_i^T\mathbf{K}_i + \lambda\mathbf{L}^T\mathbf{L}\right)^{-1}\mathbf{K}_i^T\left(\boldsymbol{y}^\delta - \boldsymbol{F}(\boldsymbol{x}_{\lambda,i}) + \mathbf{K}_i(\boldsymbol{x}_{\lambda,i} - \boldsymbol{x}_\mathrm{a})\right) && (4.14)\\ &= \boldsymbol{x}_\mathrm{a} + \mathbf{K}_{\lambda i}^\dagger\left(\boldsymbol{y}^\delta - \boldsymbol{F}(\boldsymbol{x}_{\lambda,i}) + \mathbf{K}_i(\boldsymbol{x}_{\lambda,i} - \boldsymbol{x}_\mathrm{a})\right). && (4.15)\end{aligned}$$

Here, the matrix $\mathbf{K}_\lambda^\dagger$ is the regularized generalized inverse (also known as the gain matrix [Rodgers, 2000]) and is given by

$$\mathbf{K}_\lambda^\dagger \;=\; \left(\mathbf{K}^T\mathbf{K} + \lambda\mathbf{L}^T\mathbf{L}\right)^{-1}\mathbf{K}^T. \tag{4.16}$$

The optimality of the regularized solution depends on the choice of regularization matrix $\mathbf{L}$ and the regularization parameter λ.

Regularization matrix

The penalty term in the expression of the Tikhonov function is based on the constraint norm $\|\mathbf{L}(\boldsymbol{x} - \boldsymbol{x}_\mathrm{a})\|$ describing the additional information on the solution. There are several ways to construct the regularization matrix. Frequently, we can choose $\mathbf{L}$ as the identity matrix ($\mathbf{L}_0 = \mathbf{I}_n$), not only giving preference to a suitable magnitude of the solution, but also suppressing high oscillations [Hansen, 1990]. If the smoothness of the solution is required to enforce, a discrete approximation of a derivative operator should

be used. With respect to certain discretizations, the first-order difference regularization matrix can be represented by

$$\mathbf{L}_1 = \begin{bmatrix} -1 & 1 & \cdots & 0 & 0 \\ 0 & -1 & \cdots & 0 & 0 \\ \vdots & \vdots & \ddots & \vdots & \vdots \\ 0 & 0 & \cdots & -1 & 1 \end{bmatrix} \in \mathbb{R}^{(n-1)\times n} , \tag{4.17}$$

and

$$\mathbf{L}_1 = \begin{bmatrix} 1 & 0 & \cdots & 0 & 0 \\ -1 & 1 & \cdots & 0 & 0 \\ 0 & -1 & \cdots & 0 & 0 \\ \vdots & \vdots & \ddots & \vdots & \vdots \\ 0 & 0 & \cdots & -1 & 1 \end{bmatrix} \in \mathbb{R}^{n\times n} . \tag{4.18}$$

The regularization matrix (4.17) takes effect only if its null space does not overlap with the null space of $\mathbf{K}$, while the matrix (4.18) has a regularizing effect regardless of the null space of $\mathbf{K}$ [Doicu et al., 2010]. Similarly, the possible forms for the second-order difference regularization matrix are

$$\mathbf{L}_2 = \begin{bmatrix} 1 & -2 & 1 & \cdots & 0 & 0 & 0 \\ 0 & 1 & -2 & \cdots & 0 & 0 & 0 \\ \vdots & \vdots & \vdots & \ddots & \vdots & \vdots & \vdots \\ 0 & 0 & 0 & \cdots & 1 & -2 & 1 \end{bmatrix} \in \mathbb{R}^{(n-2)\times n} \tag{4.19}$$

and

$$\mathbf{L}_2 = \begin{bmatrix} -2 & 1 & 0 & \cdots & 0 & 0 & 0 \\ 1 & -2 & 1 & \cdots & 0 & 0 & 0 \\ 0 & 1 & -2 & \cdots & 0 & 0 & 0 \\ \vdots & \vdots & \vdots & \ddots & \vdots & \vdots & \vdots \\ 0 & 0 & 0 & \cdots & 1 & -2 & 1 \\ 0 & 0 & 0 & \cdots & 0 & 1 & -2 \end{bmatrix} \in \mathbb{R}^{n\times n} . \tag{4.20}$$

If statistical information is available, we can construct the regularization matrix by the Cholesky factor of an a priori profile covariance matrix $\mathbf{S}_\mathrm{x}$, corresponding to an exponential correlation function, i.e.

$$\mathbf{S}_\mathrm{x}^{-1} = \mathbf{L}^T\mathbf{L} , \tag{4.21}$$

where

$$\left[\mathbf{S}_\mathrm{x}\right]_{ij} = \sigma_{\boldsymbol{x}i}\sigma_{\boldsymbol{x}j}\left[\boldsymbol{x}_\mathrm{a}\right]_i\left[\boldsymbol{x}_\mathrm{a}\right]_j \exp\left(-2\frac{|z_i - z_j|}{l_i + l_j}\right) \tag{4.22}$$

for $i, j = 1, \ldots, n$, where $\sigma_{\boldsymbol{x}i}$ are the profile standard deviations, and the lengths l_i determine the correlation between the parameters at different altitudes z_i. Considering an equidistant altitude grid and assuming $l_i = l$ for all $i = 1, \ldots, n$, we find that $\mathbf{L} \to \mathbf{I}_n$

as $l \to 0$, and that $\mathbf{L} \to \mathbf{L}_1$ as $l \to \infty$. Another choice of the a priori profile covariance matrix corresponds to a Gaussian correlation function (see also Eriksson et al. [2005]), i.e.

$$[\mathbf{S}_\mathrm{x}]_{ij} \;=\; \sigma_{\boldsymbol{x}i}\sigma_{\boldsymbol{x}j}\,[\boldsymbol{x}_\mathrm{a}]_i\,[\boldsymbol{x}_\mathrm{a}]_j\;\exp\left(-4\left(\frac{z_i - z_j}{l_i + l_j}\right)^2\right)\;. \tag{4.23}$$

To appraise the influence of the penalty term, we will present an intercomparison of retrieval performances for various regularization matrices in Sect. 5.1.3.

Regularization parameter

The regularization parameter λ controls the weight of the penalty term relative to the residual norm. The selection of an appropriate regularization parameter providing at the same time a small residual and a moderate value of the penalty term is crucial in the method of Tikhonov regularization. The widely used parameter choice methods are the generalized cross validation [Wahba, 1977, 1990], the L-curve method [Hansen, 1992], the discrepancy principle [Morozov, 1966], and more recently, the error consistency method [Ceccherini, 2005]. For example, in the L-curve method, the constraint norm is plotted versus the residual norm in logarithmic scale, and the optimal value of the regularization parameter corresponds to the corner of the L-curve. Determination of the regularization parameter by using the L-curve in atmospheric inverse problems has received much attention in recent years, e.g. Schimpf and Schreier [1997]; Eriksson [2000]; Hasekamp and Landgraf [2001]; de Lange et al. [2012]; Schepers et al. [2012]. Alternatively, the error consistency method formulates an analytical selection procedure based on the criterion that the differences between the least squares and the regularized solutions $\boldsymbol{x}$ and $\boldsymbol{x}_\lambda$ must be on average equal to the error in the regularized solution. Ceccherini et al. [2007] implemented this method in the operational retrieval code for analyzing the satellite measurements of MIPAS.

In our analysis, the selection of the regularization parameter λ is based on an a priori parameter choice method relying on the minimization of the relative solution error

$$\epsilon(\lambda) \;=\; \frac{\|\boldsymbol{x}_\lambda - \boldsymbol{x}_\mathrm{t}\|}{\|\boldsymbol{x}_\mathrm{t}\|}\;, \tag{4.24}$$

with $\boldsymbol{x}_\mathrm{t}$ being the exact solution, i.e. the optimal regularization parameter λ_opt is defined as

$$\lambda_\mathrm{opt} \;=\; \arg\min_\lambda \epsilon(\lambda)\;. \tag{4.25}$$

The idea is to explore a random domain where the regularized solution $\boldsymbol{x}_\lambda$ is expected to lie. For each realization of $\boldsymbol{x}_\mathrm{t}$, the optimal regularization parameter is computed by minimizing the solution error with respect to the regularization parameter.

Connection to Bayesian approach

The prevailing so-called optimal estimation method [Rodgers, 2000] based on Bayes' theorem can be regarded as a stochastic version of Tikhonov regularization, in which

the regularization parameter is incorporated into the a priori profile covariance matrix, that is,

$$\mathbf{S}_{\mathrm{x}}^{-1} \;=\; \lambda \mathbf{L}^T \mathbf{L} \;. \tag{4.26}$$

The penalty term in Eq. (4.10) is replaced by $\mathbf{S}_{\mathrm{x}}^{-1}$ and the iterative solution is then given by

$$\boldsymbol{x}_{\lambda,i+1} \;=\; \boldsymbol{x}_{\lambda,i} + \left(\mathbf{K}_i^T \mathbf{K}_i + \mathbf{S}_{\mathrm{x}}^{-1}\right)^{-1} \mathbf{K}_i^T \left(\boldsymbol{y}^{\delta} - \boldsymbol{F}(\boldsymbol{x}_{\lambda,i})\right) \;. \tag{4.27}$$

In this case, a trade-off between the measurement and the a priori profile requires a proper selection of $\mathbf{S}_{\mathrm{x}}$. Most studies choose the a priori covariance matrix in a empirical manner (e.g. [Allmaras et al., 2013]) without formulating an objective function criterion for the solution error. Furthermore, in contrast to Tikhonov regularization, the optimal estimation method is sensitive to the choice of the a priori profile. When dealing with target species lacking a priori knowledge, the retrieval with Tikhonov regularization is less affected by an inappropriate a priori information.

In atmospheric science, the optimal estimation method appears to be the most popular approach for solving ill-posed problems occurring in reconstruction of geophysical parameters from satellite observations, e.g. Livesey et al. [2006] for MLS, Takahashi et al. [2010] and Baron et al. [2011] for SMILES, Urban et al. [2005] for Odin/SMR. Recently, Tikhonov regularization has attracted great attention because of its various applications, e.g. Landgraf and Hasekamp [2007]; von Clarmann et al. [2009]; Schepers et al. [2012]. Borsdorff et al. [2014] gave insights into this regularization technique by using trace gas column retrieval from ultraviolet measurements. Performance comparisons of Tikhonov regularization and the optimal estimation method in the context of passive infrared/microwave atmospheric sounding were given by Eriksson [2000]; Steck and von Clarmann [2001]; Senten et al. [2012]. Besides, Gouveia and Scales [1997] explored the similarities and differences of both techniques for solving geophysical inverse problems in terms of mathematical fundamentals, resolution analysis, and error estimates.

4.2.2 Iterative regularization methods

Seeking a global minima of the Tikhonov function is not a trivial task. Taking into account the difficulties associated to a proper selection of the regularization parameter, iterative regularization methods can be a pleasant alternative for solving severely ill-posed problems. In this study, two iterative regularization methods are presented.

The first approach is the iteratively regularized Gauss–Newton method [Bakushinskii, 1992]. At the iteration step i, the new iterate is computed as

$$\boldsymbol{x}_{\lambda,i+1} \;=\; \boldsymbol{x}_{\mathrm{a}} + \left(\mathbf{K}_i^T \mathbf{K}_i + \lambda_i \mathbf{L}^T \mathbf{L}\right)^{-1} \mathbf{K}_i^T \left(\boldsymbol{y}^{\delta} - \boldsymbol{F}(\boldsymbol{x}_{\lambda,i}) + \mathbf{K}_i(\boldsymbol{x}_{\lambda,i} - \boldsymbol{x}_{\mathrm{a}})\right) \;. \tag{4.28}$$

In view of comparing with Eq. (4.14), it is apparent that the iteratively regularized Gauss–Newton method is the method of Tikhonov regularization with a variable regularization parameter. In our retrieval algorithm, the regularization parameters λ_i are chosen as the terms of a monotonically decreasing sequence, e.g.

$$\lambda_i \;=\; q\lambda_{i-1} \;, \tag{4.29}$$

where $q < 1$ is the ratio of the geometric sequence. In practice, we usually apply a scheme in which the regularization strength is gradually decreased during the iterative process, i.e. $q \geq 0.8$. Doicu et al. [2002, 2003] analyzed the numerical performances of this algorithm for nonlinear ill-posed problems without/with bound-constraint by means of simulated infrared spectra.

In the regularizing Levenberg–Marquardt method, the penalty term of the linearized equation depends on the previous iterate $\boldsymbol{x}_i$ rather than the a priori $\boldsymbol{x}_{\mathrm{a}}$, and we have

$$\boldsymbol{x}_{\lambda,i+1} \;=\; \boldsymbol{x}_{\lambda,i} + \left(\mathbf{K}_i^T\mathbf{K}_i + \lambda_i\mathbf{L}^T\mathbf{L}\right)^{-1}\mathbf{K}_i^T\left(\boldsymbol{y}^\delta - \boldsymbol{F}(\mathbf{x}_{\lambda,i})\right) \;. \tag{4.30}$$

Likewise, the parameter choice rule (4.29) can be used for the regularizing Levenberg–Marquardt method.

For iterative regularization methods, the regularization parameter λ is iteration-dependent and the number of iteration steps i plays the role of the regularization parameter. The iterative process has to be stopped after an appropriate number of steps i^* in order to avoid an uncontrolled explosion of the noise error: while the residual decreases as the iteration continues, the solution error begins to increase after an initial decay. In other words, the mere minimization of the residual results in a semi-convergence of the iterative solution. The discrepancy principle can be used as an a posteriori stopping rule. According to the discrepancy principle, the iterative process has to be stopped when the residual is below the noise level. Because in our applications, the noise level cannot be estimated (owing to the forward model errors), we use a modified version of the discrepancy principle. This approach first requires the convergence of the residuals within a prescribed tolerance. After the relative convergence, the stopping index i^* is chosen as

$$\left\|\boldsymbol{F}(\boldsymbol{x}_{\lambda,i^*}) - \boldsymbol{y}^\delta\right\|^2 \leq \chi\left\|\mathbf{r}^\delta\right\|^2 < \left\|\boldsymbol{F}(\boldsymbol{x}_{\lambda,i}) - \boldsymbol{y}^\delta\right\|^2 \;, \qquad 0 \leq i < i^* \;, \tag{4.31}$$

where $\left\|\mathbf{r}^\delta\right\|$ is the residual norm at the last iteration step, and $\chi > 1$ is a control parameter. As inferred from some practical applications, the optimal value of χ should be close to one so that the solution error is sufficiently small.

In practice, the regularization parameter can be decreased slowly during the iteration in order to obtain a stable solution. Furthermore, small initial λ-values should be avoided to prevent local minima.

The benefits of using iterative regularization methods stem from the low computational effort for the estimation of an appropriate regularization parameter. In contrast to Tikhonov regularization, both the iteratively regularized Gauss–Newton and the regularizing Levenberg–Marquardt methods are unaffected by an overestimated initial regularization parameter and may still yield reliable solutions over a large range of values of the regularization parameter. Section 5.1.3 will address an intercomparison between the direct (Tikhonov) regularization method and the two iterative regularization methods.

4.2.3 Multi-parameter regularization

If the inversion deals with the joint retrieval of several gas species (and optionally of some auxiliary parameters), the state vector $\boldsymbol{x}$ is a concatenation of the vectors $\boldsymbol{x}_p$ corresponding to the concentration profile of the pth molecule. Moreover, all individual regularization terms $\mathbf{L}^p$ are assembled into a global matrix $\mathbf{L}$ with a block-diagonal structure based on the assumption that the components of the state vector are independent:

$$\mathbf{L} \;=\; \begin{bmatrix} \sqrt{\lambda_1}\mathbf{L}^1 & 0 & \cdots & 0 \\ 0 & \sqrt{\lambda_2}\mathbf{L}^2 & \cdots & 0 \\ \vdots & \vdots & \ddots & \vdots \\ 0 & 0 & \cdots & \sqrt{\lambda_N}\mathbf{L}^N \end{bmatrix} , \tag{4.32}$$

where N is the number of target molecules. Note that the regularization parameters in Eq. (4.32) are included in the expression of the global regularization matrix. Multi-parameter regularization schemes can be classified into two types according to the objective of the inverse problem:

- complete multi-parameter regularization scheme, in which the regularized solution corresponding to the entire state vector is computed;
- partial multi-parameter regularization scheme, in which only some components of the state vector are retrieved with a sufficient accuracy, e.g. the joint fit of one molecule considered as a main target and an auxiliary atmospheric profile or instrument parameter considered as a contamination.

In this regard, the regularization parameters λ_k can be selected by minimizing certain objective functions with respect to the entire state vector or corresponding to the main target of the state vector, respectively [Doicu et al., 2010].

4.3 Inversion Diagnostics

4.3.1 Sensitivity analysis

In general, a sensitivity analysis reveals our expectations of the inversion outcome. The sensitivity of the forward model $\boldsymbol{F}$ with respect to the state vector $\boldsymbol{x}$ is described in terms of the Jacobian matrix (see Eq. 4.6).

In addition to the Jacobian matrix, the abundance of the species in the state vector should be taken into account. More precisely, for a change in the kth component of the state vector about the a priori $\Delta\boldsymbol{x}_k = \boldsymbol{x} - \boldsymbol{x}_\mathrm{a}$, with

$$\left[\Delta\boldsymbol{x}_k\right]_j \;=\; \begin{cases} \varepsilon\left[\boldsymbol{x}_\mathrm{a}\right]_k & \text{if } j = k \;, \\ 0 & \text{if } j \neq k \;, \end{cases} \tag{4.33}$$

the change in the forward model is given by

$$\Delta\boldsymbol{F}_k \;=\; \boldsymbol{F}\left(\boldsymbol{x}_\mathrm{a} + \Delta\boldsymbol{x}_k\right) - \boldsymbol{F}\left(\boldsymbol{x}_\mathrm{a}\right) \;=\; \mathbf{K}\left(\boldsymbol{x}_\mathrm{a}\right)\Delta\boldsymbol{x}_k \;, \tag{4.34}$$

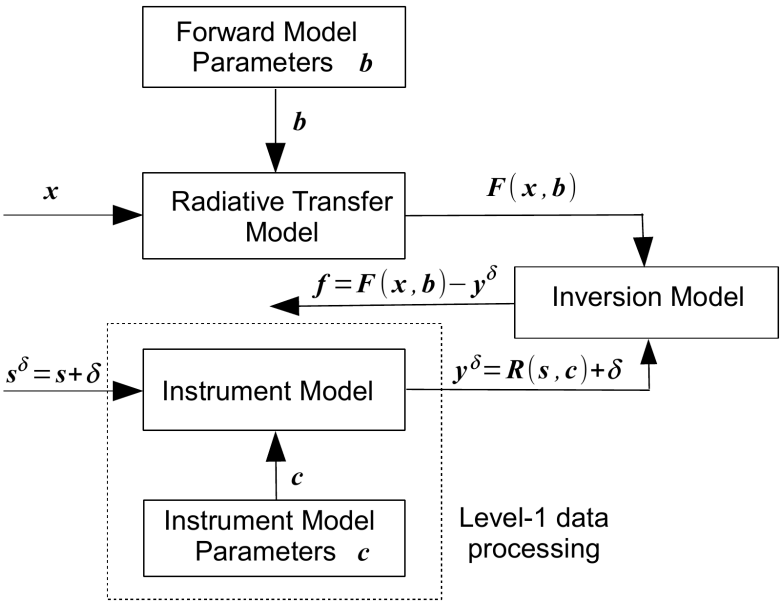

Figure 4.2: Data flow diagram for illustrating the different type of errors.

or componentwise, by

$$[\Delta \boldsymbol{F}_k]_i \;=\; \varepsilon\,[\mathbf{K}\,(\boldsymbol{x}_\mathrm{a})]_{ik}\,[\boldsymbol{x}_\mathrm{a}]_k \qquad \text{with} \quad i = 1, \ldots, m\;. \tag{4.35}$$

In this context, we can say that the instrument is sensitive over the "entire" spectral domain to a $\pm\varepsilon$-variation in the kth component of the state vector about the a priori, if $|[\Delta \boldsymbol{F}_k]_i| > \sigma$ for all $i = 1, \ldots, m$, where σ^2 is the noise variance.

By using these diagnostic techniques, the sensitivity of the limb radiances to the unknowns of the inverse problems (i.e. vertical distributions of the molecular concentration or the temperature) can be studied. For a finer altitude grid, the unfavorable situation is that the retrieval of these quantities is essentially based on information coming from the a priori knowledge and not from the measurement itself. To remediate this deficiency, we can choose a coarser retrieval grid or employ higher-order interpolation schemes.

4.3.2 Error analysis and characterization

When the iterative process converges, it is important to assess the reliability of the retrieval products through an error analysis and characterization. An elaborate discussion covering the topic of error analysis and characterization can be found in Rodgers [2000] and Doicu et al. [2010]. To explain the different type of errors, we illustrate the data flow diagram in Fig. 4.2. The state vector $\boldsymbol{x}$ and the forward model parameters $\boldsymbol{b}$ are mapped by the radiative transfer model into the forward model function $\boldsymbol{F}(\boldsymbol{x}, \boldsymbol{b})$. Similarly, the signal measured by the instrument $\boldsymbol{s}^\delta$ is mapped by the instrument model together with the instrument model parameters $\boldsymbol{c}$ into the noise data vector $\boldsymbol{y}^\delta$. The noisy data vector

$\boldsymbol{y}^{\delta}$ sums the contribution of the instrument model function and the measurement (or the instrument) noise $\boldsymbol{\delta}$, where $\boldsymbol{s}$ is the signal measured by the instrument in the noise-free case. Finally, in the inversion model, the residual vector $\boldsymbol{f}(\boldsymbol{x}) = \boldsymbol{F}(\boldsymbol{x}, \boldsymbol{b}) - \boldsymbol{y}^{\delta}$ is used to compute the Tikhonov function.

Given the regularized generalized inverse $\mathbf{K}_{\lambda}^{\dagger}$, the averaging kernel (or the model resolution) matrix is defined by

$$\mathbf{A} \;=\; \mathbf{K}_{\lambda}^{\dagger}\mathbf{K} \;. \tag{4.36}$$

Providing that the higher-order terms at the solution are neglected, the retrieval error is straightforwardly represented by

$$\boldsymbol{e}_{\lambda} \;=\; \boldsymbol{x}_{\lambda} - \boldsymbol{x}_{\mathrm{t}} \;=\; \boldsymbol{e}_{\mathrm{s}} + \boldsymbol{e}_{\mathrm{y}} + \boldsymbol{e}_{\mathrm{b}} + \boldsymbol{e}_{\mathrm{c}} \;, \tag{4.37}$$

where the smoothing (or null-space) error

$$\boldsymbol{e}_{\mathrm{s}} \;=\; (\mathbf{A} - \mathbf{I}_n)\,(\boldsymbol{x}_{\mathrm{t}} - \boldsymbol{x}_{\mathrm{a}}) \tag{4.38}$$

quantifies the loss of information due to the regularization in the inversion model,

$$\boldsymbol{e}_{\mathrm{y}} \;=\; \mathbf{K}_{\lambda}^{\dagger}\boldsymbol{\delta} \tag{4.39}$$

is the noise error quantifying the loss of information due to the measurement noise $\boldsymbol{\delta}$,

$$\boldsymbol{e}_{\mathrm{b}} \;=\; \mathbf{K}_{\lambda}^{\dagger}\boldsymbol{\delta}_{\mathrm{b}} \tag{4.40}$$

is the forward model error in the state space resulting from the forward model error in the data space $\boldsymbol{\delta}_{\mathrm{b}}$, and

$$\boldsymbol{e}_{\mathrm{c}} \;=\; \mathbf{K}_{\lambda}^{\dagger}\boldsymbol{\delta}_{\mathrm{c}} \tag{4.41}$$

is the instrument model error in the state space resulting from the instrument model error in the data space $\boldsymbol{\delta}_{\mathrm{c}}$.

Although in practice the smoothing error is not a computable quantity, it can be alternatively approximated by

$$\boldsymbol{e}_{\mathrm{s}} \;\approx\; (\mathbf{A} - \mathbf{I}_n)\,(\boldsymbol{x}_{\lambda} - \boldsymbol{x}_{\mathrm{a}}) \;. \tag{4.42}$$

Evidently, keeping the smoothing error small requires a small regularization parameter λ, whereas the stability of the inversion process requires a reasonably large regularization parameter. Thus, the optimal value of λ has to be determined through a compromise between stability and accuracy.

As can be inferred from Eq. (4.38), the deviation of the averaging kernel matrix $\mathbf{A}$ from the identity matrix $\mathbf{I}_n$ characterizes the smoothing error. In atmospheric remote sensing, the averaging kernel matrix provides more information than just a characterization of the smoothing error. The rows of $\mathbf{A}$, namely the averaging kernels, theoretically tend to peak at the diagonal value with a width which is a measure of the vertical resolution of the instrument. In the ideal case, $\mathbf{A}$ would be a unit matrix, but in practice, the regularization degrades the vertical resolution, that is reflected by the peak value

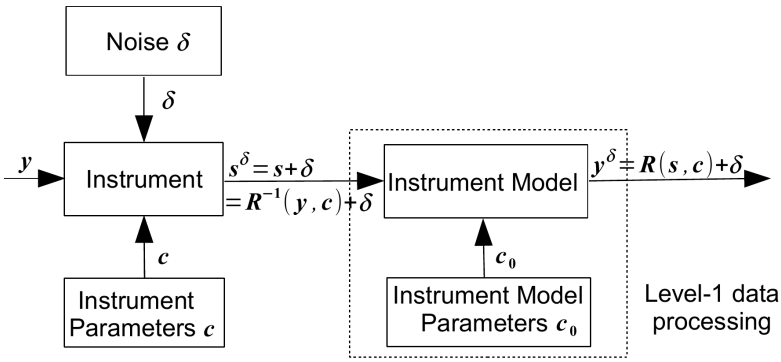

Figure 4.3: Instrument model error.

and the full width at half maximum (FWHM) of this peak. The measurement response is given by the sum of the elements of each averaging kernel row:

$$M_i \;=\; \sum_{j=1}^{n} [\mathbf{A}]_{ij} \;, \qquad i = 1, \ldots, n \;, \tag{4.43}$$

and high values around unity assure that the retrieved information comes mostly from the measurement and the contribution of the a priori profile is almost negligible. Furthermore, the trace of the averaging kernel matrix yields the degree of freedom (DOF) for the signal, that is interpreted as the number of useful independent quantities in a measurement, or a measure of information for brevity.

The forward model error $\boldsymbol{e}_\mathrm{b}$ is caused by inaccurate knowledge of the forward model parameters $\boldsymbol{b}$ (atmospheric and spectroscopic parameters in the forward model). If $\Delta\boldsymbol{b}$ are the uncertainties in $\boldsymbol{b}$, the forward model error can be approximated by

$$\boldsymbol{\delta}_\mathrm{b} \;=\; \mathbf{K}_\mathrm{b}\Delta\boldsymbol{b} \;\approx\; \boldsymbol{F}(\boldsymbol{x}_\mathrm{t}, \boldsymbol{b}+\Delta\boldsymbol{b}) - \boldsymbol{F}(\boldsymbol{x}_\mathrm{t}, \boldsymbol{b}) \;, \tag{4.44}$$

where $\mathbf{K}_\mathrm{b}$ is the Jacobian matrix with respect to the forward model parameters, $\partial\boldsymbol{F}/\partial\boldsymbol{b}$.

The instrument model error $\boldsymbol{e}_\mathrm{c}$ is due to inaccurate knowledge of the instrument model parameters $\boldsymbol{c}$ (Fig. 4.3). The signal delivered by the instrument is given by the inverse of the instrument model function $\boldsymbol{R}^{-1}$ acting on the exact data vector $\boldsymbol{y}$ and the instrument parameters $\boldsymbol{c}$, plus the additive measurement noise $\boldsymbol{\delta}$, i.e. $\boldsymbol{s}^\delta = \boldsymbol{s} + \boldsymbol{\delta} = \boldsymbol{R}^{-1}(\boldsymbol{y}, \boldsymbol{c}) + \boldsymbol{\delta}$. If in the Level-1 data processing step, the instrument model parameters $\boldsymbol{c}_0$ match the true instrument parameters $\boldsymbol{c}$, the output of the instrument model read as

$$\boldsymbol{y}^\delta \;=\; \boldsymbol{R}(\boldsymbol{s}, \boldsymbol{c}) + \boldsymbol{\delta} \;=\; \boldsymbol{R}(\boldsymbol{R}^{-1}(\boldsymbol{y}, \boldsymbol{c}), \boldsymbol{c}) + \boldsymbol{\delta} \;=\; \boldsymbol{y} + \boldsymbol{\delta} \;. \tag{4.45}$$

If this is not the case, i.e. if $\boldsymbol{c}_0 \neq \boldsymbol{c}$, we have

$$\boldsymbol{y}^\delta \;=\; \boldsymbol{R}(\boldsymbol{s}, \boldsymbol{c}_0) + \boldsymbol{\delta} \;=\; \boldsymbol{R}(\boldsymbol{R}^{-1}(\boldsymbol{y}, \boldsymbol{c}), \boldsymbol{c}_0) + \boldsymbol{\delta} \;=\; \boldsymbol{y} + \boldsymbol{\delta}_\mathrm{c} + \boldsymbol{\delta} \;, \tag{4.46}$$

where $\boldsymbol{\delta}_\mathrm{c}$ is the instrument model error in the data space defined by

$$\boldsymbol{\delta}_\mathrm{c} \;=\; \boldsymbol{R}(\boldsymbol{s}, \boldsymbol{c}_0) - \boldsymbol{R}(\boldsymbol{s}, \boldsymbol{c}) \;=\; \boldsymbol{R}(\boldsymbol{R}^{-1}(\boldsymbol{y}, \boldsymbol{c}), \boldsymbol{c}_0) - \boldsymbol{R}(\boldsymbol{R}^{-1}(\boldsymbol{y}, \boldsymbol{c}), \boldsymbol{c}) \;. \tag{4.47}$$

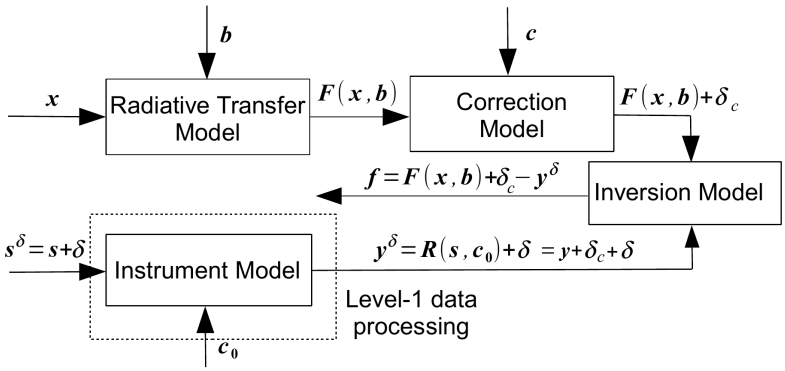

Figure 4.4: Correction step for the instrument model error.

Thus, assuming that $\Delta\boldsymbol{c}$ are the uncertainties in $\boldsymbol{c}$, the instrument model error in the data space can be computed as

$$\boldsymbol{\delta}_{\mathrm{c}} \;=\; \boldsymbol{R}(\boldsymbol{s},\boldsymbol{c}+\Delta\boldsymbol{c}) - \boldsymbol{R}(\boldsymbol{s},\boldsymbol{c}) \;. \tag{4.48}$$

Because in the Level-2 data processing, we deal only with the noisy data vector $\boldsymbol{y}^{\delta} = \boldsymbol{y} + \boldsymbol{\delta}_{\mathrm{c}} + \boldsymbol{\delta}$, it is a common practice to employ an additional correction step to account for the instrument model error $\boldsymbol{\delta}_{\mathrm{c}} = \boldsymbol{\delta}_{\mathrm{c}}(\boldsymbol{c})$. This situation is depicted in Fig. 4.4, and note that the instrument parameters can or cannot be included in the retrieval.

In a semi-stochastic framework, the smoothing and model parameter errors are deterministic, whereas the noise error is stochastic with zero mean and covariance matrix $\mathbf{S}_{\mathrm{y}}$. The quality of the regularized solution can be estimated through the mean square error matrix computed as

$$\mathbf{S}_{\lambda} \;=\; \mathcal{E}\left[(\boldsymbol{x}_{\lambda}-\boldsymbol{x}_{\mathrm{t}})\,(\boldsymbol{x}_{\lambda}-\boldsymbol{x}_{\mathrm{t}})^{T}\right] \;\approx\; \mathbf{S}_{\mathrm{s}}+\mathbf{S}_{\mathrm{y}}+\mathbf{S}_{\mathrm{b}}+\mathbf{S}_{\mathrm{c}} \;, \tag{4.49}$$

where under the assumption that the measurement noise $\boldsymbol{\delta}$ is a white noise with variance σ^2, we have

$$\mathbf{S}_{\mathrm{s}} \;=\; \boldsymbol{e}_{\mathrm{s}}\boldsymbol{e}_{\mathrm{s}}^{T} \;, \tag{4.50}$$

$$\mathbf{S}_{\mathrm{y}} \;=\; \sigma^{2}\mathbf{K}_{\lambda}^{\dagger}\mathbf{K}_{\lambda}^{\dagger T} \;, \tag{4.51}$$

$$\mathbf{S}_{\mathrm{b}} \;=\; \boldsymbol{e}_{\mathrm{b}}\boldsymbol{e}_{\mathrm{b}}^{T} \;, \tag{4.52}$$

$$\mathbf{S}_{\mathrm{c}} \;=\; \boldsymbol{e}_{\mathrm{c}}\boldsymbol{e}_{\mathrm{c}}^{T} \;. \tag{4.53}$$

The square root of the diagonal elements of $\mathbf{S}_{\lambda}$ gives the retrieval error, while the off-diagonal elements quantify the correlations between the components of the regularized solution $\boldsymbol{x}_{\lambda}$,

$$\mathbf{C}_{\lambda}(i,j) \;=\; \frac{\mathbf{S}_{\lambda}(i,j)}{\sqrt{\mathbf{S}_{\lambda}(i,i)\mathbf{S}_{\lambda}(j,j)}} \;, \tag{4.54}$$

where i and j are the row and column index, respectively.

Note that the sum of the square root of the diagonal elements of $\mathbf{S}_\lambda$ is the expected value of the retrieval error, i.e.

$$\mathcal{E}\left[\|\boldsymbol{e}_\lambda\|^2\right] \;=\; \|\boldsymbol{e}_\mathrm{s}\|^2 + \mathcal{E}\left[\|\boldsymbol{e}_\mathrm{y}\|^2\right] + \|\boldsymbol{e}_\mathrm{b}\|^2 + \|\boldsymbol{e}_\mathrm{c}\|^2 \;, \tag{4.55}$$

where $\mathcal{E}$ is the expected value operator. As stated previously, the model parameter errors are deterministic. More precisely, if for example, $\Delta\boldsymbol{b} = \varepsilon\boldsymbol{b}$ for some scalar $\varepsilon < 1$, we have

$$\mathbf{S}_\mathrm{b} \;=\; \varepsilon^2 \mathbf{K}_\lambda^\dagger \mathbf{K}_\mathrm{b} \boldsymbol{b}\boldsymbol{b}^T \mathbf{K}_\mathrm{b}^T \mathbf{K}_\lambda^{\dagger T} \;. \tag{4.56}$$

Defining the diagonal matrix $\mathbf{B}$ by $[\mathbf{B}]_{ii} = [\boldsymbol{b}]_i$, $i = 1, \ldots, n$, the matrix of all ones $\mathbf{1}$ by

$$\mathbf{1} \;=\; \begin{bmatrix} 1 & \cdots & 1 \\ \vdots & \ddots & \vdots \\ 1 & \cdots & 1 \end{bmatrix} \;, \tag{4.57}$$

and the symmetric and positive definite matrix $\mathbf{C}_\mathrm{b}$ by

$$\mathbf{C}_\mathrm{b} \;=\; \varepsilon^2 \mathbf{B}\mathbf{1}\mathbf{B}^T \;, \tag{4.58}$$

i.e.

$$[\mathbf{C}_\mathrm{b}]_{ij} \;=\; \varepsilon^2 \, [\boldsymbol{b}]_i \, [\boldsymbol{b}]_j \;, \qquad i, j = 1, \ldots, n \;. \tag{4.59}$$

yields

$$\mathbf{S}_\mathrm{b} \;=\; \mathbf{K}_\lambda^\dagger \mathbf{K}_\mathrm{b} \mathbf{C}_\mathrm{b} \mathbf{K}_\mathrm{b}^T \mathbf{K}_\lambda^{\dagger T} \;. \tag{4.60}$$

In a stochastic framework, when $\boldsymbol{b}$ is assumed to be a stochastic quantity, $\mathbf{C}_\mathrm{b}$ defined by Eqs. (4.58) and (4.59), is interpreted as the covariance matrix of $\boldsymbol{b}$. Thus, in view of Eq. (4.22) with $l \to \infty$, Eqs. (4.57)–(4.59), a deterministic treatment of $\boldsymbol{b}$ is equivalent to a stochastic treatment, in which ε is the model parameter standard deviation, and all components of $\boldsymbol{b}$ are perfectly correlated. If the components of $\boldsymbol{b}$ are not correlated, then the matrix of all ones $\mathbf{1}$ should be replaced by the identity matrix $\mathbf{I}_n$.

4.4 B-spline Scheme

In general, piecewise polynomials are extensively used to approximate continuous functions. Due to several attractive properties, such as local support, positivity, and control flexibility, B-splines are superior to polynomial approximations (e.g. Lagrange, Newton, and Chebyshev polynomials). Several applications to discrete ill-posed inverse problems in atmospheric remote sensing have been discussed by O'Sullivan and Wahba [1985], Böckmann [2001], and Doicu et al. [2004].

In most cases, the state vector $\boldsymbol{x}$ is represented by an expansion in terms of piecewise linear functions. The expansion coefficients are the discrete values of the function (e.g. VMR, number density, etc.) at each sampling level in the interval $[z_a, z_b]$. For simplicity we call this structure as "X-type". In this section, a hybrid regularization scheme combining a direct/iterative regularization method and B-spline approximation

is presented. We denote this particular retrieval procedure using B-spline approximation as "B-type". In case of the "B-type" structure, the representation of the unknown X at altitude level z is a linear combination of B-spline basis functions

$$X(z) \;=\; \sum_{j=1}^{n} \omega_j \mathrm{B}_{j,k}(z) \tag{4.61}$$

with $\mathrm{B}_{j,k}(z)$ and ω_j being the kth order B-splines and its expansion coefficients. In this case, the state vector consists of the B-spline expansion coefficients ω_j instead of the altitude-dependent unknowns $X(z)$. This regularization scheme involves two parameters: the regularization parameter λ and the order of the B-spline basis k.

The first-order basis B-splines are piecewise constants and are defined by

$$\mathrm{B}_{j,1} \;=\; \begin{cases} 1 & \text{if } t_j \le z < t_{j+1} \ , \\ 0 & \text{otherwise} \ . \end{cases} \tag{4.62}$$

The higher-order ($k > 1$) basis B-splines are constructed successively in terms of the lower-order basis B-splines $k-1$ as follows [de Boor, 2001]:

$$\mathrm{B}_{j,k} \;=\; \frac{z - t_j}{t_{j+k-1} - t_j} \mathrm{B}_{j,k-1} + \frac{t_{j+k} - z}{t_{j+k} - t_{j+1}} \mathrm{B}_{j+1,k-1} \ , \tag{4.63}$$

where $t_1 \le t_2 \le \cdots \le t_{n+k}$ denote a nondecreasing knots sequence at which two non-trivial linear pieces are tied continuously.

4.4.1 Knots selection

A proper choice of the knots is vital to the shape of the solution. The knots can be distributed in the interval $[z_a, z_b]$ in several different ways. Throughout this study, we choose the "boundary" knots as $t_1 = \cdots = t_k = z_a$ and $t_{n+1} = \cdots = t_{n+k} = z_b$, because extrapolation beyond z_a and z_b is not anticipated.

For the knots $t_{k+1}, \ldots, t_n$, some sophisticated selection schemes can be considered. It should be pointed out that an appropriate knot selection determines the anticipated shape of the solution.

In the uniformly spaced method, the knots are distributed over the altitude range as

$$t_{k+i} = z_a + i \frac{z_b - z_a}{n - k + 1} \qquad \text{with} \quad i = 1, \ldots, n-k. \tag{4.64}$$

This method is simple but may cause unpleasant results (e.g. sharp peaks, loops) when the data points are not spaced uniformly.

The roots of Chebyshev polynomials of the first and second order, i.e.

$$t_{k+i} = z_a + (z_b - z_a) \cos\left(\frac{2\,(n-k-i)+1}{4\,(n-k)} \pi \right) \qquad \text{with} \quad i = 1, \ldots, n-k, \tag{4.65}$$

and

$$t_{k+i} = z_a + (z_b - z_a) \cos\left(\frac{n-k-i+1}{2\,(n-k)+1}\pi\right) \qquad \text{with} \quad i = 1, \ldots, n-k, \tag{4.66}$$

respectively, can also be used for knot selection. The obtained grids result in more densely distributed knots with increasing altitude, and is suitable for the retrieval of profiles with steeper values at higher altitudes. Doicu et al. [2004] studied the inversion performance of temperature retrievals using equidistant and nonequidistant knot grids.

An optimal knot selection scheme proposed by [de Boor, 1977] starts from the initial guess

$$t_{k+i} \;=\; \frac{z_{i+1} + \cdots + z_{i+k-1}}{k-1} \qquad \text{with} \quad i = 1, \ldots, n-k, \tag{4.67}$$

and uses recursively Newton's method. As shown by de Boor [1977], the initial know distribution is very close to the optimum, and therefore, the knot choice (4.67) can be used directly.

4.4.2 Test example

The aim of our numerical test is to compare the inversion performance of the regularization method using the B-spline approximation ("B-type") with that of the regularization method using a piecewise linear interpolation ("X-type"). We consider the inversion problem of a vertical ozone profile from a single far infrared limb sequence. The scenario consists of an observer at an altitude of 40 km and a tangent grid with a step of 1.5 km between 10 and 32.5 km, which corresponds to the altitude range typically covered by the TELIS instrument. The signal-to-noise of the simulated limb sequence is chosen as 100.

A retrieval grid with a spacing of 1.5 km between 10 and 32.5 km and a coarser spacing of 2.5 km between 32.5–40 km is considered. The regularization matrix used in this test is the $\mathbf{L}_1$ matrix. For the B-spline approximation, the a priori and initial values of the expansion coefficients are computed from the corresponding concentration profiles. The number of distinct knots over the considered altitude range is $n - k + 2$.

In Fig. 4.5a we illustrate the relative difference of the retrieved O_3 profile with respect to the true profile for different orders of the B-splines. Here and in the following, the relative/absolute differences of the retrieved profile with respect to the true profile are defined as the altitude-dependent relative/absolute errors in the solution. The appropriate choice of the B-spline order is important: the relative differences are small and almost coincide for $k = 3$ and $k = 4$, while the retrieval deteriorates when the order increases.

Figure 4.5b shows the O_3 retrievals for different discretization schemes. The B-spline approximation with $k = 4$ leads to a better result than the linear interpolation at lower altitudes, whereas smaller deviations from the true profile are obtained by the linear interpolation at higher altitudes.

Nevertheless, our numerical example reveals that the method using B-spline approximation generates reasonable retrieval results. Further investigations will focus on

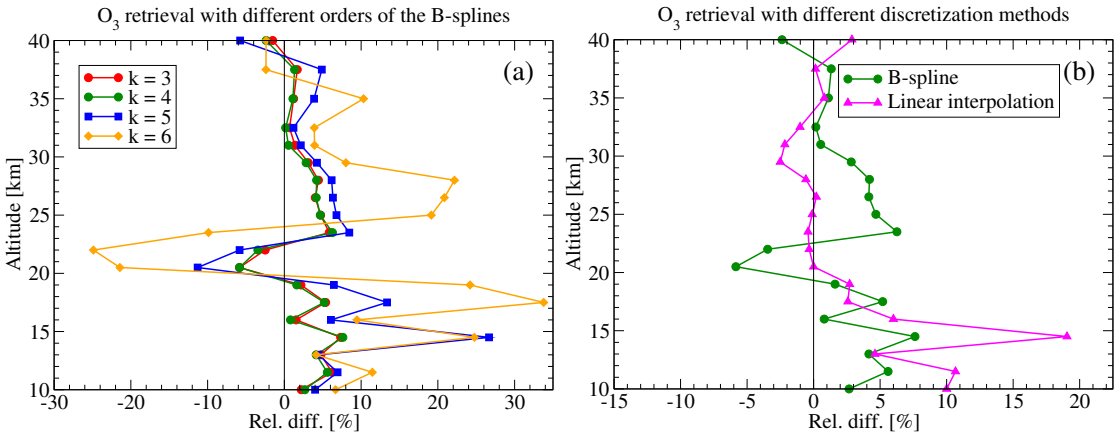

Figure 4.5: Retrieval of an O_3 profile from TELIS synthetic spectra by using B-spline approximation. Panel **(a)**: relative differences of the retrieved O_3 profile with respect to the true profile for different orders k of the B-splines. Panel **(b)**: relative differences of the retrieved O_3 profile with respect to the true profile for different discretization methods with B-spline ($k = 4$), and linear interpolation.

accelerating the computation by an appropriate reduction of the number of B-splines. Note that a reduced number of unknowns yields a smaller dimension of the Jacobian matrix, and so, a reduction of the computational time.

4.5 Implementation

In the framework of PILS, the minimization problem (4.10) is solved by using the PORT Mathematical Subroutine Library (available at `http://www.netlib.org/port/`). To determine the new iterate, the algorithm is based on a trust-region method in conjunction with a Gauss–Newton model and a quasi-Newton model [Dennis, Jr. et al., 1981a,b].

As introduced in Sect. 3.3, the derivatives with respect to the unknowns in the state vector are generated by TAPENADE 3.4. The original function is differentiated in "tangent multi-directional mode" which computes the variations of the dependent output variables concurrently for several directions in the input space.

In the case of the B-spline approximation, the relevant numerical routines developed by de Boor [de Boor, 2001] are utilized.

After the final iteration, the program delivers the diagnostic quantities described in Sect. 4.3.2, including the retrieval error, the relative/absolute differences of the retrieved profiles with respect to the true (or reference) profiles, the averaging kernels (with corresponding measurement response and degree of freedom for the signal), and the residual sum of squares.

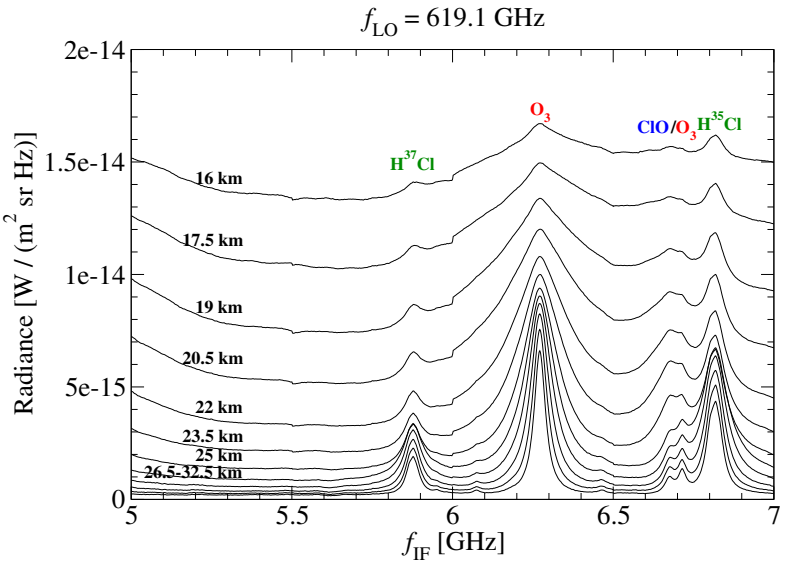

Figure 4.6: A sequence of limb spectra in the HCl microwindow measured by the TELIS 480–650 GHz channel during the 2010 flight. The limb sequence, covering tangent heights between 16 and 32.5 km in steps of 1.5 km, and observing the $H^{37}Cl$ and $H^{35}Cl$ lines, is illustrated as a function of the intermediate frequency f_{IF}. The local oscillator frequency f_{LO} is set to 619.1 GHz, and f_{IF} ranges from 5 to 7 GHz. The corresponding tangent heights are displayed on the left side of the frame. The dedicated measurement identifier is 20044.

4.6 Verification

In Sect. 3.4, we have presented an intercomparison of radiative transfer simulations between the two TELIS Level-2 data processing codes (PILS and AdL). The simulations are based on a limb-scanning sequence corresponding to a HCl microwindow (f_{LO} = 619.1 GHz, f_{IF} = 5–7 GHz) of TELIS. In this section, the inversion performances of PILS and AdL are compared by carrying out a retrieval of atmospheric HCl from real TELIS limb spectra. A TELIS submillimeter measurement for this HCl microwindow recorded on 24 January 2010 is depicted in Fig. 4.6. The two HCl transitions are visible in the second and the fourth segments, respectively.

To rule out any factors associated with the measurement itself, both algorithms used the identical frequency segment to derive the HCl profile. Regarding PILS, we study the numerical performance with different regularization setups, i.e. by using different combinations of the regularization matrix $\mathbf{L}$ and a priori profile $\boldsymbol{x}_\mathbf{a}$ (identical to the initial guess $\boldsymbol{x}_\mathbf{0}$). Table 4.2 lists the two regularization scenarios used in this comparison. In particular, we used a zero a priori profile in the case $\mathbf{L} = \mathbf{L}_0$ so that the inappropriate mapping of the a priori knowledge onto the result may be avoided. The regularization parameter is determined by the SVD approach in conjunction with the discrepancy principle.

The SRON retrieval algorithm for the TELIS's 480–650 GHz channel was explicitly

Table 4.2: Regularization setups for PILS in the retrieval intercomparison.

Scenario	Regularization matrix	$\boldsymbol{x}_\mathbf{a}$
TR-1	$\mathbf{L}_\mathrm{C}$	AFGL subarctic winter
TR-2	$\mathbf{L}_0$	zero

Table 4.3: The fitted molecules for the retrieval intercomparison of the two Level-2 processing codes PILS and AdL developed by DLR and SRON, respectively.

Retrieval	HCl	ClO	O_3
$H^{37}Cl$	✓	–	✓
$H^{35}Cl$	✓	✓	✓

described in de Lange et al. [2009, 2012]. Its inversion algorithm makes use of Tikhonov regularization and the regularization parameter is chosen by the L-curve approach. The regularization matrix is set to the identity matrix ($\mathbf{L}_0 = \mathbf{I}_n$). The a priori profile is also a zero profile, but the retrieval starts with the MLS profile as initial guess.

In addition to atmospheric profiles of species, the state vector $\boldsymbol{x}$ includes two baseline parameters accounting for radiometric and physical offsets for each spectrum in the limb sequence. The concentration profiles in the state vector for the different retrieval tests are given in Table 4.3. O_3 has to be jointly retrieved as ozone produces a sloped background for both HCl lines. Besides, a weak ClO line resides in the wing of the $H^{35}Cl$ line and needs to be included in the state vector. O_3 and ClO are not treated as the retrieval product, but rather as an improvement of the HCl retrieval. The systematic pointing bias (-5.4 arcmin) and the atmospheric refraction effect make the actual tangent point lower than the commanded lowest one (16 km), and the vertical FoV extends the observing area of the TELIS instrument. Thus, the bottom of the retrieval grid is set to 13 km, although the retrieval over 13–16 km has limited physical meaning.

Figure 4.7 illustrates a comparison of the retrieved HCl profile using the two inversion algorithms. The results of PILS correspond to the two regularization scenarios in Table 4.2 (TR-1 and TR-2). Note that the natural abundance ratio of the isotopes ($Cl^{35}/Cl^{37} = 0.7578/0.2422$) have been taken into account and that the plotted VMR profiles denote the total HCl concentration amounts.

In the case of the $H^{37}Cl$ retrieval (Fig. 4.7a), the pronounced difference is found in the altitude range of 13 to 17.5 km where the information comes mainly from the a priori. For TR-2, the regularization aims to offer smoothness of the solution, but with no a priori effect at lower altitudes. All retrieved profiles resemble the HCl absence around 23 km, which is most likely because the flight took place inside the chlorine activated air of the northern polar region. It can be seen that the profiles derived by TR-1 and AdL are close from 25 km up to the highest tangent altitude 32.5 km.

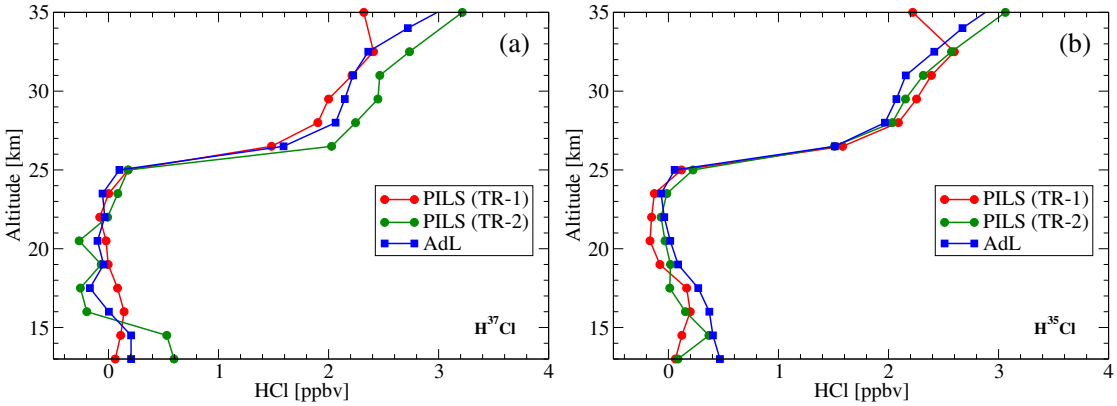

Figure 4.7: Comparison of retrieved HCl profiles delivered by the two Level-2 processing codes PILS and AdL. The inversion is carried out for the TELIS's submillimeter measurement 20044 that was observed on 24 January 2010. The retrieval results are derived for two HCl isotopes, i.e. **(a)** $H^{37}Cl$ and **(b)** $H^{35}Cl$. Red and green lines indicate the results by PILS for the different regularization scenarios in Table 4.2.

In Fig. 4.7b, the $H^{35}Cl$ retrieval results are similar to the $H^{37}Cl$ retrieval results. The HCl profiles derived by PILS and AdL agree over almost the entire altitude range of 13 to 32.5 km. Likewise, very little amount of HCl is observed below 25 km.

Above all, the HCl profiles obtained from $H^{37}Cl$ and $H^{35}Cl$ are internally consistent over the altitude range. A strong chlorine activation occurring inside the polar vortex was detected by observations of both isotopes by TELIS, which corresponds to the altitude range with nominal HCl abundances in the stratosphere. This is supported by an intercomparison between TELIS and other limb sounders (i.e. SMILES and MLS) during that day, as stated in Sect. 6.3. The retrieval calculations implemented by both retrieval codes reach a satisfactory agreement, and the major discrepancies are estimated to be produced by the a priori information and the forward simulations.

Chapter 5

Simulations

In previous chapters, the PILS's radiative transfer model and the inversion methodology have been presented. By making use of a set of retrieval simulations stressing the application to the TELIS instrument, this chapter will serve to evaluate the inversion performance and to characterize the retrieval product. To compute the iterates reliably and subsequently to characterize the error budget in the solution, we conduct a feasibility study of OH detected by the 1.8 THz channel. Not only single- and multi-target retrievals, but also different regularization algorithms and techniques including the choice of the regularization matrix are studied.

Perfect knowledge of the forward and instrument model parameters is not a realistic assumption when dealing with the actual observations. For this reason, a sensitivity study with respect to these types of potential error sources is performed.

Furthermore, the capability of multi-channel simultaneous processing of the far infrared and submillimeter measurements for HCl retrieval is investigated. The primary objective of this implementation is to accomplish an improved use of information from observations in an extended spectral range.

5.1 Retrieval Tests

A feasibility study with synthetic measurements is always a critical step for performance evaluation of the retrieval code, and serves to analyze the possible errors originating from uncertainties in model parameters. Similar feasibility studies regarding far infrared and microwave limb sounding using simulated measurements can be found in: de Lange et al. [2009] for TELIS's 480–650 GHz channel, Takahashi et al. [2010]; Baron et al. [2011] for JEM/SMILES, Baron et al. [2001]; Lossow et al. [2007] for Odin/SMR, and Pumphrey and Bühler [2000] for UARS/MLS.

The main target of the far infrared (Terahertz) observations by TELIS is OH which is a key reactive species for photochemical reactions that regulate ozone throughout most of the stratosphere and mesosphere. The demand and interest of measuring and assimilating middle atmospheric hydrogen chemistry has been increased. Except for several existing ultraviolet measurements, the OH transitions in the far infrared region have

Table 5.1: Main instrument and geometry parameters used for simulating the synthetic spectra observed in the OH microwindow. The channel notation THz stands for the 1.8 THz channel. Note that perfect instrument and atmospheric temperature and pressure knowledge is assumed in Sect. 5.1.

Parameter	Description
Channel	THz
LO frequency	1830.10 GHz
Intermediate frequency	4–6 GHz
Spectral resolution	2.16 MHz
ILS function	Hamming apodization
Field-of-view (FWHM)	Gaussian (6.3 arcmin)
Sideband ratio	1.0
Signal-to-noise ratio	35
Top-of-atmosphere	85 km
Observer altitude	35 km
Tangent heights	15–33 km
Vertical sampling	2 km

also attracted great attention for developing remote sensing techniques, most notably the MLS limb sounder on the Aura satellite that has the ability to measure OH diurnal dynamics using thermal emission from 2.5 THz rotational lines.

A number of balloon-borne instruments have been developed and successfully delivered OH measurements in the past few decades, as introduced in Chap. 2. As a predecessor of TELIS, the up-looking airborne heterodyne spectrometer THOMAS performed OH observations between about 30 and 90 km over a full diurnal cycle in August 1997 [Englert et al., 2000]. Most of the Terahertz instruments launched previously observe the OH transitions at 2.5 and 3.5 THz, whereas the TELIS instrument used 1.8 THz for monitoring OH in the lower and middle stratosphere. Although the OH emission at 1.8 THz is weaker than that at 2.5 and 3.5 THz, the former one was chosen for the sake of a higher sensitivity of the HEB (Hot Electron Bolometer) mixer at 1.8 THz, and of the risks associated with the development of solid state local oscillators at other higher frequencies [Mair et al., 2004].

5.1.1 Retrieval setup

To address an initial expectation of the measurement capabilities, we present and discuss the OH retrieval from a single limb-scanning sequence that largely resembles typical TELIS radiance spectra recorded by the 1.8 THz channel. The limb tangent height varies from 15 to 33 km in steps of 2 km, while the observer altitude is 35 km (indicating with the dotted maroon line in the following figures). The main instrument and geometry parameters used for simulating the synthetic spectra are listed in Table 5.1.

H_2O, O_3, HOCl, HCl, and HO_2 are included in this simulation test as interfering molecules. The related line parameters are taken from the HITRAN 2008 spectroscopic database, and the CKD model is used to account for the H_2O continuum. In the preparatory phase prior to the balloon flights, it is important to choose a proper spectral microwindow covering the OH lines with minimum overlapping contributions from other atmospheric spectral lines. Here, the LO frequency is set to 1830.10 GHz ($\approx 61.04\,\mathrm{cm}^{-1}$) with an intermediate frequency range of 4–6 GHz, observing the OH transition triplet at 1834.75 GHz. The atmospheric pressure, temperature and molecular concentration profiles are taken from the AFGL (**A**ir **F**orce **G**eophysics **L**aboratory) subarctic winter reference model [Anderson et al., 1986]. The retrieval grid is discretized with finer steps of 2 km between 15 and 25 km, steps of 2.5 km between 25 and 50 km, and coarser steps of 5 km between 50 and 85 km.

In this section, temperature, pressure, HCl, and HO_2 are assumed to be known and set to their a priori values. The retrieval of H_2O, O_3, and HOCl will be separately discussed in Sect. 5.1.3. To first assess the retrieval performance for the ideal case, perfect forward and instrument model parameters are assumed, i.e. $\boldsymbol{e}_\mathrm{b} = \boldsymbol{e}_\mathrm{c} = 0$.

5.1.2 Preprocessing

An efficient and reliable retrieval process should consist of a preprocessing step involving a sensitivity analysis of the forward model with respect to the target molecule(s).

Figure 5.1 depicts the partial derivatives of the radiance with respect to the vertical concentrations of all six molecules between 15 and 45 km for a tangent height of 25 km. In the derivative spectra of OH, two triplet pairs are visible at both sides of the intermediate frequency of 4.65 GHz. It should be noticed that the strong triplet lies in the upper sideband, whereas the weaker one occurs in the lower sideband. Both peaks are found to be larger than the middle trough by a factor of 1.5, and the peaks are about two to five orders of magnitude larger than those of the other molecules. Although the limb spectra contains limited information for the altitudes above 35 km, the atmosphere above the instrument may affect the retrieval at lower altitudes and cannot be simply neglected in the forward model.

The second analysis involving the variations of the limb radiances $\Delta \boldsymbol{F}_k^s$, for the sth tangent height and a 10 % variation of the concentration profile of the four relevant molecules in the kth level, is illustrated in Fig. 5.2. HCl and HO_2 are not considered as both of them have minor influence on the measurement signal in this microwindow. The results show that information about the concentration profile in a specific altitude level is mainly given by the spectra corresponding to the tangent heights below this altitude level. The instrument is sensitive to OH in the intermediate frequency range of 4.5–5 GHz, which is consistent with the Jacobian matrix shown in Fig. 5.1. In this spectral range, and for the altitude levels above 27.5 km, the sensitivity of OH is superior to that of the other molecules. Below 27.5 km, the OH concentration is rather low and of no significant importance to the measured radiance signal. In this regard, it can be expected that the retrieval of OH below altitude levels of 27.5 km essentially relies on the a priori information rather than the measurement. For the OH retrieval problem, the

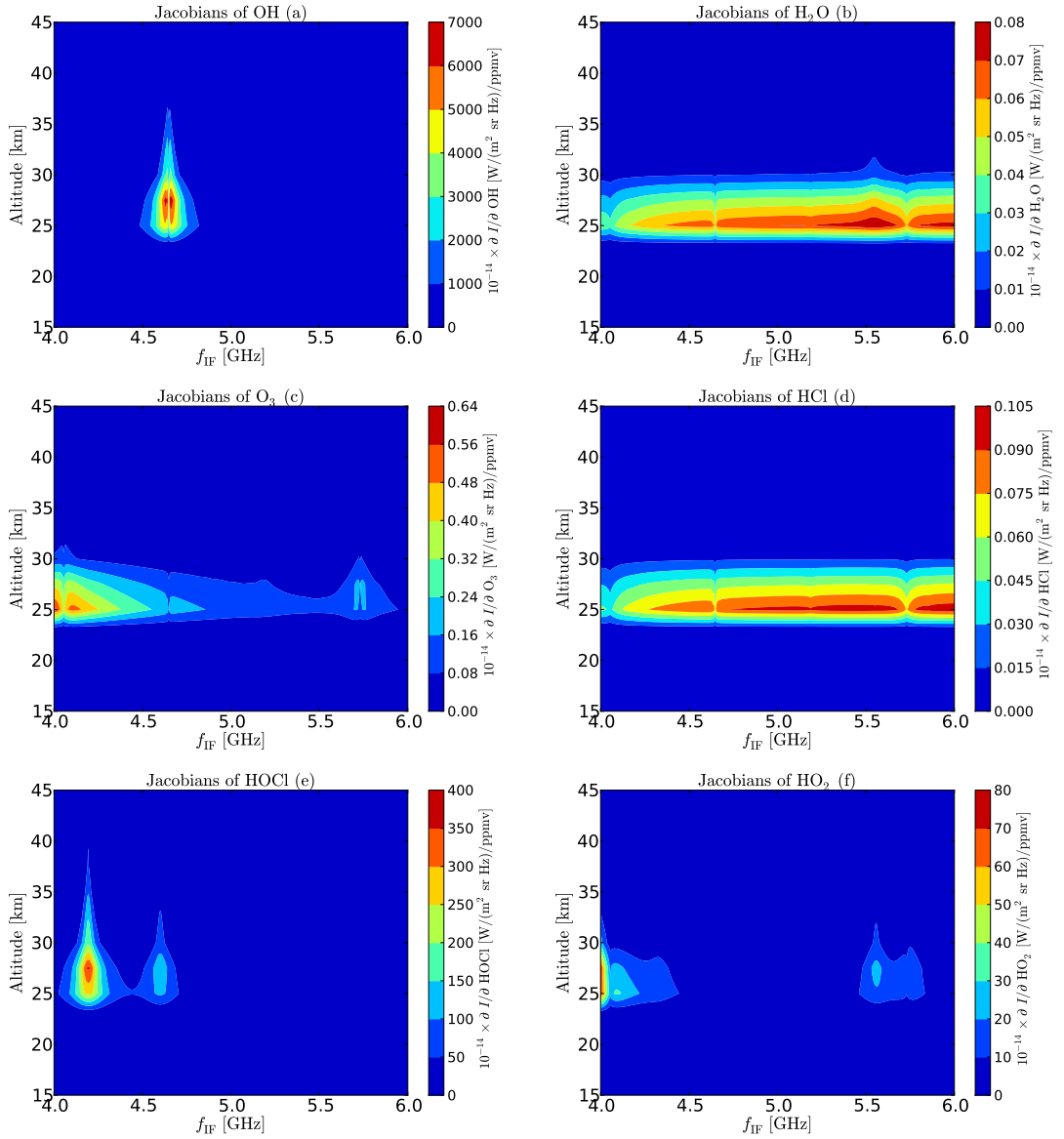

Figure 5.1: Partial derivatives of the radiance with respect to the molecular concentration profiles evaluated at altitudes between 15 and 45 km for a tangent height of 25 km. The molecules are **(a)** OH, **(b)** H_2O, **(c)** O_3, **(d)** HCl, **(e)** HOCl, and **(f)** HO_2.

variations of the spectra at 27.5 and 30 km are not substantially larger than the noise level (these results suggest that the noise error may be large at altitudes below 30 km).

Typical far infrared limb emission spectra are shown in Fig. 5.3 for the OH microwindow. To display the contributions of both sidebands, the upper- and lower sidebands spectra are included in this figure as well. The OH transition triplet mainly comes from

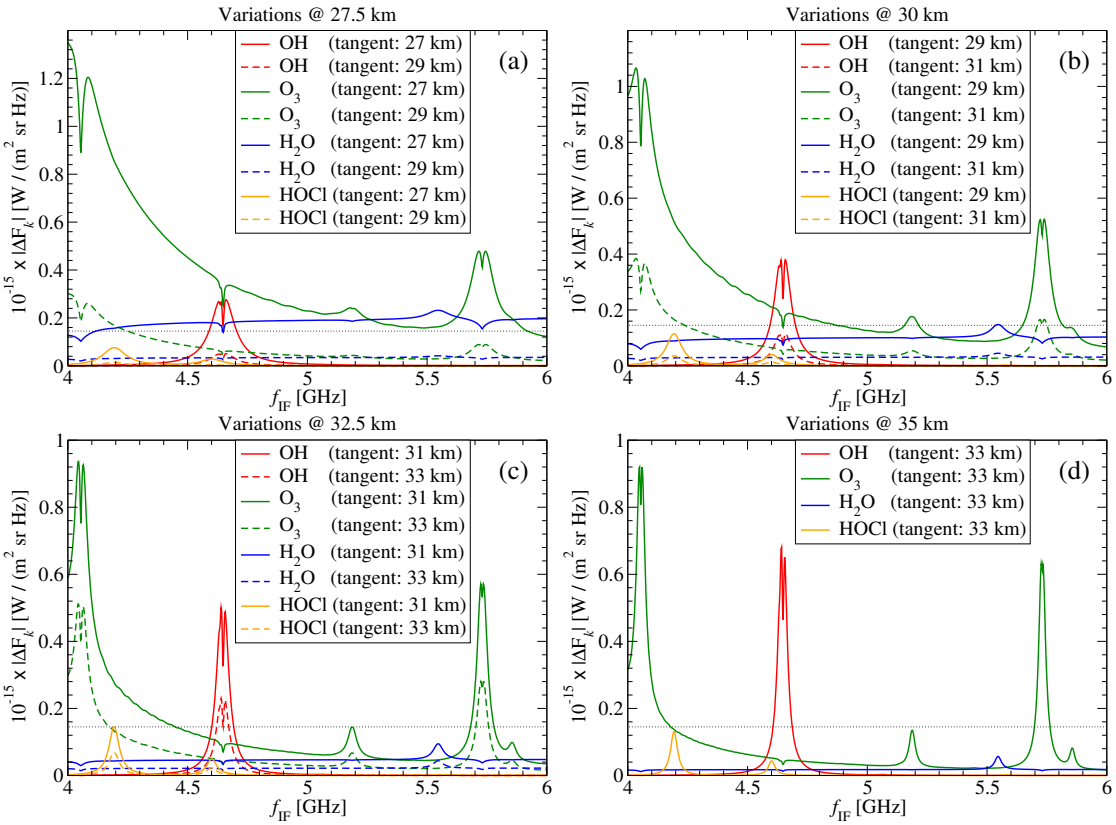

Figure 5.2: Variations of the limb radiances for a 10 % variation in the concentration profiles of OH, O_3, H_2O, and HOCl at the altitude levels of **(a)** 27.5, **(b)** 30, **(c)** 32.5, and **(d)** 35 km. The dotted horizontal lines delimit the noise domain.

the upper sideband, as previously stated. A sequence of noise contaminated spectra is essential for a realistic inversion analysis. In the present study only the radiometric noise is considered, and the signal-to-noise ratio for a single spectrum is estimated by

$$\mathrm{SNR} \;=\; \frac{T_{\mathrm{sig}}}{T_{\mathrm{sys}}}\,\sqrt{\Delta f\; t}\;, \tag{5.1}$$

where the TELIS spectral resolution Δf is 2.16 MHz, and the integration time t is 1.5 s. The average system noise temperature T_{sys} ranges between 3000 and 4000 K in the case of the 1.8 THz channel [Birk et al., 2010]. For the selected OH microwindow, T_{sys} can reach 3800 K, according to previous in-flight observations. The noise δ, which is added to the noise-free spectrum for each tangent height, is white noise and is described by a Gaussian distribution. There is no correlation in terms of the added noise over the frequency range.

The initial guess and the a priori profile of the target molecule(s) $\boldsymbol{x}_0$ and $\boldsymbol{x}_{\mathrm{a}}$, respec-

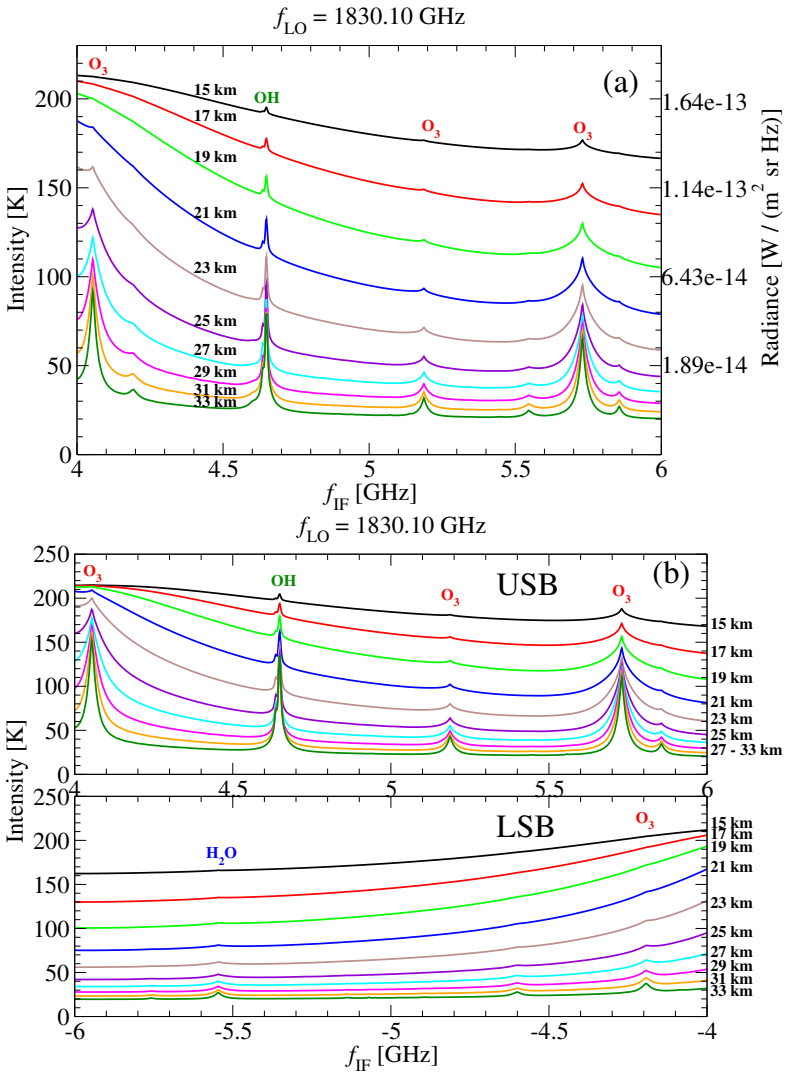

Figure 5.3: Noise-free far infrared spectra for a local oscillator frequency $f_{LO} = 1830.10\,\text{GHz}$, an intermediate frequency range of 4–6 GHz and recorded in double sideband mode with a sideband ratio of 1.0. The spectra correspond to the 1.8 THz channel and a flight altitude of 35 km. Panel **(a)**: simulated TELIS spectra (radiance and equivalent brightness temperature). Panel **(b)**: contributions to the spectra from the upper- and lower sidebands.

tively, are assumed to be identical and are chosen as

$$\boldsymbol{x}_0 = \boldsymbol{x}_\text{a} \;=\; \begin{cases} 0.1\;\boldsymbol{x}_\text{t} & \text{if } z < 30\,\text{km}\,, \\ 0.12\;\boldsymbol{x}_\text{t} & \text{if } z \geq 30\,\text{km}\,. \end{cases} \tag{5.2}$$

Note that a small deviation to the original shape is superimposed at higher altitudes so that the profile does not have exactly the same shape as the true profile.

5.1.3 Retrieval performance

The retrieval performance with respect to different configurations of the state vector and regularization matrices is presented. The selection of the regularization parameter λ is discussed for each retrieval case. The diagnostic quantities are the retrieval error (i.e. the root sum squares of the noise and smoothing errors) and the difference of the retrieved profile with respect to the true profile.

One-profile retrieval

In Fig. 5.4a, we illustrate the relative solution errors (4.24) of OH as a function of the regularization parameter λ for Tikhonov regularization, the iteratively regularized Gauss–Newton method, and the regularizing Levenberg–Marquardt method. For the two iterative methods, λ is the initial value of the regularization parameter, while at all subsequent iteration steps the regularization parameters $\lambda_i = q\lambda_{i-1}$ are the terms of a geometric sequence with $q = 0.8$. The error curve corresponding to Tikhonov regularization possesses a minimum, and by convention, the minimizers of the solution errors denote the optimal values of the regularization parameter. The iteratively regularized Gauss–Newton method still yields reliable results for large initial values of the regularization parameter. Although Tikhonov regularization converges always quickly (with ≤ 5 iteration steps), the iteratively regularized Gauss–Newton method works stably regardless of large regularization parameter. Evidently, a stronger regularization at the beginning of the iterative process yields a larger number of iterations as it can be seen in Fig. 5.4b. Similarly, the regularizing Levenberg–Marquardt method is insensitive to overestimations of the regularization parameter. However, the results in Fig. 5.4 reveal that the regularizing Levenberg–Marquardt method is inferior to the iteratively regularized Gauss–Newton method: for large initial values of the regularization parameter, the solution errors are larger.

For efficiency reasons, we choose the method of Tikhonov regularization to perform the inversion of the OH profile. By taking $\lambda = 1 \times 10^{-4}$ as the optimal regularization parameter, the retrieved OH profile along with the relative difference is plotted in Fig. 5.5a. The results show that the relative difference is up to 12 % (~ 15 km) over the altitude range. The quality of the retrieval is also assessed by the retrieval error encapsulating the combined effect of the noise and smoothing errors (Fig. 5.5b). The smoothing error dominates the retrieval error budget from 15 to 27.5 km where the noise error is fairly small. This result implies that the retrieval error in this altitude range relies on the a priori information, and that, the relevant vertical resolution is rather poor. The noise error, as the major error, stretches from 27.5 km upwards where the smoothing error appears to take less effect.

Two-profile retrieval

For the two-profile retrieval we analyze two separate combinations:

1. OH and HOCl;

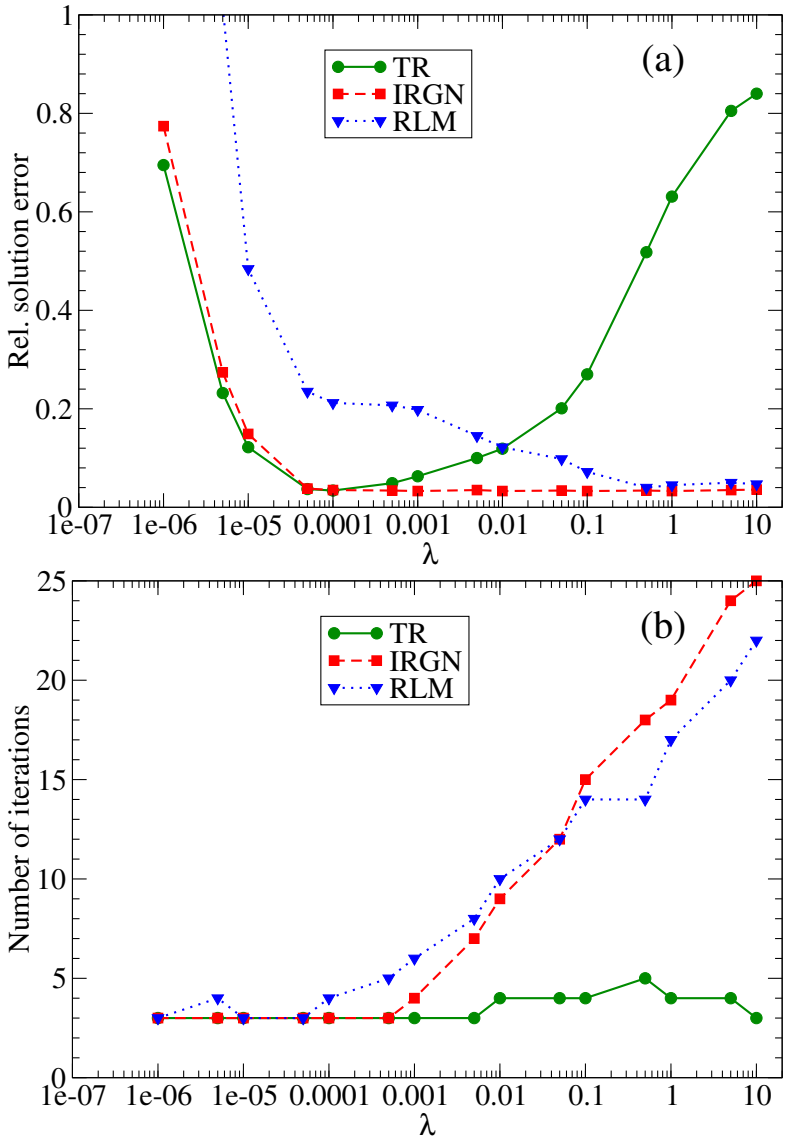

Figure 5.4: **(a)** Relative solution errors and **(b)** the number of iteration steps for different values of the regularization parameter. The results for the one-profile retrieval of OH correspond to Tikhonov regularization (TR), the iteratively regularized Gauss–Newton (IRGN) method, and the regularizing Levenberg–Marquardt (RLM) method.

2. OH and O_3.

As can be seen in Figs. 5.1 and 5.2, the spectra remain sensitive to HOCl around the intermediate frequencies of 4.2 and 4.6 GHz. The purpose of this joint retrieval is to account for HOCl such that its influence on the OH is minimized, and to perform the OH retrieval without sacrificing the quality of the HOCl fit. The joint retrieval of OH

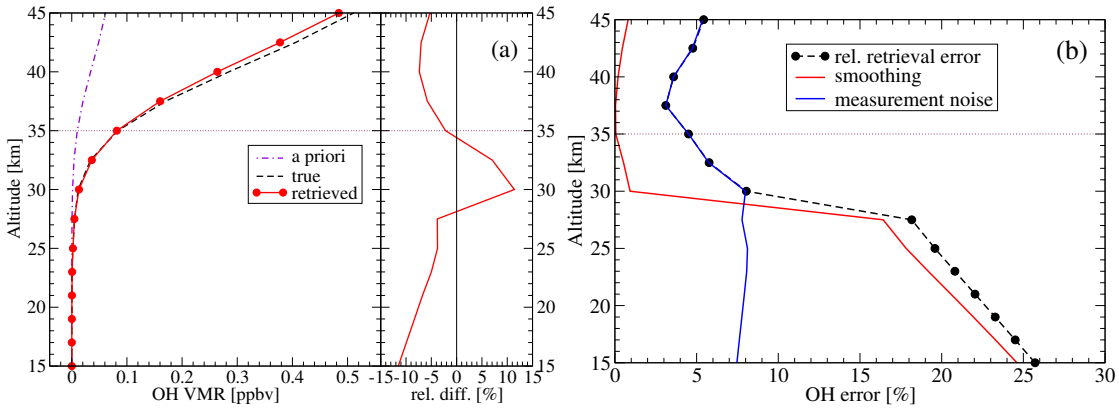

Figure 5.5: Panel **(a)**: retrieved OH profile and the relative difference with respect to the true profile. The dashed black line refers to the true profile. Panel **(b)**: relative retrieval error, smoothing and noise errors.

and HOCl relies on the combined intermediate frequency segments of 4–5 GHz.

A pair of strong O_3 lines are found in the wings of the OH triplet (see Fig. 5.3), which in turn, implies that an uncertainty in the concentration profile of O_3 may have a distinct influence on the retrieval quality of OH. To analyze how well OH can be retrieved without an accurate a priori information of ozone, O_3 is retrieved concurrently with OH. For this retrieval, a smaller spectral window of 500 MHz, corresponding to the second segment of 4.5–5 GHz, is used.

Since we are interested in computing the regularized solution for the entire state vector, the parameter choice method looks for the parameters for complete multi-parameter regularization. For the joint retrieval of OH and O_3, we minimize (4.10) in conjunction with Eq. (4.32) for a pair of regularization parameters $\boldsymbol{\lambda} = (\lambda_{\mathrm{OH}}, \lambda_{\mathrm{O_3}})$, and then compute the solution errors in each component by Eq. (4.24), that is, ϵ_{OH} and $\epsilon_{\mathrm{O_3}}$, as well as the total solution error $\epsilon(\boldsymbol{\lambda}) = \sqrt{\epsilon_{\mathrm{OH}}(\boldsymbol{\lambda})^2 + \epsilon_{\mathrm{O_3}}(\boldsymbol{\lambda})^2}$. The results in Fig. 5.6 show that for $\lambda_{\mathrm{OH}} = 1 \times 10^{-4}$ and $\lambda_{\mathrm{O_3}}$ ranging between 1×10^{-6} and 1, the total solution error is small and almost constant. However, in order to pursue smaller residuals after convergence, the regularization parameters of OH and O_3 are set to $\lambda_{\mathrm{OH}} = 1 \times 10^{-4}$ and $\lambda_{\mathrm{O_3}} = 1 \times 10^{-6}$, respectively. By employing the same approach, the regularization parameters $\lambda_{\mathrm{OH}} = 1 \times 10^{-4}$ and $\lambda_{\mathrm{HOCl}} = 5 \times 10^{-5}$ are selected for the joint retrieval of OH and HOCl.

When dealing with a practical application, we need to choose an appropriate regularization matrix $\mathbf{L}$. To compute the regularized iterate, the inversion relies on the iteratively regularized Gauss–Newton method so that the estimation of the regularization parameter is not necessary. Table 5.2 lists the relative solution errors (given by Eq. 4.24) and the residuals for different regularization matrices. $\mathbf{L}_0 = \mathbf{I}_n$, $\mathbf{L}_1$, and $\mathbf{L}_2$ are defined by Eqs. (4.18) and (4.20), respectively, while $\mathbf{L}_{\mathrm{C}}$ is the regularization matrix built by the Cholesky factorization of the a priori profile covariance matrix.

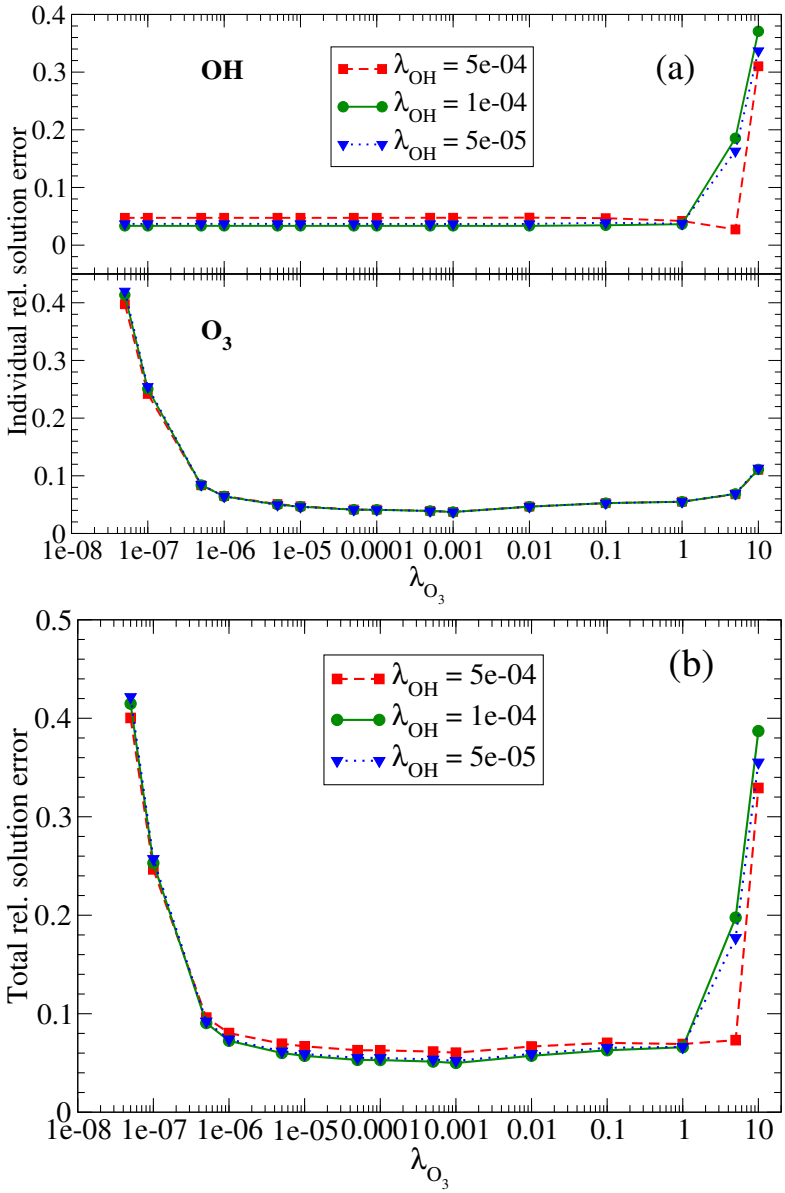

Figure 5.6: Determination of the regularization parameters for the two-profile retrieval of OH and O_3. Panel **(a)**: relative solution errors of OH and O_3 for different values of the regularization parameters for OH and O_3. Panel **(b)**: total solution errors for different values of the regularization parameters for OH and O_3.

The best solution error is obtained by $\mathbf{L}_C$ and the fit with the smallest residual corresponds to $\mathbf{L}_0$. Although the residuals for all four matrices are almost identical, the solution errors of the OH retrieval differ significantly and large solution errors are found if the contribution of the identity matrix ($\mathbf{L}_0 = \mathbf{I}_n$) to the regularization matrix

Table 5.2: Relative solution errors of OH and the corresponding residuals for different regularization matrices. $\mathbf{L}_\mathrm{C}$ denotes the regularization matrix built by the Cholesky factor of the a priori profile covariance matrix.

Regularization matrix	Relative solution error	Residual sum of squares
$\mathbf{L}_0$	0.173	22.59
$\mathbf{L}_1$	0.048	22.64
$\mathbf{L}_2$	0.078	22.62
$\mathbf{L}_\mathrm{C}$	0.033	22.64

Table 5.3: Relative solution errors and the corresponding residuals for the regularization matrix described by an exponential decay, cf. Eqs. (4.21) and (4.22) of Sect. 4.2.1.

Correlation length	Relative solution error	Residual sum of squares
2 km	0.273	22.60
20 km	0.128	22.59
50 km	0.047	22.65
100 km	0.033	22.64

increases.

Table 5.3 lists the inversion performance of the regularization matrix described by an exponential decay for different values of the correlation length. As l increases, the regularization matrix is similar to the first-order difference regularization matrix $\mathbf{L}_1$ and consequently a smaller relative solution error is obtained. The best solution with respect to the true profile is gained by setting $l = 100$ km. The regularization matrix constructed by the Cholesky factorization accounts on both the magnitude and the smoothness of the solution and appears to be the best option.

The retrieved VMR profiles of OH and HOCl, OH and O_3 are displayed along with the true profiles in panels (a) and (b) of Fig. 5.7, respectively. The corresponding relative differences are displayed in the top two panels (a, b) of Fig. 5.8. In the case of HOCl, the retrieved profile differs by 2–13 % from the true profile over the altitude range. Although O_3 is weakly regularized during the retrieval, an error of less than 5 % is found below the observer altitude; however, an underestimate above 35 km can be observed. Concerning OH, errors of less than 15 % with respect to the true profile in both joint retrievals are observed over the whole altitude range. These results are similar to those corresponding to a one-profile fit. The right panel (b) of Fig. 5.8 illustrates the retrieval error, the smoothing and noise errors for the retrieved gases. The retrieval error is dominated by the smoothing error at lower altitudes and by the noise error above 25 km. It is apparent that the vertical resolution of the OH retrieval is poorer than that of the O_3 retrieval. The smoothing error of O_3 is very small, which reveals that the main information comes

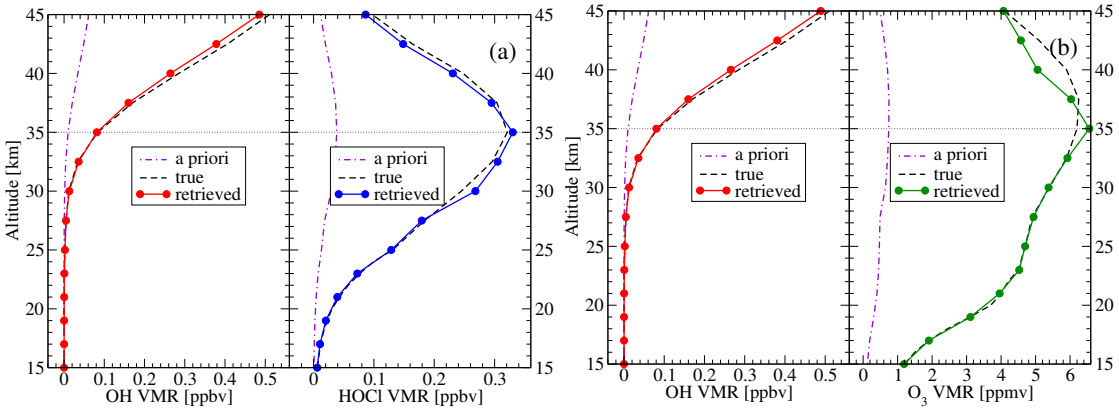

Figure 5.7: Panel **(a)**: Retrieved VMR profiles of OH and HOCl. Panel **(b)**: Retrieved VMR profiles of OH and O_3.

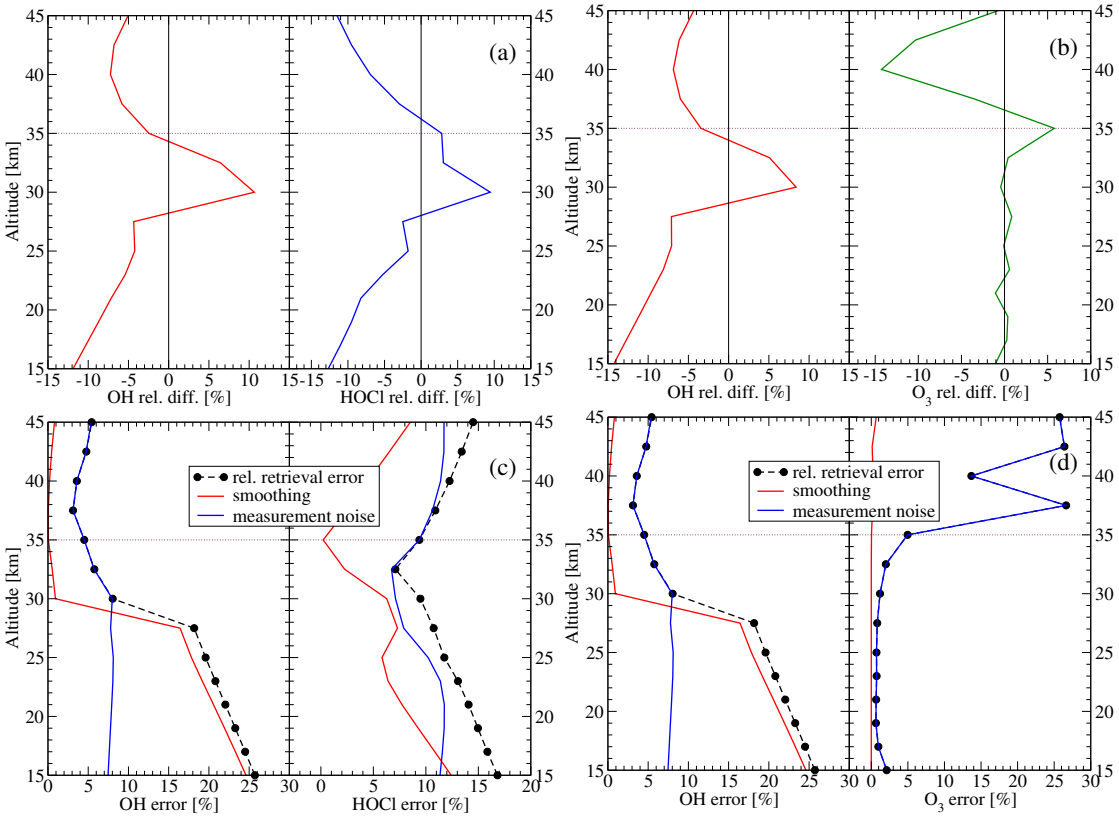

Figure 5.8: Relative differences of the retrieved profiles with respect to the true profiles for the joint retrievals of **(a)**: OH and HOCl, and **(b)**: OH and O_3. Relative retrieval error, smoothing and noise errors for **(c)**: OH and HOCl, and **(d)**: OH and O_3.

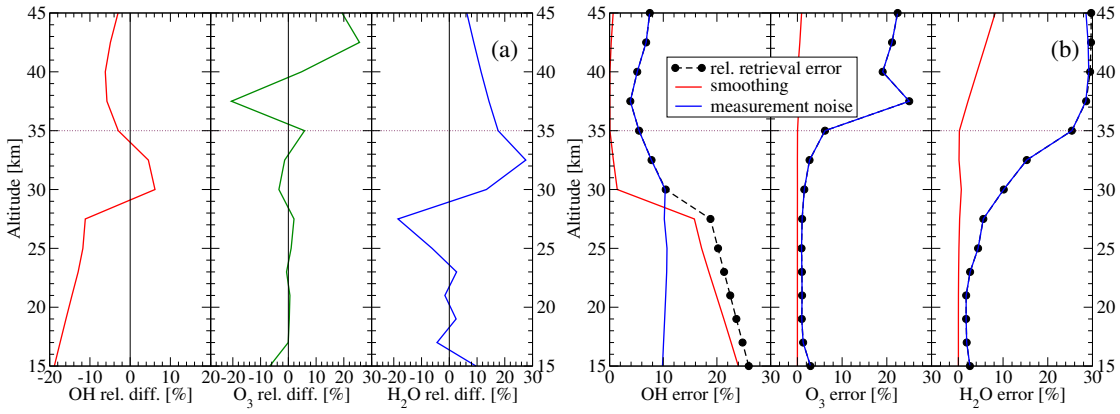

Figure 5.9: Panel **(a)**: relative differences of the retrieved profiles with respect to the true profiles for the joint retrieval of OH, O_3, and H_2O. Panel **(b)**: relative retrieval error, smoothing and noise errors for the joint retrieval of OH, O_3, and H_2O.

from the measurement itself and not from the a priori knowledge.

Three-profile retrieval

Another problem which has been considered is the three-profile retrieval. The state vector comprises three molecules, i.e. OH, O_3, and H_2O. The same spectral range as for the joint retrieval of OH and O_3 is used. The regularization parameters $\lambda_{OH} = 1 \times 10^{-4}$, $\lambda_{O_3} = 2 \times 10^{-6}$, and $\lambda_{H_2O} = 5 \times 10^{-6}$ are chosen by using the technique described in the two-profile retrieval.

The difference with respect to the true profile in Fig. 5.9a shows that the OH retrieval can be done over the whole altitude range, although the errors are slightly larger than for the one- and two-profile retrievals. This may suggest that inaccurate a priori knowledge of H_2O and O_3 could influence the OH retrieval. The retrieval error of OH in Fig. 5.9b is quite similar to the results above.

Final remarks

Using synthetic noisy measurements and assuming perfect instrument knowledge, the vertical concentration profile of OH has been retrieved in both single- and multi-profile retrieval frameworks with a decent quality. The smoothing error affects the retrieval error and yields a poor vertical resolution at lower altitudes, while the noise error dominates the retrieval error budget at higher altitudes. Although the spectral information above the observer altitude is limited, the profile of OH above 35 km can still be retrieved due to its high sensitivity in the middle stratosphere. Nevertheless, imperfect knowledge of forward and instrument model parameters can degrade the quality of the retrieved solution.

5.2 Sensitivity to Error Sources

In the retrieval results presented in the previous section, assumptions of perfect knowledge of the forward and instrument model parameters have been made. Still, it is of importance to see how imperfect model parameters influence the performance of the retrieval. A rigorous error analysis dealing with the most important error sources identified by the TELIS consortium [also known from previous studies, e.g. de Lange et al., 2009, 2012; Baron et al., 2011, 2001; Urban et al., 2005; Pumphrey and Bühler, 2000] has been carried out. As O_3 appears to be important in the OH microwindow, OH and O_3 are considered as the target molecules of a multi-profile fitting. The corresponding regularization parameters are chosen as $\lambda_{OH} = 1 \times 10^{-4}$ and $\lambda_{O_3} = 1 \times 10^{-6}$. We set the correlation length l to 100 km, yielding $\mathbf{L} \approx \mathbf{L}_1$ and a sufficiently smooth regularized solution. In contrast to Sect. 5.1.3, the initial and a priori profiles of the target molecules are scaled with a factor of 0.1. The other interfering species H_2O, HCl, HOCl, and HO_2 are assumed to be known. In this section, we concentrate on the performance of the OH retrieval affected by errors in the forward model parameters (spectroscopic parameters, atmospheric profiles, and continuum) and in the instrument model parameters (calibration, sideband ratio, pointing, and instrumental baseline). It should be mentioned that currently these parameters are not jointly retrieved and are assumed to be known.

5.2.1 Spectroscopic parameter errors

As already described in Sects. 3.1 and 3.2, a variety of spectroscopic parameters enter in the radiative transfer calculation and their accuracies are crucial for obtaining reliable retrievals. Table 5.4 gives a summary of the spectroscopic error sources and their perturbation amounts. The uncertainty in the spectroscopic parameters are analyzed, including those for the OH triplet at 1834.75 GHz ($\sim 61.20\,\mathrm{cm}^{-1}$), and the O_3 transition at 1834.15 GHz ($\sim 61.18\,\mathrm{cm}^{-1}$) that is dominant in this microwindow. Although an error in the O_3 spectroscopy is a bias in the fundamental contributor to the signal, it has an effect on the retrievals of species with weaker signal (OH in this case).

Figure 5.10 shows the absolute and the relative spectroscopic errors propagated into the OH retrieval, or according to the terminology used in Sect. 4.3.2, the absolute and the relative spectroscopic errors in the state space. An error of 0.001 ppbv is found below the instrument height and is introduced by the air broadening parameter of OH ($\gamma_{\mathrm{air,OH}}$). The line strength of OH (S_{OH}) leads to the second largest error and the temperature dependence coefficient ($n_{\mathrm{air,OH}}$) causes a slightly smaller error between 15–30 km. The relative retrieval error is not included in Fig. 5.10b because it is much larger than the relative spectroscopic errors propagated into the OH retrieval. From Fig. 5.10b it is apparent that the largest relative error corresponds to $\gamma_{\mathrm{air,OH}}$ and results in a maximum shift of $\sim 2.5\,\%$ over the plotted altitude region. Below the uppermost tangent height, the other four parameters introduce a systematic relative error of up to 1 % each. In addition, the impact of the air pressure broadening coefficients of O_3 is of minor importance.

Table 5.4: Uncertainties considered in the spectroscopic parameters of OH and O_3. These parameters are the line strength (S_{OH}), the air-broadened half width (γ_{air}, HWHM at 296 K), and the coefficient of temperature dependence (n_{air}, temperature-dependent exponent for γ_{air}). These values are perturbed for OH at 1834.75 GHz and O_3 at 1834.15 GHz.

Spectroscopic parameter	Perturbation
Target species OH at 1834.75 GHz (61.20 cm^{-1})	
Line strength (S_{OH})	1 %
Air broadening ($\gamma_{air,OH}$)	5 %
Temperature dependence ($n_{air,OH}$)	10 %
Interfering species O_3 at 1834.15 GHz (61.18 cm^{-1})	
Air broadening (γ_{air,O_3})	5 %
Temperature dependence (n_{air,O_3})	10 %

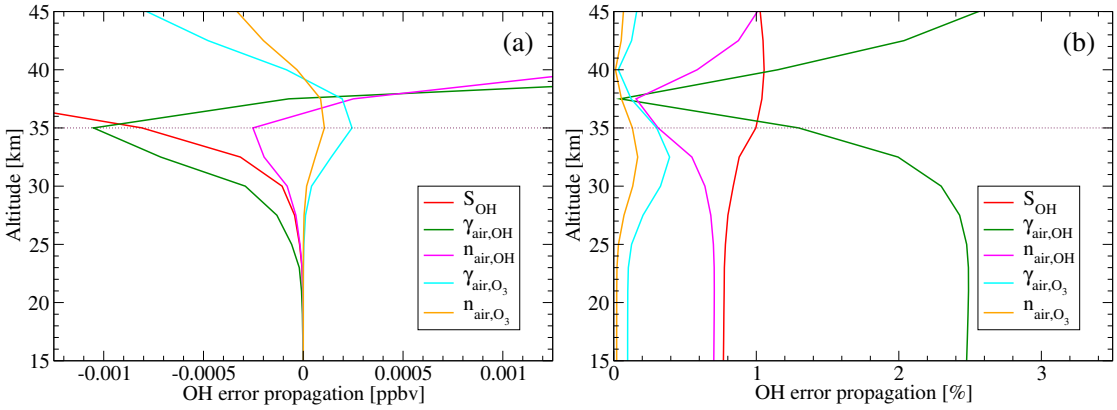

Figure 5.10: **(a)** Absolute and **(b)** relative spectroscopic errors propagated into the OH retrieval. Information on spectroscopic parameters is taken from the HITRAN 2008 spectroscopic database, while the added perturbations are summarized in Table 5.4.

5.2.2 Calibration error

Radiometric accuracy is crucial for a good quality of atmospheric profile retrieval, in particular systematic radiometric errors can lead to a shift in the retrieval. As previously mentioned in Sect. 2.3.2, a linear radiometric calibration approach has originally been foreseen for both the 1.8 THz and the 480–650 GHz channels. However, nonlinearities present in the TELIS IF-signal chain cannot be compensated by the linear calibration approach and further result in systematic errors in the radiometric calibrated spectra. To study the influence of the nonlinearity on the retrieval, the linear calibration procedure together with a nonlinear instrument response needs to be modelled.

Assuming a linear response system, the instrument output S^i for a given input signal

$I_{\mathrm{m}}^{\mathrm{i}}$ can be expressed as

$$S^i \;=\; G\,\left(I_{\mathrm{m}}^{\mathrm{i}} \;+\; I_{T_{\mathrm{sys}}}\right)\;, \qquad \text{with} \quad i = \mathrm{atm},\ \mathrm{H},\ \mathrm{C}\;, \tag{5.3}$$

where G denotes the radiometric gain, I_{m}^{i} represents a noise-free model spectrum, and the index i indicates an atmospheric (atm) spectrum, a hot load (H) spectrum or a cold load (C) spectrum. The offset $I_{T_{\mathrm{sys}}}$ is the modelled intensity of a blackbody at the system noise temperature of the heterodyne receiver. In the linear calibration scheme, the unknowns of the instrument's response, the gain, and the offset are then derived from calibration measurements of both known reference blackbodies with

$$G \;=\; \frac{S^{\mathrm{H}} - S^{\mathrm{C}}}{I_{\mathrm{m}}^{\mathrm{H}} - I_{\mathrm{m}}^{\mathrm{C}}} \tag{5.4}$$

and

$$I_{T_{\mathrm{sys}}} \;=\; \frac{I_{\mathrm{m}}^{\mathrm{H}}\,S^{\mathrm{C}} - I_{\mathrm{m}}^{\mathrm{C}}\,S^{\mathrm{H}}}{S^{\mathrm{H}} - S^{\mathrm{C}}}\;, \tag{5.5}$$

where $I_{\mathrm{m}}^{\mathrm{H}}$ and $I_{\mathrm{m}}^{\mathrm{C}}$ are computed via Planck's law from the given brightness temperatures of the hot and cold blackbodies. Consequently, the radiometric calibrated atmospheric spectrum $I_{\mathrm{cal}}^{\mathrm{atm}}$ is derived from the instrument output S^{atm} by using Eqs. (5.4) and (5.5):

$$I_{\mathrm{cal}}^{\mathrm{atm}} \;=\; \frac{S^{\mathrm{atm}}}{G} \;-\; I_{T_{\mathrm{sys}}}\;. \tag{5.6}$$

Unfortunately, the on-ground characterization measurements during the past campaigns have shown that the relation between the input and the output of the instrument is nonlinear, and thus, Eq. (5.3) does not hold true. A rather complex combination of nonlinear elements in the IF-signal chain has been found by laboratory experiments. Accordingly, we employed a more generic scheme in the forward model. The nonlinearities of the instrument can be approximated by an effective quadratic nonlinearity law, which is only sensitive to the integral power along the bandwidth W at the input, i.e.

$$S_{\mathrm{nl}}^{i} \;=\; G\left(I_{\mathrm{m}}^{i} + I_{T_{\mathrm{sys}}}\right)\left(1 + C_{\mathrm{nl}}\int_{W}\mathrm{d}\nu\;\left(I_{\mathrm{m}}^{i} + I_{T_{\mathrm{sys}}}\right)\right) \tag{5.7}$$

with C_{nl} being the coefficient which defines the quadratic nonlinearity. For the sake of simplicity, the linear coefficient is set to one in the model.

By virtue of Eqs. (5.3) and (5.7), the relationship between the outputs in the linear and the nonlinear cases can be expressed as

$$\frac{S_{\mathrm{nl}}^{i}}{S^{i}} \;=\; 1 + C_{\mathrm{nl}}\int_{W}\mathrm{d}\nu\;\left(I_{\mathrm{m}}^{i} + I_{T_{\mathrm{sys}}}\right)\;. \tag{5.8}$$

When $C_{\mathrm{nl}} < 0$ applies, we obtain a compression ζ of the output with respect to the linear case with $\zeta = 1 - S_{\mathrm{nl}}^{i}/S^{i} < 1$. This is a consequence of the fact that the nonlinearity is caused by saturation effects in the amplifier chain. To calculate the nonlinear outputs S_{nl}^{i}, the quadratic coefficient C_{nl} is chosen such that the compression of the modelled hot load

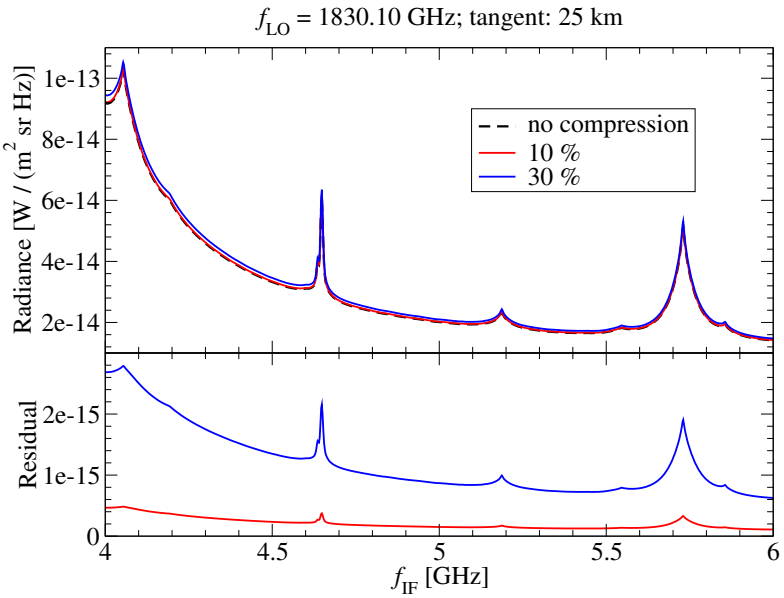

Figure 5.11: Modelled calibrated spectra measured at the tangent height of 25 km and the corresponding residuals with respect to the pure model spectrum. The assumed compressions of 10 % and 30 % in the hot load measurement are taken into account.

measurement $S_{\mathrm{nl}}^{\mathrm{H}}$ is comparable to the values obtained from laboratory measurements. The nonlinearity is then propagated into the calibration procedure by replacing S^i with S_{nl}^i in Eqs. (5.4)–(5.6).

The obtained calibrated spectra $I_{\mathrm{cal}}^{\mathrm{atm}}$, which are distorted by the nonlinearity, are compared with the pure atmospheric model spectra $I_{\mathrm{m}}^{\mathrm{atm}}$ (calibrated output in the ideal case). In the case of the OH microwindow, the blackbodies having the temperature of 278.0 and 2.725 K are used as the hot and cold load, respectively. The compression in the hot load is estimated with $\zeta = 20 \pm 10\,\%$. The modelled calibrated spectra at one tangent altitude are shown in Fig. 5.11 and compressions of 10 % and 30 % are assumed for the nonlinearity. As can be seen from the plotted residuals, the nonlinearity effect results in a line scaling effect in the calibrated spectra (in contrast to the ideal case).

Furthermore, as a worst-case scenario, the calibrated spectra with a compression of 30 % are read as input, and white noise is added, i.e. the retrieval is performed with the noisy synthetic measurements distorted by the nonlinearity. For this reason, a pseudo-correction scheme for simulating the linear calibration procedure is implemented in the forward model. This scheme according to Eq. (5.6) superimposes the nonlinearity onto the model spectrum at every iteration step with the given compression quantities ζ. The nonlinear instrument outputs S_{nl}^i are evaluated by using Eq. (5.7). The radiometric gain G and the offset $I_{T_{\mathrm{sys}}}$ in the nonlinear system are computed by using Eq. (5.4) and Eq. (5.5), respectively. To access the error propagation into the retrieval products, an additional 5 % uncertainty is assumed, i.e. the retrievals are repeated with the hot load compression ζ set to 25 % and 35 %, respectively. The retrieval results of OH and O_3 are

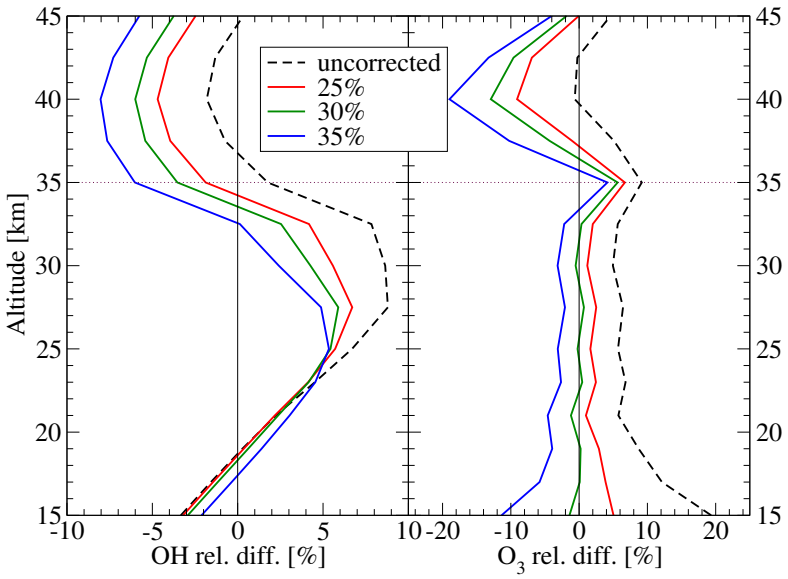

Figure 5.12: Relative differences of the retrieved OH and O_3 profiles with respect to the true profiles. The retrievals are done for noisy synthetic measurements that are generated by the calibrated spectra with a compression of 30 % in the hot load. 5 % uncertainty is taken into account in the pseudo-correction procedure, while the compression is set to 25 % and 35 % for two repeated retrievals.

then compared to the ones without the pseudo-correction process in Fig. 5.12. In this case, neither the noise errors nor the smoothing errors are increased in an evident way. Accordingly, the influence on the retrieval error is low (not shown). The errors in terms of relative difference show that the nonlinearity effect is more severe on O_3, in which case an error of 20 % at 15 km is attained. The retrieved OH profile is not affected by the nonlinearity below 21 km due to the fact that there is no strong OH signal below this altitude (see also Fig. 5.3). The results using the pseudo-correction with 25 % and 35 % compression are almost symmetric with respect to the case of 30 % (above 25 km for OH). As expected, the nonlinearity can affect the retrieval of OH at higher altitudes where the spectral feature is strong, while below the observer, this scaling effect on O_3 decreases with increasing altitude owing to the smaller contrast of the spectral lines between O_3 and OH.

In summary, the nonlinearity effect has been examined by using a modelled calibration procedure. The errors with respect to the true profile show that the nonlinearity can bring about an error in the OH retrieval in the middle stratosphere where the OH lines are easily identifiable. With the pseudo-correction scheme applied to the retrieval, the errors with respect to the true profile are reduced by up to 7 %, as can be inferred from Fig. 5.12.

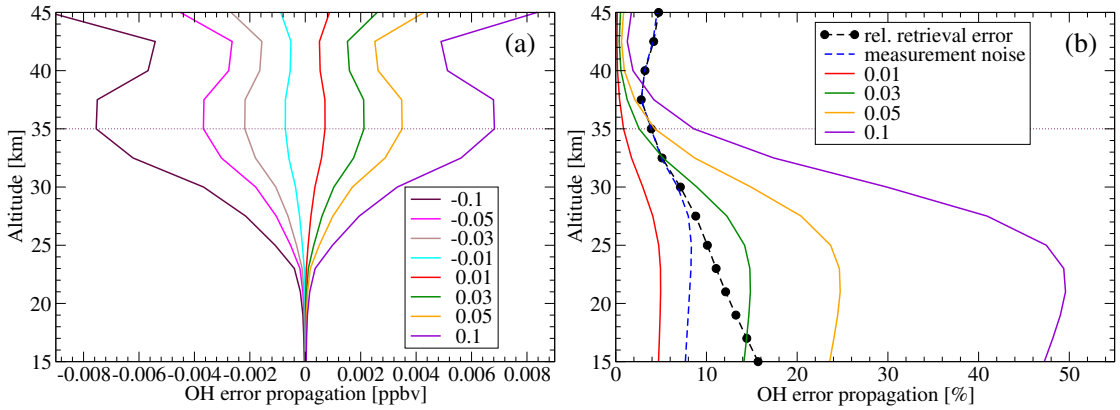

Figure 5.13: Sideband ratio error propagated into the OH retrieval for the sideband ratio bias η. Panel **(a)**: absolute errors for $\eta = \pm 0.01$, ± 0.03, ± 0.05, and ± 0.1. Panel **(b)**: relative errors for the positive values of η. For reference, the retrieval error and the noise error are included.

5.2.3 Instrument model parameter errors

Uncertainties in the instrument model parameters cause systematic biases in the retrieved vertical concentration profiles. In addition to the calibration error, the sideband ratio error and the pointing error are reviewed in this subsection. The instrumental baseline will be discussed in Sect. 5.2.5.

Sideband ratio error

For any heterodyne instrument using a double sideband mixer, the accurate information of the receiver sideband ratio is an essential prerequisite for the calculation of the spectrum I. An error in the sideband ratio r can result in a systematic change in the contributions to the spectra, and further, in an unexpected error in the retrieval. We define the distorted sideband ratio as $\tilde{r} = r(1+\eta)$ by introducing a relative bias η. Then, Eq. (3.37) is then rewritten as follows:

$$\begin{aligned} I &= \frac{r}{r+1} I_{\mathrm{USB}} + \frac{1}{r+1} I_{\mathrm{LSB}} \\ &= \frac{r}{r+1}\left(1 + \frac{\eta}{r(1+\eta)+1}\right) I_{\mathrm{USB}} + \frac{1}{r+1}\left(1 - \frac{r\eta}{r(1+\eta)+1}\right) I_{\mathrm{LSB}} \ . \end{aligned} \quad (5.9)$$

In our case the strong OH line lies in the upper sideband of the LO frequency. A positive η implies an overestimated contribution of the upper sideband in the spectrum, whereas a negative η results in an underestimated intensity. Recent laboratory measurements for characterizing the sideband ratio suggest that r lies in the range of 0.95 to 1.05 for the 1.8 THz channel, i.e. a maximal uncertainty of 5 % with respect to the ideal sideband ratio $r = 1.0$.

To study the impact of the error in the sideband ratio, the relative bias η with the values ± 0.01, ± 0.03, ± 0.05, and ± 0.1 are used in the following simulation. The

propagated error in the retrieval is evaluated by using the linear mapping approach (see Eqs. (4.40) and (4.44)) which relates the changes in the solution to the changes in the spectra via $\mathbf{K}_\lambda^\dagger$. For the atmosphere below the observer altitude 35 km, the bias η in the sideband ratio produces a propagated error of less than 3 % in the retrieved O_3 profile (not shown here). This is because the bias results in a smaller error as both sidebands contribute to the signal of O_3. The errors propagated into the OH retrieval are depicted in Fig. 5.13. For comparison, the relative retrieval error and the noise error are also included. The errors introduced by small biases (0.01 and 0.03) reach 5–15 % at 21 km and decrease with increasing altitude. The results are found to be severely affected by larger biases (0.05 and 0.1). Essentially, a larger sideband ratio biases result in significant errors in the OH retrieval.

In Fig. 5.14 the errors for the joint retrieval of OH and O_3 are illustrated for different values of η. The synthetic measurement is generated for the ideal sideband ratio $r = 1.0$. The errors of O_3 for all these biases are consistent with the estimated error propagation and are systematically distributed over the altitude range 15–35 km. In our case, the intensity contributed by OH is sensitive to the bias in the sideband ratio. As judged from Figs. 5.13 and 5.14, the retrieved OH profile is overestimated for positive biases in the sideband ratio, and underestimated for negative ones. For a double sideband heterodyne receiver, a deviation in the sideband ratio could lead to a larger error in the retrieval of the molecule whose contribution originates from only one sideband.

If more than one line of a single molecule occurs in both sidebands, the retrieval of the sideband ratio is feasible by assuming a constant value over the intermediate frequency range. For this OH microwindow, O_3 lines are found in both sidebands and the OH line only resides in the upper sideband. In the case of the OH retrieval and when the sideband ratio bias η is set to zero, the result is virtually unaffected, regardless of whether the sideband ratio is jointly retrieved or not. If a constant η in the range $[-0.1, 0.1]$ is assumed and a joint-fitting of the sideband ratio is performed, the retrieval results of OH are almost identical to that with perfect knowledge of the sideband ratio.

In practice, however, the retrieval of the sideband ratio still remains to be a difficult undertaking stemming from the fact that the laboratory measurements of the sideband ratio around 1.8 THz exhibit a curved variation in the sideband ratio range $[0.95, 1.05]$ over the intermediate frequency range. For the 480–650 GHz channel, the variation in the sideband ratio range $[0.6, 1.4]$ is much higher than that for the 1.8 THz channel [de Lange et al., 2012].

Pointing error

Retrieval of trace gases from limb sounding measurements requires accurate information of the instrument pointing. A pointing error can be characterized by a systematic pointing bias and a random pointing offset:

- the systematic pointing bias means that all tangent heights experience a positive or negative deviation;

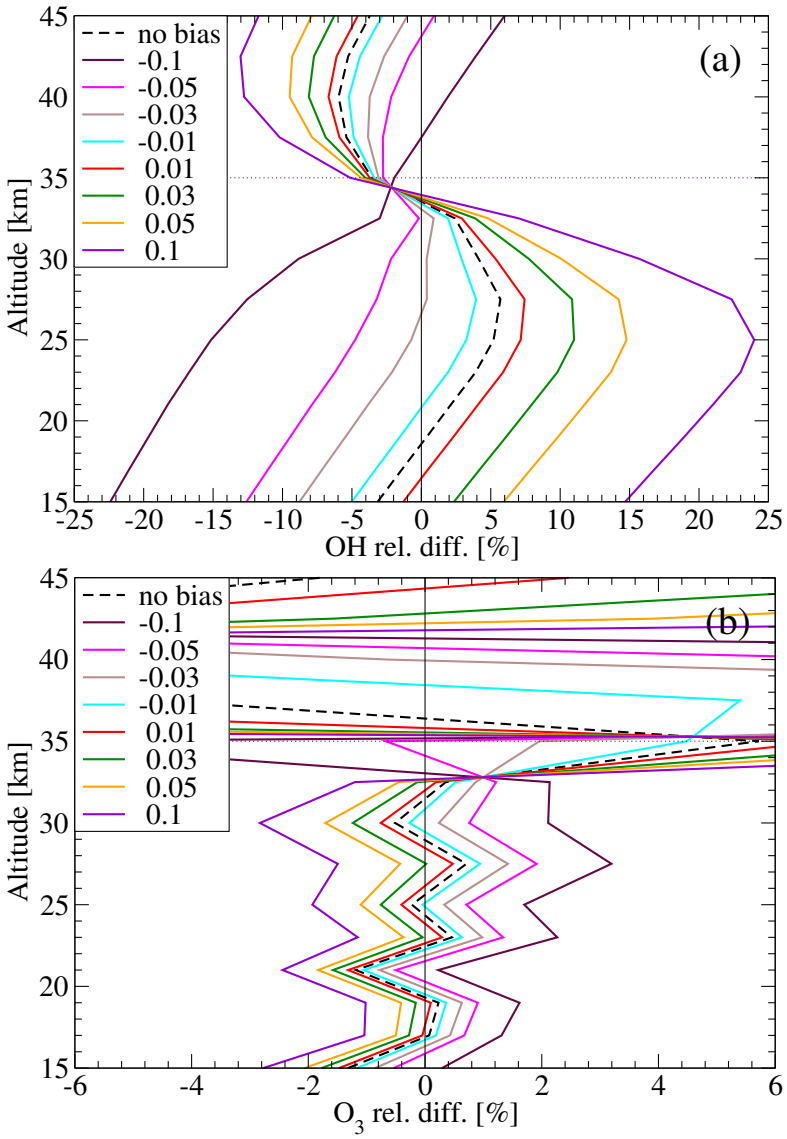

Figure 5.14: Relative differences of the retrieved **(a)** OH and **(b)** O_3 profiles with respect to the true profiles and for different values of the relative bias η. The retrievals are performed using a synthetic measurement for the ideal sideband ratio $r = 1.0$. For reference, the retrieval result for the assumed sideband ratio is shown in dashed black line.

- the random pointing offset is mainly determined by the behaviour of the scan mechanism and the tangent heights can be uncorrelated with each other.

The pointing error can be expressed by an altitude error at the tangent point, or by an error in the zenith angle of the line-of-sight. Although TELIS received the pointing information from the AHRS equipment aboard on MIPAS-B, the stability of the con-

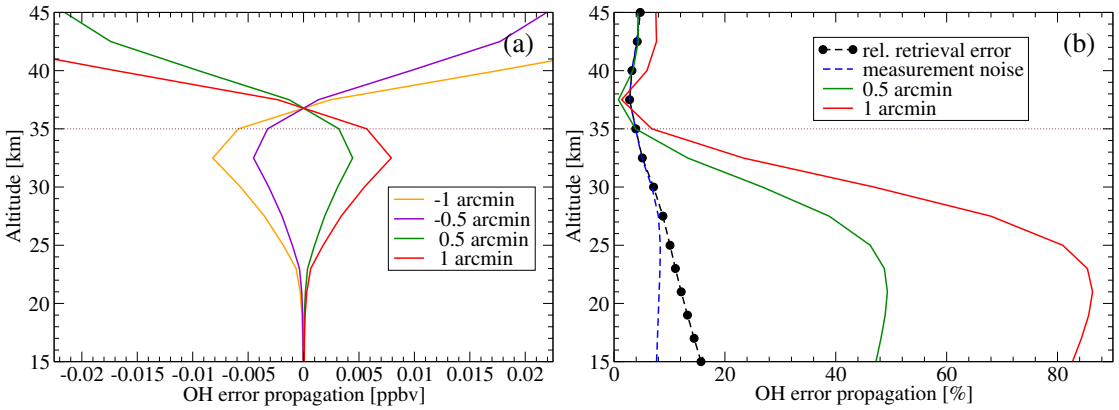

Figure 5.15: **(a)** Absolute and **(b)** relative pointing errors propagated into the OH retrieval for an uncertainty of ±0.5 and ±1 arcmin in the systematic pointing bias. For reference, the retrieval error and the noise error caused by the measurement noise are included.

nection between both instruments remains to be examined. It has been probed that the systematic pointing bias is 3.4 arcmin in the zenith angle in the 1.8 THz channel, corresponding to a 500 m upward deviation for the lowest tangent height (15 km in this case).

Assuming that the uncertainty in the systematic pointing bias is up to 1 arcmin, the pointing errors propagated into the OH retrieval are plotted in Fig. 5.15. As this bias is deterministic, the propagated error is estimated by using Eq. (4.44) in the framework of a linearized forward model about the true state. An absolute error of up to 0.01 ppbv for an uncertainty of 1 arcmin is found below the observer altitude. As a result of very low concentrations at lower altitude, the largest propagated error occurs between 15 and 25 km.

The relative differences of the retrieved OH profile with respect to the true profile for a single-target retrieval by assuming uncertainties of 0.5 and 1 arcmin in the systematic pointing bias (3.4 arcmin) are shown in Fig. 5.16a. These results are in agreement with the error propagation in Fig. 5.15b, leading to the conclusion that the forward model is not too nonlinear. The pointing error yields a shift of all gas profiles. As in our case, O_3 is the foremost contributor to the measurement signal, an unresolved shift of the O_3 profile is the reason for large relative differences in the OH profile. The relative differences in the OH profile become vastly smaller if a joint retrieval of OH and O_3 is performed, as it can be seen in Fig. 5.16b.

The instrument pointing information can be derived from small spectral windows containing species whose molecular abundances are well-known or alter only slightly. For instance, von Clarmann et al. [2003] proposed a strategy using CO_2 lines covered by MIPAS spectra in the mid infrared region. Concerning far infrared and microwave limb sounding, the common approach is to extract the pointing information (systematic pointing bias) from measurements of oxygen emission lines. The intensity of the line is essentially a function of atmospheric temperature and pressure. The pointing offset can

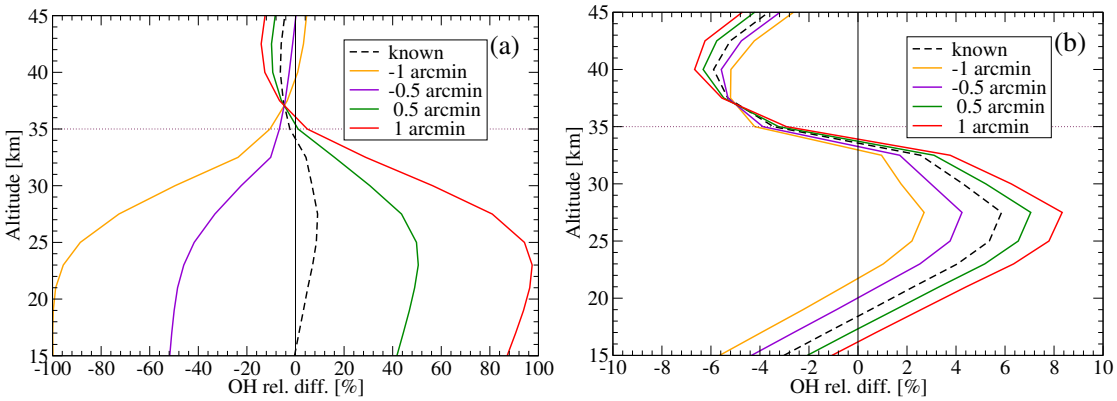

Figure 5.16: Relative differences of the retrieved OH profile with respect to the true profile for **(a)** a single-target retrieval and **(b)** a joint retrieval of OH and O_3. The retrievals are performed for uncertainties of 0.5 and 1 arcmin in the systematic pointing bias. For reference, the retrieval result corresponding to perfect knowledge of the pointing information is given in dashed black line.

be retrieved as an angular pointing bias, or as an altitude error at the tangent point. However, both on-ground and in-flight observations of the system noise temperature in the O_2 microwindow of the 1.8 THz channel during the three TELIS balloon flights were found to be extremely high, which makes the pointing retrieval nearly impossible. Verdes et al. [2002] derived the pointing offset from two nonoxygen bands (498.5–505.5 GHz and 296–306 GHz), which has been applied to the pointing retrieval from MLS observations. Baron et al. [2011] suggested the use of the strong ozone line at 625.371 GHz, measured by SMILES with high signal-to-noise ratio, for deriving the pointing information properly. Due to the reliability of the data received by the pointing system of MIPAS-B, the pointing information of TELIS is assumed to be well known, and hence, it is not necessarily to be retrieved. This fact was also mentioned by de Lange et al. [2012]. Nevertheless, measurements in future campaigns can still provide an opportunity of exploring the pointing acccuracy, only if the signal-to-noise ratio of the instrument is improved.

5.2.4 Atmospheric profile errors

Apart from the instrument model parameters, uncertainties in the atmospheric profiles used by the forward model have an effect on the retrieval accuracy. Errors related to the atmospheric temperature, pressure, and other interfering gases are discussed in the following.

Temperature and pressure errors

The accuracy of the temperature profile is vital to the reliability of target gas retrievals. For the retrieval of TELIS spectra, the MIPAS-B temperature retrieval may be a pleasant candidate. MIPAS-B and TELIS were both carried on the same gondola frame during

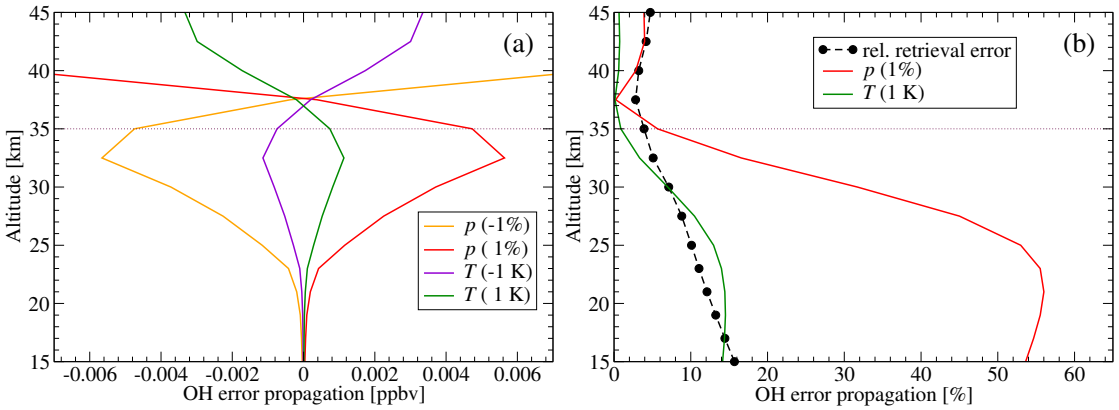

Figure 5.17: **(a)** Absolute and **(b)** relative temperature and pressure errors propagated into the OH retrieval by assuming errors of ±1 K in the temperature profile and errors of ±1 % in the pressure profile, respectively. The dashed black line refers to the retrieval error with respect to the reference case.

the previous campaigns and have almost identical viewing geometries.

We assume an uncertainty of 1 K in the temperature profile for altitudes up to 45 km to investigate the corresponding effect on the retrieval. In Fig. 5.17, the temperature error propagated into the OH retrieval via Eq. (4.44) is depicted. Below 27.5 km, the error lies in the range 10–14 %. The retrieved profile is saturated and depleted by up to 0.0006 ppbv for absolute errors of 1 and −1 K in the temperature profile, respectively. Between 27.5 and 35 km, a relative error of up to 7 % is found despite an increased absolute error because of a higher concentration in the stratosphere by two orders of magnitude. This fact implies that a slight deviation in the temperature profile may cause appreciable errors especially at lower altitudes (upper troposphere and lower stratosphere) where the concentration of OH is relatively low.

The temperature profile can be estimated from microwave oxygen emission lines in limb sounding geometry [Verdes et al., 2002; von Engeln and Bühler, 2002]. As already mentioned in Sect. 5.2.3, the temperature information turns out to be very difficult to extract resulting from the large noise error in the dedicated O_2 microwindow.

To assess the pressure error propagated into the OH retrieval, errors of ±1 % in the pressure profile over the whole altitude grid are introduced. Compared to the error propagation of the temperature profile, the errors of the pressure profile lead to considerable effects between 15 and 30 km (Fig. 5.17). An absolute error of up to 0.006 ppbv is found over the altitude range below the observer, and the largest value is located at the altitude of 21 km (56 %). Below the observer, the retrieved profile is saturated with a positive error, while depleted with a negative error. O_3 is not affected by the errors of the pressure profile; the accuracy of the pressure profile is therefore important for the retrieval of OH and other weak molecules.

For the analysis of real measurements, the pressure profile can be generated from sufficiently accurate meteorological data (e.g. ECMWF). Alternatively, atmospheric pressure

Table 5.5: Relative solution errors of OH and O_3 and the residual sum of squares without and with baseline offset fitting. The result corresponding to perfect instrumental baseline knowledge is taken as a reference.

Retrieval scenario	ϵ_{OH}	ϵ_{O_3}	Residual sum of squares
reference	0.034	0.059	22.22
without baseline offset fitting	0.334	2.615	49.88
with baseline offset fitting	0.033	0.085	25.02

can be calculated from the temperature profile via the hydrostatic equation. However, a disadvantage of this method is the propagation of the temperature error into the pressure profile.

Interfering gas errors

Ozone has a dominant spectral feature in the OH microwindow, and the error in its concentration profile may degrade the retrieval quality of OH. In addition to O_3, the impact of the a priori errors of HOCl and H_2O have been discussed in Sect. 5.1.3. Inaccurate a priori knowledge of HCl and HO_2 appears to have no profound impact on the modelled spectrum, as can be inferred from the sensitivity analysis in Sect. 5.1.2. Since the water continuum is another important source which may affect the OH retrieval, this topic will be discussed in the next subsection.

5.2.5 Baseline offset: instrumental and physical effects

For the measured spectrum, the baseline is usually distorted owing to several factors related to instrument characteristics and physical interactions. This baseline error is expected to result in a large discrepancy between the retrieved and true profiles. We discuss this baseline distortion accounting on instrumental and physical effects.

Imperfect radiometric calibration process, self-emission of the instrument, and other unknown instrumental effects usually cause remaining structures in the spectral baseline. In general, the instrumental baseline offset is not perfectly known and has to be taken into account in the retrieval. For limb-viewing measurements, it is a common practice to simulate this quantity by a polynomial baseline function of wavenumber/frequency for each tangent height.

By considering an instrumental baseline offset of 2 K, the retrievals are performed with and without baseline-fitting. Given the retrieval result with perfect baseline knowledge as a reference profile, Table 5.5 shows a significant improvement of the relative solution errors of OH and O_3 as well as the corresponding residual for a joint-fitting of a constant baseline (zero-order polynomial) at each tangent height. The relative differences in the retrievals in Fig. 5.18 illustrate the performances of this approach: the retrieved profile is comparable to the reference profile, whereas the retrieval without baseline-fitting deteriorates and the errors are beyond the plotted range (not shown

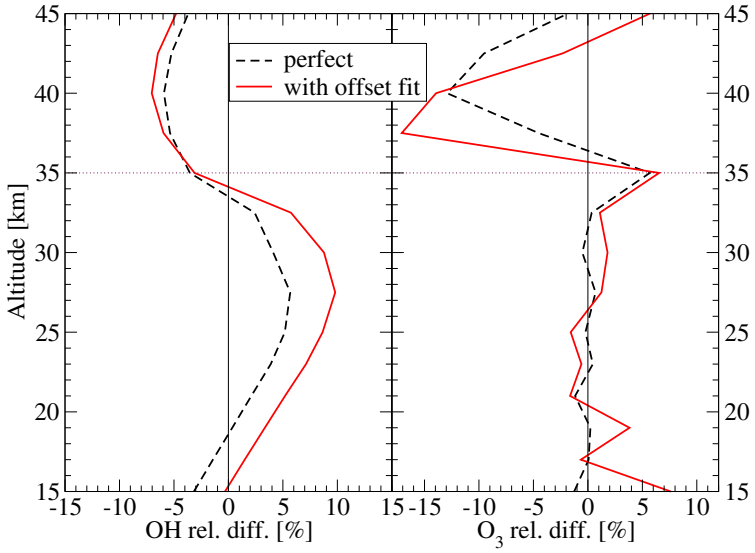

Figure 5.18: Relative differences of the retrieved OH and O_3 profiles with respect to the true profiles for a joint retrieval of molecular concentrations and instrumental baseline offset. The black dashed line refers to the result from the spectra without baseline distortion.

here).

In addition to the instrumental effect on the spectral baseline, the distortion caused by an inaccurate physical knowledge of the continuum shall not be ruled out. In practice, reliable continuum knowledge turns out to be vital to the retrieval of vertical profiles of chemical species and physical parameters. In particular, the spectral baseline is firmly influenced by continuum-behaved contributions from the far-wings in the upper troposphere and lower stratosphere (UTLS) region ($\sim$5–22 km). Consequently, it is inevitable to correct the physical distortion that could further propagate into the retrieval result. Because the present continuum models are not able to perfectly describe these continuum-like contributions, we consider an artificial and retrievable "greybody" profile which can, albeit not in a physical meaning, help to reach a better agreement between the measured and modelled spectra and to achieve smaller residuals. An extensive discussion of the "greybody" approach for real submillimeter data will be presented in Sect. 6.1.1.

It should be pointed out that the retrieval of the instrumental baseline and "greybody" profile is correlated to the pointing information and compensates in some sense the errors stemming from the pointing uncertainty.

5.3 Capability of Multi-channel Simultaneous Fitting

As TELIS can measure two of three channels concurrently during the flight, it is tempting to consider improving the retrieval accuracy by simultaneous processing of several different spectral windows. Multi-window retrieval is commonly used for instruments

Table 5.6: Main instrument and geometry parameters for multi-channel simultaneous retrieval simulation of HCl. The notation GHz stands for the 480–650 GHz channel.

Parameter	Description	
Channel	THz	GHz
LO frequency	1877.63 GHz	619.10 GHz
Intermediate frequency	4–6 GHz	5–7 GHz
ILS function	Hamming apodization	Lorentzian
Field-of-view (FWHM)	Gaussian (6.3 arcmin)	Gaussian (10.8 arcmin)
Signal-to-noise ratio	30	110
Systematic pointing bias	3.4 arcmin	-5.4 arcmin
Sideband ratio	0.95–1.05	0.6–1.4
Top-of-atmosphere	85 km	
Observer altitude	34 km	
Tangent heights	10–32.5 km	
Vertical sampling	1.5 km	

covering broad spectral bands, notably Fourier transform spectrometers, e.g. MIPAS [Fischer et al., 2008], whereas the synergistic analysis of spectra measured by different instruments is discussed in a few papers only, e.g. IASI and GOME-2 [Landgraf and Hasekamp, 2007], IASI and MIPAS [Ceccherini et al., 2010], etc. Here, a retrieval of common molecule(s) from both far infrared and submillimeter observations offers a novel aspect (to the best of our knowledge, Aura/MLS does not exploit the combination of both GHz and THz measurements simultaneously).

In this section, we investigate the retrieval quality of HCl by multi-channel simultaneous fitting. Note that these two channels are characterized by different spectral response functions, and a Lorentzian function is used for the 480–650 GHz channel as a simplified version of the actual one. The corresponding systematic pointing bias and sideband ratios for both microwindows based on actual observations are taken into account. Consistent spectroscopic input data are well known to be a serious problem for synergistic retrievals exploiting infrared and ultraviolet observations, see also, e.g. Flaud et al. [2006]. But regarding our synthetic measurements, the consistency of spectroscopic information over the 1.8 THz and 619 GHz ranges is not an issue, as the line parameters are taken from the HITRAN database only and have been examined to be consistent.

Table 5.6 summarizes the main instrument and geometry parameters used for generating the synthetic observations. TELIS can measure signals at different observing and tangent altitudes during the flight, and a corresponding change of geometry with respect to Table 5.1 is done. In this test, the synthetic measurements are simulated for two HCl microwindows observed with the LO frequencies of 1877.63 and 619.10 GHz, as utilized during the previous flights. Random noise is superimposed onto the simulated measurement for each microwindow with the estimated signal-to-noise ratio. In addition

to the target molecule HCl, H_2O, O_3, O_2, NO_2, ClO, and HOCl are taken as interfering molecules in this simulation.

The state vector $\boldsymbol{x}$ is constructed from the VMR profiles of the main target molecule HCl and the auxiliary molecule O_3, assuming an a priori error of 90 %. The retrieval grid is discretized in 1.5 km between 10 and 32.5 km, which is equivalent to the vertical tangent sampling. Above 32.5 km, the same grid spacing as in Sect. 5.1 is used. The regularization parameters are estimated by minimizing an objective function corresponding to the main component of the state vector, i.e. the reconstruction of HCl. All three retrievals are performed with $\lambda_{\mathrm{HCl}} = 1 \times 10^{-4}$ and $\lambda_{\mathrm{O_3}} = 0$. The selected regularization strength implies that the goal of the O_3 retrieval is not to deliver a data product, but are merely included to improve the HCl fit and so to find a small residual.

In the upper panel (a) of Fig. 5.19, the averaging kernels for the HCl retrieval using the multi-channel measurement are compared against those using only the single-channel measurement. The averaging kernels for the multi-channel case indicate an improved vertical resolution below 20.5 km where the averaging kernels obtained from the measurement in the THz-channel are rather wide. On the other hand, the averaging kernels for the multi-channel case below 20.5 km imply that the GHz-channel data provides a better resolution of the retrieval product over the same altitude range. Above 20.5 km, the averaging kernels for the profile obtained from the multi-channel data are quite similar to those evaluated from the far infrared measurement alone. A noticeable quality improvement in terms of the degree of freedom for the signal is also gained.

By using both channels concurrently, the corresponding smoothing error (Fig. 5.19b) indicates that the regularization results in a less loss of information below 22 km. Meanwhile, the noise error below 19 km is decreased by about a factor of 5, as compared to the results using only the THz-channel data. Therefore, the relative retrieval error is 5–10 % better over the altitude range of 10–20.5 km. For the retrieval using only the THz-channel, the noise error dominates the retrieval error over the whole altitude range due to the worse signal-noise-ratio, whereas the noise error is very close to zero for the retrieval with the submillimeter data. The smoothing error for all retrievals is large below 20.5 km, and the regularization can have an effect on the retrieval quality of HCl. By comparison with the results using the GHz-channel alone, a smaller smoothing error given by the multi-channel measurement is achieved, although a slightly worse retrieval error is found above 20.5 km due to much larger noise in the far infrared measurement. According to these results, at higher altitudes, the sensitivity of HCl in the THz microwindow is superior to that in the GHz microwindow, while at lower altitudes, the GHz-channel data delivers a stronger HCl signal.

In Fig. 5.20, the relative differences of the retrieved HCl profile with respect to the true profile for the three cases are depicted. The error for the multi-channel measurement is overall better than that for the THz-channel measurement. A slight improvement can be found below 17.5 km, as compared to that only using the GHz-channel measurement. The large noise of the THz-channel spectra substantially biases the multi-channel retrieval, and therefore the relative difference for the multi-channel case becomes larger at higher altitudes. The largest difference appears around 20.5 km where the noise error

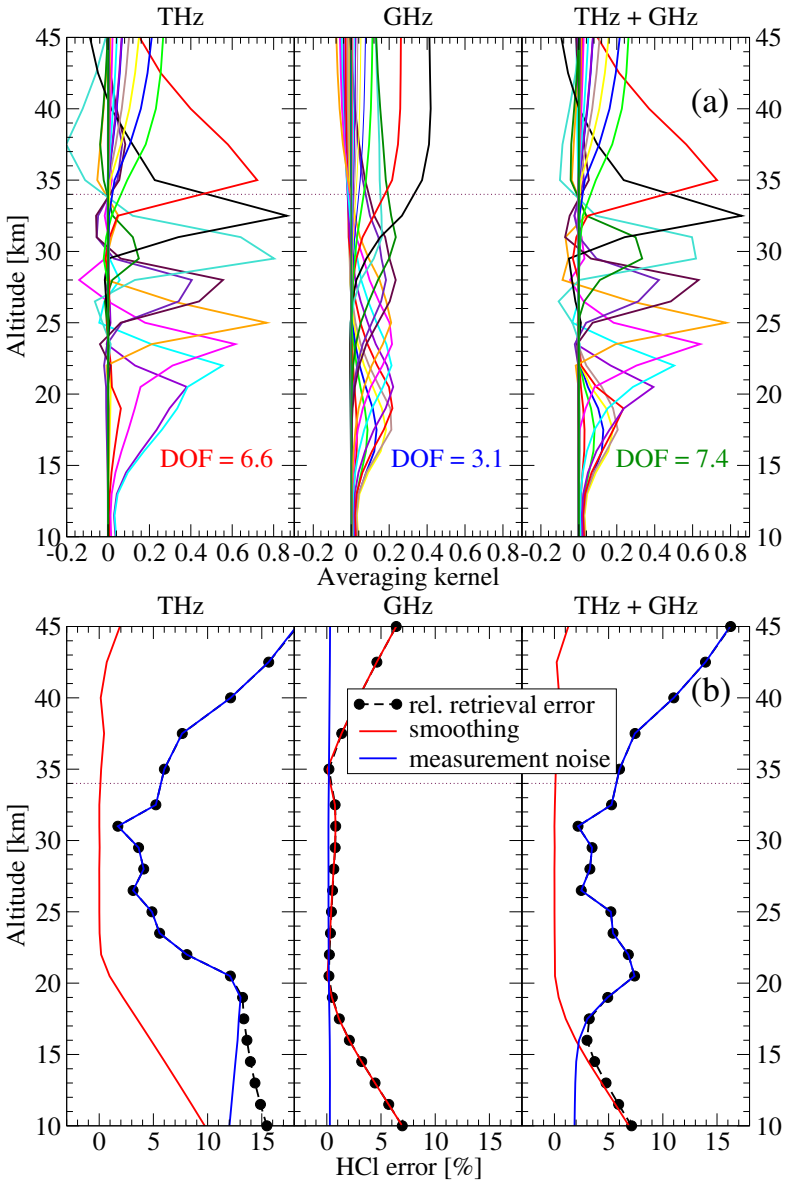

Figure 5.19: Panel **(a)**: averaging kernels for HCl retrieval corresponding to the single-channel measurements in the 1.8 THz and 480–650 GHz channels, and to the multi-channel measurement in both channels. The notation DOF stands for the degree of freedom for the signal. Panel **(b)**: relative retrieval error, smoothing and noise errors of HCl for the single- and multi-channel fitting.

(see Fig. 5.19b) in the THz-channel measurement is significant. The noise error for the multi-channel retrieval remains rather severe above 20 km because of the large noise error in the THz-channel spectra. This is also why the relative difference for the multi-channel retrieval is not superior to that for the GHz-channel case at higher altitudes.

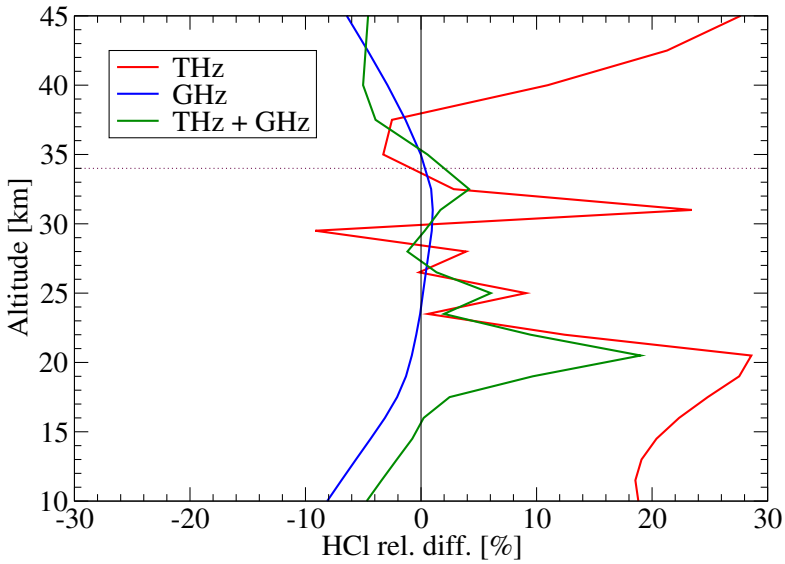

Figure 5.20: Relative differences of the retrieved HCl profile with respect to the true profile for the single- and multi-channel retrievals. The retrievals are done in the 1.8 THz channel, the 480–650 GHz channel, and the combination of both channels, respectively.

Nevertheless, the averaging kernels and the degree of freedom for the signal indicate that the multi-channel simultaneous retrieval improves the quality of the retrieval by a better exploitation of information from the observations. Furthermore, the multi-channel fitting requires less iteration steps than both single-channel fittings.

5.4 Summary

The measurement capabilities of the TELIS instrument with respect to the stratospheric target species OH and HCl have been theoretically investigated by means of nonlinear inversion simulations with synthetic data. In a first step, we have examined the performance of single- and multi-target retrievals for the OH retrieval observed by TELIS's 1.8 THz channel. In contrast to most stochastic data models used in atmospheric remote sensing, the presented data analysis operates in a semi-stochastic setting.

Various numerical regularization methods have been tested for the one-profile retrieval, proving that both the direct (Tikhonov regularization) and the iterative regularization methods yield satisfactory results. Although the inversion process utilizing Tikhonov regularization converges faster, the iterative regularization methods are unaffected by overestimations of the initial value of regularization parameter.

The retrieval error comprises the smoothing error due to regularization, the noise error due to the radiometric noise, and the model parameter error. The latter including the forward and instrument model errors have been individually and quantitatively analyzed.

A concise discussion on how various spectroscopic parameters of OH and O_3 affect the OH retrieval has been provided. The air-broadened half width of OH plays an important role in the retrieval accuracy, while the air broadening parameters of O_3 (half width and temperature dependence) do not exert a strong influence on the OH retrieval.

The calibration error (primarily nonlinearities in the IF-signal chain) does not have an adverse effect on the OH retrieval at lower altitudes, but induces an error in the middle stratosphere where the OH feature becomes stronger. The O_3 retrieval cannot be ignored especially in the lower stratosphere as O_3 is the major contributor to the signal in the selected microwindow, which is not true with increasing altitude due to the smaller intensity contrast between O_3 and OH. However, it can be expected that the retrieval of the target molecule is strongly affected by the nonlinearity effect, in case that the spectral features of interfering molecules are relatively weak.

The inaccurate knowledge of the receiver sideband ratio introduces an error in the retrieval, because the strong OH triplet only lies in the upper sideband of the selected microwindow. Likewise, the pointing accuracy can be another major error source for the OH retrieval. When dealing with a multi-species retrieval, the pointing error yields a shift of all profiles.

Besides, the baseline distortions due to the instrumental and physical effects have been discussed. By implementing the joint-retrieval of a tangent-dependent constant baseline, the retrieval errors due to an instrumental baseline bias can largely be eliminated. The physical effect on the baseline, reflected by broad continuum-like contributions, can be compensated by fitting an additional "greybody" profile.

Finally, due to the fact that TELIS enables a simultaneous analysis of common molecules from both far infrared and submillimeter limb spectra, the capability of multi-channel fitting has been studied for HCl. The retrieval quality has been characterized by means of averaging kernels, number of degrees of freedom for the signal, and retrieval errors. All these quantifiers demonstrate that an improved quality of the HCl retrieval can be achieved by the adopted multi-window approach to gain the complementary information provided by the two channels.

The retrievals of trace gas species using synthetic spectra of TELIS have been carried out with PILS, thereby establishing the inversion program's capabilities to analyze real measurement data.

Chapter 6

TELIS Retrievals

The retrieval program PILS has been successfully tested for synthetic measurements generated in accordance with the instrument characteristics of TELIS and the in-flight configurations during the previous scientific campaigns. The use of synthetic data is important for an initial assessment of PILS's accuracy and serves as a rough estimate of the measurement capabilities of the TELIS instrument. The calibrated spectra of the past three polar winter flights in the Northern Hemisphere (11 March 2009, 24 January 2010, and 31 March 2011) offer the possibility to analyze the proposed inversion algorithm and to study the chemical interactions associated with ozone depletion in the middle atmosphere over the north polar region. The TELIS Level-2 data products have been processed from the latest version (3v02) of the Level-1b data product, in which the nonlinearity effect and the bias in the sideband ratio have been largely corrected. This chapter presents recent retrieval results of O_3, HCl, CO, and OH from these far infrared limb spectra.

The obtained retrieval results are the subject of an evaluation process consisting of a theoretical error analysis and a comparison with retrieval results of satellite and balloon-borne measurements. The error analysis conducted here is based on the methodology described in Sect. 4.3.2 and the model parameter errors comprise uncertainties in the radiometric calibration process (mainly nonlinearity), sideband ratio, pointing information, spectroscopic parameters, and atmospheric profiles.

The concentration profiles retrieved from spectra in the TELIS's 1.8 THz channel, in other channel and by other instruments, are used for cross-comparison purposes. Internal comparisons between the data retrieved in the 1.8 THz and the 480–650 GHz channels are presented for species common for both channels (e.g. HCl). The HCl profiles retrieved from the submillimeter limb spectra in the 480–650 GHz channel are provided by SRON's Level-2 processing group (Arno de Lange, personal communication, 2013).

Furthermore, the vertical concentration profiles acquired by four infrared/microwave limb sounders (i.e. JEM/SMILES, Aura/MLS, Odin/SMR, and MIPAS-B) with close local times and geolocation information are selected for external comparisons. The SMILES profiles for our comparison are taken from the NICT Level-2 version 2.1.5 data product (hereafter SMILES v2.1.5, available at `http://smiles.nict.go.jp/pub/`

data/). The employed version of the Aura/MLS Level-2 data product is 3.3 (hereafter MLS v3.3, available at https://mls.jpl.nasa.gov/index-eos-mls.php), and a detailed description of this Level-2 data processing algorithm can be found in Livesey et al. [2006]. The Odin/SMR profiles, correspond to the latest official version (2.1) of the Level-2 data product (hereafter SMR v2.1, available at http://odin.rss.chalmers.se/searchl2/), which is delivered by the Chalmers University of Technology, Sweden [Urban et al., 2005]. The MIPAS-B retrievals were performed by the Institute for Meteorology and Climate Research – Atmospheric Trace Gases and Remote Sensing (IMK-ASF) at KIT. A description of the MIPAS-B Level-2 data processing algorithm is given by Wetzel et al. [2012] and references therein.

6.1 Retrieval Strategy

In this study, we employ PILS to carry out the inversion from actual TELIS radiance measurements and to evaluate the quality of the retrieval product. All retrievals are performed on an altitude grid with an equidistant vertical spacing (1.5 or 2 km) which is identical to the tangent height step of the recorded limb spectra below the float altitude of the balloon gondola. The lowest level of the retrieval grid depends on the vertical range of different limb sequences; it is initially set below the lowest tangent point by an amount of 1.5 km due to the extended vertical FoV of the TELIS instrument and the pointing error. The atmosphere above the uppermost tangent altitude (typically 32.5 km) is discretized with a step of 2.5 km between 32.5 and 40 km and a coarser step of 5 km between 40 and 65 km. The top-of-atmosphere is set to 65 km because of two reasons. First, the atmosphere above TELIS is not easily negligible and may be vital to the retrieval of some molecules, e.g. OH. Second, a sufficient size of the state vector needs to be ensured so as to reach a best compromise between computational efficiency and inversion quality. In most cases, the state vector $\boldsymbol{x}$ comprises the vertical profiles over an altitude region of 8.5–65 km or 14.5–65 km.

The inversion represents an ill-posed problem, i.e. the least squares solution can be overwhelmed by the measurement noise, and requires a regularization constraint. In the framework of Tikhonov regularization, the value of the regularization parameter is of importance for the retrieval and has to be chosen with great care. Alternatively, iterative regularization methods can be regarded as a variant of Tikhonov regularization. The simulation tests in Sect. 5.1.3 have revealed that this approach can reach a more reliable solution compared to Tikhonov regularization, and with much less computational effort on the estimation of the regularization parameter. For these reasons, the iteratively regularized Gauss–Newton method will be used to solve the ill-posed inverse problem involving the reconstruction of molecular concentration profiles from the TELIS spectra. To prevent the occurrence of negative values in the concentration retrieval, simple bounds on the iterates can be imposed. However, this constraint may be problematic, because the bound-constraint algorithm may result in unexpected situations, e.g. earlier termination of the inversion and false convergence. In our case, the correlation length l is chosen to be identical to the vertical spacing of two adjoint tangent points, i.e. 1.5 or

2 km. This choice allows some freedom to deviate away from the a priori profile while suppressing large oscillations in the non-unique solution space. For theoretical aspects of numerical regularization methods, we refer to Sect. 4.2.

Basically, accurate forward model parameters are always critical to the reliability of the retrieval product. Temperature profiles are taken from the MIPAS-B retrievals (Gerald Wetzel, personal communication, 2011 and 2013) as both instruments probed (almost) the same air masses simultaneously during the past campaigns. According to Wetzel et al. [2002], the error in the temperature profile is expected to be lower than ~ 1 K. The ECMWF (**E**uropean **C**enter for **M**edium-range **W**eather **F**orecasts) meteorological analysis is used for deriving a priori pressure data. The profiles of interfering gas species that are of minor importance are fixed to the standard AFGL subarctic winter atmosphere. For completeness, Table 6.1 summarizes the a priori profiles, the discretization scheme, and other forward model parameters used in this analysis.

Appendix A briefs additional information related to TELIS's far infrared measurements during the winter flights in 2009–2011. For the target molecules measured by the TELIS instrument in the far infrared spectral domain, all considered molecular emission lines are listed in Table A.1. Information on the employed LO frequencies for each target microwindow is also provided. Besides, a summary of the far infrared measurements is given in Appendix A.2.

Excepting O_3, the retrievals are performed by using a single frequency segment (500 MHz) instead of the whole microwindow (2 GHz). In this way, the fitting of the spectral baseline is improved and the effects from other interfering molecular features are reduced.

In the forward model, the radiometric calibration process of the TELIS instrument is performed at each iteration, which ought to be done for a realistic modelling of the calibrated radiance spectra. The mathematical formulation of the model is described in Sect. 5.2.2. The relevant cold/hot blackbodies and system noise temperatures are determined from the in-flight data.

6.1.1 Auxiliary parameters

As stated in Sect. 5.2, the discrepancies of spectral baselines between the measured and modelled spectra are not only influenced by instrumental effects, but also by insufficient physical knowledge of model parameters. In particular, imperfect knowledge of continuum absorption affects the spectral information in atmospheric measurements at low altitudes.

Water vapor absorption is arguably the dominant source of opacity in the troposphere and lower stratosphere, whereas dry air (mechanical mixture of various atmospheric gases, e.g. N_2, O_2, CO_2) plays an important role of continuum absorption in the stratosphere. A large number of strong H_2O molecular lines lie in submillimeter and millimeter spectral bands. If many strong lines are situated some spectral distance away, the effect of these individual far-off lines can be accumulated. Besides, the interaction produced by these molecules might have broad transitions and hence broad spectral features.

Table 6.1: Retrieval configurations for the reconstruction of atmospheric vertical concentration profiles from TELIS limb spectra in the far infrared region. The settings for the chosen retrieval grid, atmospheric inputs, and other forward model parameters are summarized.

Retrieval configuration	Description
Bottom-of-atmosphere	8.5 or 14.5 km
Top-of-atmosphere	65 km
Discretization	
8.5–32.5 km (14.5–32.5 km)	1.5 or 2 km
32.5–40 km	2.5 km
40–65 km	5 km
Temperature profile	MIPAS-B retrievals
Pressure profile	ECMWF
Remaining interfering species	AFGL subarctic winter model
Water vapor continuum	CKD model
Spectroscopic line parameters	HITRAN 2008

Different continuum models developed from laboratory and field measurements can provide an estimate of the continuum absorption for the spectral range of interest. However, significant effects referred in this context as "continuum-like contributions" are found in observed limb emission spectra. As already mentioned in Sect. 5.2.5, the continuum-like contributions can exert a great influence on the spectral baseline in the UTLS region. Woiwode et al. [2012] have explained that these different superimposed contributions are possibly due to

- broad spectral signatures of many different trace gases,
- effects with respect to spectral line shape,
- low concentrations of aerosol and cloud along the line-of-sight.

It is practically possible to model molecular line absorption accurately, but the fact remains that the actual background continuum radiation cannot be reproduced by any physical continuum model. Even if one assumes the gas profile (e.g. water vapor) to be exactly known, the error introduced by the uncertainty in the continuum model causes a fairly significant error in the retrieval of other species or auxiliary parameters. To account for the impact on the retrieval of trace gas species or atmospheric parameters (e.g. temperature) of interest, we can retrieve an additional artificial molecular species called "greybody" in order to simulate the continuum-like absorption at each retrieval altitude. This locally (i.e. within a microwindow) wavenumber/frequency independent species then always must be retrieved along with the species of interest.

Figure 6.1 shows a comparison between the modelled and measured spectra in the 480–650 GHz channel during the 2010 flight with and without the joint-fitting of this

altitude-dependent profile. Ozone is the major contributor to the measurement signal in this microwindow and seems to be saturated already at low altitudes. This strong O_3 feature lies between the two HCl lines at the intermediate frequency of about 5.9 and 6.8 GHz, respectively. In the wing of the latter HCl line, a ClO feature occurs. Apparently, the continuum-like absorptions in this microwindow have severe impact on the spectral baseline around 6.3 and 6.7 GHz below 25 km and consequently give rise to evident residuals. These large discrepancies over the ozone lines, easily identifiable at the lower tangent heights, are significantly removed by implementing this "greybody" fitting approach. As a result, the residuals at the solution are reduced.

In addition to the vertical concentration profiles of the target molecule(s) and "greybody", a polynomial should be retrieved for each spectrum so that the instrumental effect on the spectral baseline can be accounted for. In order to distinguish the physical and instrumental offsets, the degree of the baseline polynomial is set to zero, i.e. fitting a scalar quantity for each spectrum. While at lower altitudes (UTLS) the baseline offset found in the spectra is mostly correlated with the continuum, an unambiguous offset (instrumental baseline information) is crucial for the spectra at higher tangent heights (where the continuum effect nearly vanishes).

6.1.2 Overview of error analysis

A sensitivity analysis of the uncertainties in the forward and instrument model parameters has been conducted in Sect. 5.2. The smoothing error stems from the a priori information used in the regularization process, while the noise error is a consequence of the radiometric noise in the measurement. Imperfect calibration procedure, inaccurate sideband ratio, pointing offset, and atmospheric pressure turned out to be the most serious model parameter errors.

In this chapter, an overall accuracy ($\boldsymbol{x}_\lambda \pm \boldsymbol{e}_\lambda$) for the most potential model parameter errors is estimated for each retrieval. The smoothing error introduced in the inversion and the noise error in the TELIS measurement are considered as the two random error sources of the retrieval. The model parameter errors and their perturbation parameters are summarized in Table 6.2.

Chapter 3 states explicitly that the line-by-line calculations require reliable spectroscopic knowledge. In this work, all relevant spectroscopic parameters are extracted from the HITRAN 2008 database. The impact of inaccurate spectroscopic knowledge is surveyed in terms of the line strength (S) and air broadening parameters (the air-broadened half width γ_{air} and the coefficient of temperature dependence n_{air}). In the case of HCl, a line strength uncertainties of 2 % is taken, which is consistent with the one used by de Lange et al. [2012]. Nevertheless, this perturbation amount can be seen as a conservative estimate, as these values are very well determined from electric dipole moments. Another common issue is the O_3 contamination, and consequently the effects of air broadening parameters for O_3 lines in the frequency region of interest have also to be considered.

To some extent, a possible pressure shift can also have an influence on the retrieval (particularly for HCl). Its impact has been investigated by a systematic analysis in

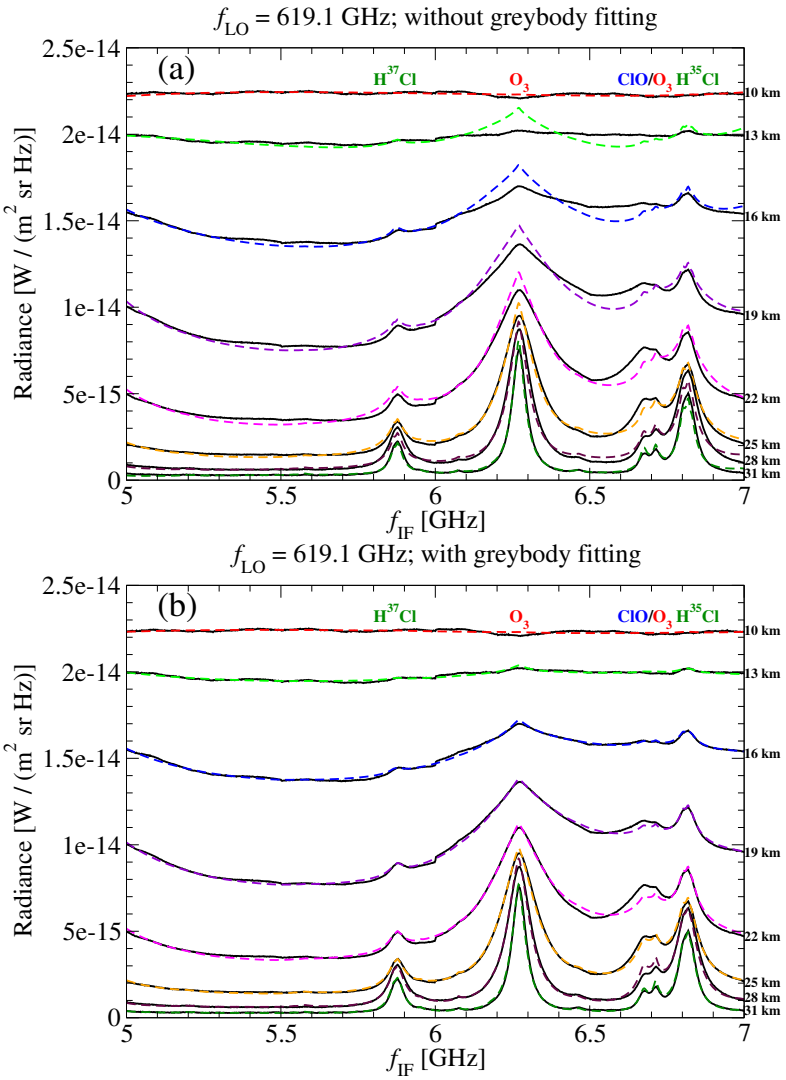

Figure 6.1: Comparison of modelled and measured spectra in the 480–650 GHz channel. Retrievals are carried out **(a)**: without joint-fitting of "greybody" profile and **(b)**: with joint-fitting of "greybody" profile.

Sect. 5.2. A perturbation of the corresponding parameter (air pressure-induced line shift) did not lead to any considerable difference in the result of the HCl retrieval test problem. Accordingly, the subject of pressure shift is not further considered in this study.

In particular, uncertainties in the instrument parameters related to the TELIS 1.8 THz channel have been confirmed in the past laboratory campaigns by the instrument team. Although nonlinearities present in the calibration chain have been considerably corrected in the latest Level-1b data product, 5 % is used as a reasonable assumption of the com-

Table 6.2: Model parameter errors and their perturbation parameters considered in the retrievals from TELIS far infrared data. For each error, the corresponding perturbation amount is indicated in the right column. Note that line strength is perturbed with the equivalent amount except for HCl. See the text for a detailed explanation of the error sources.

Model parameter error	Perturbation
Spectroscopic parameters	
Line strength (S)	1 % (O_3)
	2 % (HCl)
	1 % (CO)
	1 % (OH)
Air broadening (γ_{air})	5 %
Temperature dependence (n_{air})	10 %
Radiometric calibration	5 %*
Sideband ratio	0.05
Pointing information	
Systematic bias	3.4 arcmin
Uncertainty in the systematic bias	1 arcmin
Atmospheric parameters	
Temperature	1 K
Pressure	1 %

* In this study, we only consider the nonlinearity effect as the main error source in the radiometric calibration. The value represents the assumed compression in the measurement of the emission from a hot load.

pression in the hot load measurement related to the calibrated output. The sideband ratio varies from 0.95 to 1.05 for this channel, and in this study, an uncertainty of 5 % is assumed. The systematic pointing bias is estimated to be 3.4 arcmin in the commanded zenith angle based on the antenna beam profile measurements. An additional 1 arcmin is superimposed onto this systematic pointing bias according to the accuracy of the AHRS system. Most of these values have already been used in the sensitivity study presented in Sect. 5.2.

Potential errors introduced by atmospheric profiles (essentially temperature and pressure) are taken into account in conjunction with their accuracies. The upper limit of 1 K is taken as the uncertainty in the MIPAS-B temperature profile, and the accuracy in the ECMWF pressure profile is estimated to be 1 %.

The retrieval makes use of a weaker regularization in order to allow for a better altitude resolution with the drawback of slightly noisier profiles. It could be expected that the smoothing error will be much smaller than the model parameter error in the stratosphere, and the noise error may become severe for some far infrared microwindows in which in-flight system noise temperature was observed to be extremely high. The nonlinearity effect owing to the calibration procedure may be the main contribution to

the model parameter error, particularly at altitudes where the abundances are high.

In this study, the total retrieval error $\boldsymbol{e}_\lambda$ is defined as the root sum squares (RSS) of all these error components mentioned above (see also Eq. (4.49)), rather than treating them as a direct sum.

6.1.3 Comparison approach

The internal and external comparisons enable us to analyze the differences in the retrieval algorithms and measurement characteristics. All measurements selected for these comparisons are attained by limb emission instruments in the infrared and microwave spectral domains.

The comparisons are performed by searching for pairs of coincident observations between TELIS and other satellite/balloon-borne instruments under certain criteria. The criteria should be stringent enough to confirm that the same air masses are observed, especially for polar cases. The distance between observation geolocations within 300 km and the difference in the solar zenith angle within 3° are considered. A 1 h threshold for the time difference is applied for the internal comparison of TELIS and the external comparisons with MIPAS-B, SMILES, MLS, and SMR.

The differences in the averaging kernels and the a priori knowledge should be taken into account in case of comparing original concentration profiles retrieved from different remote sensing measurements [Rodgers and Connor, 2003]. It can seen that the most significant impact of the different averaging kernels is an obvious difference in the vertical resolutions of different instruments. In our case, the TELIS instrument provides a better vertical resolution than the other spaceborne limb sounders in the lower and middle stratosphere.

To cope with these differences in the measurement characteristics properly, we need to convolve the original high-resolution profile $\boldsymbol{x}_{\text{high}}$ with the averaging kernel matrix $\mathbf{A}_{\text{low}}$ of the instrument with lower vertical resolution. The smoothed profile is then given by

$$\boldsymbol{x}_{\text{smooth}} \;=\; \mathbf{A}_{\text{low}}\boldsymbol{x}_{\text{high}} + (\mathbf{I}_n - \mathbf{A}_{\text{low}})\,\boldsymbol{x}_{\text{a}}\;, \tag{6.1}$$

where $\boldsymbol{x}_{\text{a}}$ is the a priori profile used in the retrieval of the data of the lower resolution instrument. To compare coincident profiles with similar vertical resolutions, a linear interpolation can also be considered.

For comparisons with other data, the data quality for the TELIS profiles should consider the following parameters: measurement response, goodness of fit (residual term), and averaging kernels. The retrieved profiles obtained by other instruments for the comparison also have to fulfill a certain data quality selection criteria.

6.2 O_3 Retrieval

In practice, the TELIS consortium did not define any dedicated ozone (O_3) frequency microwindow during previous balloon campaigns, because ozone appears in almost all observed microwindows. In Fig. A.1 of Appendix A.1, the signatures of O_3, H_2O, and

Table 6.3: The three microwindows for ozone retrievals from the calibrated limb spectra measured during the 2010 flight. The scan identifiers and the corresponding measurement time of the MIPAS-B reference profiles are listed.

Measurement	Microwindow	Time (UTC)	MIPAS-B scan	Time (UTC)
8092	CO	04:45–04:58	02	04:33–04:53
12206	HDO	06:59–07:15	06b	07:00–07:12
13352	O_2	07:38–07:54	06e	07:34–07:44

the target molecules are plotted for all microwindows measured during the 2010 flight. In this section, we first evaluate the retrieval performance of different far infrared microwindows (i.e. different O_3 transitions) and then compare the retrieval results with infrared/microwave spaceborne observations (SMILES, MLS, and SMR).

6.2.1 Check on different microwindows

Ozone retrievals have been performed from three different limb-scanning measurements measured during the 2010 flight. To verify the inversion results, the retrieved TELIS ozone profiles are compared with the ones obtained by MIPAS-B. Ozone profiles recorded by MIPAS-B have a typical vertical resolution of 2–3 km and a total error of 0.1–0.5 ppmv [Wetzel et al., 2006]. Temperature and ozone profiles estimated from the MIPAS-B mid infrared spectra were observed between 04:33 and 10:25 UTC (with a gap between 04:54 and 06:11 UTC). An overview of the analyzed TELIS far infrared radiance measurements is given in Table 6.3. The MIPAS-B observations for comparisons are selected in accordance with the measuring time.

In principle, ozone can be retrieved from any 500 MHz frequency segment containing O_3 features. Thus, different segments have been analyzed, or equivalently, a variety of ozone lines originating from both or single sidebands, with different sensitivities to atmospheric condition, e.g. temperature, have been investigated. Table 6.4 lists the most significant ozone lines residing in the three target microwindows. To regard an ozone transition as a favorable choice for the retrieval, one should not exclude the quantity of the lower state energy which reflects the sensitivity to temperature. If ozone contributions come from both sidebands and are analyzed simultaneously, it might be that an error in the sideband ratio can be "averaged out" so that the impact on the retrieval result is limited. From this perspective, processing the whole microwindow or the combination of at least two frequency segments, could be beneficial.

CO microwindow

TELIS measurement 8092 is dedicated to the CO microwindow and was observed before the local sunrise. Figure 6.2 demonstrates that a pair of O_3 signatures are discernible in the wings of the strong CO line and occur in two different frequency segments. It

Table 6.4: Various ozone lines corresponding to the three selected far infrared microwindows. Only the most significant ozone transitions are listed. E_i represents the energy of the lower state where the O_3 transition occurs. Information about the corresponding sideband and segment where the O_3 line can be found is given as well. Associated line parameters (position of line center and E_i) are extracted from the HITRAN 2008 spectroscopic database.

Position (cm^{-1})	Microwindow	Sideband	Segment	E_i (cm^{-1})
61.1129	CO	LSB	1	286.8056
61.4391	CO	USB	3	1196.0930
61.4598	CO	USB	4	364.7143
60.6502	HDO	LSB	4	1383.2810
60.9857	HDO	USB	1	828.9916
60.9895	HDO	USB	1-2	183.4307
61.0067	HDO	USB	2	1990.1950
61.0300	HDO	USB	4	1370.5580
62.2060	O_2	LSB	4	354.1466
62.2074	O_2	LSB	4	228.7342
62.5711	O_2	USB	3	550.3134

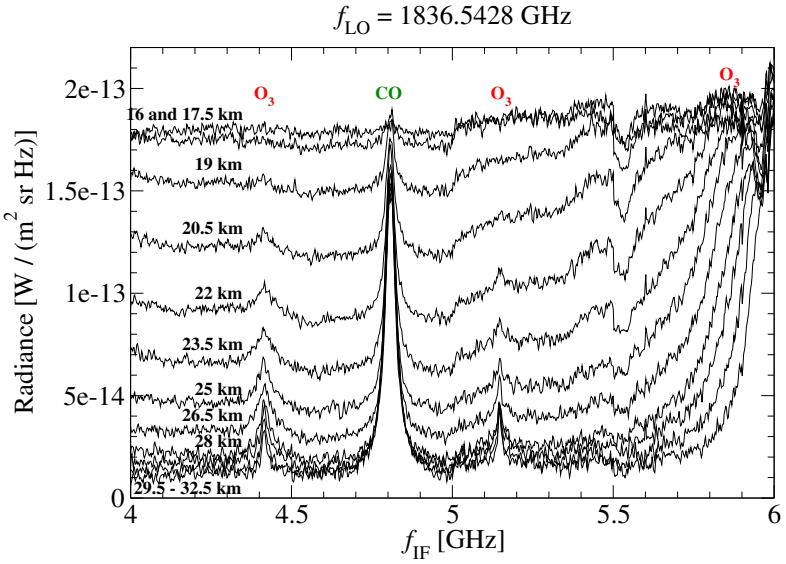

Figure 6.2: Far infrared limb spectra in the CO microwindow containing O_3 features. The data were measured by TELIS during the 2010 flight. The dedicated measurement identifier is 8092.

can be seen that the fourth frequency segment (5.5–6 GHz) contains very strong O_3 lines which are saturated from 20.5 km upward. As a result, the sensitivity to ozone concentrations above this altitude level is reduced and this frequency segment seems to be inappropriate for ozone retrieval compared to frequency segments 1 and 3. Frequency

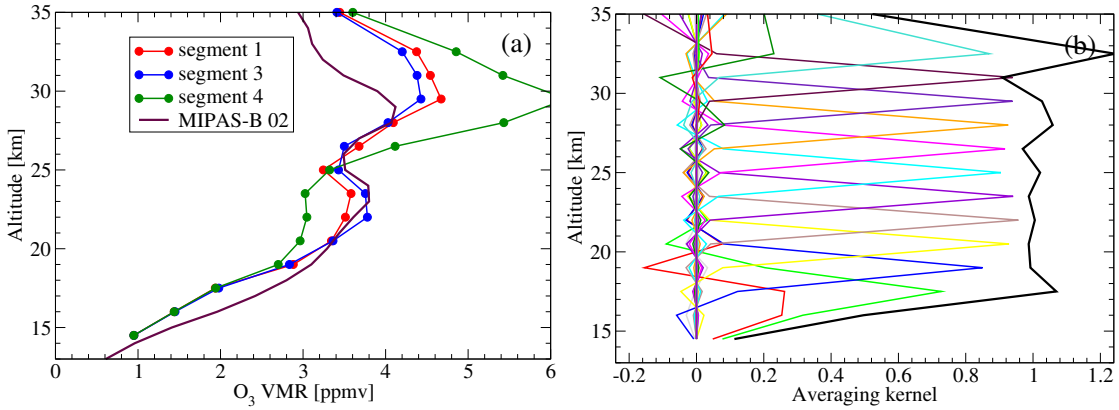

Figure 6.3: Panel **(a)**: retrieved ozone profiles in different frequency segments of the CO microwindow. The lowest tangent height is 16 km and the retrieval results below this altitude have little physical meaning. Panel **(b)**: averaging kernels for the O_3 retrieval using the measurement in frequency segment 1. The thick black line refers to the corresponding measurement response.

segment 1 appears to be the most suitable choice for the O_3 retrieval as it can be deduced from the lower state energies of listed in Table 6.4. The MIPAS-B O_3 profile (identifier 02) used as reference was the first ozone data delivered during this flight and was observed earlier than the TELIS CO data.

The retrieval results of O_3 in frequency segments 1, 3, and 4 along with the MIPAS-B reference profile are shown in Fig. 6.3a. A double peak structure in the stratosphere is clearly seen in the MIPAS-B ozone profile, and the TELIS retrievals in frequency segments 1 and 3 closely resemble this shape. All depicted ozone profiles capture the concentration peak around 30 km, albeit with a higher concentration as compared to the MIPAS-B retrieved profile ($\approx 50\,\%$ higher from frequency segment 4). The less noticeable peak around 23 km of the MIPAS-B reference profile is also reproduced by the retrievals in frequency segments 1 and 3. The ozone profile from the third frequency segment is overall closest to the MIPAS-B profile, although the O_3 transition in this frequency segment may be very sensitive to the error in the temperature profile because of the high lower state energy (E_i, see Table 6.4). Nevertheless, the profiles retrieved from different frequency segments are shown to be consistent with each other below 20 km.

For the retrieval in frequency segment 1, the averaging kernels over the altitude range between 13 and 35 km are shown in Fig. 6.3b. The vertical resolution is 1.5–1.8 km between 20.5 and 31 km, and this quantity is close to the vertical spacing of two consecutive tangent points (~ 1.5 km). Outside this altitude range, the FWHM reaches 2–3 km above 17.5 km and below 32.5 km; the averaging kernel does not peak to the corresponding tangent height, showing a very low sensitivity of the retrieval. This is mostly because the signal becomes saturated at lower altitudes.

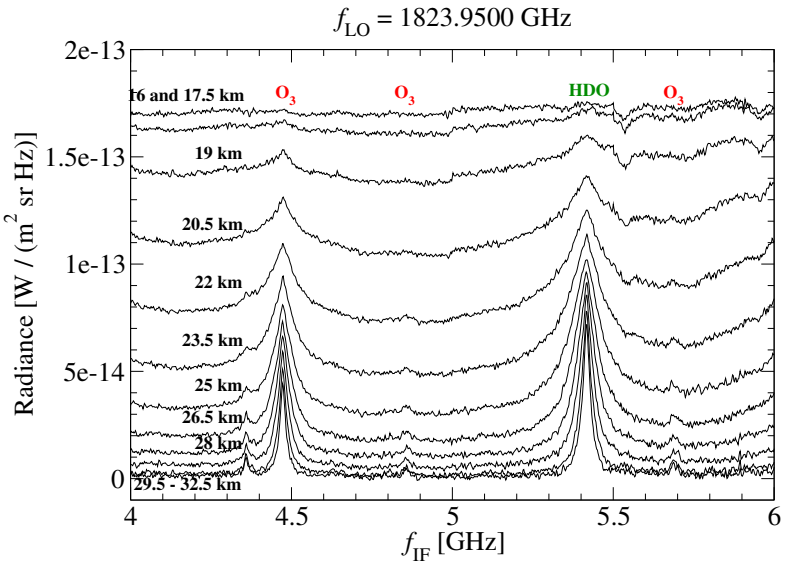

Figure 6.4: Far infrared limb spectra in the HDO microwindow containing O_3 features. The data were measured by TELIS during the 2010 flight. The dedicated measurement identifier is 12206.

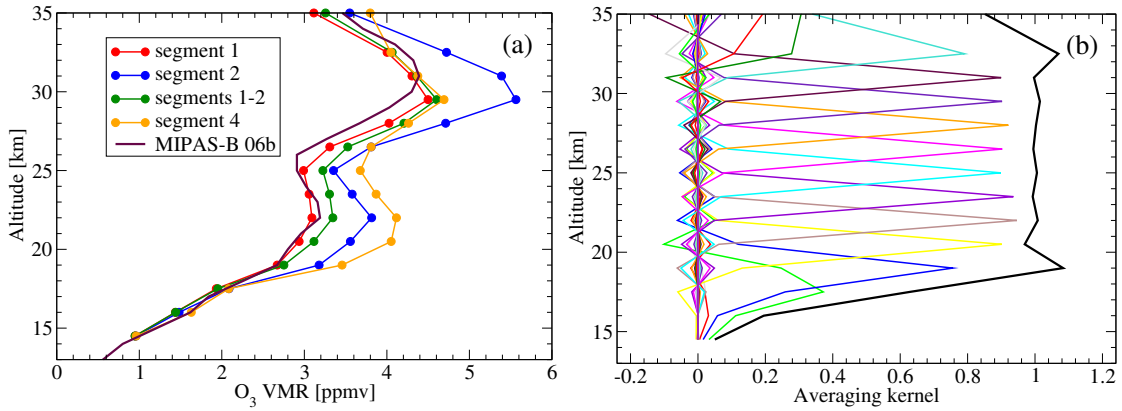

Figure 6.5: Panel **(a)**: retrieved ozone profiles in different frequency segments of the HDO microwindow. The lowest tangent height is 16 km and the retrieval results below this altitude have little physical meaning. Panel **(b)**: averaging kernels for the O_3 retrieval using the measurement in the combined frequency segments 1–2.

HDO microwindow

In the case of the HDO microwindow, the two strong O_3 and HDO features occur separately and approximately at the intermediate frequency 4.5 and 5.4 GHz, respectively. As the wings of the strong O_3 feature distributes over frequency segments 1 and 2, both frequency segments can be used for the retrieval, although only the upper sideband

exhibits the ozone line. A retrieval exercise with a combination of segments 1 and 2 shall also be taken into account as the strong O_3 feature is near the border of these two adjoint frequency segments. Two relatively weak ozone lines are found in frequency segment 4, but both are in the wing of a strong ozone line centered outside the detected frequency range. According to Table 6.4, the strongest O_3 transition around the intermediate frequency 4.5 GHz has the smallest lower state energy and is estimated to be most insensitive to the error in the temperature.

Figure 6.5a presents the O_3 retrievals using different measurements in frequency segments 1, 2, and 4, and in the combined frequency segments 1–2. The MIPAS-B retrieval exhibits a double peak shape which is also shown by all TELIS ozone profiles. All four plotted TELIS profiles capture the peak around 29 km, but with a stronger signature than the peak value of the MIPAS-B profile. It can be noticed that the altitudes of the ozone peaks in the TELIS profiles are slightly shifted from that in the MIPAS-B profile. The profiles derived in frequency segments 2 and 4 show a larger peak around 23 km than the MIPAS-B profile (differences $\approx$ 25–30 %), whereas both profiles derived in frequency segment 1 and the combined frequency segments 1–2 resemble the structure of the MIPAS-B profile below 22 km. Apparently, the first frequency segment and the combined frequency segments 1–2 appear to be the optimal choices for the ozone retrieval by taking into account the results and the sensitivity to the temperature accuracy.

In Fig. 6.5b, we plot the averaging kernels for the retrieval in the combined frequency segments 1–2. A vertical resolution of 1.5–2 km in conjunction with a reasonable measurement response (> 0.9) is found over the altitude range between 19 and 32.5 km. Below 17.5 km, the FWHM increases and the peak value becomes quite small, which reveals a larger smoothing error caused by regularization.

O_2 microwindow

The O_2 microwindow has been considered for this analysis as it contains several strong O_3 signatures. However, the system noise temperature was overall somewhat higher than most other THz microwindows during the 2010 balloon flight, which has the smallest noise degradation. To reduce the noise error in the retrieval, we selected measurement 13352. It is noted that a sideband ratio of 1 was still assumed for this particular microwindow in the latest version of the calibrated spectra due to the fact that the instrument parameter in this microwindow has not been fully resolved during the past dedicated on-ground calibration campaigns. There is a very strong O_3 signature in frequency segment 3, and it is most likely that this strong ozone line is saturated even in the lower stratosphere. In frequency segment 4, an O_3 feature around 5.8 GHz is seen in both the upper and lower sidebands, making this segment ideal for the retrieval with less risk of encountering errors stemming from the imperfect sideband ratio knowledge. A significant HCl feature resides in the wings of these two ozone lines and HCl has to be jointly retrieved in order to improve the O_3 fit. Since the O_3 contributions to the spectra in frequency segments 3 and 4 origin from both sidebands, ozone can be retrieved in principle from a combination of these two frequency segments as well. How-

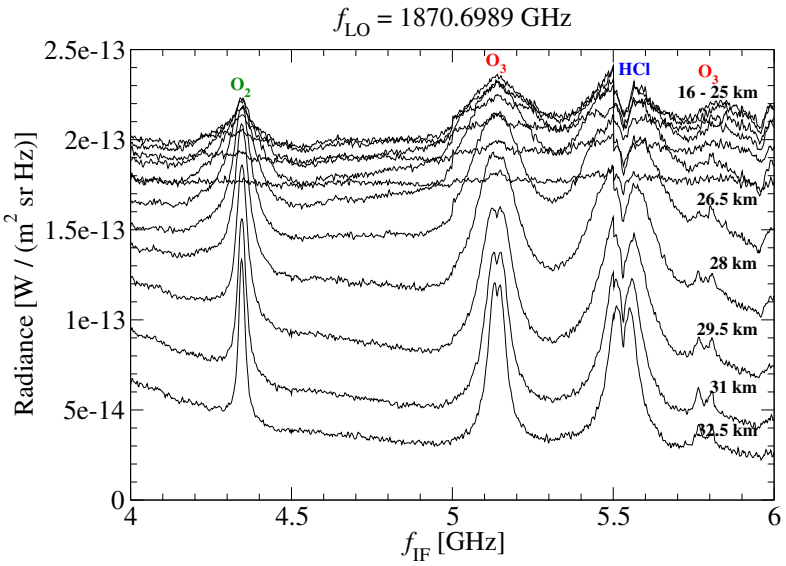

Figure 6.6: Far infrared limb spectra in the O_2 microwindow containing O_3 features. The data were measured by TELIS during the 2010 flight. The dedicated measurement identifier is 13352.

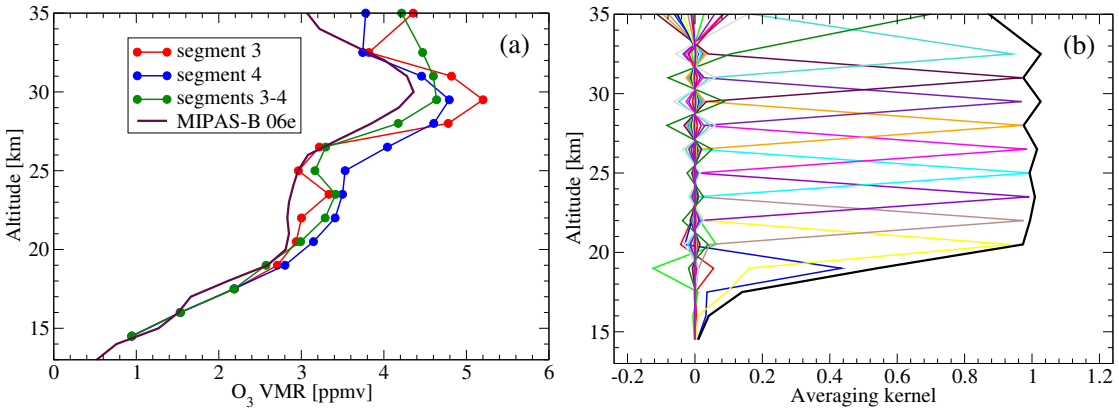

Figure 6.7: Panel **(a)**: retrieved ozone profiles in different (combinations of) frequency segments of the O_2 microwindow. The lowest tangent height is 16 km and the retrieval results below this altitude have little physical meaning. Panel **(b)**: averaging kernels for the O_3 retrieval using the measurement in the combined segments 3–4.

ever, on the border of the latter two frequency segments ($\sim$5.5 GHz) there is a noticeable discontinuity in the spectra, which to some extent could hamper the retrieval.

Figure 6.7a illustrates the retrieved ozone profiles in frequency segments 3 and 4, and in the combination of these two segments. The peak around 30 km is overestimated in the ozone profiles from the TELIS data (6 %–20 % higher than the MIPAS-B profile). The profiles in frequency segment 3 and the combined frequency segments 3–4 show a double peak structure with maxima at 23.5 and 29.5 km, which is slightly different from the

MIPAS-B profile. The two profiles are virtually identical below 26.5 km, revealing that the retrieval with the combined spectrum of both frequency segments at lower altitudes gains its information mainly from frequency segment 3. Although the magnitude of the O_3 profile derived in frequency segment 4 is higher than that of the MIPAS-B profile, the shape resembles the shape of the MIPAS-B profile best.

The associated averaging kernels for the O_3 retrieval in the combined frequency segments are plotted in Fig. 6.7b. The kernel is nicely peaked with a maximum FMWH of 2 km between 19 and 32.5 km, which is analogous to the widths in the above two cases of the O_3 retrievals. The sensitivity of the retrieval is lower below 17.5 km where O_3 features are hardly recognizable.

Final remarks

In conclusion, the O_3 retrievals have been done for three different far infrared microwindows and the retrieved profiles have been compared with the coincident MIPAS-B data products. Of all three microwindows that have been analyzed, a good vertical resolution of about 1.5–2 km in the altitude range of 19–31 km is achieved, which is in accordance with a measurement response close to 1. The kernels broaden out at lower altitudes resulting from atmospheric attenuation by water vapor absorption, which means a rather low sensitivity of the retrieval to the measurement signal. In this altitude range, the a priori knowledge is dominant as limited information can be inferred from the measurement.

In general, the TELIS retrievals result in higher ozone concentrations as compared to the MIPAS-B retrievals, and the retrievals in different (combinations of) frequency segments of the same microwindow are consistent with each other. One reason for this discrepancy is that the retrievals of both instruments are derived from different O_3 transitions located in two different spectral ranges (far infrared and mid infrared). Accordingly, differences in spectroscopic information may account for the discrepancies between both concentration profiles. Different O_3 transitions could lead to the differences in the nonlinearity effect owing to the calibration procedure.

In our case, the O_3 retrieval counts on the temperature profile which was shared with the MIPAS-B retrieval. However, TELIS and MIPAS-B did not have exactly identical viewing geometries despite the fact that both instruments were mounted on the same gondola. It is also worth mentioning that the MIPAS-B temperature profiles differed for the last two measurements during the 2010 flight, even though the time difference was only half an hour and nearly same air masses were probed.

6.2.2 Error characterization

For the O_3 retrieval, we implement a quantitative characterization of the errors for two individual microwindows that were observed during the 2010 flight. Different uncertainties (especially due to spectroscopic parameters) may lead to significant discrepancies between both error budgets, given that different O_3 far infrared transitions are covered by these two microwindows.

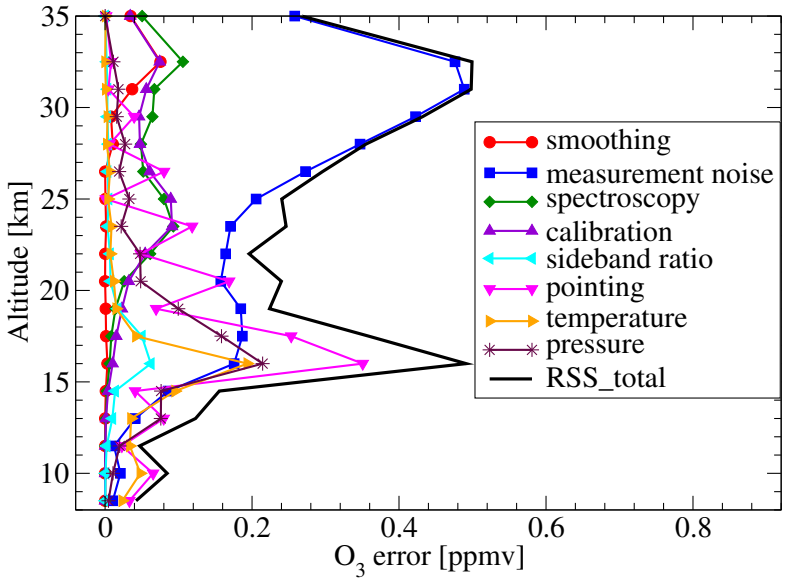

Figure 6.8: Smoothing, noise, and model parameters errors for the O_3 retrieval using TELIS's far infrared measurement 20864 in the CO microwindow during the 2010 flight. Assumed uncertainties in the model parameter errors can be found in Table 6.2. The solid black line (RSS_total) refers to the total retrieval error represented by the RSS of all error components.

Figure 6.8 depicts the estimated smoothing, noise, and model parameters errors in the O_3 retrieval for TELIS measurement 20864 (the CO microwindow). The noise error dominates the error budget above 20 km as the system noise temperature was fairly high (see Table A.4) for this measurement, while the error arising from the pointing uncertainty seems to have the leading role in determining the retrieval quality at lower altitudes. Another factor for exhibiting such high noise error is the use of a relatively weak regularization in this retrieval so that an improved vertical resolution is obtained. In this case, the total retrieval error is estimated to be 0.2–0.5 ppmv over the altitude range between 15 and 35 km.

Furthermore, the smoothing, noise, and model parameters errors in the O_3 retrieval for TELIS measurement 7276 (the HDO microwindow) are presented in Fig. 6.9. In contrast to Fig. 6.8, the error budget at higher altitudes (above 25 km) is essentially dominated by the calibration (nonlinearities in the IF-signal chain) and spectroscopic errors. Above 20 km, these two error sources result in a double peak structure that is consistent with the shape discovered in the concentration profile of O_3. The uncertainties in the sideband ratio, pressure, and pointing information are the most influential error sources below 20 km. The maximum total retrieval error is evaluated to be about 0.8 ppbv at the highest tangent point 32.5 km, and the second error peak reaches 0.6 ppbv around the altitude range between 16 and 17.5 km.

As it can be seen from these two retrieval error plots, the spectroscopic accuracy is the second largest error source of the O_3 retrieval in the HDO microwindow but is of

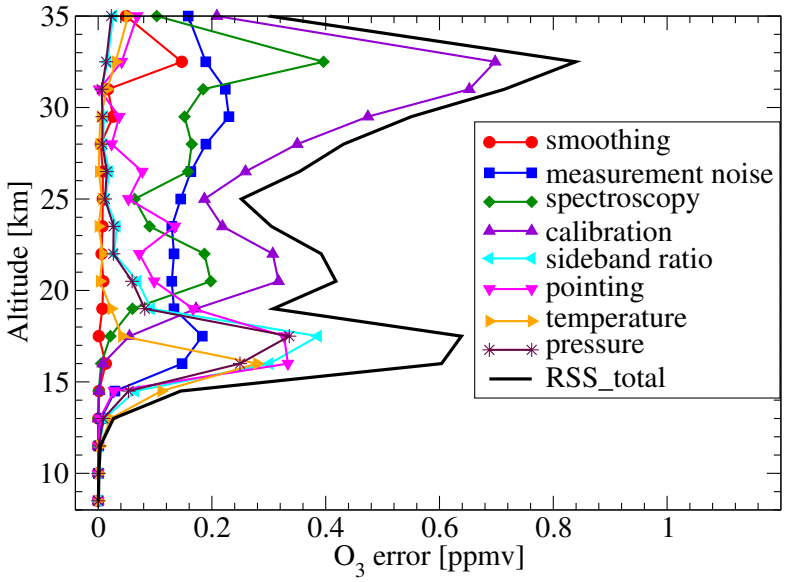

Figure 6.9: Smoothing, noise, and model parameters errors for the O_3 retrieval using TELIS's far infrared measurement 7276 in the HDO microwindow during the 2010 flight.

Table 6.5: Summary of spaceborne observations and coincident TELIS limb scans used in the O_3 intercomparison. Information about the corresponding Level-2 data version, the measuring time, and the number of coincident data points with respect to each spaceborne instrument is included. Two TELIS THz microwindows monitored during the 2010 flight are selected for external comparisons.

Instrument	Data version	Time (UTC)	Number of coincidences	TELIS scan
SMILES	2.1.5	11:18–11:19	2	20864
MLS	3.3	11:11	1	20864
SMR	2.1	04:45–04:47	2	7276

minor importance in the CO microwindow. One explanation for this striking difference in the error budgets of the two microwindows may be that this spectroscopy error scales with O_3 abundances and in the case of the HDO microwindow a stronger O_3 signal occurs. Other error contributors (e.g. uncertainties in the radiometric calibration and the sideband ratio) are also likely to be determined by spectral line strengths, and thus by O_3 concentrations.

6.2.3 Comparison with spaceborne observations

The O_3 profiles derived from the far infrared limb spectra of TELIS are compared with three spaceborne observations, i.e. SMILES, MLS, and SMR. A summary of spaceborne

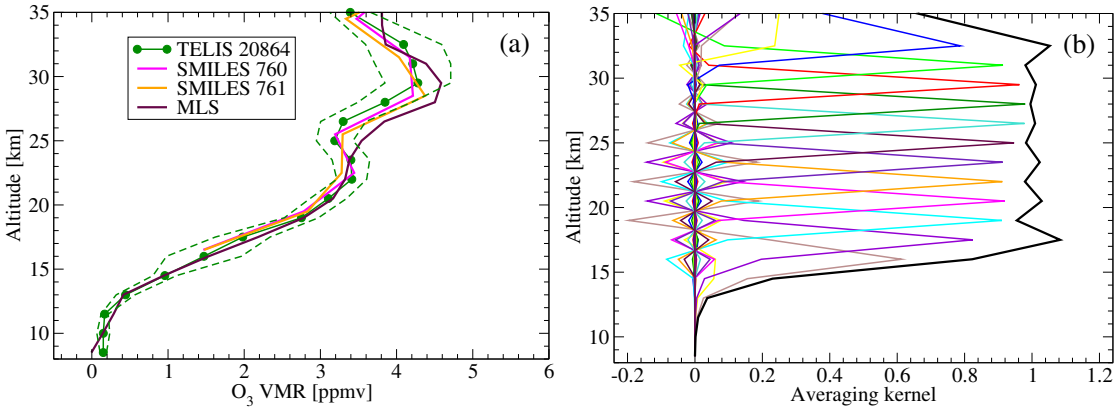

Figure 6.10: Panel **(a)**: Comparison of O_3 retrievals from TELIS, SMILES, and MLS on 24 January 2010. The lowest tangent height is 10 km and the retrieval results below this altitude have little physical meaning. The dashed green lines indicate the overall accuracy in the TELIS profile. The time difference of the SMILES and TELIS measurements was about 0.5 h. Panel **(b)**: averaging kernels for the TELIS O_3 retrieval.

data points and coincident TELIS observations used for the intercomparison on 24 January 2010 is given in Table 6.5.

SMILES probed O_3 at the transition frequency of 625.371 GHz that is allocated in two frequency regions: Band-A (624.32–625.52 GHz) and Band-B (625.12–626.32 GHz). Considering the coincidence criteria and the accuracy affected by the gain calibration uncertainty, the Band-B data are used for the intercomparison between the SMILES and TELIS observations. Kasai et al. [2013] reported a comprehensive quality assessment of the SMILES-NICT O_3 product, including a theoretical error analysis, internal comparisons between the two radiometer bands, performance comparison between two different retrieval algorithms for SMILES, and external comparisons with diverse satellite and balloon observations (including TELIS).

MLS obtains the standard Level-2 product for O_3 from the 240 GHz radiometer measurements. A discussion of upper tropospheric ozone observations (v3.3) can be found in Livesey et al. [2013]. Several validation studies of the MLS v2.2 ozone data were documented in Jiang et al. [2007]; Froidevaux et al. [2008a]; Livesey et al. [2008].

Two SMILES v2.1.5 (760 and 761) and one MLS v3.3 profiles are selected for this comparison with regard to the matched observation coverage and measuring time. For the comparison against SMILES and MLS, the TELIS O_3 profile is retrieved from THz measurement 20864. Similar to measurement 8092 (see Fig. 6.2 and Fig. 6.23), measurement 20864 which was observed during daytime (local noon), was taken in the CO microwindow as well. The TELIS retrieval is performed in the first frequency segment containing an O_3 feature which is not very sensitive to temperature uncertainties. In Fig. 6.10, the comparison of the retrieved profiles between three instruments along with the corresponding averaging kernel for the TELIS retrieval is shown. Both two SMILES profiles fall well within the error margin of the TELIS profile, but large discrepancies

are found 35 km above (not shown) as a result of the limited information of the TELIS instrument in this altitude range. Apart from that, a promising agreement between SMILES and TELIS is reached between 16 and 35 km. The MLS and TELIS VMR profiles agree within the overall accuracy of the TELIS profile excepting a region around 25–28 km, while a maximum difference of about 25 % is found at 28 km.

The standard SMR v2.1 O_3 data are retrieved from a weak ozone line around 501.5 GHz, whereas previous versions of retrieval products used a strong ozone line at 544.9 GHz in addition to the weak line. An extensive intercomparison with coincident MIPAS and balloon sonde stratospheric O_3 data suggests that the SMR v2.1 data using only the weak O_3 transition is more appropriate for scientific studies [Jones et al., 2007]. According to Urban et al. [2005], only data with good quality (assigned flag `QUALITY` = 0) and measurement response associated with each altitude level larger than approximately 0.9 are recommended for use. The vertical resolution for the SMR measurements is about 3 km [Jégou et al., 2008].

There were two coincident SMR measurements on 24 January 2010 within a ±200 km circle and with a time difference of ±1 h. Both SMR profiles below 18 km are less meaningful as the corresponding measurement response is even less than 0.7. For this comparison, these two SMR profiles have been averaged out and linearly interpolated onto the TELIS altitude grid to yield a smoother profile. The TELIS O_3 profile derived from measurement 7276 (HDO microwindow) is compared to this average SMR profile in Fig. 6.11a. A combination of the frequency segments 1 and 2 is used according to the conclusion in Sect. 6.2.1. The TELIS and SMR profiles reach an acceptable agreement despite some oscillations in the SMR profile. A too weak regularization in the SMR retrieval can provoke this under-smoothing feature in the profile. The averaging kernels of the TELIS retrieval (Fig. 6.11b) are adequately peaked over 17.5–31 km and the corresponding measurement response is approximately 1 over this altitude range.

6.3 HCl Retrieval

Chlorine activation occurs in the stratosphere during the polar winter, when the sun does not rise over the polar region and atmospheric temperatures are extremely low [Jacobson, 2012]. Hydrogen chloride (HCl) is the main chlorine reservoir species monitored by both the 1.8 THz and 480–650 GHz channels of TELIS, whereas the active chlorine species chlorine monoxide (ClO) can only be observed by the submillimeter channel. These species have been used for a quantitative estimation of the total budget of chlorine in the stratosphere and allow us a better understanding of their impact on stratospheric ozone depletion. Unfortunately, the far infrared microwindow of HCl were only observed during the 2010 balloon campaign. Nevertheless, the 2010 TELIS/MIPAS-B/mini-DOAS joint flight took place over northern Scandinavia inside the activated Arctic vortex where chlorine activation can be examined.

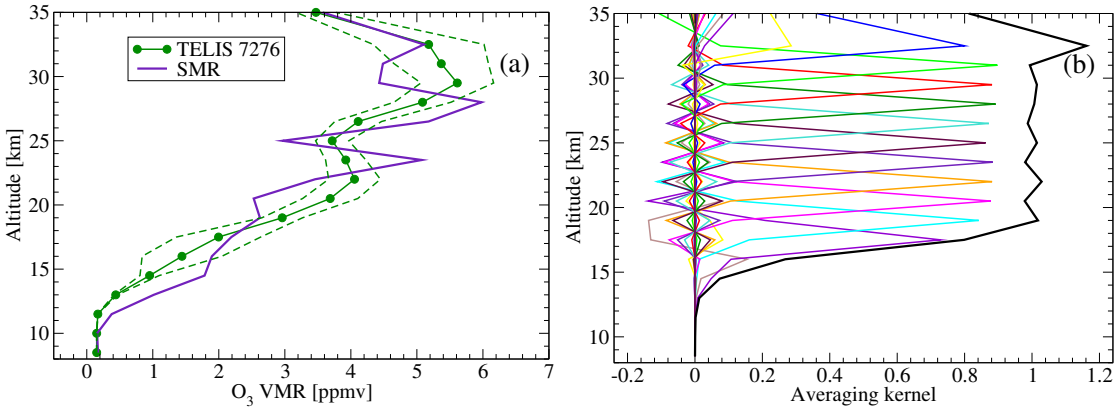

Figure 6.11: Panel **(a)**: comparison of O_3 retrievals from TELIS and SMR on 24 January 2010. The lowest tangent height is 10 km and the retrieval results below this altitude have little physical meaning. The time difference of the SMR and TELIS measurements was about 0.5 h. The SMR profile is linearly interpolated onto the of the TELIS retrieval grid retrieval by taking the associated averaging kernel into account. Panel **(b)**: averaging kernels for the TELIS O_3 retrieval.

Table 6.6: Setup for the HCl retrieval from the TELIS far infrared data. Information on the used spectral range and the state vector parameters is listed.

Parameter	Description
f_{IF} range	4–4.5 GHz
Target species	HCl
Retrieved interfering species	none
Auxiliary parameter	"greybody", baseline offset

6.3.1 Observation in the polar winter 2010

In the 1.8 THz channel, one $H^{37}Cl$ transition line at 1873.40 GHz (62.49 cm^{-1}) was detected during the 2010 flight. With the LO frequency f_{LO} = 1877.6323 GHz, this line fall within the intermediate frequency range f_{IF} = 4–6 GHz. Figure 6.12 shows a limb-scanning sequence of the far infrared spectra of the HCl microwindow observed by TELIS at local noon on 24 January 2010. For this measurement, the limb sequence covers tangent heights between 16 and 32.5 km in equidistant steps of 1.5 km. The $H^{37}Cl$ line is clearly identifiable around the intermediate frequency of about 4.2 GHz (frequency segment 1) with negligible overlapping contributions from other species (e.g. O_3 and H_2O). The targeted HCl signal comes from the lower sideband and an abnormal dip is clearly seen as a result of the atmospheric spectra calibrated by the up-looking spectrum with a zenith angle of 25° instead of the cold signal reference at the temperature of 2.725 K.

The setup for the HCl retrieval is given in Table 6.6. The retrieval is performed in

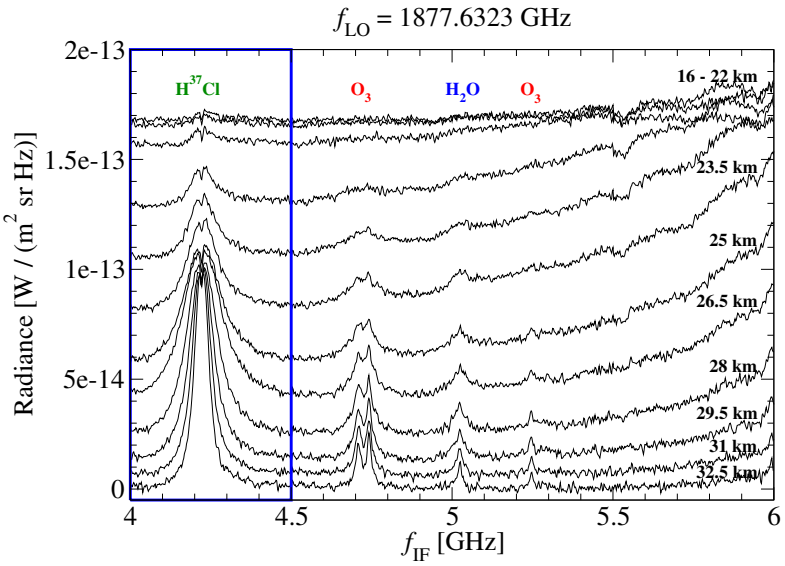

Figure 6.12: A sequence of limb spectra of the HCl microwindow measured by the TELIS 1.8 THz channel during the 2010 flight. The limb sequence observing a $H^{37}Cl$ line and covering tangent heights between 16 and 32.5 km in steps of 1.5 km, is illustrated as a function of the intermediate frequency f_{IF}. The spectral segment of 500 MHz selected for HCl retrieval is indicated by a blue rectangular box. The dedicated measurement identifier is 20044.

the first frequency segment (4–4.5 GHz) where the $H^{37}Cl$ feature occurs. No additional species is concurrently fitted because in this microwindow, different molecular transitions are isolated from each other and the first frequency segment covers only the HCl feature. It is noted that the natural abundance ratio of the isotopes ($Cl^{35}/Cl^{37} = 0.7578/0.2422$) has been accounted for and that in the following, the plotted profiles denote total HCl concentration amounts.

Figure 6.13 shows a comparison of observed TELIS spectra and modelled spectra corresponding to the retrieved profile in the first frequency segment. The relative residuals are within 4 % at the lower tangent heights (19 and 22 km) with a maximum difference around the line center. After convergence, the modelled spectra approximate the measurement fairly well at higher altitudes, with larger discrepancies in the line wings of HCl. By simulating the radiometric calibration process of the TELIS spectra, the abnormal dip around the line center is mostly fitted.

HCl retrievals have been carried out for every single limb sequence during the 2010 flight and the results of VMR profile as a function of altitude are shown in Fig. 6.14. The absence of HCl near 23.5 km is seen in all plotted profiles, implying a conversion of stratospheric HCl into active chlorine species (e.g. ClO) at that time. In Fig. 6.14, the total retrieval error is estimated for these three HCl profiles and the dashed lines represent the corresponding overall accuracies. The three profiles are estimated to have nearly the same error budget, except for 30 km where the error margin corresponding to measurement 21537 is large.

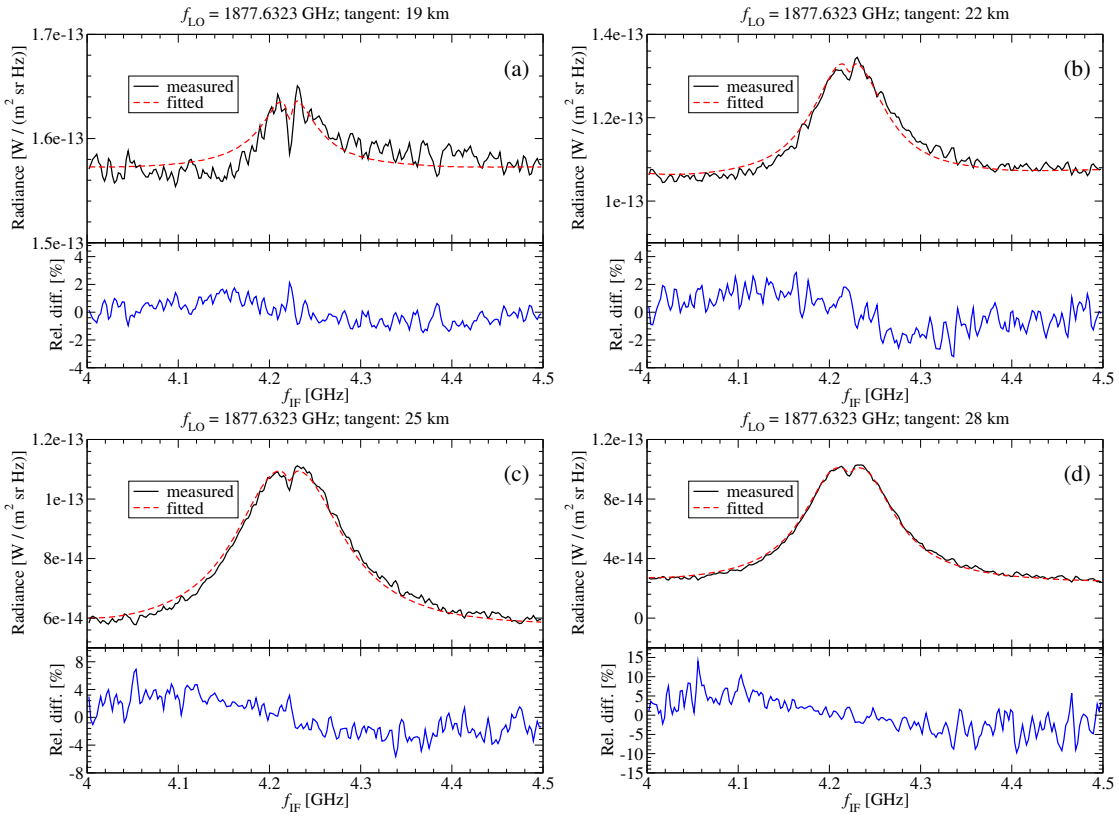

Figure 6.13: Comparison of the measured and modelled TELIS HCl spectra in frequency segment 1. The spectra are plotted for tangent heights of **(a)** 19, **(b)** 22, **(c)** 25, and **(d)** 28 km. For each tangent height, the relative differences with respect to the measured spectrum are shown in the lower panel. The dedicated measurement identifier is 20044.

6.3.2 Error characterization

First, we briefly discuss how the a priori knowledge affects the performance of the HCl retrieval. In Fig. 6.15, the retrieved profiles of HCl using a priori profiles of the standard AFGL subarctic winter model and a MLS profile climatology are depicted. Besides, the retrieval using a zero a priori profile is plotted. It can be seen that the retrieval is dominated by regularization with the a priori information below 20 km where the signal is attenuated by the continuum absorption. Despite the fact that the most significant difference is found in the lower stratosphere, the three retrievals at higher altitudes rely on the measurement itself and reach a satisfying agreement as the smoothing effect is merely limited.

In Fig. 6.16, an example of the estimated retrieval error budget for the HCl retrieval is shown. Between 22 and 32.5 km, the total retrieval error reaches 0.3 ppbv and exceeds 0.5 ppbv below 22 km. All errors steeply increase for altitudes up to 20 km and from 30 km upwards. One explanation for larger errors around the lowest tangent height

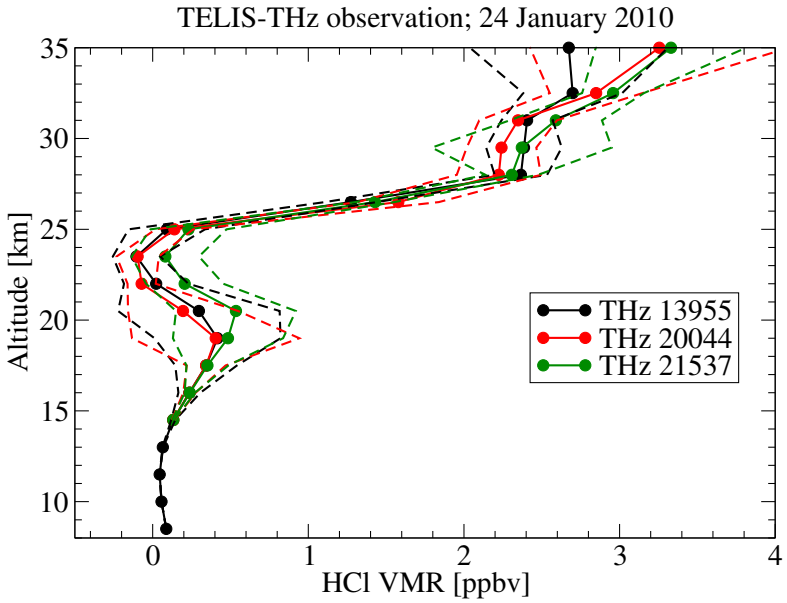

Figure 6.14: HCl profiles retrieved from the TELIS balloon flight data on 24 January 2010. The solid black, red, green lines correspond to the HCl profiles obtained from measurements 13955, 20044, and 21537, respectively. The dashed lines refer to the overall accuracy of these three HCl profiles.

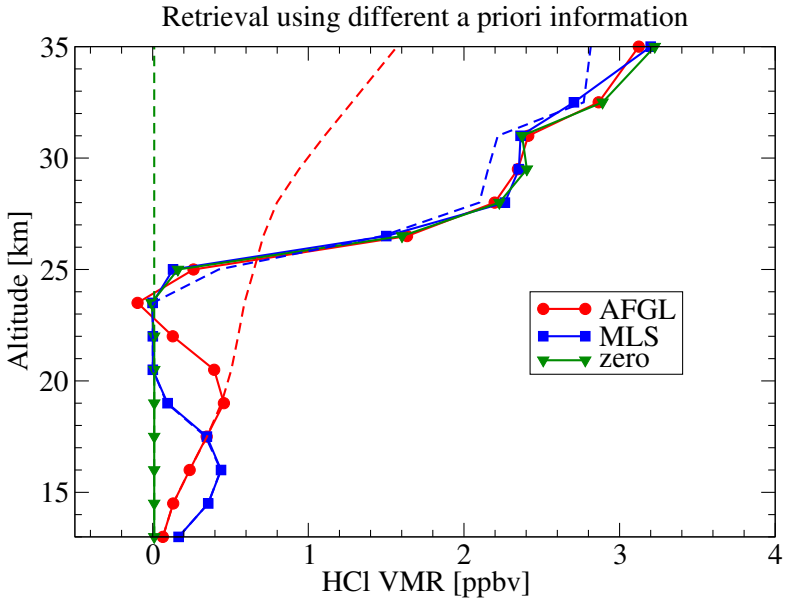

Figure 6.15: Comparison of HCl retrieval using different a priori information. The a priori profiles are illustrated as the dashed lines.

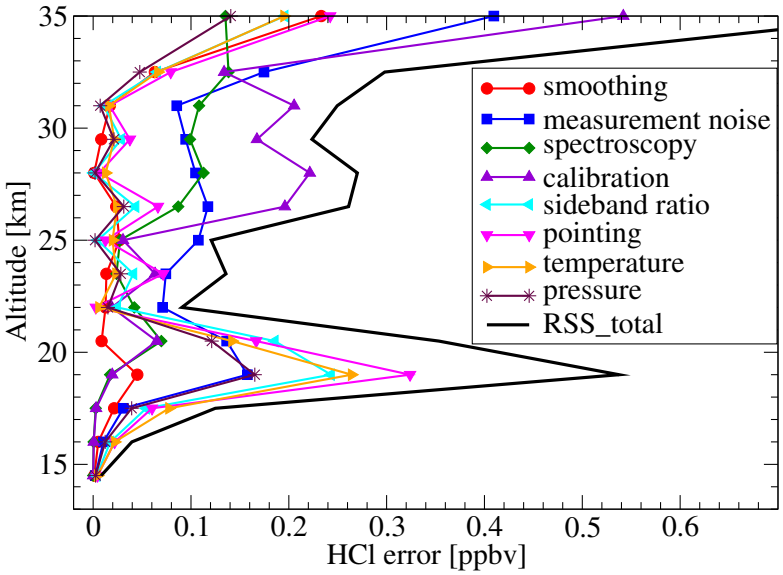

Figure 6.16: Smoothing, noise, and model parameters errors for the HCl retrieval. The estimates correspond to TELIS's far infrared measurement 20044 during the 2010 flight.

(16 km) is that the nominal abundances (< 1 ppbv) below 20 km are discovered and a reasonable retrieval below this altitude is difficult.

At higher altitudes (below the float altitude of approximately 34 km), maximum errors of 0.18 and 0.22 ppbv arise from the uncertainties in the calibration process and the spectroscopic parameters, respectively. As the nonlinearity effect has the highest impact on altitude levels with very large concentrations, this explains why the calibration error is dominant in this altitude range.

The noise error is found to be larger than the other error components above 20 km, which is not true for the HCl retrieval from the submillimeter limb spectra by TELIS (≈ 0.01 ppbv) [de Lange et al., 2012]. The reason is that due to different receiver characteristics, particularly low in-flight measurement noise was observed in the HCl microwindow of the 480–650 GHz channel in contrast to that in the 1.8 THz channel.

6.3.3 Internal comparison

Before performing comparisons with other instruments, a set of internal comparisons in two far infrared and submillimeter channels of TELIS have been performed. The 480–650 GHz channel measures both $H^{37}Cl$ and $H^{35}Cl$ rotational transitions near 625.0 and 625.9 GHz, respectively, and the first retrieval results by SRON's Level-2 team have been validated by a comparison with the MLS daytime profile. The overall accuracy of the HCl retrievals with respect to the submillimeter data is 0.05–0.4 ppbv [de Lange et al., 2012].

Figures 6.17 and 6.18 illustrate two sets of HCl vertical profiles derived from far

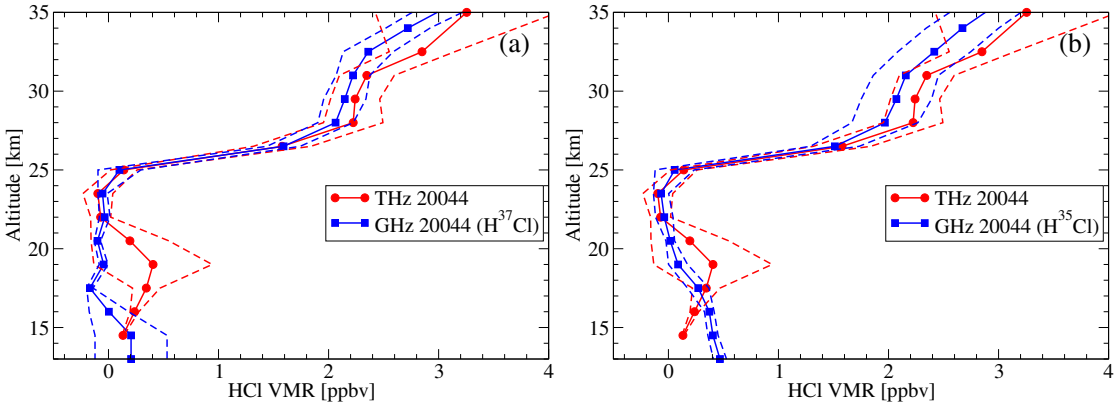

Figure 6.17: Comparison of HCl retrievals in the far infrared (1.8 THz) and submillimeter (480–650 GHz) channels. The measurements have the same identifier (20044) and the submillimeter results are determined from two different isotopes, i.e. **(a)** $H^{37}Cl$ and **(b)** $H^{35}Cl$.

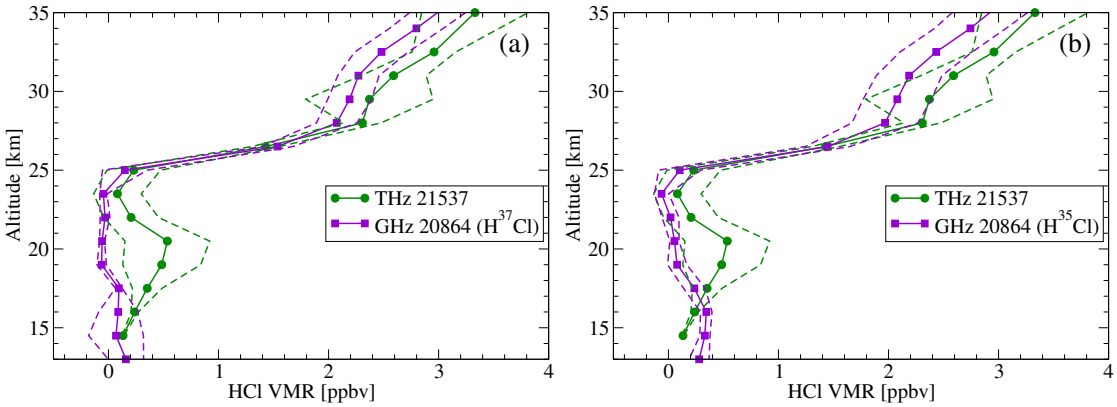

Figure 6.18: Comparison of HCl retrievals in the far infrared (1.8 THz) and submillimeter (480–650 GHz) channels. The far infrared measurement identifier is 21537, while the submillimeter measurement identifier is 20864. The submillimeter results are determined from two different isotopes, i.e. **(a)** $H^{37}Cl$ and **(b)** $H^{35}Cl$.

infrared and the submillimeter data, respectively. In these figures, the HCl profiles derived from the $H^{37}Cl$ transition in the 1.8 THz channel are compared with those from both $H^{37}Cl$ and $H^{35}Cl$ transitions in the 480–650 GHz channel. In Fig. 6.17, measurement 20044 is considered. This measurement can be regarded as an ideal limb sequence, since both frequency channels observed HCl at the same time. Obvious discrepancies due to regularization occur in the altitude range between 16 and 21 km, while an agreement over the altitude range above 23 km reveals the consistency of retrieval products in both channels. A far infrared measurement (21537) and a submillimeter measurement (20864) are selected for the second internal comparison. Similar discrepancies are found at lower altitudes and the far infrared profile is higher than the submillimeter profile at higher

Table 6.7: A combination of far infrared and submillimeter limb spectra of the TELIS instrument used for a multi-channel retrieval of HCl. The systematic pointing biases with respect to both frequency microwindows are taken into account. Note that the THz-channel detects the $H^{37}Cl$ transition only, while the GHz-channel covers both isotopes of HCl.

Parameter	Description	
Measurement	20044	
Channel	THz	GHz
LO frequency	1877.63 GHz	619.10 GHz
Intermediate frequency	4–6 GHz	5–7 GHz
Systematic pointing bias	3.4 arcmin	−5.4 arcmin

altitudes.

HCl is one of the common molecules which can be simultaneously detected in both frequency channels of the TELIS instrument. This feature provides a chance for deriving the concentration profile by a joint-processing of two different spectral windows. In Sect. 5.3, we have succeeded in gaining more information from the measurement by analyzing the synthetic multi-channel data concurrently. For this purpose, we consider measurement 20044 on 24 January 2010 as both far infrared and submillimeter channels measured HCl. Table 6.7 lists the frequency configurations of measurement 20044 in the 1.8 THz channel and the 480–650 GHz channel, respectively.

Figure 6.19 shows comparison results of HCl from two $H^{37}Cl$ transitions which are located in the far infrared and submillimeter spectral range, respectively. For reference, the HCl profiles obtained from single-channel data are included. The retrieval corresponding to a combination of the far infrared and submillimeter microwindows agree well with the GHz-channel profile at lower altitudes, whereas it tends to get closer to the THz-channel profile above 30 km.

The plotted averaging kernels for the multi-channel fitting indicate a better vertical resolution than those for the THz-channel in the lower stratosphere, i.e. between 16 and 19 km. Thus, in this altitude range, the information comes from the GHz-channel measurement. Furthermore, a gain in the degree of freedom for the signal is attained by the multi-channel fitting, showing that the sensitivity of HCl at lower altitudes in the GHz microwindow is superior to that in the THz microwindow.

6.3.4 External comparison

SMILES measured the same HCl transitions as the TELIS 480–650 GHz channel, and the data were obtained in Band-A ($H^{37}Cl$) and Band-B ($H^{35}Cl$). For specific time and geolocation, the HCl observation acquired in Band-B is taken into account.

Likewise, retrieved MLS HCl profiles come from the same two HCl emission lines measured by the 640 GHz radiometer. Froidevaux et al. [2008b] compared MLS v2.2 HCl data with satellite, balloon, and aircraft data, and characterized the vertical res-

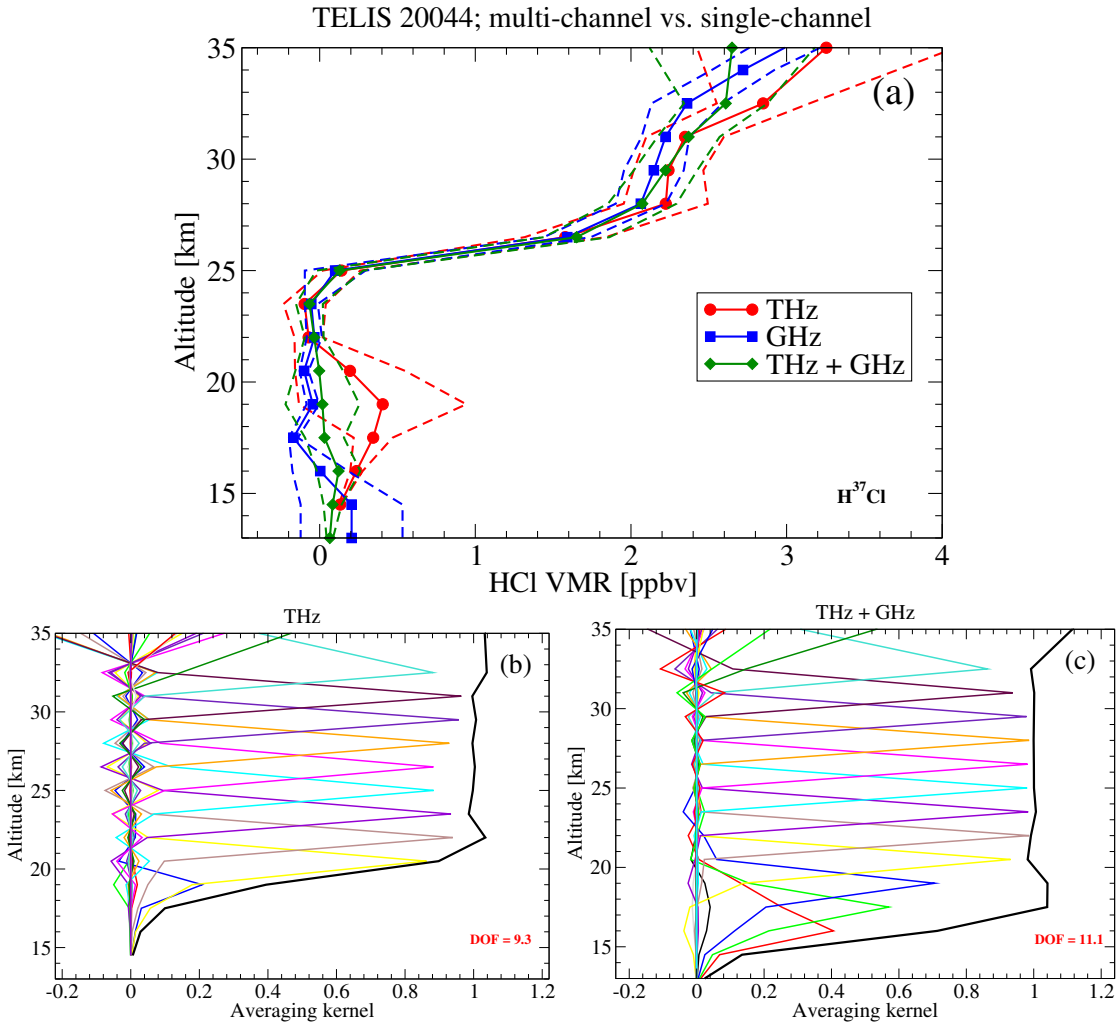

Figure 6.19: Retrieval result of HCl by using single- and multi-channel data observed in the far infrared and submillimter spectral domains of the TELIS instrument. Panel **(a)**: intercomparison of retrieval result of HCl for single- and multi-channel data. The HCl profile derived from GHz-channel data is included for reference. Panel **(b)**: averaging kernels for single-channel (THz) data. Panel **(c)**: averaging kernels for multi-channel data.

olution and the retrieval errors. The retrieval errors are 0.2–0.7 ppbv (v3.3) and 0.1–0.25 ppbv (v2.2), and the vertical resolution is about 2.7 to 3 km in the lower and middle stratosphere.

A comparison between HCl concentration profiles retrieved in the TELIS 1.8 THz channel and from spaceborne limb sounders SMILES and MLS on 24 January 2010 is shown in Fig. 6.20. For the 1.8 THz channel, there were two observations (20044 and 21537) that can be considered for this comparison. In the case of SMILES profiles, measurements 761 and 762 are the best candidates for comparison due to the close

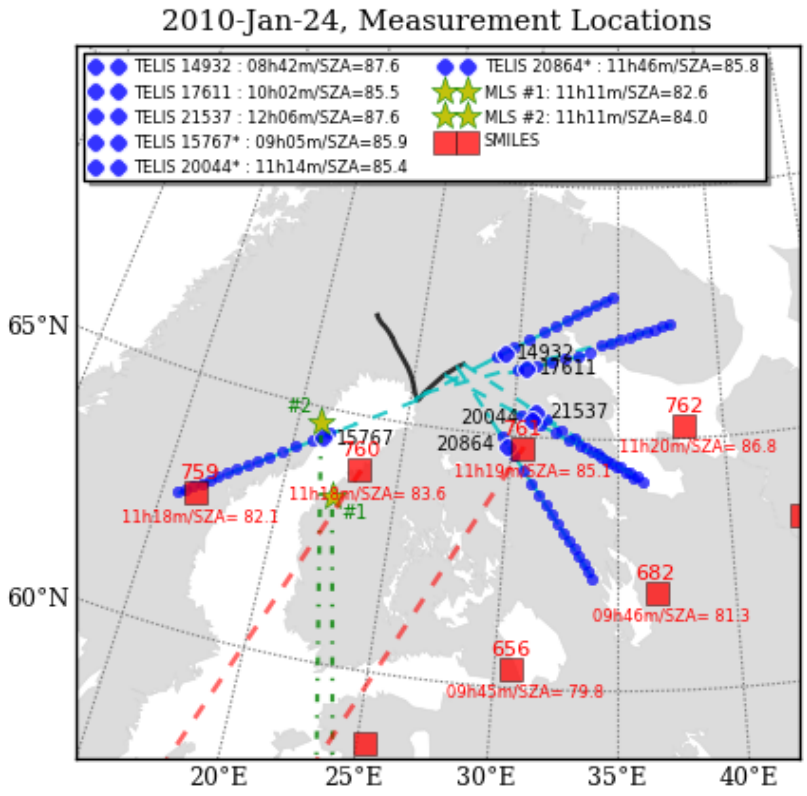

Figure 6.20: Locations of selected TELIS, SMILES, and MLS measurements on 24 January 2010. For each measurement, corresponding local time and solar zenith angle (SZA) are displayed in the legend. Blue circles represent the trajectory of the TELIS measurements, and the dashed blue lines indicate the direction of observational line-of-sight towards every tangent point. For the displayed TELIS measurements, identifiers 20044 and 21537 refer to the far infrared observations received in the 1.8 THz channel. Red squares represent the measurement locations of SMILES, while dashed red lines indicate the tangent point when the instrument pointed to a tangent height of 23 km. Yellow stars represent two MLS observations, while dashed green lines indicating the corresponding line-of-sights.

geolocation and solar zenith angles. In addition, two MLS measurements indicated by stars show very good coincidence with TELIS observation 20044.

The comparison of the HCl profiles retrieved from TELIS and SMILES is shown in Fig. 6.21. The original profiles corresponding to the two limb sounders are plotted in the left panel (a). It can be noticed that the vertical resolution of TELIS is better than that of SMILES over the plotted altitude range and a proper comparison should takes this fact into account. The smoothed TELIS profiles convolved with the averaging kernels for the SMILES v2.1.5 data products are compared against the original profiles

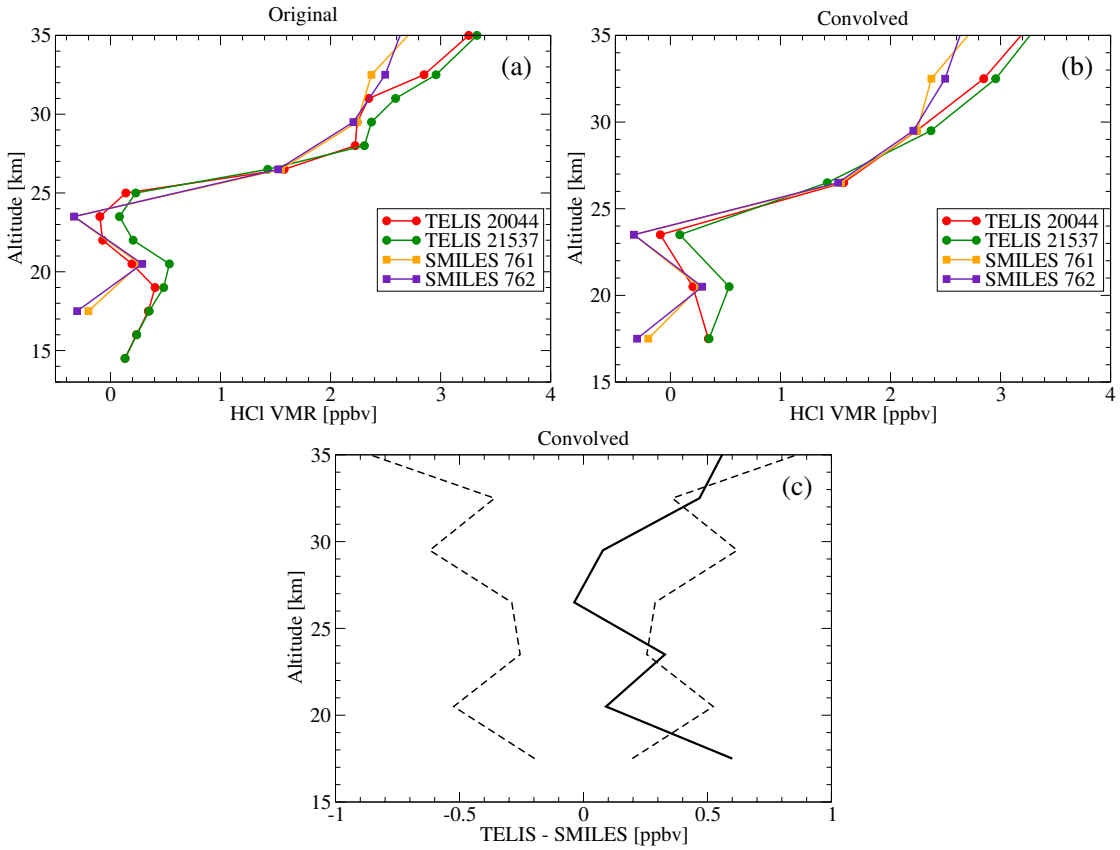

Figure 6.21: Comparison of HCl retrievals from TELIS and SMILES on 24 January 2010. The geolocation information and solar zenith angles for SMILES data are: 64.3° N, 30.6° E for SMILES data 761 and 64.8° N, 38.2° E for SMILES data 762. The time difference of the SMILES and TELIS measurements was about 0.5 h. Panel **(a)**: comparison of original profiles from both instruments. Panel **(b)**: comparison of convolved profiles with the averaging kernels corresponding to the SMILES retrieval. Panel **(c)**: the difference between TELIS and SMILES HCl products. The dashed black lines represent the RSS of the smoothing, noise, and model parameters errors of both particular profiles.

of SMILES in the right panel (b). Both profiles at six altitude levels below the height of TELIS are plotted. Note that the lowest altitude point for the SMILES retrieval is 17.5 km where the convolved comparison starts. The large differences at higher altitudes between both products are mainly due to the calibration and spectroscopic parameters errors. In Fig. 6.21c, the difference between the TELIS and SMILES profiles is shown together with the RSS of the smoothing, noise, and model parameters errors of both profiles. The TELIS and SMILES products agree well within the accuracy domain, excepting the small disagreements at 17.5, 23.5, and 32.5 km.

Figure 6.22 shows the comparison between the MLS and TELIS profiles. Within the plotted overall accuracy of the TELIS profile, the HCl profiles agree over almost the

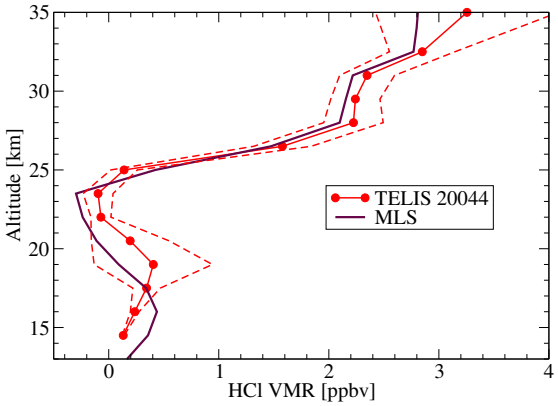

Figure 6.22: Comparison of HCl retrievals from TELIS and MLS on 24 January 2010. The lowest tangent height of TELIS is 16 km and the retrieval results below this altitude have little physical meaning. The solar zenith angles of the MLS and TELIS measurements are 84.0° and 85.4°, respectively (see Fig. 6.20). The time difference of the TELIS and MLS measurements was about 0.1 h. The MLS profile is linearly interpolated onto the retrieval grid of the TELIS retrieval by taking the averaging kernel into account.

entire altitude range between 15 and 35 km. Only around 23 km and below 16 km, the MLS profile is outside the accuracy domain.

As it can be seen in Figs. 6.21 and 6.22, the full depletion of HCl in the lower stratosphere due to strong chlorine activation inside the Northern Hemisphere polar vortex was seen by both spaceborne instruments, . The profiles derived in the TELIS 1.8 THz channel also successfully capture this depletion and show an overall agreement with the profiles from SMILES and MLS.

6.4 CO Retrieval

Carbon monoxide (CO) is a long-lived tracer in connection with atmospheric transport and affects the ability of the atmosphere to cleanse itself of many other polluting gases. Winter polar descent in the vortex brings CO-rich air downward into the stratosphere [Allen et al., 1999]. CO is the major sink of OH in most of the troposphere and the lower stratosphere [Jacob, 1999]. Moreover, as there is no OH in the stratosphere and lower mesosphere to destroy CO during the polar night of the wintertime, CO is an ideal tracer of vortex dynamics until springtime. Due to a photochemical lifetime in the troposphere, the CO data inside the polar vortex measured by the TELIS instrument helps to understand regional-scale transport of pollution [Filipiak et al., 2005].

6.4.1 Observations in the polar winters 2010–2011

TELIS probed CO at the transition frequency of 1841.36 GHz (61.42 cm^{-1}) and in this study, the dedicated spectra recorded on 24 January 2010 and 31 March 2011 are an-

Table 6.8: Setup for the CO retrieval from the TELIS far infrared data. Information on the used spectral range and the state vector parameters is listed.

Parameter	Description
f_{IF} range	4.5–5 GHz
Target species	CO
Retrieved interfering species	HOCl
Auxiliary parameter	"greybody", baseline offset

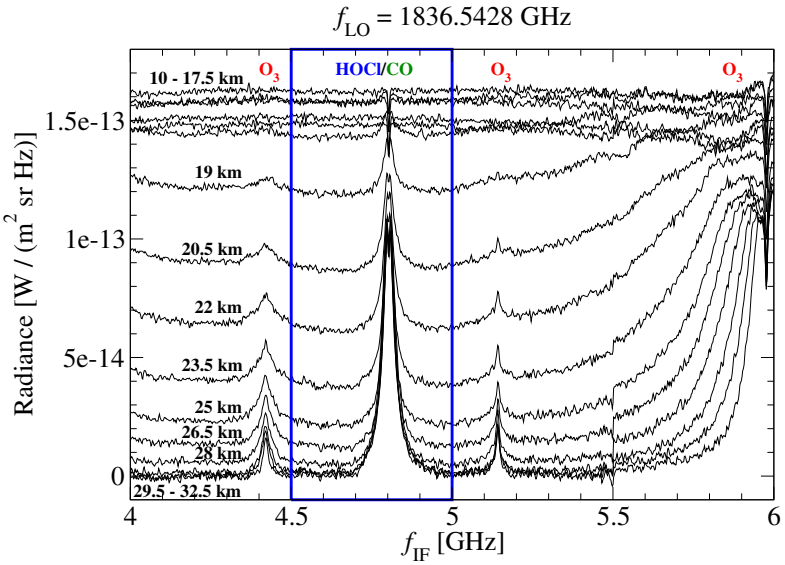

Figure 6.23: A sequence of limb spectra in the CO microwindow measured by the TELIS's 1.8 THz channel during the 2010 flight. The limb sequence observing a CO line and covering tangent heights between 10 and 32.5 km in steps of 1.5 km, is illustrated as a function of the intermediate frequency f_{IF}. The spectral segment of 500 MHz selected for CO retrieval is indicated by a blue rectangular box. The dedicated measurement identifier is 20864.

alyzed. During the 2010 flight, three radiance measurements were done in this CO microwindow at early morning and local noon, respectively. During the 2011 flight, CO was only measured twice before the local sunrise.

As Fig. 6.23 shows, the frequency segment of 4.5–5 GHz contains a strong CO feature that comes from the upper sideband (see Fig. A.1). As a weak HOCl feature resides in the left wing of the CO line, which is also retrieved as a part of the unknowns in the state vector.

A comparison of observed TELIS spectra and modelled spectra (after convergence) in the second frequency segment is shown in Fig. 6.24. At the lower tangent height (17.5 km), the largest difference (5 %) occurs around the line center. The largest differences for the other three tangent heights occur at the intermediate frequency of 4.7 GHz.

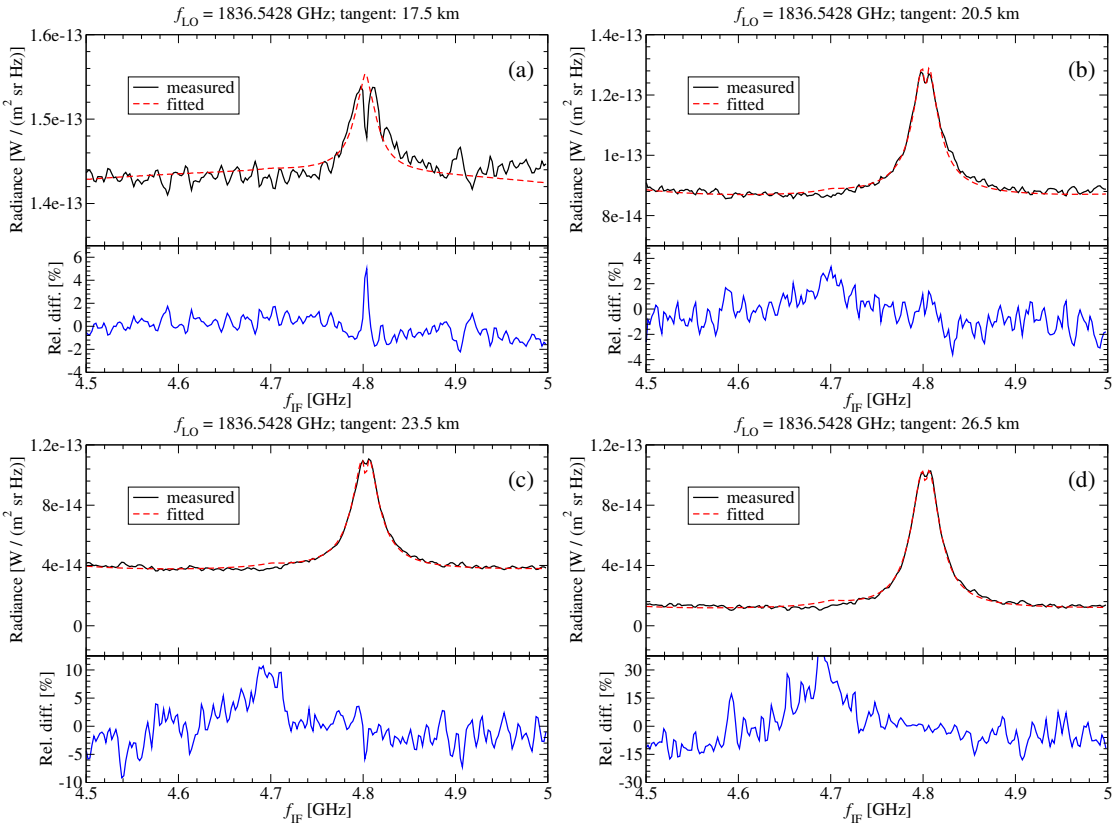

Figure 6.24: Comparison of measured and modelled TELIS CO spectra in frequency segment 2. The spectra are plotted for tangent heights of **(a)** 17.5, **(b)** 20.5, **(c)** 22.5, and **(d)** 26.5 km. The dedicated measurement identifier is 20864.

Figure 6.25 depicts the CO profiles derived from TELIS's far infrared measurements on 24 January 2010. TELIS measurements 7960 and 8092 were taken before the sunrise, while measurement 20864 was observed around local noon. Both earlier measurements observed the lowest tangent point at 16 km as compared to 10 km for the noon measurement. A gradual decrease below 30 km is found and all three profiles capture the peak value at 32.5 km.

A CO profile retrieved from the far infrared measurement 12909 on 31 March 2011 is shown in Fig. 6.26. As stated previously, there are two available measurements before the local sunrise. However, measurement 3756 was recorded only 0.5 h after the balloon was launched and hence the observer altitude was below 20 km. The information was limited, and here, only the retrieval from measurement 12909 was performed. A strong depletion of CO around 15 km was detected and the peak value is at about 25 km. Negative VMR values are unphysical and are produced by the numerical regularization scheme without bound-constraints on variables.

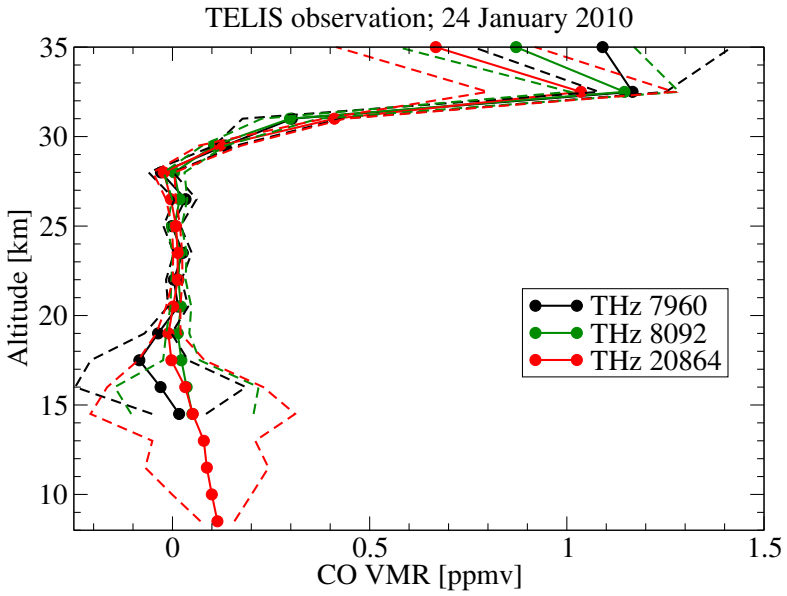

Figure 6.25: CO profiles retrieved from the TELIS balloon flight data on 24 January 2010. The solid black, green, and red lines correspond to the CO profiles obtained from measurements 7960, 8092, and 20864, respectively. The dashed lines refer to the overall accuracy of these three CO profiles.

Figure 6.27 shows the corresponding averaging kernels for the CO retrievals from two far infrared measurements during the flights in 2010 and 2011. The vertical resolution is estimated to be about 1.8–3 km over the altitude range between 16 and 32.5 km where the associated measurement response is larger than 0.8.

6.4.2 Error characterization

In Fig. 6.28, we display the error budget of the CO retrieval from measurement 20864 during the 2010 flight. At lower altitudes, the uncertainties in the temperature and pointing information are the two major error sources, with the peak appearing near 15 km. The measurement noise dominates the error budget between 17.5 and 26.5 km, although the propagated noise error is only a bit larger than others. At higher altitudes, the spectroscopic parameters turn out to be the most important error source. The total retrieval error is of about 0.01–0.25 ppmv.

6.4.3 Comparison with MLS data

Furthermore, we compare the TELIS CO profile taken from measurement 20864 against the coincident MLS profile. The standard MLS v3.3 CO product is retrieved from the rotational transition at 230.538 GHz with a vertical resolution of about 4 km [Filipiak et al., 2005]. The MLS profiles have been successfully validated by Pumphrey et al. [2007]; Livesey et al. [2008].

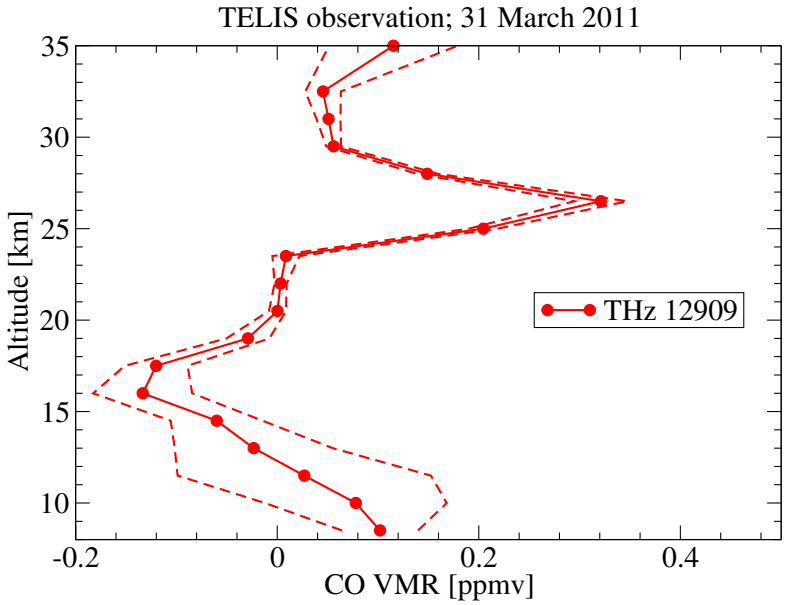

Figure 6.26: Same as Fig. 6.25, but for the data measured on 31 March 2011. The solid red line corresponds to the CO profile obtained from measurement 12909. The dashed line refer to the overall accuracy of this CO profile.

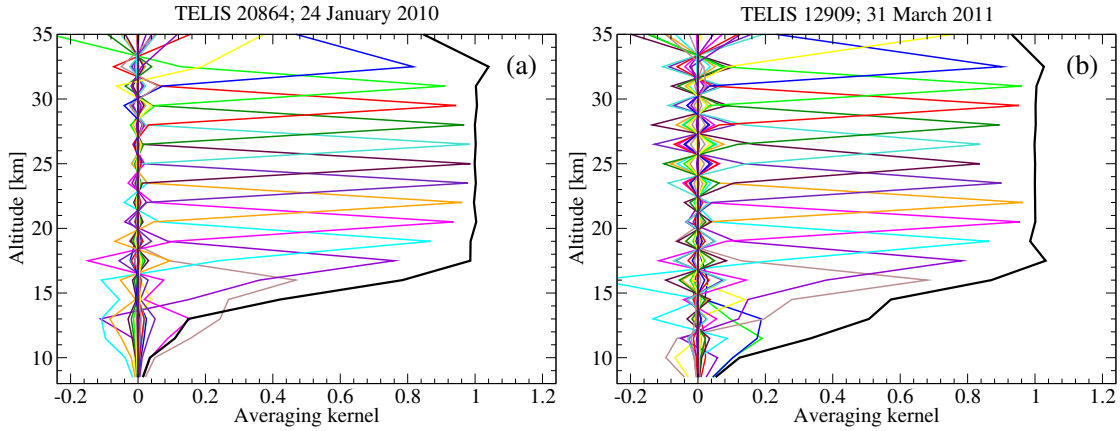

Figure 6.27: Averaging kernels for the CO retrievals from TELIS far infrared measurements 20864 (24 January 2010) and 12909 (31 March 2011), respectively.

In this case, a clear difference in the vertical resolution between TELIS and MLS retrieved CO profiles can be identified. Consequently, a convolution of the TELIS profile with the averaging kernel matrix for the MLS retrieval is necessary for obtaining reasonable comparison.

In Fig. 6.29, the CO profile retrieved from measurement 20864 is compared against the MLS profile due to the small time difference (approximately 0.5 h) and close geolo-

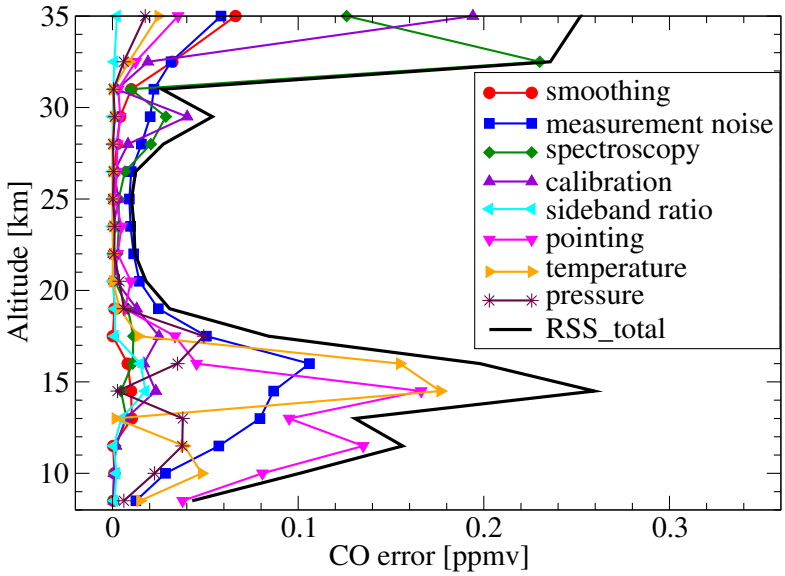

Figure 6.28: Smoothing, noise, and model parameters errors for the CO retrieval. The estimates correspond to TELIS's far infrared measurement 20864 during the 2010 flight.

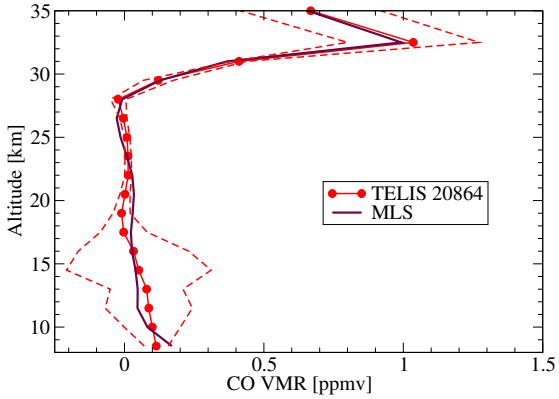

Figure 6.29: Comparison of CO retrievals from TELIS and MLS on 24 January 2010. The lowest tangent height of TELIS is 10 km and the retrieval results below this altitude have little physical meaning. The solar zenith angles of the MLS and TELIS data are 84.0° and 85.8°, respectively (see also Fig. 6.20). The time difference of the TELIS and MLS measurements was less than 0.5 h. The MLS profile is linearly interpolated onto the retrieval grid of the TELIS retrieval by taking the averaging kernel into account.

cation. The difference in the solar zenith angle within 2° ensures that both instruments observed the same air mass around local noon on 24 January 2010. An excellent agreement can be seen in both profiles and the peak at 32.5 km monitored by TELIS was also successfully captured by the MLS instrument. The MLS profile overall falls within the accuracy domain of the TELIS profile and both profiles show virtually identical shape.

Table 6.9: Setup for the OH retrieval from the TELIS far infrared data. Note that each microwindow covers an OH transition triplet. Information on the used spectral range and the state vector parameters is listed.

Parameter	Description	
Microwindow	1	2
f_{IF} range	5–5.5 GHz	4–4.5 GHz
Target species	OH	
Retrieved interfering species	O_3	
Auxiliary parameter	"greybody", baseline offset	

6.5 OH Retrieval

OH is one of the most interesting species observed in TELIS far infrared spectra. As already described in Sect. 5.1, the OH transition triplet around 1.8 THz was monitored by the TELIS instrument during the last three balloon campaigns. Based on the sensitivity analysis of the OH retrieval in the 1.8 THz channel given in Chap. 5, it is plausible that the retrieval at lower altitude levels mainly relies on the a priori information, while the retrieval at higher altitudes mainly relies on the information contained in the measurement.

6.5.1 Observations in the polar winters 2009–2010

TELIS makes the regional measurements of OH during both day and night, and this fact gives a chance to inquire into its diurnal variability. In previous flights, TELIS used two OH transition triplets as listed in Table A.1 of Appendix A. Most OH measurements during the 2009 flight observed the 1834.75 GHz transition, and typical radiance spectra are shown in Fig. 6.30. On the left-hand side of the OH line a significant ozone line occurs and induces a sloped background. Therefore, the retrieval of OH is dependent on the morphology and amount of atmospheric ozone. To account for the influence of this ozone line on the OH product, O_3 is included in the retrieval as well. The discontinuities between adjacent frequency segments (as seen in Fig. 6.30) are possibly produced by baseline shifts and the variations in spectral response across the frequency segments. To improve the retrieval, these jumps in the spectra should be ignored.

Figure 6.31 shows a limb sequence of OH spectra taken during the 2010 balloon campaign. Unlike other microwindows from the 2010 flight data, the tangent height step for this OH microwindow was adjusted to 2 km, instead of the nominal 1.5 km. Two measurements covering the OH triplet located around 1837.80 GHz were recorded. As seen in Fig. 6.31, the retrieval analyzed the frequency segment of 4–4.5 GHz where an ozone signature is also present in the wing of the OH triplet. This feature suggests that inaccurate knowledge of O_3 can affect the OH retrieval.

Table 6.9 summarizes the setup for the OH retrieval from the TELIS far infrared

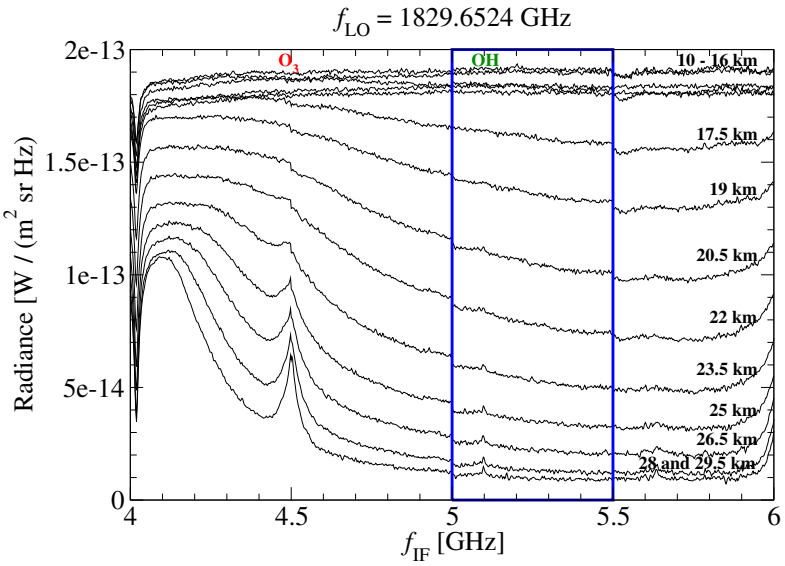

Figure 6.30: A sequence of limb spectra in the OH microwindow measured by the TELIS 1.8 THz channel during the 2009 flight. The limb sequence observing an OH triplet and covering tangent heights between 10 and 29.5 km in steps of 1.5 km, is illustrated as a function of the intermediate frequency f_{IF}. The spectral segment of 500 MHz selected for OH retrieval is indicated by a blue rectangular box. The dedicated measurement identifier is 10890.

limb spectra. In both microwindows, O_3 is the most important contributor to the measurement signal and has to be jointly retrieved with OH. In this case, no regularization is imposed on the O_3 profile as we are interested in the retrieval of OH only.

The 2009 campaign provided observation of OH in the night up to about 35 km. Six measurements with the observer altitude above 25 km were analyzed and are shown in Fig. 6.32. All measurements employed the 1834.75 GHz transition triplet, excluding measurements 13942 and 4757 which employed the 1837.80 GHz triplet. Below the highest tangent point, most profiles capture the peak around 25 km and the abundances increase with time.

The comparison of measured and modelled spectra in frequency segment 3 of the first OH microwindow is shown in Fig. 6.33. The relative differences between both spectra do not change dramatically (±1 %) for the lower tangent heights of 13 and 17.5 km, and are of about ±2 % for the tangent height of 22 km. At the higher tangent height of 26.5 km, the modelled spectrum is roughly ±8 % off the measured spectrum and the largest difference occurs near the intermediate frequency of about 5.5 GHz. The OH feature around the intermediate frequency of approximately 5.1 GHz is not clearly noticeable at lower altitudes, but is becoming stronger with increasing altitude.

The OH observation on 24 January 2010 is displayed in Fig. 6.34. OH measurements 10318 and 16295 were taken before local sunrise and 2 h before local noon, respectively, The major differences in both retrieved profiles are located around 20–25 km and are due to the fact that OH responds very quickly to solar radiation.

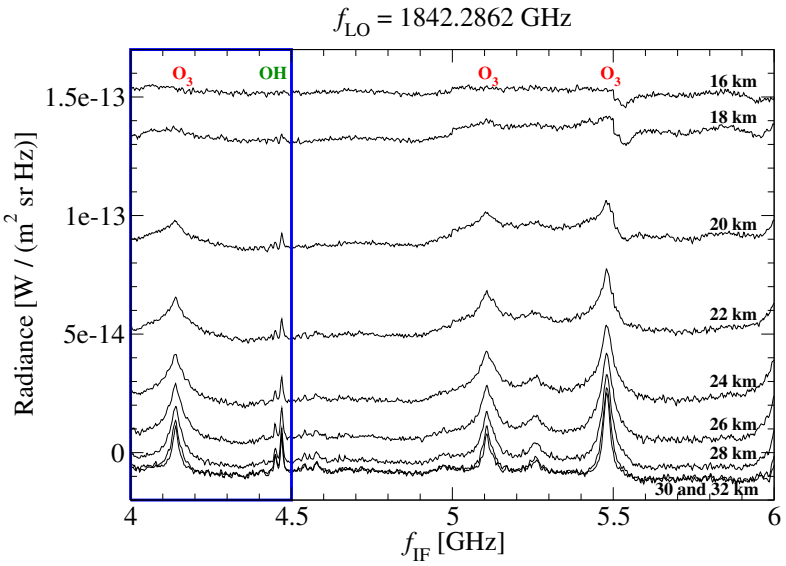

Figure 6.31: A sequence of limb spectra in the OH microwindow measured by the TELIS 1.8 THz channel during the 2010 flight. The limb sequence observing an OH triplet and covering tangent heights between 16 and 32 km in steps of 2 km, is illustrated as a function of the intermediate frequency f_{IF}. The spectral segment of 500 MHz selected for OH retrieval is indicated by a blue rectangular box. The dedicated measurement identifier is 16295.

Figure 6.35 shows a comparison of measured and modelled spectra in frequency segment 1. At the tangent heights of 18 and 22 km, the relative differences in both cases range between $-2\,\%$ and $2\,\%$, and $-4\,\%$ and $4\,\%$, respectively. For the spectra at 26 and 30 km, the relative differences near the OH triplet increase up to $15\,\%$ and $30\,\%$, respectively. The spectra around the OH triplet are overall well fitted, as compared to those around the O_3 line. The differences around the O_3 line center exceeds $50\,\%$ when the spectrum is observed at the highest tangent point.

As can be noticed in Fig. 6.36, the averaging kernels corresponding to both microwindows reveal that the retrieval sensitivity is better at higher altitudes where the abundances are several orders of magnitude larger. An acceptable measurement response is obtained from 20 km upwards, but the fact remains that kernels close to the location of the instrument show strong oscillations and some peaks do not correspond to the tangent heights. A high sensitivity above the instrument and large spectral noise may be the main reasons for this behaviour. In agreement with the averaging kernels, the OH retrieval is acceptable only above 20 km, indicating a low information content in the measurement below this altitude level.

6.5.2 Error characterization

An error budget of the OH retrieval is estimated for these two different far infrared transitions. The results are presented in Figs. 6.37 and 6.38. For both microwindows,

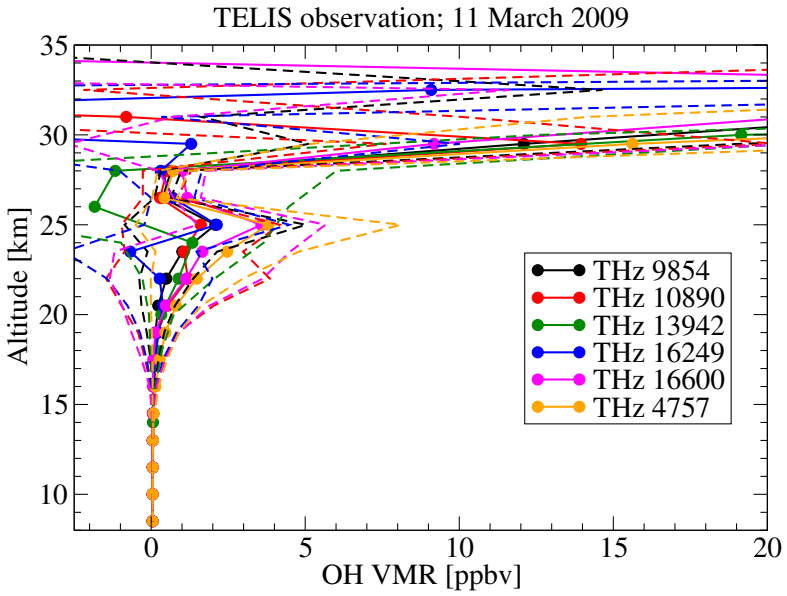

Figure 6.32: OH profiles retrieved from the TELIS balloon flight data on 11 March 2009. The solid black, red, green, blue, magenta, and orange lines correspond to the OH profiles obtained from measurements 9854, 10890, 13942, 16249, 16600, and 4757, respectively. The dashed lines refer to the overall accuracy of all OH profiles.

the overall retrieval error is less than 4 ppbv below 30 km and increases rapidly with the increasing altitude.

In 2009, MIPAS-B only measured the temperature profiles twice and there was an approximately 5 hours gap between both observations. This fact can be problematic for the TELIS retrieval as the a priori temperature profile is taken from the MIPAS-B data.

The pointing information and the measurement noise turn out to be the most noticeable errors around 23 and 25 km, respectively. The spectroscopy accuracy does not cause an obvious effect on the OH retrieval below the observer altitude (approximately 33 km). This result is consistent with the sensitivity analysis regarding the identical transition triplet in Sect. 5.2.1.

In the case of the second OH microwindow, all error components excepting the temperature error, are smaller than 1.5–2 ppbv below 30 km. The model parameter errors due to spectroscopy and calibration stretch from 25 km upwards where OH abundances start to increase. Above 30 km, however, all errors steeply increase.

The most obvious difference between the error budgets estimated for the two OH microwindows is reflected by the contribution of the spectroscopic parameter and calibration errors. For example, the spectroscopy error seems to have a significant contribution above 20 km in the case of the second microwindow. This is mainly due to the strength of the OH triplet and the interfering effect from the O_3 line.

For the first time, OH retrievals from TELIS measurements are presented. Because of the large measurement noise, the precision in the OH retrievals is not highly satisfactory.

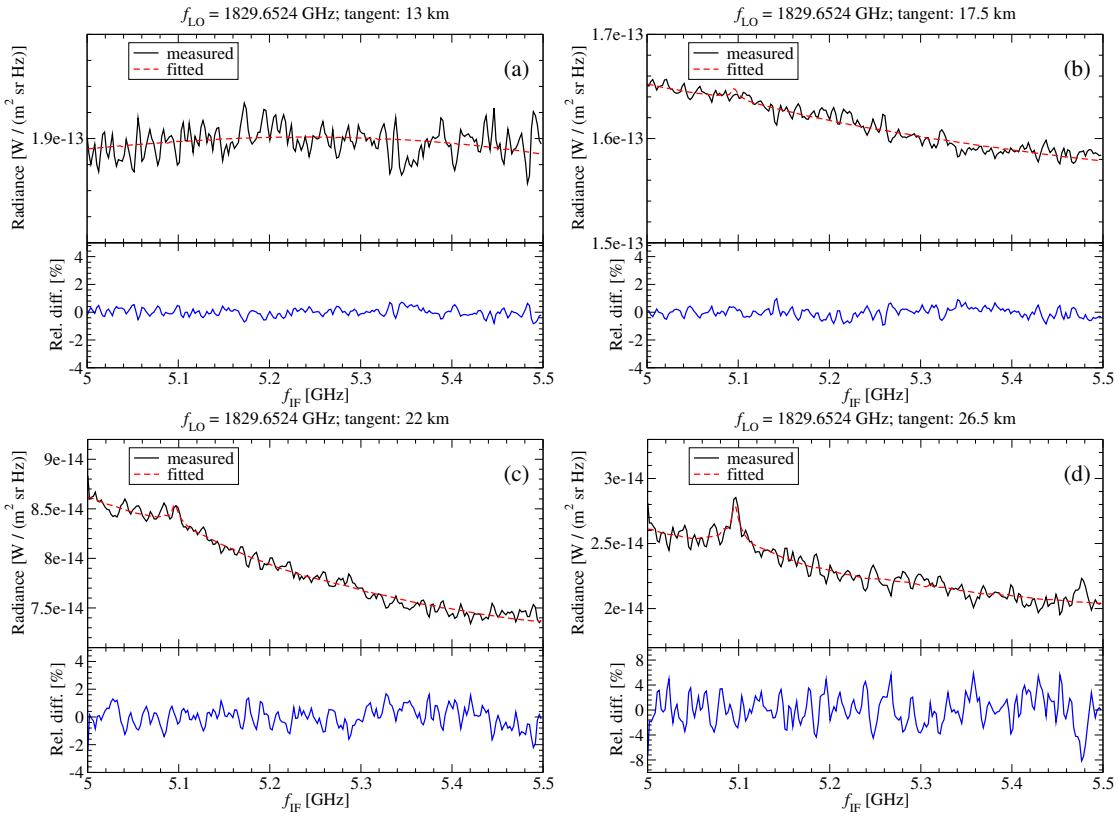

Figure 6.33: Comparison of measured and modelled TELIS OH spectra in frequency segment 3 of the first OH microwindow during the 2009 flight. The spectra are plotted for tangent heights of **(a)** 13, **(b)** 17.5, **(c)** 22, and **(d)** 26.5 km. The dedicated measurement identifier is 10890.

Unfortunately, there is no other instrument measuring the same transitions of OH as TELIS, and only a few far infrared observations are available. The MLS instrument has not been measuring OH regularly, because the THz module on MLS has been in standby mode most of the time after 2009, and a limited number of measurements have been acquired since 2011. Another option is to compare the retrieved profiles with ground-based measurements and sophisticated chemical models. Further investigations into cross-validations of the TELIS OH profiles are ongoing.

6.6 Summary

This chapter has presented retrieval results of atmospheric species from far infrared TELIS spectra, i.e. vertical VMR profiles of O_3, HCl, CO, and OH. A corresponding theoretical error analysis, including the quantification of smoothing, noise, and model parameters errors has been performed. The conclusions of our analysis can be summarized as follows:

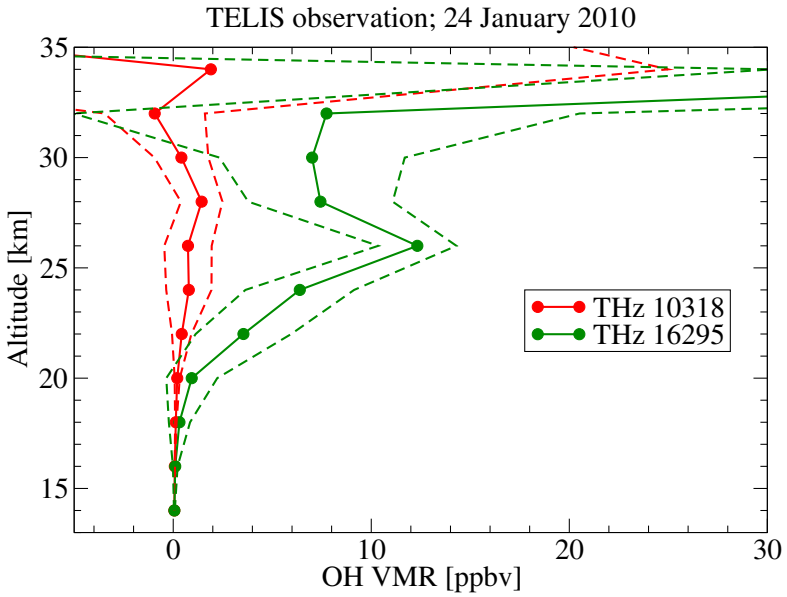

Figure 6.34: OH profiles retrieved from the TELIS balloon flight data on 24 January 2010. The solid red and green lines correspond to the OH profiles obtained from measurements 10318 and 16295, respectively. The dashed lines refer to the overall accuracy of both OH profiles.

- O_3 has been first retrieved by looking into different microwindows containing diverse O_3 signatures. The inversion results obtained in different frequency segments of the same microwindow demonstrate that from a spectroscopic point of view, a consolidated O_3 retrieval is attained by considering not only the pronounced transitions with less interfering contributions from other molecules, but also by selecting that transitions with low sensitivity to the temperature accuracy. Although the TELIS profiles are somewhat overestimated around 23 and 30 km as compared to the MIPAS-B profiles, the shape of both profiles are overall consistent.

  Two sets of comparisons of TELIS profiles against three spaceborne O_3 profiles have been discussed. The first comparison indicates that the TELIS O_3 product is rather comparable with the profiles obtained by SMILES, whereas some discrepancies between the TELIS and MLS profiles between 25 and 28 km show up. In spite of the fact that the chosen SMR ozone data shows some oscillations due to a weaker regularization, the TELIS and SMR profiles for the second comparison agree well.

- HCl observations have been performed from the flight data on 24 January 2010 inside the activated Arctic vortex; these data were utilized for several internal and external comparisons. The absence of HCl was observed at about 23 km, which is consistent with the retrieval results provided by the TELIS submillimeter spectra and other spaceborne observations.

  Compared to the HCl profiles retrieved from the 625.0 and 625.9 GHz transitions by SRON, the profile retrieved from the 1873.40 GHz transition resembles (almost)

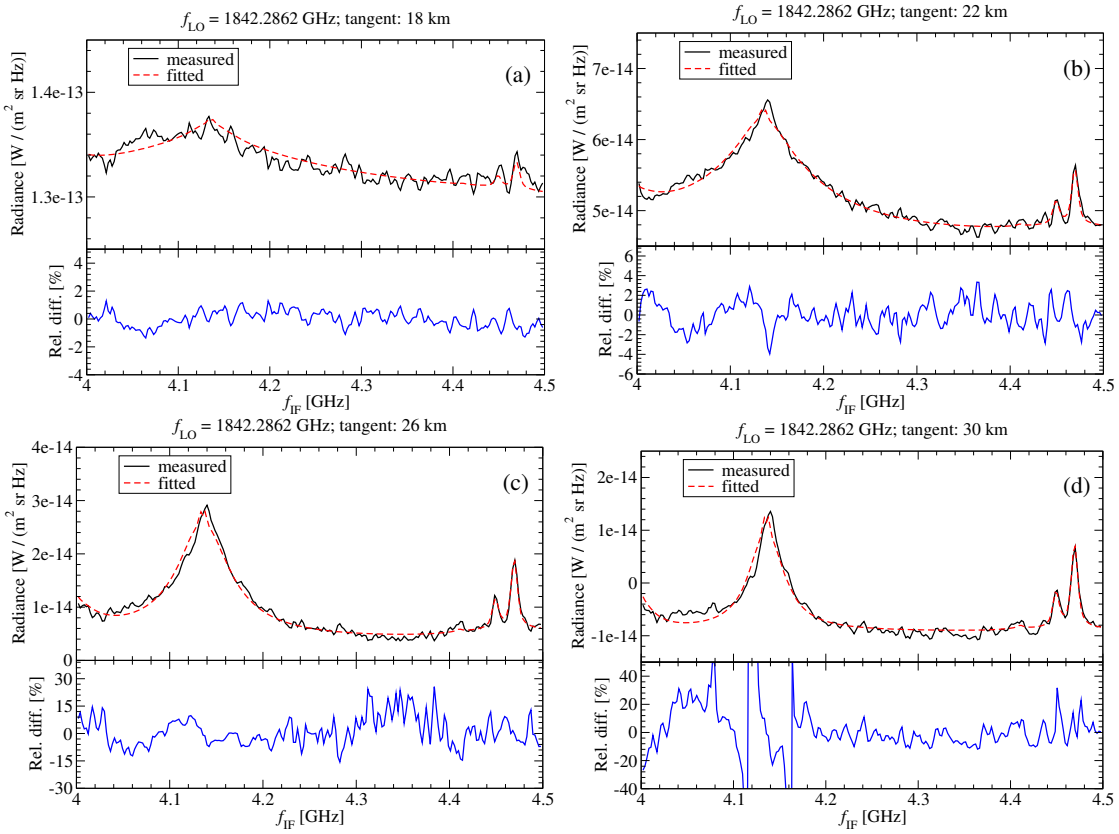

Figure 6.35: Comparison of measured and modelled TELIS OH spectra in frequency segment 1 of the second OH microwindow during the 2010 flight. The spectra are plotted for tangent heights of **(a)** 18, **(b)** 22, **(c)** 26, and **(d)** 30 km. The dedicated measurement identifier is 16295.

the same structure in the stratosphere, albeit with a bit higher concentration above 30 km. One of the main differences between the error characterizations of the two channels arise from the different transition lines in the corresponding ranges. Also, the two TELIS-THz HCl profiles have been compared with the coincident spaceborne observations performed by SMILES and MLS for the local noon measurements on 24 January 2010.

The simultaneous fitting of a combination of far infrared and submillimeter spectra demonstrates a successful attempt on exploiting more useful information from extended frequency ranges. This result has been proven by the improved averaging kernels, particularly at lower altitudes.

- CO observations have been presented for the 2010 and 2011 balloon flights. In 2010, three CO measurements have been analyzed and the concentration amount below 30 km has been found to be very small. The peak at 32.5 km is captured by all three profiles. Only one CO profile retrieved from the 2011 flight data was

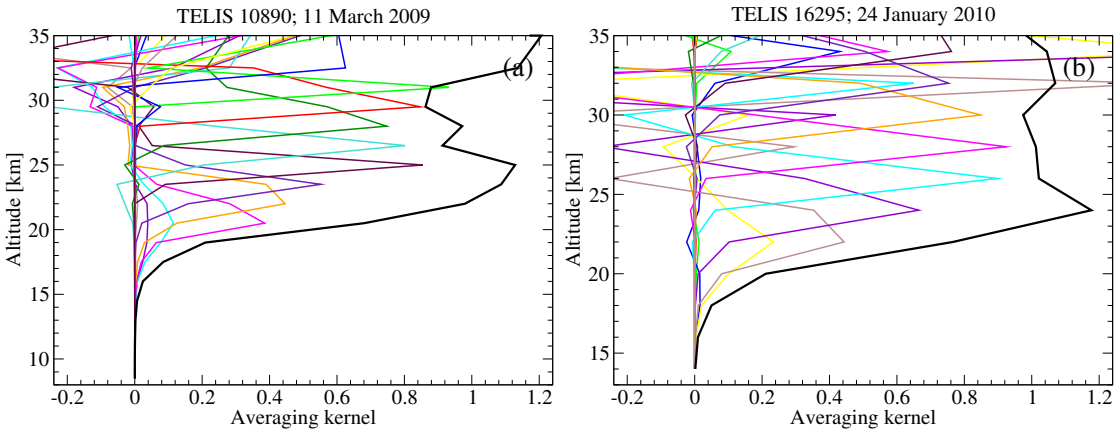

Figure 6.36: Averaging kernels for the OH retrievals from TELIS far infrared measurements **(a)** 10890 and **(b)** 16295, respectively.

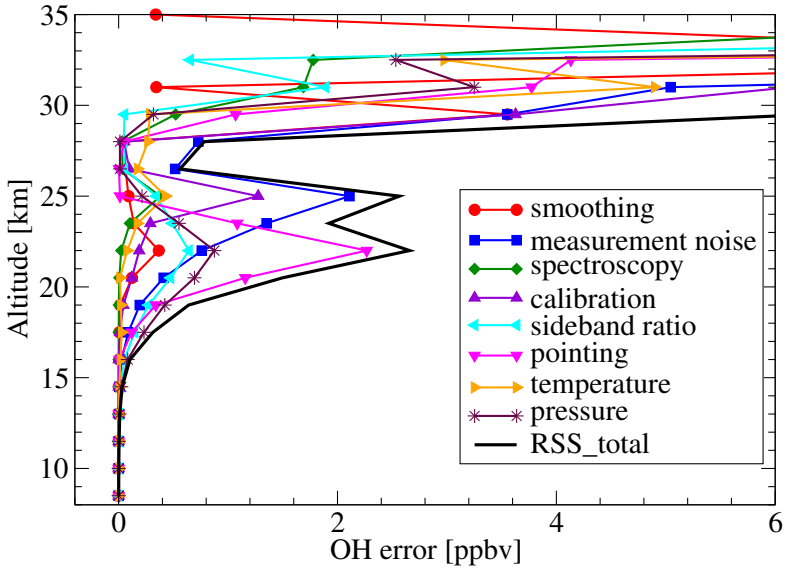

Figure 6.37: Smoothing, noise, and model parameters errors for the OH retrieval in the first microwindow. The estimates correspond to TELIS's far infrared measurement 10890 during the 2009 flight.

useful, and the peak value occurs at 26.5 km. The other measurement was not used for the retrieval as it was recorded when the balloon was unstable. The 2010 CO data are selected for comparisons against MLS observations and both agree very well over the considered altitude range.

- First OH retrievals have been performed for the measurements recorded during the 2009 and 2010 flights. We have retrieved the profiles for both OH transition

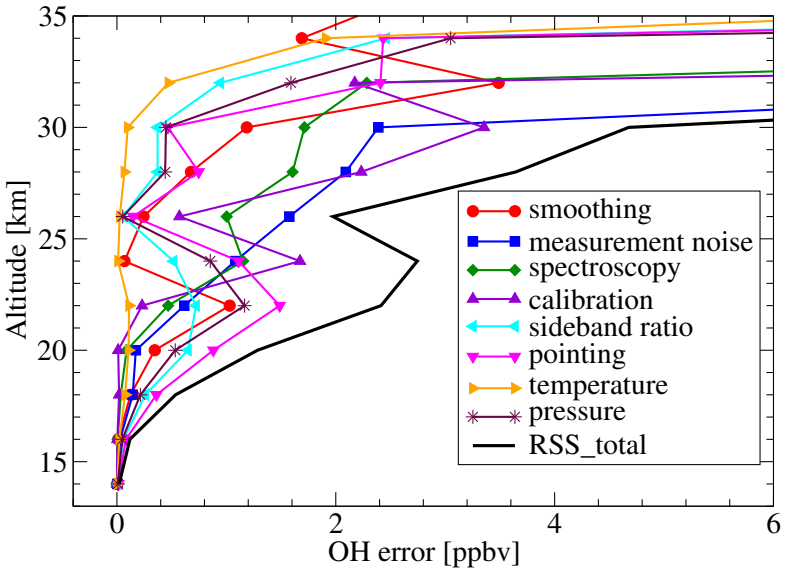

Figure 6.38: Smoothing, noise, and model parameters errors for the OH retrieval in the second microwindow. The estimates correspond to TELIS's far infrared measurement 16295 during the 2010 flight.

triplets and found that the transition around 1837.80 GHz offers a higher sensitivity. The concentration changed gradually for the 2009 retrievals, especially below 25 km. The retrieval error is estimated to be large above 30 km due to the limited information.

- For all these retrievals, the most important model parameter errors at lower altitudes are the pointing and pressure profile, while the errors in the radiometric calibration and spectroscopic parameters are dominant in the middle stratosphere (above 25 km) where the concentration of the target species is high. Among possible error sources for the 1.8 THz channel, the measurement noise appears to be a severe issue despite the fact that the noise errors are not discernible in the 480–650 GHz channel (e.g. approximately 0.01 ppbv for HCl). The smoothing error, in most cases, only affects the retrieval below 20 km since the useful information is limited. In fact, the retrieval performance can still be improved by a better characterization of the instrument, since the current overall accuracy is dominated by the measurement noise and instrument model parameter errors. In most cases (excepting OH), the associated measurement response is 0.8 over the altitude range from about 20 km up to the observer altitude.

These results have demonstrated TELIS's high capability of observing atmospheric minor constituents in the middle atmosphere, i.e. lower and middle stratosphere, and through the comparisons with other limb sounders the retrieval program PILS proves to deliver reliable products from the TELIS data.

Chapter 7

Conclusions

7.1 Final Remarks

This work has given a detailed description of the practical treatment of nonlinear inverse problems in atmospheric remote sensing, placing an emphasis on analysis of limb emission measurements by the balloon-borne instrument TELIS. To convert these measurements into estimates of atmospheric state parameters, we have developed a retrieval code PILS and described its physical and mathematical aspects. In this study, we have focused on the retrieval tasks pertaining to the 1.8 THz channel which delivers the far infrared limb spectra.

TELIS is a cryogenic multi-channel heterodyne instrument that probes the Earth's stratosphere by detecting far infrared and microwave radiation. Together with the MIPAS-B instrument, TELIS offers complementary observations of atmospheric species from one platform.

The forward model developed for high spectral resolution infrared/microwave radiative transfer calculation is based on an extensive and modular line-by-line program GARLIC. The physical fundamentals of the radiative transfer theory and related algorithmic/computational aspects have been presented. A noteworthy feature of the forward model is the use of automatic differentiation techniques that allow for a rapid implementation of exact Jacobians.

The inversion algorithm relies on regularization techniques for nonlinear least squares problems. By employing a variety of Tikhonov-type regularization methods, solutions that are less sensitive to perturbations in the data can be found.

For numerical regularization methods, the selection of an optimal regularization parameter plays a crucial role in determining the retrieval efficiency and product reliability. Tikhonov regularization is a classical method yielding a reasonable solution to the underlying inverse problems. However, its inversion performance highly depends on the selection of the regularization parameter. Alternatively, iterative regularization methods (the iteratively regularized Gauss–Newton and regularizing Levenberg–Marquardt methods) are insensitive to overestimations of the initial value of the regularization parameter. To preserve the iterative solution from an amplification of the noise error, the

discrepancy principle is employed.

For an assessment of PILS's performance, we have carried out a comparison of the forward and inversion algorithms implemented in PILS and in the Level-2 processing code developed by SRON. Both forward modules agree well in terms of evaluations of absorption cross sections, monochromatic spectra, and spectra convolved with the ILS function. The comparison of the HCl retrieval results is also promising despite slight discrepancies at lower altitudes due to a priori effects. However, which forward model and retrieval algorithm gives a best fit to the reality in practice cannot be answered satisfactorily by a pure code comparison. In fact, we should compare the results against other independent "estimates" of the state of the atmosphere.

An error analysis characterizes the solution accuracy and clarifies pragmatically the nature of the errors as much as one might wish. This fact has been explored during a feasibility study of OH retrieval from a synthetic sequence of TELIS spectra. From all error sources, uncertainties in radiometric calibration, pointing, and pressure are estimated to be the most significant.

Retrievals of stratospheric chemical species (O_3, HCl, CO, and OH) from real TELIS spectra have been performed, and their quality has been analyzed in a quantitative manner. In addition to the major model parameter errors, the measurement noise turns out to be a severe error source in the 1.8 THz channel. The errors due to the instrument parameters and pressure dominate in the upper troposphere and lower stratosphere, whereas the errors at higher altitudes are mainly due to the spectroscopic parameters and the calibration. In conjunction with internal and external comparisons, this error analysis serves to improve our understanding of the TELIS measurement characteristics. Furthermore, the inversion diagnostic quantifiers demonstrate that an improved retrieval quality of HCl can be accomplished by a multi-channel fitting which exploits the complementary information provided by two frequency channels. An important lesson learned from the TELIS data analysis in regard to future projects/missions is the importance and necessity of a thorough pre-launch/laboratory characterization of the instrument. In our trace gas retrievals, the pointing accuracy turns out to be critical at lower altitudes, whereas some parameters (calibration, spectral noise) that are not severe at lower altitudes becomes critical at higher altitudes.

The retrieval code PILS has been performing very well on the TELIS data. The quality of the retrievals is in line with pre-launch expectations, and the retrieved profiles are consistent with the profiles retrieved from other limb sounders. These retrievals help us to understand the measurement capabilities of TELIS and to study the chemical interactions occurring in the stratosphere.

7.2 Outlook

In its present version, PILS only deals with 1-D inverse problems arising in the infrared/microwave limb sounding. As in the future, more limb imaging instruments, e.g. GLORIA (**G**imballed **L**imb **O**bserver for **R**adiance **I**maging of the **A**tmosphere) [Friedl-Vallon et al., 2014], will enable to observe trace gas and temperature profiles

in a 3-D atmosphere, one of the future work will focus on 2-D and 3-D tomographic retrievals. Tomographic retrievals have been conducted for MIPAS and MLS, and ultimately require a fast forward model to process many more spectra than is usual for a conventional 1-D retrieval.

Regarding the forward modelling, several features are necessary to be implemented in the future. These include line mixing effects in the microwave spectrum, the consideration of horizontal inhomogeneity effects, an upgrade of the water continuum, and implementations of modern algorithmic approaches (e.g. parallelization of the radiative transfer with respect to the limb sequence and/or frequency by using OpenMP and MPI).

Moreover, a hybrid regularization method based on B-spline approximation and the first retrieval attempt have been presented. In this method, the retrieval quantities are the B-spline expansion coefficients, while the knots characterize the shape of the solution. The inversion performance of the O_3 retrieval proves that this method generates a satisfactory solution with an appropriate order of the B-splines and an optimal knots selection scheme using Newton's method. Our implementation of the B-spline approximation can be regarded as an accurate alternative to the conventional approximation approach, but is more computationally expensive. A further study of lowering the computational burden without sacrificing the accuracy is ongoing.

Regarding the retrieval techniques, the fact remains that the optimal estimation method and Tikhonov regularization are dominant in atmospheric remote sensing. The comparison of the retrieval performance appears to be less meaningful if most retrieval codes use almost the same regularization methods. The drawbacks and errors in these numerical techniques could further propagated into the retrievals. Our goal is to search for new reliable and efficient alternatives including the regularized total least squares method and the maximum entropy regularization method.

Currently, one limitation of the retrieval is encountered that currently the temperature data has to be taken from elsewhere (MIPAS-B, climatology). Recently, temperature derivatives have been implemented in GARLIC. Upgrading PILS similarly would allow to retrieve atmospheric temperature from TELIS spectra, and would offer new opportunities to study atmospheric environment over the polar regions.

This implementation will also be applied to the MTP (**M**icrowave **T**emperature **P**rofiler) instrument [Denning et al., 1989] which is a state-of-the-art passive microwave radiometer that measures thermal emission and absorption from oxygen molecules in the UTLS region of the atmosphere. In particular, characteristic features in the atmospheric profile can determine the radiance spectrum at certain altitudes, while a contribution by the surface to the radiance spectrum has also to be considered in the future work.

In September 2014, a combination of TELIS/MIPAS-B/mini-DOAS has accomplished a new balloon flight over Canada. Based on these latest measurements, a future research will focus on the retrieval of reactive bromine in the stratosphere and on cross-validations with the retrieval of other active satellite instruments as Aura/MLS and ACE-FTS. TELIS's 1.8 THz channel solely performed OH observations and delivered rather good spectra as compared to previous winter flights data. On the other hand,

it is very likely that the retrieval performance can be improved by a consolidated characterization of the instrument. Particular emphasis will be placed on the reduction of the radiometric noise and the consolidation of the nonlinearity error, especially in the 1.8 THz channel.

Appendix A

Supplementary Information on TELIS's Far Infrared Spectra

In this chapter, supplementary information on far infrared limb emission spectra received by the 1.8 THz channel of TELIS is provided.

A.1 Molecular Emission Lines in TELIS's 1.8 THz Channel

Table A.1 summarizes the microwindow specification of the 1.8 THz channel and the major molecular lines that have been monitored in this channel. The line positions are extracted from the HITRAN spectroscopic database (version 2008).

In Table A.2, we list the LO frequencies of all microwindows of the TELIS instrument observed during the three winter balloon flights between 2009 and 2011.. These LO frequencies can only be selected when the microwindow covers the line of the target molecule and the corresponding optimum power is achieved.

A.2 Measurements Overview

In this section, we list all TELIS's far infrared measurements that are analyzed in Chap. 6 during the flights on 11 March 2009 (Table A.3), on 24 January 2010 (Table A.4), and on 31 March 2011 (Table A.5), respectively. The relevant information including the system noise temperature (T_{sys}) and the measuring time (UTC) is given. For the 2010 flight, the geolocation of the observer and the solar zenith angle are listed.

A.3 Main Spectral Features in the 1.8 THz Channel

Figure A.1 shows simulated far infrared emission radiance spectra at a tangent height of 25 km using the HITRAN 2008 spectroscopic database and the AFGL subarctic winter reference model. The considered molecules comprise ozone, water vapor, and the target molecule covered by each dedicated microwindow of TELIS's 1.8 THz channel. For

Table A.1: Molecular far infrared spectral lines measured by the 1.8 THz channel of TELIS. The line positions in units of frequency and wavenumber, and the corresponding sideband with respect to the chosen LO frequency (see Table A.2) are given.

Microwindow	Molecule of interest	Line center (wavenumber)	Sideband
1	OH	1834.75 GHz ($61.20\,cm^{-1}$)	USB
2	OH	1837.80 GHz ($61.30\,cm^{-1}$)	LSB
3	$H_2^{17}O$	1880.75 GHz ($62.74\,cm^{-1}$)	USB
4	$H_2^{18}O$	1815.85 GHz ($60.57\,cm^{-1}$)	LSB
5	$H_2^{19}O$	1840.15 GHz ($61.38\,cm^{-1}$)	USB
7	O_2	1875.04 GHz ($62.54\,cm^{-1}$)	USB
9	CO	1841.36 GHz ($61.42\,cm^{-1}$)	USB
26	HCl	1873.40 GHz ($62.49\,cm^{-1}$)	LSB
27	HDO	1818.50 GHz ($60.66\,cm^{-1}$)	LSB

Table A.2: LO frequencies corresponding to different far infrared microwindows of the TELIS instrument observed during the three winter balloon flights between 2009 and 2011.

Microwindow	LO frequency (2009)	LO frequency (2010)	LO frequency (2011)
1	1829.6524 GHz	1830.1276 GHz	1829.8225 GHz
2	1842.4050 GHz	1842.2862 GHz	1842.4752 GHz
3	1876.0496 GHz	1876.4924 GHz	1876.4168 GHz
4	1820.4821 GHz	1820.2661 GHz	1820.3633 GHz
5	1835.8015 GHz	1835.9419 GHz	1835.6287 GHz
7	1870.4937 GHz	1870.6989 GHz	1870.2669 GHz
9	1836.3916 GHz	1836.5428 GHz	1836.5536 GHz
26	1868.7009 GHz	1877.6323 GHz	1877.8268 GHz
27	1824.0580 GHz	1823.9500 GHz	1824.0375 GHz

microwindows 3, 4, 5, and 27, only the two main species are displayed as the species of interest is one of the water isotopologues. The simulations are performed in accordance with the microwindow configurations (see Table A.1) and the observation geometry for the winter balloon campaign on 24 January 2010. Contributions of individual molecules are indicated by different colors. Separate spectra from both the upper sideband (central panel) and the lower sideband (bottom panel) are also correspondingly plotted. It should be noted that a sideband ratio of 1 (as the ideal scenario) has been assumed for the simulation.

Table A.3: Summary of TELIS's far infrared measurements observed on 11 March 2009. Details about the system noise temperature (T_{sys}) and the measuring time (UTC) are provided. Only the measurements analyzed in Chap. 6 are listed.

Measurement	Microwindow	T_{sys} (K)	Time (UTC)
9854	1	4779.0	01:08–01:15
10890	1	4673.9	01:19–01:40
13942	2	7107.7	02:43–02:57
16249	1	6989.9	03:55–04:07
16600	1	7029.1	04:08–04:13
4757	2	6009.0	05:59–06:13

Table A.4: Summary of TELIS's far infrared measurements observed on 24 January 2010. Details about the system noise temperature (T_{sys}), the geolocation information (latitude, longitude) of the observer, solar zenith angle (SZA), and the measuring time (UTC) are provided. Only the measurements analyzed in Chap. 6 are listed.

Measurement	Microwindow	T_{sys} (K)	Geolocation	SZA	Time (UTC)
7276	27	6468.4	66.9° N, 22.8° E	108.1°	04:23–04:27
7960	9	14531.1	66.9° N, 23.0° E	104.8°	04:42–04:43
8092	9	13533.2	66.8° N, 23.1° E	105.3°	04:45–04:58
10318	2	6672.9	66.5° N, 23.8° E	99.1°	05:59–06:13
12206	27	6130.3	66.1° N, 24.7° E	93.9°	06:59–07:15
13352	7	7738.7	65.8° N, 25.0° E	91.0°	07:38–07:54
13955	26	6532.1	65.7° N, 25.1° E	89.6°	07:57–08:14
16295	2	6847.3	65.5° N, 25.4° E	86.7°	09:15–09:50
20044	26	6538.1	66.1° N, 26.5° E	85.4°	11:06–11:19
20864	9	7647.9	66.2° N, 27.1° E	85.8°	11:33–11:54
21537	26	4629.1	66.3° N, 27.3° E	87.6°	11:56–12:11

Table A.5: Summary of TELIS's far infrared measurements observed on 31 March 2011. Details about the system noise temperature (T_{sys}) and the measuring time (UTC) are provided. Only the measurements analyzed in Chap. 6 are listed. Note that in the case of measurement 3756, the tangent height ranges only up to 17.5 km due to the lower float altitude.

Measurement	Microwindow	T_{sys} (K)	Time (UTC)
3756	9	5781.1	01:01–01:15
12909	9	9860.9	04:41–04:50

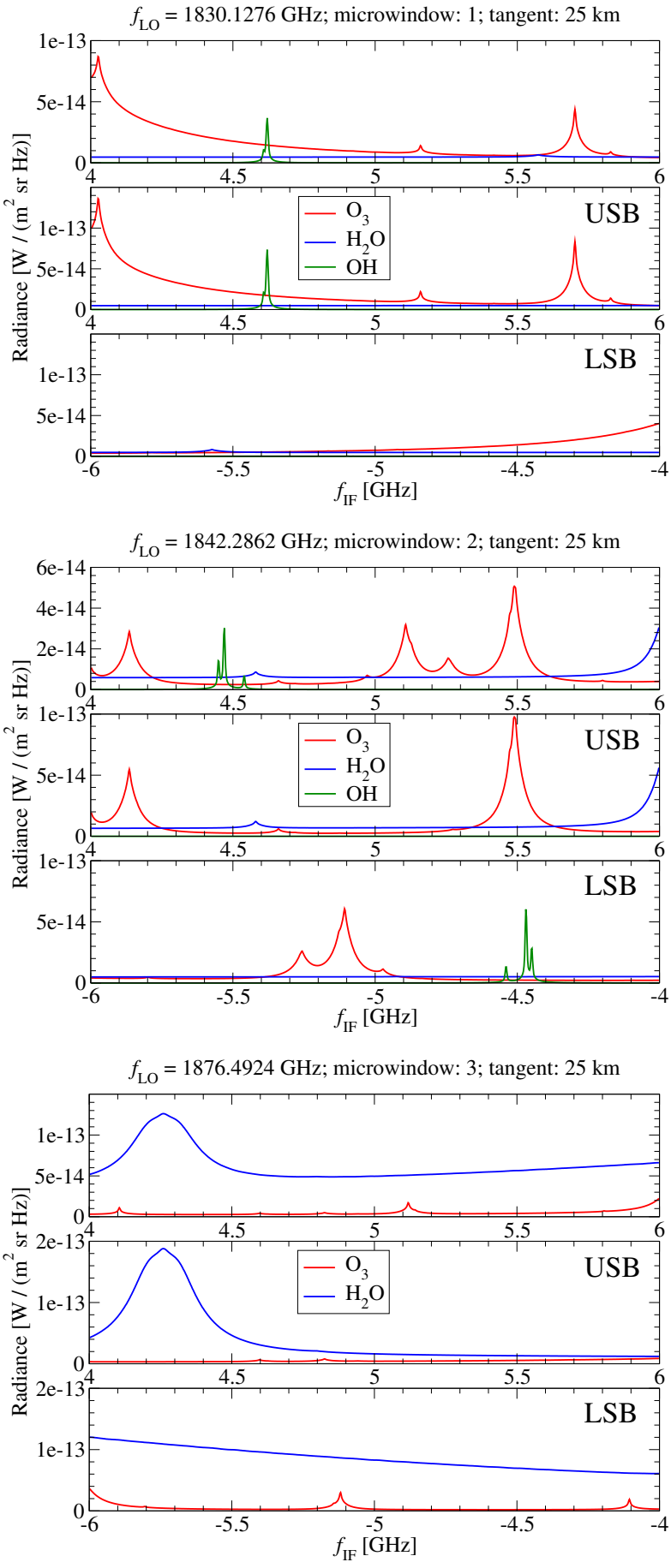

Figure A.1: Simulated far infrared emission radiance spectra for TELIS. The alternating colors refer to the contributions from different molecules. Continued on the next pages.

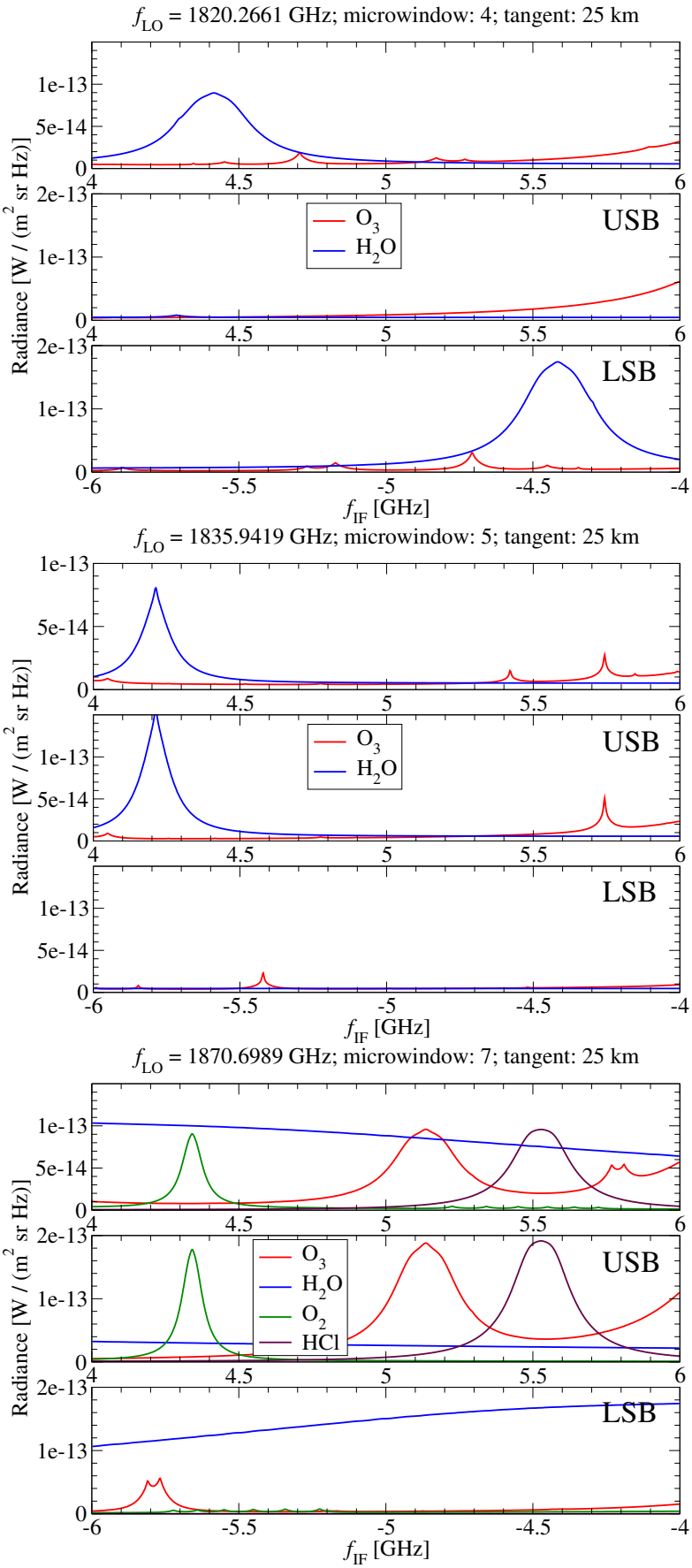

Figure A.1: Continued from the previous page.

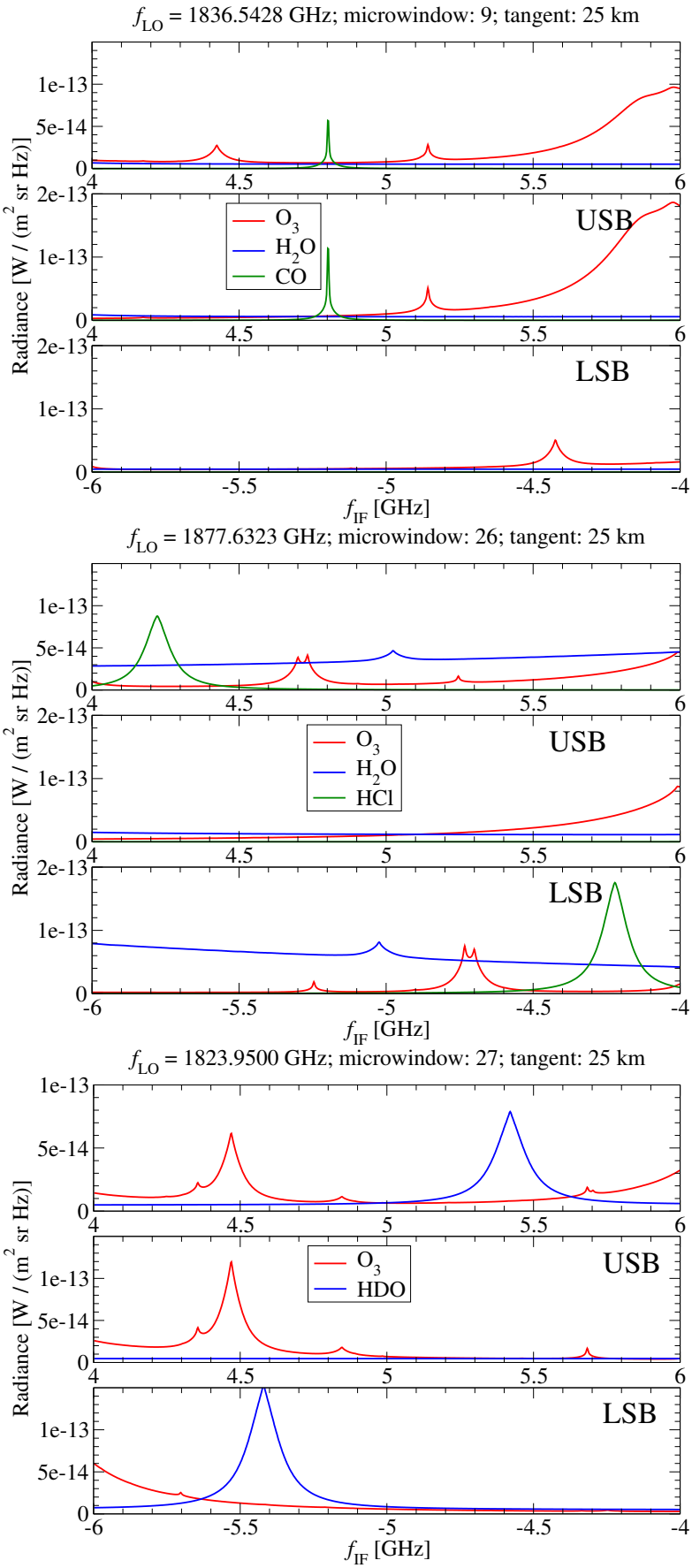

Figure A.1: Continued from the previous page.

Appendix B

PILS Input File

Input to PILS is managed by means of a user supplied main input file and a user-defined forward setup file assigned to the standard Fortran input logical unit. The main input file specifies the task (forward calculations or inversion) to be executed and its configurations (e.g. input data, numerical scheme, retrieval setup, etc.), while the forward setup file specifies the settings of the line-by-line calculation of absorption cross sections.

B.1 Main Input Body

The PILS main input file defines the groups of NAMELIST: `FLAGS`, `PORT`, `ATMOSPHERE`, `FETCH`, and `OBSERVED`. Note that an empty `ATMOSPHERE` card terminates reading this card, i.e. PILS will return to the appropriate main program; an empty `FETCH` card terminates reading this card, i.e., PILS will return to `ATMOSPHERE` routine.

`PORT` flag defines the configurations for PORT library and the regularization scheme. `XFtol` and `RFCtol` are given by real numbers which specify the false-convergence tolerance and the relative function-convergence tolerance, respectively. `mxIter` is the maximum number of iterations allowed. `separable` tells whether to use separable nonlinear least squares fitting, and `useBounds` tells whether to set simple bounds on the solution. `regMethod` specifies the regularization method to be used, and `typeL` refers to the type of regularization matrix. `alpha`, `beta` and `lCor` specify the value of regularization parameter, scaling factor (in case of iterative regularization methods), and correlation length.

```
&FLAGS forward='forward-TELIS_pils.in', mxGas=50, mxPath=99, nWindows=1,
       specFile='O3_3v02_mid20864_THz_2010_hamming',
       intPol='A', quad='T', verbose='s', order=, tType='',                &END

&PORT  XFtol=1.e-2, RFCtol=1.e-2, mxIter=10, aux='B', targetGas='multi',
       separable=f, useBounds=f, knownX=f,
       regMethod='IRGN', alpha=2e+1,0.,0.,0.,0., beta=.85,
       typeL='LC', lCor=1.5,1.5,1.5,100.,100.
       logFile='=.port',                                                   &END

&ATMOSPHERE file='/home/donau103/xu_jn/data/external/pressure_240110.dat',
            where='ECMWF',       hgtMin=9.0, hgtMax=65.0,                  &END
&FETCH      what='Pres',                                                   &END
&FETCH                                                                     &END
&ATMOSPHERE file='/home/donau103/xu_jn/data/external/mipas-b_temp_240110.dat',
            where='s09b',        hgtMin=9.0, hgtMax=65.0,                  &END
&FETCH      what='Temp',                                                   &END
&FETCH                                                                     &END
&ATMOSPHERE file='/home/donau103/xu_jn/data/external/telis_apriori_1,5km.dat',
            where='MIPAS-daily', hgtMin=9.0, hgtMax=65.0,                  &END
&FETCH      what='O3',           retrieve=t,                               &END
&FETCH                                                                     &END
&ATMOSPHERE file='/home/donau103/xu_jn/data/external/telis_apriori_1,5km.dat',
            where='AFGL-sw',     hgtMin=9.0, hgtMax=65.0,                  &END
&FETCH      what='CO',           retrieve=t,                               &END
&FETCH      what='H2O',          retrieve=f,                               &END
&FETCH      what='Grey',         retrieve=t,                               &END
&FETCH                                                                     &END
&ATMOSPHERE file='/home/donau101/mirror/IR/data/atm/glatm.dat',
            where='subarctic winter', hgtMin=9.0, hgtMax=65.0,             &END
&FETCH      what='CO2',          retrieve=f,                               &END
&FETCH      what='CH4',          retrieve=f,                               &END
&FETCH      what='O2',           retrieve=f,                               &END
&FETCH      what='NO',           retrieve=f,                               &END
&FETCH      what='SO2',          retrieve=f,                               &END
&FETCH      what='NO2',          retrieve=f,                               &END
&FETCH      what='NH3',          retrieve=f,                               &END
&FETCH      what='HNO3',         retrieve=f,                               &END
&FETCH      what='OH',           retrieve=f,                               &END
&FETCH      what='HCl',          retrieve=f,                               &END
&FETCH      what='HBr',          retrieve=f,                               &END
&FETCH      what='HI',           retrieve=f,                               &END
&FETCH      what='ClO',          retrieve=f,                               &END
&FETCH      what='H2CO',         retrieve=f,                               &END
&FETCH      what='HOCl',         retrieve=f,                               &END
&FETCH      what='HCN',          retrieve=f,                               &END
&FETCH      what='CH3Cl',        retrieve=f,                               &END
&FETCH      what='HO2',          retrieve=f,                               &END
&FETCH                                                                     &END
&ATMOSPHERE                                                                &END

&OBSERVED  FACTORS= 0.5,2.0,0.5,2.0, FoV='gauss','dg',0.1043,0.0,3,
           file='/home/donau103/xu_jn/data/TELIS/DLR_MID20864_CO_interpol_radiance_NLC_3v02.vR',
           xLow=5.0e+9, xHigh=5.5e+9, refraction=t,
           specMode='dsb', instrument='fts_h: 12597.;',                    &END
&OBSERVED                                                                  &END
```

B.2 Forward Configurations

The forward setup file comprising the settings of the radiative transfer calculation is given below. Likewise, an empty LbL input card terminates reading this card, i.e. PILS will search for another XSection card.

```
&FORWARD  intPol='A', quad='T', verbose='s',
          contFile='/home/donau101/mirror/IR/data/continua/ckd',
          MFile='/home/donau101/mirror/IR/data/molecules.nml',             &END

&Sources  surfaceTemp=288.2                                                &END

&Xsection file='/home/donau101/mirror/IR/data/hitran/2008/lines',
          what='multi',                                                    &END
&LbL      molecule='H2O',      lineShape='Voigt CKD'                       &END
&LbL      molecule='CO2',                                                  &END
&LbL      molecule='O3',                                                   &END
&LbL      molecule='CO',                                                   &END
&LbL      molecule='CH4',                                                  &END
&LbL      molecule='O2',                                                   &END
&LbL      molecule='NO',                                                   &END
&LbL      molecule='SO2',                                                  &END
&LbL      molecule='NO2',                                                  &END
&LbL      molecule='NH3',                                                  &END
&LbL      molecule='HNO3',                                                 &END
&LbL      molecule='OH',                                                   &END
&LbL      molecule='HCl',                                                  &END
&LbL      molecule='HBr',                                                  &END
&LbL      molecule='HI',                                                   &END
&LbL      molecule='ClO',                                                  &END
&LbL      molecule='H2CO',                                                 &END
&LbL      molecule='HOCl',                                                 &END
&LbL      molecule='HCN',                                                  &END
&LbL      molecule='CH3Cl',                                                &END
&LbL      molecule='HO2',                                                  &END
&LbL                                                                       &END
&Create   molecule='Grey', xs(0)=1.e-20, xs(1)=2.e-20                      &END
&Create                                                                    &END
&LbL      molecule='H2O',      lineShape='Voigt CKD'                       &END
&LbL      molecule='CO2',                                                  &END
&LbL      molecule='O3',                                                   &END
&LbL      molecule='CO',                                                   &END
&LbL      molecule='CH4',                                                  &END
&LbL      molecule='O2',                                                   &END
&LbL      molecule='NO',                                                   &END
&LbL      molecule='SO2',                                                  &END
&LbL      molecule='NO2',                                                  &END
&LbL      molecule='NH3',                                                  &END
&LbL      molecule='HNO3',                                                 &END
&LbL      molecule='OH',                                                   &END
&LbL      molecule='HCl',                                                  &END
&LbL      molecule='HBr',                                                  &END
&LbL      molecule='HI',                                                   &END
&LbL      molecule='ClO',                                                  &END
&LbL      molecule='H2CO',                                                 &END
&LbL      molecule='HOCl',                                                 &END
&LbL      molecule='HCN',                                                  &END
&LbL      molecule='CH3Cl',                                                &END
&LbL      molecule='HO2',                                                  &END
&LbL                                                                       &END
&Create   molecule='Grey', xs(0)=1.e-20, xs(1)=2.e-20                      &END
&Create                                                                    &END
&LbL                                                                       &END
&Xsection                                                                  &END
```

Appendix C

Symbols

Symbol	Denotation
$\mathbf{A}$	averaging kernel matrix
B	B-spline basis function
B	Planck function
$\boldsymbol{b}$	forward model parameters
$\boldsymbol{c}$	instrument model parameters
c	speed of light
cond	condition number
$\mathbb{E}$	relative exponential function
$\mathcal{E}$	expected value operator
E	energy
$\boldsymbol{e}_\lambda$	retrieval error
$\boldsymbol{F}$	forward model
$\mathcal{F}$	objective function
$\boldsymbol{f}$	residual vector
f	frequency
G	radiometric gain
g	line profile/shape function
h	Planck constant
$\mathbf{I}_n$	identity matrix
I	radiance (intensity)
k_B	Boltzmann constant
k_m	molecular cross section
K	Voigt function
$\mathbf{K}$	Jacobian matrix
$\mathbf{K}_\lambda^\dagger$	regularized general inverse
k	order of the B-spline basis
$\mathbf{L}$	regularization matrix
L	maximum optical path difference
l	correlation length

Symbol	Denotation
M	measurement response
m	molecular mass
n_{air}	temperature dependence of air width
n_m	number density
p	atmospheric pressure
Q	partition function
q	scale factor for iterative regularization methods
R	instrumental line shape (spectral response function)
r_{e}	Earth radius
r	sideband ratio
S	instrument output
S_l	line strength
$\mathbf{S}$	error covariance matrix
$\mathcal{T}$	transmission
T	atmospheric temperature
T_{b}	brightness temperature
t	B-spline knot
$\mathbf{U}$	left singular matrix
$\mathbf{V}$	right singular matrix
$\boldsymbol{x}_{\mathrm{a}}$	a priori profile
$\boldsymbol{x}_{\mathrm{t}}$	true profile
$\boldsymbol{x}_{\lambda}$	regularized solution
α	volume absorption coefficient
γ	half width (at half maximum, HWHM)
ϵ	solution error
ε	model parameter standard deviation
$\boldsymbol{\delta}$	measurement noise
ζ	compression quantity
λ	regularization parameter
μ	refractive index of air
ν	wavenumber
$\hat{\nu}_l$	spectral line center position
$\mathbf{\Sigma}$	rectangular diagonal matrix with singular values
σ^2	variance
χ	control parameter using the discrepancy principle
τ	optical depth
ω	B-spline expansion coefficients

Appendix D

Acronyms

Acronym	Denotation
1-D	one-dimensional
ACE-FTS	Atmospheric Chemistry Experiment - Fourier Transform Spectrometer
AD	automatic differentiation
AFGL	Air Force Geophysics Laboratory
AHRS	Attitude and Heading Reference System
AIRS	Atmospheric Infrared Sounder
ALADIN	Atmospheric Laser Doppler Instrument
AMIL2DA	Advanced MIPAS Level 2 Data Analysis
ARTS	Atmospheric Radiative Transfer Simulator
ATMOS	Atmospheric Trace Molecule Spectroscopy
BIRRA	Beer Infrared Retrieval Algorithm
BUV	backscatter ultraviolet
DLR	Deutsches Zentrum für Luft- und Raumfahrt (German Aerospace Center)
DOAS	Differential Optical Absorption Spectrometer
DOF	degree of freedom
DSB	double sideband
ECMWF	European Center for Medium-range Weather Forecasts
EOS	Earth Observing System
ESA	European Space Agency
FoV	field-of-view
FWHM	full width half maximum
GARLIC	Generic Atmospheric Radiation Line-by-line Infrared Code
GEISA	Gestion et Etude des Informations Spectroscopiques Atmosphériques
GLORIA	Gimballed Limb Observer for Radiance Imaging of the Atmosphere
GOME	Global Ozone Monitoring Experiment

Acronym	Denotation
GOMOS	Global Ozone Monitoring by Occultation of Stars
GOSAT	Greenhouse Gases Observing Satellite
HALOE	Halogen Occultation Experiment
HEB	Hot Electron Bolometer
HITRAN	High-resolution Transmission
HWHM	half width at half maximum
IASI	Infrared Atmospheric Sounding Interferometer
IF	intermediate frequency
ILS	instrumental line shape
IMF	Institut für Methodik der Fernerkundung (Remote Sensing Technology Institute)
IMK-ASF	Institut für Meteorologie und Klimaforschung - Atmosphärische Spurengase und Fernerkundung (Institute for Meteorology and Climate Research - Atmospheric Trace Gases and Remote Sensing)
IRGN	iteratively regularized Gauss–Newton
IRTMW01	International Radiative Transfer Modelling Workshop 2001
ISS	International Space Station
JAXA	Japan Aerospace Exploration Agency
JEM	Japanese Experiment Module
JPL	Jet Propulsion Laboratory
KIT	Karlsruhe Institute of Technology
KOPRA	Karlsruhe Optimized and Precise Radiative Transfer Algorithm
LO	local oscillator
LoS	line of sight
LRIR	Limb Radiance Inversion Radiometer
LSB	lower sideband
LTE	local thermodynamic equilibrium
MARC	Millimeter-wave Atmospheric-Retrieval Code
MIPAS	Michelson Interferometer for Passive Atmospheric Sounding
MIPAS-B	Michelson Interferometer for Passive Atmospheric Sounding – Balloon
MIRART	Modular Infrared Atmospheric Radiative Transfer
MOLIERE	Microwave Observation Line Estimation and Retrieval
MOPD	maximum optical path difference
MLS	Microwave Limb Sounder
MTP	Microwave Temperature Profiler
NASA	National Aeronautics and Space Administration
NICT	National Institute of Information and Communications Technology

Acronym	Denotation
OEM	Optimal Estimation Method
OSIRIS	Optical Spectrograph and Infrared Imager System
PILS	Profile Inversion for Limb Sounding
POLDIRAD	Polarimetric Diversity Doppler Radar
RAL	Rutherford Appleton Laboratory
RLM	regularizing Levenberg–Marquardt
RSS	root sum squares
SBR	sideband ratio
SCIAMACHY	Scanning Imaging Absorption Spectrometer for Atmospheric Cartography
SIR	Superconducting Integrated Receiver
SMILES	Superconducting Submillimeter-wave Limb Emission Sounder
SMR	Sub-Millimeter Radiometer
SNR	signal-to-noise ratio
SRF	spectral response function
SRON	Netherlands Institute for Space Research
SVD	singular value decomposition
SZA	solar zenith angle
TCCON	Total Carbon Column Observing Network
ToA	Top-of-Atmosphere
TR	Tikhonov regularization
TELIS	Terahertz and Submillimeter Limb Sounder
TES	Tropospheric Emission Spectrometer
THOMAS	Terahertz OH Measurement Airborne Sounder
TSVD	truncated singular value decomposition
UARS	Upper Atmosphere Research Satellite
USB	upper sideband
VMR	volume mixing ratio

Bibliography

Abrams, M., Goldman, A., Gunson, M., Rinsland, C., and Zander, R.: Observations of the Infrared Solar Spectrum from Space by the ATMOS experiment, Appl. Opt., 35, 2747–2751, doi:10.1364/AO.35.002747, 1996a.

Abrams, M., Gunson, M., Chang, A., Rinsland, C., and Zander, R.: Remote Sensing of the Earth's Atmosphere from Space with High–resolution Fourier transform spectroscopy: Development and Methodology of Data Processing for the Atmospheric Trace Molecule Spectrocopy experiment, Appl. Opt., 35, 2774–2786, doi:10.1364/AO.35.002774, 1996b.

Allen, D. R., Stanford, J. L., López-Valverde, M. A., Nakamura, N., Lary, D. J., Douglass, A. R., Cerniglia, M. C., Remedios, J. J., and Taylor, F. W.: Observations of middle atmosphere CO from the UARS ISAMS during the early northern winter 1991/92, J. Atmos. Sci., 56, 563–583, doi:10.1175/1520-0469(1999)056⟨0563:OOMACF⟩2.0.CO;2, 1999.

Allmaras, M., Bangerth, W., Linhart, J., Polanco, J., Wang, F., Wang, K., Webster, J., and Zedler, S.: Estimating Parameters in Physical Models through Bayesian Inversion: A Complete Example, SIAM Review, 55, 149–167, doi:10.1137/100788604, 2013.

Anderson, E., Bai, Z., Bischof, C., Demmel, J., Dongarra, J., Croz, J. D., Greenbaum, A., Hammarling, S., McKenney, A., Ostrouchov, S., and Sorensen, D.: LAPACK Users' Guide, SIAM, Philadelphia, PA, third edn., 1999.

Anderson, G., Clough, S., Kneizys, F., Chetwynd, J., and Shettle, E.: AFGL Atmospheric Constituent Profiles (0 – 120 km), Tech. Rep. TR-86-0110, AFGL, 1986.

Aumann, H., Chahine, M., Gautier, C., Goldberg, M., Kalnay, E., McMillin, L., Revercomb, H., Rosenkranz, P., Smith, W., Staelin, D., Strow, L., and Susskind, J.: AIRS/AMSU/HSB on the Aqua mission: design, science objectives, data products, and processing systems, IEEE Trans. Geosci. Remote Sens., 41, 253–264, doi:10.1109/TGRS.2002.808356, 2003.

Austin, J., Scinocca, J., Plummer, D., Oman, L., Waugh, D., Akiyoshi, H., Bekki, S., Braesicke, P., Butchart, N., Chipperfield, M., Cugnet, D., Dameris, M., Dhomse, S., Eyring, V., Frith, S., Garcia, R. R., Garny, H., Gettelman, A., Hardiman, S. C., Kinnison, D., Lamarque, J. F., Mancini, E., Marchand, M., Michou, M., Morgenstern, O., Nakamura, T., Pawson, S., Pitari, G., Pyle, J., Rozanov, E., Shepherd, T. G., Shibata, K., Teyssèdre, H., Wilson, R. J., and Yamashita, Y.: Decline and recovery of total column ozone using a multimodel time series analysis, J. Geophys. Res., 115, n/a–n/a, doi:10.1029/2010JD013857, 2010.

Bakushinskii, A.: The problem of the convergence of the iteratively regularized Gauss–Newton method, Comput. Math. Phys., 32, 1353–1359, 1992.

Barath, F. T., Chavez, M. C., Cofield, R. E., Flower, D. A., Frerking, M. A., Gram, M. B., Harris, W. M., Holden, J. R., Jarnot, R. F., Kloezeman, W. G., Klose, G. J., Lau, G. K., Loo, M. S., Maddison, B. J., Mattauch, R. J., McKinney, R. P., Peckham, G. E., Pickett, H. M., Siebes, G., Soltis, F. S., Suttie, R. A., Tarsala, J. A., Waters, J. W., and Wilson, W. J.: The Upper Atmosphere Research Satellite microwave limb sounder instrument, J. Geophys. Res., 98, 10 751–10 762, doi:10.1029/93JD00798, 1993.

Baron, P., Merino, F., and Murtagh, D.: Simultaneous retrievals of temperature and volume mixing ratio constituents from nonoxygen Odin submillimeter radiometer bands, Appl. Opt., 40, 6102–6110, 2001.

Baron, P., Ricaud, P., Noë, J. d. L., Eriksson, P., Merino, F., Ridal, M., and Murtagh, D.: Studies for the Odin sub-millimetre radiometer. II. Retrieval methodology, Can. J. Phys., 80, 341–356, doi:10.1139/p01-150, 2002.

Baron, P., Urban, J., Sagawa, H., Möller, J., Murtagh, D. P., Mendrok, J., Dupuy, E., Sato, T. O., Ochiai, S., Suzuki, K., Manabe, T., Nishibori, T., Kikuchi, K., Sato, R., Takayanagi, M., Murayama, Y., Shiotani, M., and Kasai, Y.: The Level 2 research product algorithms for the Superconducting Submillimeter-Wave Limb-Emission Sounder (SMILES), Atmos. Meas. Tech., 4, 2105–2124, doi:10.5194/amt-4-2105-2011, 2011.

Beer, R.: TES on the Aura Mission: Scientific Objectives, Measurements, and Analysis Overview, IEEE Trans. Geosci. Remote Sens., 44, 1102–1105, doi:10.1109/TGRS.2005.863716, 2006.

Bernath, P., McElroy, C. T., Abrams, M. C., Boone, C. D., Butler, M., Camy-Peyret, C., Carleer, M., Clerbaux, C., Coheur, P.-F., Colin, R., DeCola, P., DeMaziere, M., Drummond, J. R., Dufour, D., Evans, W. F. J., Fast, H., Fussen, D., Gilbert, K., Jennings, D. E., Llewellyn, E. J., Lowe, R. P., Mahieu, E., McConnell, J. C., McHugh, M., McLeod, S. D., Michaud, R., Midwinter, C., Nassar, R., Nichitiu, F., Nowlan, C., Rinsland, C. P., Rochon, Y. J., Rowlands, N., Semeniuk, K., Simon, P., Skelton, R., Sloan, J. J., Soucy, M.-A., Strong, K., Tremblay, P., Turnbull, D., Walker, K. A., Walkty, I., Wardle, D. A., Wehrle, V., Zander, R., and Zou, J.: Atmospheric Chemistry Experiment (ACE): Mission overview, Geophys. Res. Letters, 32, L15S01, doi:10.1029/2005GL022 386, 2005.

Birk, M., Wagner, G., de Lange, G., de Lange, A., Ellison, B. N., Harman, M. R., Murk, A., Oelhaf, H., Maucher, G., and Sartorius, C.: TELIS: TErahertz and subMMW LImb Sounder – Project Summary After First Sucessful Flight, in: Proceedings of 21st International Symposium on Space Terahertz Technology, pp. 195–200, University of Oxford and STFC Rutherford Appleton Laboratory, 2010.

Bischof, C., Carle, A., Hovland, P., Khademi, P., and Mauer, A.: ADIFOR 2.0 User's Guide (Revision D), Tech. Rep. ANL/MCS-TM-192, Argonne National Laboratory — Mathematics and Computer Science Division, 1998.

Bischof, C. H. and Bücker, H. M.: Computing Derivatives of Computer Programs, in: Modern Methods and Algorithms of Quantum Chemistry: Proceedings, edited by Grotendorst, J., vol. 3 of *NIC Series*, pp. 315–327, John von Neumann Institute for Computing, Jülich, second edn., 2000.

Böckmann, C.: Hybrid regularization method for ill-posed inversion of multiwavelength lidar data in the retrieval of aerosol size distributions, Appl. Opt., 40, 1329–1342, 2001.

Bohren, C. F. and Clothiaux, E. E.: Fundamentals of Atmospheric Radiation, Wiley-VCH Verlag, Weinheim, Germany, 2006.

Borsdorff, T., Hasekamp, O. P., Wassmann, A., and Landgraf, J.: Insights into Tikhonov regularization: application to trace gas column retrieval and the efficient calculation of total column averaging kernels, Atmos. Meas. Tech., 7, 523–535, doi:10.5194/amt-7-523-2014, 2014.

Bühler, S., Eriksson, P., Kuhn, T., von Engeln, A., and Verdes, C.: ARTS, the atmospheric radiative transfer simulator, J. Quant. Spectrosc. & Radiat. Transfer, 91, 65–93, doi:10.1016/j.jqsrt.2004.05.051, 2005.

Burrows, J. P., Weber, M., Buchwitz, M., Rozanov, V., Ladstätter-Weißenmayer, A., Richter, A., DeBeek, R., Hoogen, R., Bramstedt, K., Eichmann, K.-U., Eisinger, M., and Perner, D.: The Global Ozone Monitoring Experiment (GOME): Mission Concept and First Scientific Results, J. Atmos. Sci., 56, 151–175, doi:10.1175/1520-0469(1999)056⟨0151:TGOMEG⟩2.0.CO;2, 1999.

Callies, J., Corpaccioli, E., Eisinger, M., Hahne, A., and Lefebvre, A.: GOME-2 – Metop's Second-Generation Sensor for Operational Ozone Monitoring, ESA Bulletin, pp. 28–36, 2000.

Carli, B., Carlotti, M., Dinelli, B., Mencaraglia, F., and Park, J.: The mixing ratio of stratospheric hydroxyl radical from far infrared emission measurements, J. Geophys. Res., 94, 11 049, 1989.

Carli, B., Bazzini, G., Castelli, E., Cecchi-Pestellini, C., Bianco, S. D., Dinelli, B., Gai, M., Magnani, L., Ridolfi, M., and Santurri, L.: MARC: A code for the retrieval of atmospheric parameters from millimeter-wave limb measurements, J. Quant. Spectrosc. & Radiat. Transfer, 105, 476–491, doi:10.1016/j.jqsrt.2006.11.011, 2007.

Carlotti, M.: Global–Fit Approach to the Analysis of Limb–Scanning Atmospheric Measurements, Appl. Opt., 27, 3250–3254, doi:10.1364/AO.27.003250, 1988.

Carlotti, M., Höpfner, M., Raspollini, P., Ridolfi, M., and Carli, B.: High level algorithm definition and physical and mathematical optimisations, Tech. Rep. TN-IROE-RSA9601, IROE, Florence, Italy, 1998.

Carlotti, M., Ade, P., Carli, B., Chipperfield, M., Hamilton, P., Mencaraglia, F., Nolt, I., and Ridolfi, M.: Diurnal variability and night detection of stratospheric hydroxyl radical from far infrared emission measurements, Journal of Atmospheric and Solar-Terrestrial Physics, 63, 1509 – 1518, doi:10.1016/S1364-6826(01)00030-X, 2001.

Cayla, F.: IASI Infrared Interferometer for Operations and Research, in: High Spectral Resolution Infrared Remote Sensing for Earths Weather and Climate Studies, edited by Chedin, A., Chahine, M., and Scott, N., vol. 9 of *NATO ASI Series*, pp. 9–19, Springer Berlin Heidelberg, doi:10.1007/978-3-642-84599-4_2, 1993.

Ceccherini, S.: Analytical determination of the regularization parameter in the retrieval of atmospheric vertical profiles, Opt. Lett., 30, 2554–2556, doi:10.1364/OL.30.002554, 2005.

Ceccherini, S., Belotti, C., Carli, B., Raspollini, P., and Ridolfi, M.: Technical Note: Regularization performances with the error consistency method in the case of retrieved atmospheric profiles, Atm. Chem. Phys., 7, 1435–1440, doi:10.5194/acp-7-1435-2007, 2007.

Ceccherini, S., Carli, B., Cortesi, U., Bianco, S. D., and Raspollini, P.: Retrieval of the vertical column of an atmospheric constituent from data fusion of remote sensing measurements, J. Quant. Spectrosc. & Radiat. Transfer, 111, 507–514, doi:10.1016/j.jqsrt.2009.09.001, 2010.

Clough, S., Kneizys, F., Anderson, G., Shettle, E., Chetwynd, J., Abreu, L., Hall, L., and Worsham, R.: FASCOD3: spectral simulation, in: IRS'88: Current Problems in Atmospheric Radiation, edited by Lenoble, J. and Geleyn, J., pp. 372–375, A. Deepak Publishing, 1988.

Clough, S., Kneizys, F., and Davies, R.: Line Shape and the Water Vapor Continuum, Atmos. Res., 23, 229–241, doi:10.1016/0169-8095(89)90020-3, 1989.

Dahlquist, G. and Björck, Å.: Numerical Methods in Scientific Computing, vol. 1, SIAM, 2008.

de Boor, C.: Computational Aspects of Optimal Recovery, in: Optimal Estimation in Approximation Theory, edited by Micchelli, C. and Rivlin, T., The IBM Research Symposia Series, Plenum Press, New York, 1977.

de Boor, C.: A Practical Guide to Splines, Springer-Verlag, New York, revised edn., 2001.

de Lange, A., Landgraf, J., and Hoogeveen, R.: Stratospheric isotopic water profiles from a single submillimeter limb scan by TELIS, Atmos. Meas. Tech., 2, 423–435, doi:10.5194/amt-2-423-2009, 2009.

de Lange, A., Birk, M., de Lange, G., Friedl-Vallon, F., Kiselev, O., Koshelets, V., Maucher, G., Oelhaf, H., Selig, A., Vogt, P., Wagner, G., and Landgraf, J.: HCl and ClO in activated Arctic air; first retrieved vertical profiles from TELIS submillimetre limb spectra, Atmos. Meas. Tech., 5, 487–500, doi:10.5194/amt-5-487-2012, 2012.

de Lange, G., Birk, M., Boersma, D., Derckson, J., Dmitriev, P., Ermakov, A., Filippenko, L., Golstein, H., Hoogeveen, R., de Jong, L., Khudchenko, A., Kinev, N., Kiselev, O., van Kuik, B., de Lange, A., van Rantwijk, J., Selig, A., Sobolev, A., Torgashin, M., de Vries, E., Wagner, G., Yagoubov, P., and Koshelets, V.: Development and characterization of the superconducting integrated receiver channel of the TELIS atmospheric sounder, Supercond. Sci. Technol., 23, doi:10.1088/0953-2048/23/4/045016, 2010.

Denning, R., Guidero, S., Parks, G., and Gary, B.: Instrument Description of the Airborne Microwave Temperature Profiler, J. Geophys. Res., 94, 16 757–16 765, 1989.

Dennis, Jr., J., Gay, D., and Welsch, R.: An Adaptive Nonlinear Least–Squares Algorithm, ACM Trans. Math. Soft., 7, 348–368, doi:10.1145/355958.355965, 1981a.

Dennis, Jr., J., Gay, D., and Welsch, R.: Algorithm 573: NL2SOL—An Adaptive Nonlinear Least–Squares Algorithm, ACM Trans. Math. Soft., 7, 369–383, doi:10.1145/356022.356031, 1981b.

Doicu, A., Schreier, F., and Hess, M.: Iteratively Regularized Gauss–Newton Method for Atmospheric Remote Sensing, Comp. Phys. Comm., 148, 214–226, doi:10.1016/S0010-4655(02)00555-6, 2002.

Doicu, A., Schreier, F., and Hess, M.: Iteratively Regularized Gauss–Newton Method for Bound–Constraint Problems in Atmospheric Remote Sensing, Comp. Phys. Comm., 153, 59–65, doi:10.1016/S0010-4655(03)00138-3, 2003.

Doicu, A., Schreier, F., and Hess, M.: Iterative Regularization Methods for Atmospheric Remote Sensing, J. Quant. Spectrosc. & Radiat. Transfer, 83, 47–61, doi:10.1016/S0022-4073(02)00292-3, 2004.

Doicu, A., Trautmann, T., and Schreier, F.: Numerical Regularization for Atmospheric Inverse Problems, Springer and Praxis Publishing, Berlin Heidelberg, doi:10.1007/978-3-642-05439-6, 2010.

Edlén, B.: The refractive index of air, Metrologia, 2, 71–80, doi:10.1088/0026-1394/2/2/002, 1966.

Edwards, D.: Atmospheric transmittance and radiance calculations using line–by–line computer models, in: Modelling of the Atmosphere, vol. 928, pp. 94–116, Proc. SPIE, 1988.

Englert, C., Schimpf, B., Birk, M., Schreier, F., Krocka, M., Nitsche, R., Titz, R., and Summers, M.: The 2.5 THz heterodyne spectrometer THOMAS: Measurement of OH in the middle atmosphere and comparison with photochemical model results, J. Geophys. Res., 105, 22 211–22 223, doi:10.1029/2000JD900305, 2000.

Eriksson, P.: Analysis and comparison of two linear regularization methods for passive atmospheric observation, J. Geophys. Res., 105, 18 157–18 167, 2000.

Eriksson, P., Jiménez, C., and Buehler, S. A.: Qpack, a general tool for instrument simulation and retrieval work, J. Quant. Spectrosc. & Radiat. Transfer, 91, 47 – 64, doi:10.1016/j.jqsrt.2004.05.050, 2005.

Eriksson, P., Buehler, S., Davis, Emde, C., and Lemke, O.: ARTS, the atmospheric radiative transfer simulator, version 2, J. Quant. Spectrosc. & Radiat. Transfer, 112, 1551–1558, doi:10.1016/j.jqsrt.2011.03.001, 2011.

Filipiak, M., Harwood, R., Jiang, J., Li, Q., Livesey, N., Manney, G., Read, W., Schwartz, M., Waters, J., and Wu, D.: Carbon Monoxide Measured by the EOS Microwave Limb Sounder on Aura: First Results, Geophys. Res. Letters, 32, L14 825, doi:10.1029/2005GL022765, 2005.

Fischer, H., Birk, M., Blom, C., Carli, B., Carlotti, M., von Clarmann, T., Delbouille, L., Dudhia, A., Ehhalt, D., Endemann, M., Flaud, J. M., Gessner, R., Kleinert, A., Koopman, R., Langen, J., López-Puertas, M., Mosner, P., Nett, H., Oelhaf, H., Perron, G., Remedios, J., Ridolfi, M., Stiller, G., and Zander, R.: MIPAS: an instrument for atmospheric and climate research, Atm. Chem. Phys., 8, 2151–2188, doi:10.5194/acp-8-2151-2008, 2008.

Flaud, J., Perrin, A., Picquet-Varrault, B., Gratien, A., Orphal, J., and Doussin, J.: Quantitative Spectroscopy and Atmospheric Measurements, in: Remote Sensing of the Atmosphere for Environmental Security, edited by Perrin, A., Ben Sari-Zizi, N., and Demaison, J., vol. 14 of *NATO Security through Science Series*, pp. 107–121, Springer, doi:10.1007/978-1-4020-5090-9_7, 2006.

Fox, P., Hall, A., and Schryer, N.: The PORT Mathematical Subroutine Library, ACM Trans. Math. Soft., 4, 104–126, doi:10.1145/355780.355789, 1978.

Friedl-Vallon, F., Maucher, G., Seefeldner, M., Trieschmann, O., Kleinert, A., Lengel, A., Keim, C., Oelhaf, H., and Fischer, H.: Design and characterization of the balloon-borne Michelson Interferometer for Passive Atmospheric Sounding (MIPAS-B2), Appl. Opt., 43, 3335–3355, doi:10.1364/AO.43.003335, 2004.

Friedl-Vallon, F., Gulde, T., Hase, F., Kleinert, A., Kulessa, T., Maucher, G., Neubert, T., Olschewski, F., Piesch, C., Preusse, P., Rongen, H., Sartorius, C., Schneider, H., Schönfeld, A., Tan, V., Bayer, N., Blank, J., Dapp, R., Ebersoldt, A., Fischer, H., Graf, F., Guggenmoser, T., Höpfner, M., Kaufmann, M., Kretschmer, E., Latzko, T., Nordmeyer, H., Oelhaf, H., Orphal, J., Riese, M., Schardt, G., Schillings, J., Sha, M. K., Suminska-Ebersoldt, O., and Ungermann, J.: Instrument concept of the imaging Fourier transform spectrometer GLORIA, Atmos. Meas. Tech. Disc., 7, 2301–2337, doi:10.5194/amtd-7-2301-2014, 2014.

Froidevaux, L., Jiang, Y. B., Lambert, A., Livesey, N. J., Read, W. G., Waters, J. W., Browell, E. V., Hair, J. W., Avery, M. A., McGee, T. J., Twigg, L. W., Sumnicht, G. K., Jucks, K. W., Margitan, J. J., Sen, B., Stachnik, R. A., Toon, G. C., Bernath, P. F., Boone, C. D., Walker, K. A., Filipiak, M. J., Harwood, R. S., Fuller, R. A., Manney, G. L., Schwartz, M. J., Daffer, W. H., Drouin, B. J., Cofield, R. E., Cuddy, D. T., Jarnot, R. F., Knosp, B. W., Perun, V. S., Snyder, W. V., Stek, P. C., Thurstans, R. P., and Wagner, P. A.: Validation of Aura Microwave Limb Sounder stratospheric ozone measurements, J. Geophys. Res., 113, n/a–n/a, doi:10.1029/2007JD008771, 2008a.

Froidevaux, L., Jiang, Y. B., Lambert, A., Livesey, N. J., Read, W. G., Waters, J. W., Fuller, R. A., Marcy, T. P., Popp, P. J., Gao, R. S., Fahey, D. W., Jucks, K. W., Stachnik, R. A., Toon, G. C., Christensen, L. E., Webster, C. R., Bernath, P. F., Boone, C. D., Walker, K. A., Pumphrey, H. C., Harwood, R. S., Manney, G. L., Schwartz, M. J., Daffer, W. H., Drouin, B. J., Cofield, R. E., Cuddy, D. T., Jarnot, R. F., Knosp, B. W., Perun, V. S., Snyder, W. V., Stek, P. C., Thurstans, R. P., and Wagner, P. A.: Validation of Aura Microwave Limb Sounder HCl measurements, J. Geophys. Res., 113, n/a–n/a, doi:10.1029/2007JD009025, 2008b.

Fuerholz, P. and Murk, A.: Phase-Corrected Near-Field Measurements of the TELIS Telescope at 637 GHz, IEEE Trans. Antennas. Propag., 57, 2518–2525, doi:10.1109/TAP.2009.2024486, 2009.

Gimeno García, S., Schreier, F., Lichtenberg, G., and Slijkhuis, S.: Near infrared nadir retrieval of vertical column densities: methodology and application to SCIAMACHY, Atmos. Meas. Tech., 4, 2633–2657, doi:10.5194/amt-4-2633-2011, 2011.

Goody, R. and Yung, Y.: Atmospheric Radiation — Theoretical Basis, Oxford University Press, second edn., 1989.

Gottwald, M. and Bovensmann, H., eds.: SCIAMACHY — Exploring the Changing Earth's Atmosphere, Springer, Dordrecht, NL, doi:10.1007/978-90-481-9896-2, 2011.

Gouveia, W. and Scales, J.: Resolution of Seismic Waveform Inversion: Bayes versus Occam, Inverse Problems, 13, 323–349, doi:10.1088/0266-5611/13/2/009, 1997.

Griewank, A.: Evaluating Derivatives: Principles and Techniques of Algorithmic Differentiation, SIAM, Philadelphia, PA, 2000.

Griewank, A. and Corliss, G., eds.: Automatic Differentiation of Algorithms, SIAM, Philadelphia, PA, 1991.

Hansen, P.: Analysis of discrete ill–posed problems by means of the L–curve, SIAM Review, 34, 561–580, 1992.

Hansen, P.: Rank–Deficient and Discrete Ill–Posed Problems: Numerical Aspects of Linear Inversion, SIAM, Philadelphia, PA, 1998.

Hansen, P.: Discrete Inverse Problems: Insight and Algorithms, SIAM, Philadelphia, PA, doi: 10.1137/1.9780898718836, 2010.

Hansen, P. C.: Truncated singular value decomposition solutions to discrete ill-posed problems with ill-determined numerical rank, SIAM J. Sci. Stat. Comput., 11, 503–518, doi:10.1137/0911028, 1990.

Hascoët, L. and Pascual, V.: The Tapenade Automatic Differentiation tool: Principles, Model, and Specification, ACM Trans. Math. Soft., 39, doi:10.1145/2450153.2450158, 2013.

Hasekamp, O. and Landgraf, J.: Ozone Profile Retrieval from Backscattered Ultraviolet Radiances: The Inverse Problem Solved by Regularization, J. Geophys. Res., 106, 8077–8088, 2001.

Hofmann, B.: Mathematik inverser Probleme, Teubner-Verlag, Stuttgart - Leipzig, 1999.

Höpfner, M., Oelhaf, H., Wetzel, G., Friedl-Vallon, F., Kleinert, A., Lengel, A., Maucher, G., Nordmeyer, H., Glatthor, N., Stiller, G., Clarmann, T., Fischer, H., Kröger, C., and Deshler, T.: Evidence of scattering of tropospheric radiation by PSCs in mid–IR limb emission spectra: MIPAS-B observations and KOPRA simulations, Geophys. Res. Letters, 29, 119–1 to 119–4, 2002.

Humliček, J.: Optimized computation of the Voigt and complex probability function, J. Quant. Spectrosc. & Radiat. Transfer, 27, 437–444, doi:10.1016/0022-4073(82)90078-4, 1982.

Irimajiri, Y., Manabe, T., Ochiai, S., Masuko, H., Yamagami, T., Saito, Y., Izutsu, N., Kawasaki, T., Namiki, M., and Murata, I.: BSMILES - a balloon-borne superconducting submillimeter-wave limb-emission sounder for stratospheric measurements, Geoscience and Remote Sensing Letters, 3, 88–92, doi:10.1109/LGRS.2005.856712, 2006.

Jacob, D. J.: Introduction to Atmospheric Chemistry, Princeton University Press, New York, NY, second edn., 1999.

Jacobson, M. Z.: Air Pollution and Global Warming: History, Science, and Solutions, Cambridge University Press, New York, NY, second edn., 2012.

Jacquinet-Husson, N., Crepeau, L., Armante, R., Boutammine, C., Chédin, A., Scott, N., Crevoisier, C., Capelle, V., Boone, C., Poulet-Crovisier, N., Barbe, A., Campargue, A., Benner, D. C., Benilan, Y., Bézard, B., Boudon, V., Brown, L., Coudert, L., Coustenis, A., Dana, V., Devi, V., Fally, S., Fayt, A., Flaud, J.-M., Goldman, A., Herman, M., Harris, G., Jacquemart, D., Jolly, A., Kleiner, I., Kleinböhl, A., Kwabia-Tchana, F., Lavrentieva, N., Lacome, N., Xu, L.-H., Lyulin, O., Mandin, J.-Y., Maki, A., Mikhailenko, S., Miller, C., Mishina, T., Moazzen-Ahmadi, N., Müller, H., Nikitin, A., Orphal, J., Perevalov, V., Perrin, A., Petkie, D., Predoi-Cross, A., Rinsland, C., Remedios, J., Rotger, M., Smith, M., Sung, K., Tashkun, S., Tennyson, J., Toth, R., Vandaele, A.-C., and Auwera, J. V.: The 2009 edition of the GEISA spectroscopic database, J. Quant. Spectrosc. & Radiat. Transfer, 112, 2395–2445, doi:10.1016/j.jqsrt.2011.06.004, 2011.

Jégou, F., Urban, J., de La Noë, J., Ricaud, P., Le Flochmoën, E., Murtagh, D. P., Eriksson, P., Jones, A., Petelina, S., Llewellyn, E. J., Lloyd, N. D., Haley, C., Lumpe, J., Randall, C., Bevilacqua, R. M., Catoire, V., Huret, N., Berthet, G., Renard, J. B., Strong, K., Davies, J., Mc Elroy, C. T., Goutail, F., and Pommereau, J. P.: Technical Note: Validation of Odin/SMR

limb observations of ozone, comparisons with OSIRIS, POAM III, ground-based and balloon-borne instruments, Atm. Chem. Phys., 8, 3385–3409, doi:10.5194/acp-8-3385-2008, 2008.

Jiang, Y. B., Froidevaux, L., Lambert, A., Livesey, N. J., Read, W. G., Waters, J. W., Bojkov, B., Leblanc, T., McDermid, I. S., Godin-Beekmann, S., Filipiak, M. J., Harwood, R. S., Fuller, R. A., Daffer, W. H., Drouin, B. J., Cofield, R. E., Cuddy, D. T., Jarnot, R. F., Knosp, B. W., Perun, V. S., Schwartz, M. J., Snyder, W. V., Stek, P. C., Thurstans, R. P., Wagner, P. A., Allaart, M., Andersen, S. B., Bodeker, G., Calpini, B., Claude, H., Coetzee, G., Davies, J., De Backer, H., Dier, H., Fujiwara, M., Johnson, B., Kelder, H., Leme, N. P., König-Langlo, G., Kyro, E., Laneve, G., Fook, L. S., Merrill, J., Morris, G., Newchurch, M., Oltmans, S., Parrondos, M. C., Posny, F., Schmidlin, F., Skrivankova, P., Stubi, R., Tarasick, D., Thompson, A., Thouret, V., Viatte, P., Vömel, H., von Der Gathen, P., Yela, M., and Zablocki, G.: Validation of Aura Microwave Limb Sounder Ozone by ozonesonde and lidar measurements, J. Geophys. Res., 112, n/a–n/a, doi:10.1029/2007JD008776, 2007.

Jones, A., Murtagh, D., Urban, J., Eriksson, P., and Rösevall, J.: Intercomparison of Odin/SMR ozone measurements with MIPAS and balloon sonde data, Can. J. Phys., 85, 1111–1123, doi:10.1139/p07-118, 2007.

Jucks, K., Johnson, D., Chance, K., Traub, W., Margitan, J., Osterman, G., Salawitch, R., and Sasano, Y.: Observations of OH, HO_2, H_2O, and O_3 in the upper stratosphere: Implications for HO_x photochemistry, Geophys. Res. Letters, 25, 3935–3938, doi:10.1029/1998GL900009, 1998.

Kahaner, D., Moler, C., and Nash, S.: Numerical Methods and Software, Prentice–Hall, Englewood Cliffs, NJ, 1989.

Kasai, Y., Sagawa, H., Kreyling, D., Dupuy, E., Baron, P., Mendrok, J., Suzuki, K., Sato, T. O., Nishibori, T., Mizobuchi, S., Kikuchi, K., Manabe, T., Ozeki, H., Sugita, T., Fujiwara, M., Irimajiri, Y., Walker, K. A., Bernath, P. F., Boone, C., Stiller, G., von Clarmann, T., Orphal, J., Urban, J., Murtagh, D., Llewellyn, E. J., Degenstein, D., Bourassa, A. E., Lloyd, N. D., Froidevaux, L., Birk, M., Wagner, G., Schreier, F., Xu, J., Vogt, P., Trautmann, T., and Yasui, M.: Validation of stratospheric and mesospheric ozone observed by SMILES from International Space Station, Atmos. Meas. Tech., 6, 2311–2338, doi:10.5194/amt-6-2311-2013, 2013.

Kikuchi, K., Nishibori, T., Ochiai, S., Ozeki, H., Irimajiri, Y., Kasai, Y., Koike, M., Manabe, T., Mizukoshi, K., Murayama, Y., Nagahama, T., Sano, T., Sato, R., Seta, M., Takahashi, C., Takayanagi, M., Masuko, H., Inatani, J., Suzuki, M., and Shiotani, M.: Overview and early results of the Superconducting Submillimeter-Wave Limb-Emission Sounder (SMILES), J. Geophys. Res., 115, D23 306, doi:10.1029/2010JD014379, 2010.

Knight, S.: Building software with SCons, Computing in Science & Eng., 7, 79–88, doi:10.1109/MCSE.2005.11(410)7, 2005.

Ko, M., Daniel, J. S., Herman, J. R., Newman, P. A., and Ramaswamy, V.: The Future and Recovery, in: Trends in Emissions of Ozone-Depleting Substances, Ozone Layer Recovery, and Implications for Ultraviolet Radiation Exposure, edited by Ravishankara, A., Kurylo, M. J., and Ennis, C. A., pp. 133–154, Department of Commerce, NOAA's National Climatic Data Center, Asheville, NC, 2008.

Kuze, A., Suto, H., Nakajima, M., and Hamazaki, T.: Thermal and near infrared sensor for carbon observation Fourier-transform spectrometer on the Greenhouse Gases Observing Satellite for greenhouse gases monitoring, Appl. Opt., 48, 6716–6733, doi:10.1364/AO.48.006716, 2009.

Kyrölä, E., Tamminen, J., Leppelmeier, G., Sofieva, V., Hassinen, S., Bertaux, J., Hauchecorne, A., Dalaudier, F., Cot, C., Korablev, O., d'Andon, O. F., Barrot, G., Mangin, A., Théodore, B., Guirlet, M., Etanchaud, F., Snoeij, P., Koopman, R., Saavedra, L., Fraisse, R., Fussen, D., and Vanhellemont, F.: GOMOS on Envisat: an overview, Adv. Space Res., 33, 1020–1028, doi:10.1016/S0273-1177(03)00590-8, 2004.

Landgraf, J. and Hasekamp, O. P.: Retrieval of tropospheric ozone: The synergistic use of thermal infrared emission and ultraviolet reflectivity measurements from space, J. Geophys. Res., 112, D08 310, doi:10.1029/2006JD008097, 2007.

Lawson, C., Hanson, R., Kincaid, D., and Krogh, F.: Basic Linear Algebra Subprograms for Fortran Usage, ACM Trans. Math. Soft., 5, 308–323, 1979.

Liebe, H., Hufford, G., and Cotton, M.: Propagation Modeling of Moist Air and Suspended Water/Ice Particles at Frequencies below 1000 GHz, in: 52nd Specialists Meeting of the Electromagnetic Wave Propagation Panel, AGARD, 1993.

Liou, K.-N.: An Introduction to Atmospheric Radiation, Academic Press, second edn., 2002.

Livesey, N., Van Snyder, W., Read, W., and Wagner, P.: Retrieval algorithms for the EOS Microwave limb sounder (MLS), IEEE Trans. Geosci. Remote Sens., 44, 1144–1155, doi:10.1109/TGRS.2006.872327, 2006.

Livesey, N. J., Filipiak, M. J., Froidevaux, L., Read, W. G., Lambert, A., Santee, M. L., Jiang, J. H., Pumphrey, H. C., Waters, J. W., Cofield, R. E., Cuddy, D. T., Daffer, W. H., Drouin, B. J., Fuller, R. A., Jarnot, R. F., Jiang, Y. B., Knosp, B. W., Li, Q. B., Perun, V. S., Schwartz, M. J., Snyder, W. V., Stek, P. C., Thurstans, R. P., Wagner, P. A., Avery, M., Browell, E. V., Cammas, J.-P., Christensen, L. E., Diskin, G. S., Gao, R.-S., Jost, H.-J., Loewenstein, M., Lopez, J. D., Nedelec, P., Osterman, G. B., Sachse, G. W., and Webster, C. R.: Validation of Aura Microwave Limb Sounder O_3 and CO observations in the upper troposphere and lower stratosphere, J. Geophys. Res., 113, n/a–n/a, doi:10.1029/2007JD008805, 2008.

Livesey, N. J., Logan, J. A., Santee, M. L., Waters, J. W., Doherty, R. M., Read, W. G., Froidevaux, L., and Jiang, J. H.: Interrelated variations of O_3, CO and deep convection in the tropical/subtropical upper troposphere observed by the Aura Microwave Limb Sounder (MLS) during 20042011, Atm. Chem. Phys., 13, 579–598, doi:10.5194/acp-13-579-2013, 2013.

Llewellyn, E., Lloyd, N., Degenstein, D., Gattinger, R., Petelina, S., Bourassa, A., Wiensz, J., Ivanov, E., McDade, I., Solheim, B., McConnell, J., Haley, C., von Savigny, C., Sioris, C., McLinden, C., Griffioen, E., Kaminski, J., Evans, W., Puckrin, E., Strong, K., Wehrle, V., Hum, R., Kendall, D., Matsushita, J., Murtagh, D., Brohede, S., Stegman, J., Witt, G., Barnes, G., Payne, W., Piché, L., Smith, K., Warshaw, G., Deslauniers, D.-L., Marchand, P., Richardson, E., King, R., Wevers, I., McCreath, W., Kyrölä, E., Oikarinen, L., Leppelmeier, G., Auvinen, H., Mégie, G., Hauchecorne, A., Lefèvre, F., de La Nöe, J., Ricaud, P., Frisk, U., Sjoberg, F., von Schéele, F., and Nordh, L.: The OSIRIS instrument on the Odin spacecraft, Can. J. Phys., 82, 411–422, doi:10.1139/p04-005, 2004.

Lossow, S., Urban, J., Eriksson, P., Murtagh, D., and Gumbel, J.: Critical parameters for the retrieval of mesospheric water vapour and temperature from Odin/SMR limb measurements at 557 GHz, Adv. Space Res., 40, 835–845, doi:10.1016/j.asr.2007.05.026, 2007.

Mair, U., Krocka, M., Wagner, G., Birk, M., Hübers, H.-W., Richter, H., Semenov, A., Hoogeveen, R., de Graauw, T., Yagoubov, P., Maurellis, A., Selig, A., Koshelets, V., Shitov, S., Goltsman, G., Voronov, B., Ellison, B., Kerridge, B., Matheson, D., Siddans, R., and Reburn, J.: TELIS — Development of a New Balloon Borne THz/Submm Heterodyne Limb Sounder, in: Proceedings of the 14. International Symposium on Space Terahertz Technology, Tucson, AZ, USA, April 2003, pp. 204–214, 2004.

Mendrok, J., Schreier, F., and Höpfner, M.: Estimating cirrus cloud properties from MIPAS data, Geophys. Res. Letters, 34, L08 807, doi:10.1029/2006GL028246, 2007.

Morozov, V. A.: On the solution of functional equations by the method of regularization, Soviet Math. Dokl., 7, 414–417, 1966.

Murtagh, D., Frisk, U., Merino, F., Ridal, M., Jonsson, A., Stegman, J., Witt, G., Eriksson, P., Jiménez, C., Megie, G., de la Noë, J., Ricaud, P., Baron, P., Pardo, J. R., Hauchcorne, A., Llewellyn, E. J., Degenstein, D. A., Gattinger, R. L., Lloyd, N. D., Evans, W. F., McDade, I. C., Haley, C. S., Sioris, C., von Savigny, C., Solheim, B. H., McConnell, J. C., Strong, K., Richardson, E. H., Leppelmeier, G. W., Kyrölä, E., Auvinen, H., and Oikarinen, L.: An overview of the Odin atmospheric mission, Can. J. Phys., 80, 309–319, doi:10.1139/p01-157, 2002.

Ngo, N., Lisak, D., Tran, H., and Hartmann, J.-M.: An isolated line-shape model to go beyond the Voigt profile in spectroscopic databases and radiative transfer codes, J. Quant. Spectrosc. & Radiat. Transfer, 129, 89 – 100, doi:10.1016/j.jqsrt.2013.05.034, erratum: JQSRT 134, 105 (2014), 2013.

Norton, R. and Rinsland, C.: ATMOS data processing and science analysis methods, Appl. Opt., 30, 389–400, doi:10.1364/AO.30.000389, 1991.

Olivero, J. and Longbothum, R.: Empirical Fits to the Voigt Line Width: a brief Review, J. Quant. Spectrosc. & Radiat. Transfer, 17, 233–236, doi:10.1016/0022-4073(77)90161-3, 1977.

O'Sullivan, F. and Wahba, G.: A cross validated Bayesian retrieval algorithm for nonlinear remote sensing experiments, J. Comput. Phys., 59, 441–455, 1985.

Parker, R.: Geophysical Inverse Theory, Princeton University Press, 1994.

Petty, G. W.: A First Course in Atmospheric Radiation, Sundog Publishing, Madison, Wisconsin, second edn., 2006.

Pickett, H.: Microwave Limb Sounder THz module on Aura, IEEE Trans. Geosci. Remote Sens., 44, 1122–1130, doi:10.1109/TGRS.2005.862667, 2006.

Pickett, H. and Peterson, D.: Stratospheric OH Measurements with a Far–Infrared Limb Observing Spectrometer, J. Geophys. Res., 98, 20 507–20 515, 1993.

Pickett, H., Poynter, R., Cohen, E., Delitsky, M., Pearson, J., and Müller, H.: Submillimeter, millimeter, and microwave spectral line catalog, J. Quant. Spectrosc. & Radiat. Transfer, 60, 883–890, doi:10.1016/S0022-4073(98)00091-0, 1998.

Pumphrey, H. C. and Bühler, S.: Instrumental and spectral parameters: their effort on and measurement by microwave limb sounding of the atmosphere, J. Quant. Spectrosc. & Radiat. Transfer, 64, 421–437, doi:10.1016/S0022-4073(99)00106-5, 2000.

Pumphrey, H. C., Filipiak, M. J., Livesey, N. J., Schwartz, M. J., Boone, C., Walker, K. A., Bernath, P., Ricaud, P., Barret, B., Clerbaux, C., Jarnot, R. F., Manney, G. L., and Waters, J. W.: Validation of middle-atmosphere carbon monoxide retrievals from the Microwave Limb Sounder on Aura, J. Geophys. Res., 112, n/a–n/a, doi:10.1029/2007JD008723, 2007.

Ridolfi, M., Carli, B., Carlotti, M., Clarmann, T. v., Dinelli, B. M., Dudhia, A., Flaud, J.-M., Hpfner, M., Morris, P. E., Raspollini, P., Stiller, G., and Wells, R. J.: Optimized forward model and retrieval scheme for MIPAS near-real-time data processing, Appl. Opt., 39, 1323–1340, 2000.

Rodgers, C.: Inverse Methods for Atmospheric Sounding: Theory and Practise, World Scientific, Singapore, 2000.

Rodgers, C. and Connor, B.: Intercomparison of remote sounding instruments, J. Geophys. Res., 108, 4116, doi:10.1029/2002JD002299, 2003.

Rothman, L., Gordon, I., Babikov, Y., Barbe, A., Benner, D. C., Bernath, P., Birk, M., Bizzocchi, L., Boudon, V., Brown, L., Campargue, A., Chance, K., Cohen, E., Coudert, L., Devi, V., Drouin, B., Fayt, A., Flaud, J.-M., Gamache, R., Harrison, J., Hartmann, J.-M., Hill, C., Hodges, J., Jacquemart, D., Jolly, A., Lamouroux, J., Roy, R. L., Li, G., Long, D., Lyulin, O., Mackie, C., Massie, S., Mikhailenko, S., Müller, H., Naumenko, O., Nikitin, A., Orphal, J., Perevalov, V., Perrin, A., Polovtseva, E., Richard, C., Smith, M., Starikova, E., Sung, K., Tashkun, S., Tennyson, J., Toon, G., Tyuterev, V., and Wagner, G.: The HITRAN2012 molecular spectroscopic database, J. Quant. Spectrosc. & Radiat. Transfer, 130, 4–50, doi:10.1016/j.jqsrt.2013.07.002, 2013.

Russell, J. M., Gordley, L. L., Park, J. H., Drayson, S. R., Hesketh, W. D., Cicerone, R. J., Tuck, A. F., Frederick, J. E., Harries, J. E., and Crutzen, P. J.: The Halogen Occultation Experiment, J. Geophys. Res., 98, 10 777–10 797, doi:10.1029/93JD00799, 1993.

Schepers, D., Guerlet, S., Butz, A., Landgraf, J., Frankenberg, C., Hasekamp, O., Blavier, J.-F., Deutscher, N. M., Griffith, D. W. T., Hase, F., Kyro, E., Morino, I., Sherlock, V., Sussmann, R., and Aben, I.: Methane retrievals from Greenhouse Gases Observing Satellite (GOSAT) shortwave infrared measurements: Performance comparison of proxy and physics retrieval algorithms, J. Geophys. Res., 117, D10 307, doi:10.1029/2012JD017549, 2012.

Schimpf, B. and Schreier, F.: Robust and Efficient Inversion of Vertical Sounding Atmospheric High–Resolution Spectra by Means of Regularization, J. Geophys. Res., 102, 16 037–16 055, 1997.

Schreier, F.: Optimized evaluation of a large sum of functions using a three-grid approach, Comp. Phys. Comm., 174, 783–802, doi:10.1016/j.cpc.2005.12.015, 2006.

Schreier, F.: Optimized Implementations of Rational Approximations for the Voigt and Complex Error Function, J. Quant. Spectrosc. & Radiat. Transfer, 112, 1010–1025, doi:10.1016/j.jqsrt.2010.12.010, 2011.

Schreier, F. and Böttger, U.: MIRART, A Line-By-Line Code for Infrared Atmospheric Radiation Computations incl. Derivatives, Atmos. & Oceanic Optics, 16, 262–268, 2003.

Schreier, F. and Schimpf, B.: A New Efficient Line–By–Line Code for High Resolution Atmospheric Radiation Computations incl. Derivatives, in: IRS 2000: Current Problems in Atmospheric Radiation, edited by Smith, W. and Timofeyev, Y., pp. 381–384, A. Deepak Publishing, 2001.

Schreier, F., Gimeno García, S., Milz, M., Kottayil, A., Höpfner, M., von Clarmann, T., and Stiller, G.: Intercomparison of three microwave/infrared high resolution line-by-line radiative transfer codes, in: Radiation Processes in the Atmosphere and Ocean (IRS2012): Proceedings of the International Radiation Symposium (IRC/IAMAS), edited by Cahalan, R. F. and Fischer, J., vol. 1531 of *AIP Conference Proceedings*, pp. 119–122, doi:10.1063/1.4804722, 2013.

Schreier, F., Gimeno García, S., Hedelt, P., Hess, M., Mendrok, J., Vasquez, M., and Xu, J.: GARLIC – A General Purpose Atmospheric Radiative Transfer Line-by-Line Infrared-Microwave Code: Implementation and Evaluation, J. Quant. Spectrosc. & Radiat. Transfer, 137, 29–50, doi:10.1016/j.jqsrt.2013.11.018, 2014.

Senten, C., De Mazière, M., Vanhaelewyn, G., and Vigouroux, C.: Information operator approach applied to the retrieval of the vertical distribution of atmospheric constituents from ground-based high-resolution FTIR measurements, Atmos. Meas. Tech., 5, 161–180, doi:10.5194/amt-5-161-2012, 2012.

SLATEC: Common Mathematical Library (Version 4.1), Available from NetLib, `http://www.netlib.org/slatec`, 1993.

Snieder, R. and Trampert, J.: Inverse Problems in Geophysics, Samizdat Press, `http://samizdat.mines.edu/`, 2000.

Steck, T. and von Clarmann, T.: Constrained profile retrieval applied to the observation mode of the Michelson interferometer for passive atmospheric sounding, Appl. Opt., 40, 3559–3571, 2001.

Stiller, G., von Clarmann, T., Funke, B., Glatthor, N., Hase, F., Höpfner, M., and Linden, A.: Sensitivity of trace gas abundances retrievals from infrared limb emission spectra to simplifying approximations in radiative transfer modelling, J. Quant. Spectrosc. & Radiat. Transfer, 72, 249–280, doi:10.1016/S0022-4073(01)00123-6, 2002.

Suttiwong, N.: Development and characteristics of the balloon borne instrument TELIS (TEhertz and submillimeter LImb Sounder): 1.8 THz receiver, Ph.D. thesis, University of Bremen, 2010.

Suttiwong, N., Birk, M., Wagner, G., Krocka, M., Wittkamp, M., Haschberger, P., Vogt, P., and Geiger, F.: Development and characterization of the balloon borne instrument TELIS (TEhertz and Submm LImb Sounder): 1.8 THz receiver, in: Proc. 19th ESA Symposium on European Rocket and Balloon Programmes and Related Research, Bad Reichenhall, Germany, 2009.

Takahashi, C., Ochiai, S., and Suzuki, M.: Operational retrieval algorithms for JEM/SMILES level 2 data processing system, J. Quant. Spectrosc. & Radiat. Transfer, 111, 160–173, doi:10.1016/j.jqsrt.2009.06.005, 2010.

Thomas, G. and Stamnes, K.: Radiative Transfer in the Atmosphere and Ocean, Cambridge University Press, doi:10.2277/0521890616, 1999.

Tikhonov, A.: On the Solution of Incorrectly Stated Problems and a Method of Regularization, Dokl. Acad. Nauk SSSR, 151, 501–504, 1963.

Tran, H., Ngo, N., and Hartmann, J.-M.: Efficient computation of some speed-dependent isolated line profiles, J. Quant. Spectrosc. & Radiat. Transfer, 129, 199 – 203, doi:10.1016/j.jqsrt.2013.06.015, erratum: JQSRT 134, 104 (2014), 2013.

Trefethen, L. and Bau III, D.: Numerical Linear Algebra, SIAM, Philadelphia, PA, 1997.

Twomey, S.: Introduction to the Mathematics of Inversion in Remote Sensing and Indirect Measurements, Elsevier, 1977.

Urban, J., Baron, P., Lautié, N., Schneider, N., Dassas, K., Ricaud, P., and Noë, J. D. L.: Moliere (v5): a versatile forward– and inversion model for the millimeter and sub–millimeter wavelength range, J. Quant. Spectrosc. & Radiat. Transfer, 83, 529–554, doi:10.1016/S0022-4073(03)00104-3, 2004.

Urban, J., Lautié, N., Flochmoën, E. L., Jiménez, C., Eriksson, P., Dupuy, E., Amraoui, L. E., Ekström, M., Frisk, U., Murtagh, D., de La Noë, J., Olberg, M., and Ricaud, P.: Odin/SMR Limb Observations of Stratospheric Trace Gases: Level 2 Processing of ClO, N_2O, O_3, and HNO_3, J. Geophys. Res., 110, doi:10.1029/2004JD005 741, 2005.

Van Vleck, J. H. and Huber, D. L.: Absorption, emission, and linebreadths: A semihistorical perspective, Rev. Mod. Phys., 49, 939–959, doi:10.1103/RevModPhys.49.939, 1977.

Van Vleck, J. H. and Weisskopf, V. F.: On the shape of collision-broadened lines, Rev. Mod. Phys., 17, 227–236, doi:10.1103/RevModPhys.17.227, 1945.

Varghese, P. and Hanson, R.: Collisional narrowing effects on spectral line shapes measured at high resolution, Appl. Opt., 23, 2376–2385, doi:10.1364/AO.23.002376, 1984.

Vasquez, M., Gottwald, M., Gimeno García, S., Krieg, E., Lichtenberg, G., Slijkhuis, S., Schreier, F., Snel, R., and Trautmann, T.: Venus Observations from ENVISAT–SCIAMACHY: Measurements and Modeling, Adv. Space Res., 51, 835–848, doi:10.1016/j.asr.2012.09.046, 2013a.

Vasquez, M., Schreier, F., Gimeno García, S., Kitzmann, D., Patzer, B., Rauer, H., and Trautmann, T.: Infrared radiative transfer in atmospheres of Earth-like planets around F, G, K, and M stars. II. Thermal emission spectra influenced by clouds, A & A, 557, A46, doi:10.1051/0004-6361/201220566, 2013c.

Vasquez, M., Schreier, F., Gimeno García, S., Kitzmann, D., Patzer, B., Rauer, H., and Trautmann, T.: Infrared radiative transfer in atmospheres of Earth-like planets around F, G, K, and M stars. I. Clear-sky thermal emission spectra and weighting functions, A & A, 549, A26, doi:10.1051/0004-6361/201219898, 2013b.

Verdes, C., Bühler, S., von Engeln, A., Kuhn, T., Künzi, K., Eriksson, P., and Sinnhuber, B.-M.: Pointing and temperature retrieval from millimeter–submillimeter limb soundings, J. Geophys. Res., 107, 4299, doi:10.1029/2001JD000777, 2002.

Vogel, C.: Computational Methods for Inverse Problems, SIAM, 2002.

von Clarmann, T., Glatthor, N., Grabowski, U., Höpfner, M., Kellmann, S., Kiefer, M., Linden, A., Tsidu, G. M., Milz, M., Steck, T., Stiller, G., Wang, D. Y., Fischer, H., Funke, B., Gil-López, S., and López-Puertas, M.: Retrieval of temperature and tangent altitude pointing from limb emission spectra recorded from space by the Michelson Interferometer for Passive Atmospheric Sounding (MIPAS), J. Geophys. Res., 108, 4736, doi:10.1029/2003JD003602, 2003.

von Clarmann, T., Höpfner, M., Kellmann, S., Linden, A., Chauhan, S., Funke, B., Grabowski, U., Glatthor, N., Kiefer, M., Schieferdecker, T., Stiller, G. P., and Versick, S.: Retrieval of temperature, H_2O, O_3, HNO_3, CH_4, N_2O, $ClONO_2$ and ClO from MIPAS reduced resolution nominal mode limb emission measurements, Atmos. Meas. Tech., 2, 159–175, doi:10.5194/amt-2-159-2009, 2009.

von Engeln, A. and Bühler, S.: Temperature profile determination from microwave oxygen emissions in limb sounding geometry, J. Geophys. Res., 107, ACL 12–1–ACL 12–15, doi:10.1029/2001JD001029, 2002.

Wahba, G.: Practical Approximate Solutions to Linear Operator Equations When the Data are Noisy, SIAM J. Num. Anal., 14, 651–667, 1977.

Wahba, G.: Spline Models for Observational Data, SIAM, Philadelphia, PA, 1990.

Waters, J., Hardy, J., Jarnot, R., Pickett, H., and Zimmerman, P.: A balloon–borne microwave limb sounder for stratospheric measurements, J. Quant. Spectrosc. & Radiat. Transfer, 32, 407–433, 1984.

Waters, J., Froidevaux, L., Harwood, R., Jarnot, R., Pickett, H., Read, W., Siegel, P., Cofield, R., Filipiak, M., Flower, D., Holden, J., Lau, G., Livesey, N., Manney, G., Pumphrey, H., Santee, M., Wu, D., Cuddy, D., Lay, R., Loo, M., Perun, V., Schwartz, M., Stek, P., Thurstans, R., Boyles, M., Chandra, K., Chavez, M., Chen, G.-S., Chudasama, B., Dodge, R., Fuller, R., Girard, M., Jiang, J., Jiang, Y., Knosp, B., LaBelle, R., Lam, J., Lee, K., Miller, D., Oswald, J., Patel, N., Pukala, D., Quintero, O., Scaff, D., Van Snyder, W., Tope, M., Wagner, P., and Walch, M.: The Earth observing system microwave limb sounder (EOS MLS) on the Aura Satellite, IEEE Trans. Geosci. Remote Sens., 44, 1075 – 1092, doi:10.1109/TGRS.2006.873771, 2006.

Weideman, J.: Computation of the Complex Error Function, SIAM J. Num. Anal., 31, 1497–1518, doi:10.1137/0731077, 1994.

Wetzel, G., Oelhaf, H., Ruhnke, R., Friedl-Vallon, F., Kleinert, A., Kouker, W., Maucher, G., Reddmann, T., Seefeldner, M., Stowasser, M., Trieschmann, O., von Clarmann, T., and Fischer, H.: NO_y partitioning and budget and its correlation with N_2O in the Arctic vortex and in summer midlatitudes in 1997, J. Geophys. Res., 107, ACH 3–1–ACH 3–10, doi:10.1029/2001JD000916, 2002.

Wetzel, G., Oelhaf, H., Friedl-Vallon, F., Kleinert, A., Lengel, A., Maucher, G., Nordmeyer, H., Ruhnke, R., Nakajima, H., Sasano, Y., Sugita, T., and Yokota, T.: Intercomparison and validation of ILAS-II version 1.4 target parameters with MIPAS-B measurements, J. Geophys. Res., 111, n/a–n/a, doi:10.1029/2005JD006287, 2006.

Wetzel, G., Oelhaf, H., Kirner, O., Friedl-Vallon, F., Ruhnke, R., Ebersoldt, A., Kleinert, A., Maucher, G., Nordmeyer, H., and Orphal, J.: Diurnal variations of reactive chlorine and

nitrogen oxides observed by MIPAS-B inside the January 2010 Arctic vortex, Atm. Chem. Phys., 12, 6581–6592, doi:10.5194/acp-12-6581-2012, 2012.

Woiwode, W., Oelhaf, H., Gulde, T., Piesch, C., Maucher, G., Ebersoldt, A., Keim, C., Höpfner, M., Khaykin, S., Ravegnani, F., Ulanovsky, A. E., Volk, C. M., Hösen, E., Dörnbrack, A., Ungermann, J., Kalicinsky, C., and Orphal, J.: MIPAS-STR measurements in the Arctic UTLS in winter/spring 2010: instrument characterization, retrieval and validation, Atmos. Meas. Tech., 5, 1205–1228, doi:10.5194/amt-5-1205-2012, 2012.

Wunch, D., Toon, G. C., Blavier, J.-F. L., Washenfelder, R. A., Notholt, J., Connor, B. J., Griffith, D. W. T., Sherlock, V., and Wennberg, P. O.: The Total Carbon Column Observing Network, Phil. Trans. R. Soc. A, 369, 2087–2112, doi:10.1098/rsta.2010.0240, 2011.

Xu, J., Schreier, F., Vogt, P., Doicu, A., and Trautmann, T.: A sensitivity study for far infrared balloon-borne limb emission sounding of stratospheric trace gases, Geosci. Instrum. Method. Data Syst. Disc., 3, 251–303, doi:10.5194/gid-3-251-2013, 2013.

Zdunkowski, W., Trautmann, T., and Bott, A.: Radiation in the Atmosphere — A Course in Theoretical Meteorology, Cambridge University Press, 2007.